

UNCLASSIFIED

AD NUMBER

AD866735

LIMITATION CHANGES

TO:

Approved for public release; distribution is unlimited.

FROM:

Distribution authorized to U.S. Gov't. agencies and their contractors;  
Administrative/Operational Use; MAR 1970. Other requests shall be referred to Air Force Flight Dynamics Lab., Wright-Patterson AFB, OH 45433.

AUTHORITY

AFFDL ltr 25 Jun 1981

THIS PAGE IS UNCLASSIFIED

THIS REPORT HAS BEEN DELIMITED  
AND CLEARED FOR PUBLIC RELEASE  
UNDER DOD DIRECTIVE 5200.20 AND  
NO RESTRICTIONS ARE IMPOSED UPON  
ITS USE AND DISCLOSURE.

**DISTRIBUTION STATEMENT A**

APPROVED FOR PUBLIC RELEASE;  
DISTRIBUTION UNLIMITED.

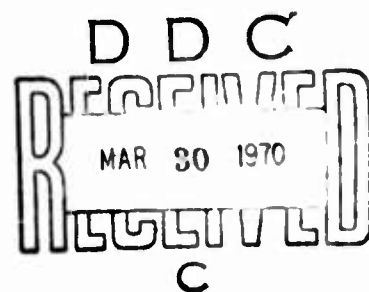
AD 866735

# PROPULSION EFFECTS ON AERODYNAMIC CHARACTERISTICS OF LIFTING REENTRY VEHICLES

Lockheed Missiles & Space Company  
A Group Division of Lockheed Aircraft Corporation

TECHNICAL REPORT AFFDL-TR-70-12

MARCH 1970



This document is subject to special export controls  
and each transmittal to foreign governments or foreign  
nationals may be made only with prior approval of the  
Air Force Flight Dynamics Laboratory.



AIR FORCE FLIGHT DYNAMICS LABORATORY  
AIR FORCE SYSTEMS COMMAND  
WRIGHT-PATTERSON AIR FORCE BASE, OHIO

## NOTICE

When Government drawings, specifications, or other data are used for any purpose other than in connection with a definitely related Government procurement operation, the United States Government thereby incurs no responsibility nor any obligation whatsoever; and the fact that the government may have formulated, furnished, or in any way supplied the said drawings, specifications, or other data, is not to be regarded by implication or otherwise as in any manner licensing the holder or any other person or corporation, or conveying any rights or permission to manufacture, use, or sell any patented invention that may in any way be related thereto.

ACCESSION IN:		
OFSTI	WHITE SECTION	<input type="checkbox"/>
DDC	DIFF SECTION	<input checked="" type="checkbox"/>
UNANNOUNCED		<input type="checkbox"/>
JUSTIFICATION		
BY		
DISTRIBUTION/AVAILABILITY CODES		
DIST.	AVAIL.	DDC/OF SPECIAL
2		

Copies of this report should not be returned unless return is required by security considerations, contractual obligations, or notice on a specific document.



# **PROPULSION EFFECTS ON AERODYNAMIC CHARACTERISTICS OF LIFTING REENTRY VEHICLES**

**Michael C. Fong and Carl F. Ehrlich, Jr.**

**This document is subject to special export controls  
and each transmittal to foreign governments or foreign  
nationals may be made only with prior approval of the  
Air Force Flight Dynamics Laboratory.**

## FOREWORD

This is the final report of work accomplished by the Lockheed Missiles & Space Company, Sunnyvale, California, a division of the Lockheed Aircraft Corporation, under Contract No. F33615-69-C-1228. The contract was initiated under Project No. 1366, Aerodynamics and Flight Mechanics, Task No. 136609, High Speed Aerodynamic Analysis Methods. The Lockheed document number for this report is LMSC-A960076.

This report provides the results of work performed during the period from 1 December 1968 to 31 August 1969. The work was administered under the direction of the Gas Dynamics Branch, Flight Mechanics Division of the Air Force Flight Dynamics Laboratory, Wright-Patterson Air Force Base, Ohio, Mr. Jack Flaherty (FDMG), Project Engineer.

At the Lockheed Missiles & Space Company, the work was performed by Dr. M. C. Fong, principal investigator, under the direction of Mr. C. F. Ehrlich, Jr., Program Manager. In addition to the authors, Mr. R. J. Kraus contributed to the exhaust plume correlation, Mr. A. J. Hief participated in the propulsion system study, and Mr. C. L. Stoner provided valuable guidance in code development of the separated flow program.

Special appreciation is given to Mrs. V. S. Sheetz for computation of aerodynamic characteristics, preparation of illustrations, and improvement of the computer program for the cross-flow boundary layer solution.

This report was submitted by the authors in March 1970. This technical report has been reviewed and is approved.



PHILIP P. ANTONATOS  
Chief, Flight Mechanics Division  
Air Force Flight Dynamics Laboratory

## ABSTRACT

A modified version of the Chapman-Korst model involving mass diffusion, equilibrium thermochemistry, and appropriate semiempirical relations is utilized to predict the overall flow characteristics within the plume-induced separated flow region during synergetic maneuvering of a lifting reentry vehicle. The exhaust plume selected in conjunction with the separated flow analysis is predicted on the basis of the method-of-characteristics solution with an average specific-heat ratio of 1.38. Thermochemical equilibrium is assumed to exist within the plume-induced separated flow region, and equilibrium temperature curves for various altitudes, vehicle Mach numbers, and propellant-air mixture ratios are presented. The strip method is incorporated in the analysis to estimate the three-dimensional separated flow characteristics caused by the vehicle geometry and vehicle attitude during the maneuver. The extent of validity of the strip method is established with the aid of a cross-flow boundary layer solution. On the basis of the present analytical model, the propulsion effects on aerodynamic characteristics of a simple lifting body configuration with delta planform and triangular cross section under a wide spectrum of freestream conditions have been evaluated and illustrated by appropriate design charts. Although the usefulness of the prediction method has been demonstrated, additional relevant data are required to finalize the theory development and to ensure a broad applicability of the analytical model.

(This abstract is subject to special export controls and each transmittal to foreign governments or foreign nationals may be made only with prior approval of the Air Force Flight Dynamics Laboratory.)

## TABLE OF CONTENTS

Section		Page
I	INTRODUCTION	1
II	ANALYSIS AND DISCUSSION	7
	1. Candidate Propulsion Systems	7
	2. Thermochemistry in Nozzle and in Plume Flow Field	10
	a. Propellant Combustion and Nozzle Flow	10
	b. Thermochemistry in Plume Flow Field	11
	3. Exhaust Plume Description	13
	a. Inviscid Plume Prediction	13
	b. $\gamma$ Variation in Exhaust Plume	45
	c. Nozzle Boundary Layer Effects	45
	d. Effect of Sting Support Concentric to the Nozzle	48
	e. Three-Dimensional Plume Effect	48
	4. Viscous Mixing Layer	50
	a. Laminar Shear Layer	50
	b. Turbulent Shear Layer	52
	c. Generalized Crocco Relation	55
	d. Afterburning in Mixing Layer	55
	e. Initial Boundary Layer Effects	57
	f. Shocks Imbedded in the Shear Layer	60
	5. Plume-Induced Boundary Layer Separation	60
	a. The Modified Chapman-Korst Model	61
	b. Computation Scheme	67
	6. Three-Dimensional Boundary Layer Effects	69
	a. Small Cross-Flow Solution	73
	b. Surface Separated Flow Pattern	78

Section		Page
III	APPLICATION TO A SIMPLE CONFIGURATION	81
	1. Prediction of Plume-Induced Flow Separation	82
	a. Important Features of Problem Solution	85
	b. Plume Effects on Aerodynamic Characteristics	91
	2. Critical Analysis	114
	a. Plateau Pressure Correlation	114
	b. Nash Factor	114
	c. Nozzle Wall Friction	114
	d. Chemical Kinetics in Nozzle and in Plume	114
	e. Rarefied Gas Effect	114
	f. Three-Dimensional Flow Effect	115
	g. Viscosity Parameter	115
	h. Shear Layer Profiles	115
	i. Equivalent Origin	115
	3. Simulation Parameters	115
	a. Mach Number	117
	b. Reynolds Number	117
	c. Jet-to-Ambient Pressure Ratio	118
	d. Jet Initial Turning Angle	118
	e. Jet Momentum Coefficient	118
	f. The Kawamura Lambda Parameter	118
	g. Knudsen Number	119
IV	CONCLUSIONS AND RECOMMENDATIONS	120
	a. Experimental Phase	120
	b. Theoretical Phase	121
Appendix		
I	PLUME-INDUCED BOUNDARY LAYER SEPARATION	122
II	LAMINAR CROSS-FLOW BOUNDARY LAYER ANALYSIS	156
III	ILLUSTRATIONS OF PREDICTED SEPARATION FOOTPRINTS	180
	REFERENCES	224

## ILLUSTRATIONS

Figure		Page
1	Analytical Model for Plume-Induced Separated Flow Prediction	3
2	Freestream Stagnation Enthalpy Versus Mach Number for Various Atmospheric Conditions	14
3	Hydrogen-Fluorine/Air Equilibrium Temperatures for $\Delta h_f = 0$	15
4	Hydrogen-Fluorine/Air Equilibrium Temperatures for $\Delta h_f = 5000$ Cal/Mole	16
5	Hydrogen-Fluorine/Air Equilibrium Temperatures for $\Delta h_f = 10,000$ Cal/Mole	17
6	Hydrogen-Fluorine/Air Equilibrium Temperatures for $\Delta h_f = 25,000$ Cal/Mole	18
7	Hydrogen-Fluorine/Air Equilibrium Temperatures for $\Delta h_f = 50,000$ Cal/Mole	19
8	Hydrogen-Fluorine/Air Equilibrium Temperatures for $\Delta h_f = 75,000$ Cal/Mole	20
9	Hydrogen-Fluorine/Air Equilibrium Temperatures for $\Delta h_f = 100,000$ Cal/Mole	21
10	Hydrogen-Fluorine/Air Equilibrium Temperatures for $\Delta h_f = 149,000$ Cal/Mole	22
11	Hydrogen-Oxygen/Air Equilibrium Temperatures for $\Delta h_f = 0$	23
12	Hydrogen-Oxygen/Air Equilibrium Temperatures for $\Delta h_f = 86,000$ Cal/Mole	24
13	Hydrogen-Oxygen/Air Equilibrium Temperatures for $\Delta h_f = 149,000$ Cal/Mole	25
14	Liquid Hydrogen/Liquid Fluorine/Air Equilibrium Temperatures for O/F = 12, $P_c = 500$ psi	26
15	Liquid Hydrogen/Liquid Fluorine/Air Equilibrium Temperatures for O/F = 12, $P_c = 500$ psi	27
16	Liquid Hydrogen/Liquid Fluorine/Air Equilibrium Temperatures for O/F = 12, $P_c = 500$ psi	28
17	Liquid Hydrogen/Liquid Oxygen/Air Equilibrium Temperatures for O/F = 6, $P_c = 500$ psi	29

Figure		Page
18	Liquid Hydrogen/Liquid Oxygen/Air Equilibrium Temperatures for O/F = 6, $P_c = 500$ psi	30
19	Liquid Hydrogen/Liquid Oxygen/Air Equilibrium Temperatures for O/F = 6, $P_c = 500$ psi	31
20	Sketches of Plume Structure	32
21	MOC Jet Plume in Quiescent Air	34
22	Plume Boundary Properties	35
23	MOC Jet Plume at $M_\infty = 10$	36
24	Effect of $\gamma$ on Exhaust Plume Contour	37
25	Exhaust Plume Contours for Various Ambient Pressures	39
26	Prediction of Distance to Maximum Plume Radius	41
27	Prediction of Maximum Plume Radius	42
28	Local Plume Radius as a Function of Maximum Plume Radius	43
29	Jet Boundary Coordinate System	44
30	Jet Boundaries Calculated by Approximate Method Compared With Method of Characteristics Solution from NASA TRR-6	46
31	Radius Ratio of Jet Boundary for $\gamma = 1.4$	47
32	Hydrogen-Fluorine Plume Boundary: $M_\infty = 0$ , $AR = 60$ , $P_\infty = 0.117$ psf	49
33	Comparison of Predicted and Measured Exhaust Plume Boundary at Angle of Attack	51
34	Velocity Function vs Distance Function for Constant Pressure Laminar Mixing Layer	53
35	Error Function Velocity Profile for Constant Pressure Turbulent Mixing Layer	54
36	Experimental and Theoretical Sigma Values for Free Jets	56
37	Initial Boundary Layer Effect on Plume-Induced Flow Separation	58
38	Plume-Induced Separation	62
39	Reynolds Number Effect on Plateau Pressure Coefficient	64
40	Variation of $A$ With $P_j/P_o$	65
41	Determination of Trailing Shock Pressure	68
42	Computer Flow for Simplified Scheme	70
43	Streamline Coordinate System and Control Volume	71

Figure		Page
44	Surface Oil Flow Pattern on the Compression Side of a Blunted Delta Slab at Mach 6.8	74
45	Comparison of Outer-Edge Velocities Based on Strip Theory and Small Cross-Flow Theory	75
46	Typical Similar Cross-Flow Velocity Profile	77
47	Separation Wedges and Surface Separation Contour	79
48	Computation Scheme for Determination of Separation Footprint	80
49	Plume-Induced Separation on Body With Delta Planform and Triangular Cross Section	82
50	Moment Arms From Leeside Centroid to Point at 60-Percent Chord	83
51	Suggested Upper Surface Flow Model	84
52	Separation Distance as a Function of Mach Number at Various Altitudes	86
53	Separation Distance vs Pressure Ratio for Various Mach Numbers	87
54	Geometrical Parameters for Delta-Triangle Body	92
55	$C_N$ , $C_A$ , and $C_M$ vs $\alpha$ for $M_\infty = 6$ at 230,000 ft	97
56	$C_N$ , $C_A$ , and $C_M$ vs $\alpha$ for $M_\infty = 6$ at 250,000 ft	98
57	$C_N$ , $C_A$ , and $C_M$ vs $\alpha$ for $M_\infty = 6$ at 280,000 ft	99
58	$C_N$ , $C_A$ , and $C_M$ vs $\alpha$ for $M_\infty = 10$ at 230,000 ft	100
59	$C_N$ , $C_A$ , and $C_M$ vs $\alpha$ for $M_\infty = 10$ at 250,000 ft	101
60	$C_N$ , $C_A$ , and $C_M$ vs $\alpha$ for $M_\infty = 10$ at 280,000 ft	102
61	$C_N$ , $C_A$ , and $C_M$ vs $\alpha$ for $M_\infty = 15$ at 230,000 ft	103
62	$C_N$ , $C_A$ , and $C_M$ vs $\alpha$ for $M_\infty = 15$ at 250,000 ft	104
63	$C_N$ , $C_A$ , and $C_M$ vs $\alpha$ for $M_\infty = 15$ at 280,000 ft	105
64	$C_N$ vs $C_M$ for Various Mach Numbers at 230,000 ft	106
65	$C_N$ vs $C_M$ for Various Mach Numbers at 250,000 ft	107
66	$C_N$ vs $C_M$ for Various Mach Numbers at 280,000 ft	108
67	$C_N$ vs $\alpha$ for Various Mach Numbers and Jet Pressure Ratios	109
68	$C_A$ vs $\alpha$ for Various Mach Numbers and Jet Pressure Ratios	110
69	$C_M$ vs $\alpha$ for Various Mach Numbers and Jet Pressure Ratios	111
70	Exhaust Plume Effect on L/D	112
71	Position of Separation as a Function of Incidence	116



Figure		Page
I-1	Plume-Induced Separation	125
I-2	Interpolation Scheme for Determination of $T_B$ and $Y_B$	143
I-3	Computer Flow	146
I-4	Comparison of Predicted and Measured Plume-Induced Length for a Cone-Cylinder-Flare Body in Supersonic Stream	147
I-5	Conservation of Mass and Species Fluxes for $X_s = 20$ ft	149
I-6	Conservation of Mass and Species Fluxes for $X_s = 30$ ft	150
I-7	Conservation of Mass and Species Fluxes for $X_s = 40$ ft	151
I-8	Determination of $Y_B$ and $\eta_{se}$ Satisfying all Conservation Requirements	152
I-9	Streamline Total Pressures for Various $\eta_{se}$ and $Y_B$	154
I-10	Determination of Trailing Shock Pressure and Separation Distance	155
II-1	Streamline Coordinate System	158
II-2	Cross-Flow Velocity Profile for $\beta = 0$ and $S_w = 0$	169
II-3	Cross-Flow Velocity Profile for $\beta = -0.1$ and $S_w = -0.8$	170
II-4	Cross-Flow Velocity Profile for $\beta = -0.1$ and $S_w = 1.0$	171
II-5	Cross-Flow Velocity Profile for $\beta = -0.235$ and $S_w = -0.4$	172
II-6	Cross-Flow Velocity Profile for $\beta = -0.326$ and $S_w = -1.0$	173
II-7	Cross-Flow Velocity Profile for $\beta = -0.325$ and $S_w = -0.325$	174
II-8	Cross-Flow Velocity Profile for $\beta = 0.5$ and $S_w = 1.0$	175
II-9	Cross-Flow Velocity Profile for $\beta = 1.0$ and $S_w = 1.0$	176
II-10	Cross-Flow Velocity Profile for $\beta = 1.5$ and $S_w = 1.0$	177
II-11	Cross-Flow Velocity Profile for $\beta = 2.0$ and $S_w = 1.0$	178
II-12	Blasius Velocity Profile	179
III-1	Separation Footprint on Windside Surface for $M_\infty = 6,230$ -Kft Alt, and $\alpha = 0$ deg	181
III-2	Separation Footprint on Leaside Surface for $M_\infty = 6,230$ -Kft Alt, and $\alpha = 0$ deg	182
III-3	Separation Footprint on Windside Surface for $M_\infty = 6,250$ -Kft Alt, and $\alpha = 0$ deg	183
III-4	Separation Footprint on Leaside Surface for $M_\infty = 6,250$ -Kft Alt, and $\alpha = 0$ deg	184
III-5	Separation Footprint on Windside Surface for $M_\infty = 6,280$ -Kft Alt, and $\alpha = 0$ deg	185

Figure		Page
III-6	Separation Footprint on Leeward Surface for $M_\infty = 6,280$ -Kft Alt, and $\alpha = 0$ deg	186
III-7	Separation Footprint on Windward Surface for $M_\infty = 10,230$ -Kft Alt, and $\alpha = 0$ deg	187
III-8	Separation Footprint on Windward Surface for $M_\infty = 10,250$ -Kft Alt, and $\alpha = 0$ deg	188
III-9	Separation Footprint on Leeward Surface for $M_\infty = 10,250$ -Kft Alt, and $\alpha = 0$ deg	189
III-10	Separation Footprint on Windward Surface for $M_\infty = 10,280$ -Kft Alt, and $\alpha = 0$ deg	190
III-11	Separation Footprint on Leeward Surface for $M_\infty = 10,280$ -Kft Alt, and $\alpha = 0$ deg	191
III-12	Separation Footprint on Windward surface for $M_\infty = 15,230$ -Kft Alt, and $\alpha = 0$ deg	192
III-13	Separation Footprint on Windward surface for $M_\infty = 15,250$ -Kft Alt, and $\alpha = 0$ deg	193
III-14	Separation Footprint on Windward surface for $M_\infty = 15,280$ -Kft Alt, and $\alpha = 0$ deg	194
III-15	Separation Footprint on Leeward Surface for $M_\infty = 15,280$ -Kft Alt, and $\alpha = 0$ deg	195
III-16	Separation Footprint on Windward Surface for $M_\infty = 6,230$ -Kft Alt, and $\alpha = +10$ deg	196
III-17	Separation Footprint on Leeward Surface for $M_\infty = 6,230$ -Kft Alt, and $\alpha = +10$ deg	197
III-18	Separation Footprint on Windward Surface for $M_\infty = 6,250$ -Kft Alt, and $\alpha = +10$ deg	198
III-19	Separation Footprint on Leeward Surface for $M_\infty = 6,250$ -Kft Alt, and $\alpha = +10$ deg	199
III-20	Separation Footprint on Windward Surface for $M_\infty = 6,280$ -Kft Alt, and $\alpha = +10$ deg	200
III-21	Separation Footprint on Leeward Surface for $M_\infty = 6,280$ -Kft Alt, and $\alpha = +10$ deg	201
III-22	Separation Footprint on Windward Surface for $M_\infty = 10,230$ -Kft Alt, and $\alpha = +10$ deg	202
III-23	Separation Footprint on Windward Surface for $M_\infty = 10,250$ -Kft Alt, and $\alpha = +10$ deg	203
III-24	Separation Footprint on Leeward Surface for $M_\infty = 10,250$ -Kft Alt, and $\alpha = +10$ deg	204

Figure		Page
III-25	Separation Footprint on Windside Surface for $M_\infty = 10$ , 280-Kft Alt, and $\alpha = +10$ deg	205
III-26	Separation Footprint on Leaside Surface for $M_\infty = 10$ , 280-Kft Alt, and $\alpha = +10$ deg	206
III-27	Separation Footprint on Leaside Surface for $M_\infty = 15$ , 230-Kft Alt, and $\alpha = +10$ deg	207
III-28	Separation Footprint on Leaside Surface for $M_\infty = 15$ , 250-Kft Alt, and $\alpha = +10$ deg	208
III-29	Separation Footprint on Windside Surface for $M_\infty = 15$ , 280-Kft Alt, and $\alpha = +10$ deg	209
III-30	Separation Footprint on Leaside Surface for $M_\infty = 15$ , 280-Kft Alt, and $\alpha = +10$ deg	210
III-31	Separation Footprint on Leaside Surface for $M_\infty = 6$ , 230-Kft Alt, and $\alpha = +20$ deg	211
III-32	Separation Footprint on Windside Surface for $M_\infty = 6$ , 250-Kft Alt, and $\alpha = +20$ deg	212
III-33	Separation Footprint on Leaside Surface for $M_\infty = 6$ , 250-Kft Alt, and $\alpha = +20$ deg	213
III-34	Separation Footprint on Windside Surface for $M_\infty = 6$ , 280-Kft Alt, and $\alpha = +20$ deg	214
III-35	Separation Footprint on Leaside Surface for $M_\infty = 6$ , 280-Kft Alt, and $\alpha = +20$ deg	215
III-36	Separation Footprint on Leaside Surface for $M_\infty = 10$ , 230-Kft Alt, and $\alpha = +20$ deg	216
III-37	Separation Footprint on Leaside Surface for $M_\infty = 10$ , 250-Kft Alt, and $\alpha = +20$ deg	217
III-38	Separation Footprint on Windside Surface for $M_\infty = 10$ , 280-Kft Alt, and $\alpha = +20$ deg	218
III-39	Separation Footprint on Leaside Surface for $M_\infty = 10$ , 280-Kft Alt, and $\alpha = +20$ deg	219
III-40	Separation Footprint on Leaside Surface for $M_\infty = 15$ , 230-Kft Alt, and $\alpha = +20$ deg	220
III-41	Separation Footprint on Leaside Surface for $M_\infty = 15$ , 250-Kft Alt, and $\alpha = +20$ deg	221
III-42	Separation Footprint on Windside Surface for $M_\infty = 15$ , 280-Kft Alt, and $\alpha = +20$ deg	222
III-43	Separation Footprint on Leaside Surface for $M_\infty = 15$ , 280-Kft Alt, and $\alpha = +20$ deg	223

## TABLES

		Page
I	Summary of Problem Solutions for Various Flow Regions	5
II	Propulsion Parameters (H <sub>2</sub> - F <sub>2</sub> System)	8
III	Propulsion Parameters (H <sub>2</sub> - O <sub>2</sub> System)	9
IV	Equilibrium Thermochemical Claculations for H <sub>2</sub> - F <sub>2</sub> and H <sub>2</sub> - O <sub>2</sub> Systems	12
V	Problem Solution Summary, α = 0 Degree	88
VI	Problem Solution Summary, α = 10 Degrees	89
VII	Problem Solution Summary, α = 20 Degrees	90
VIII	Predicted Aerodynamic Characteristics for Simple Delta Slab Configuration With and Without Plume Effects	113

## SYMBOLS

$A$	Coefficient in plateau pressure formula
$AR$	Nozzle area ratio
$A_f$	Separation footprint area
$A_l$	Leeside surface area
$A_w$	Windside surface area
$C_A$	Axial force coefficient
$C_M$	Pitching moment coefficient
$C_N$	Normal force coefficient
$c_p$	Constant-pressure specific heat
$C_p$	Pressure coefficient
$Cr$	Crocco Number, $\left[ \frac{\gamma - 1}{2} M^2 / \left( 1 + \frac{\gamma - 1}{2} M^2 \right) \right]^{1/2}$
$CR$	Mass flux ratio for exhaust gas in shear layer region, $\dot{m}_{\text{exhaust}} / (\dot{m}_{\text{exhaust}} + \dot{m}_{\text{air}})$
$D$	Drag
$d_c$	Distance of 60% along chord measured from the tip of the windside surface
$e_1, e_2$	metric coefficients
$\dot{E}$	Energy flux
$f$	Similarity function
$f_1, f_2$	Functions used in plume prediction formulas
$F_1, F_2$	Auxiliary integral functions associated with laminar flows

$F_A$	Axial force component
$F_N$	Normal force component for leeside surface
$F_w$	Normal force component for windside surface
$g$	Similarity function for cross flow
$h$	Static enthalpy
$H$	Stagnation enthalpy, $h + 1/2 (u^2 + v^2)$
$\Delta h_f$	Equivalent heat of formation for air at high Mach number
$I_1, I_2, I_3$	Auxiliary integral functions associated with turbulent flows
$K_1$	Curvature parameter, $(2\xi/e_1)(\partial e_1/\partial \xi)$
$K_2$	Dilatation parameter, $(2\xi/e_2)(\partial e_2/\partial \xi)$
$l$	Body length
$L$	Lift
$m$	$\frac{\gamma-1}{2} M_e^2$
$\hat{m}$	$1 + \frac{\gamma-1}{2} M_e^2$
$\dot{m}$	Mass flux
$\dot{m}_B$	Base bleed
$M$	Mach number
$\eta$	Molecular weight
$\eta$	Cross-flow length element (Appendix II)
$N$	Nash factor, $\frac{P_{ts} - P_B}{P_w - P_B}$ , or viscosity parameter, $\frac{\rho\mu}{\rho_o\mu_o}$
$p$	Static pressure
$Pr$	Prandtl number
$p_t$	Stagnation pressure
$q$	Dynamic pressure parameter, $1/2 \rho u^2 A$
$r$	Local body or plume radius

$R$	Gas constant or plume circular arc radius
$Re$	Reynolds number based on characteristic length
$\mathcal{Q}$	Universal gas constant
$s$	Streamwise length element (Appendix II) or Lees-Dorodnitsyn variable
$S$	Total enthalpy function, $\theta - 1$
$Sc$	Schmidt number
$T$	Static temperature
$T_t$	Total temperature
$u, v, w$	Velocity components
$x, y, z$	Curvilinear orthogonal coordinates
$x_o, y_o$	Coordinates for equivalent origin
$X, X', Z$	Moment arms for reference surfaces
$X_f, X'_f, Z_f$	Moment arms for separation footprints
$X_s$	Separation length measured from the forward stagnation point
$Y$	Species concentration
$\dot{Y}$	Diffusion rate
$\alpha$	Angle of attack
$\beta$	Pressure gradient parameter, $(2\xi/u_e)(\partial u_e/\partial \xi) \hat{m}$
$\beta^*$	$-(2\xi/\rho_e u_e^2)(\partial p/\partial \xi)$
$\bar{\beta}^*$	$\beta^* m$
$\gamma$	Ratio of specific heats
$\delta$	Boundary layer thickness
$\delta^*$	Displacement thickness
$\delta^{**}$	Momentum thickness
$\epsilon$	Small perturbation parameter, also exponent to indicate whether the flow is two-dimensional or axisymmetric

E	Eddy viscosity
$\xi, \eta, \zeta$	Transformed coordinates (Appendix II)
$\eta$	Similarity variable (for turbulent flow only in Appendix I)
$\zeta$	Similarity variable for laminar flow (Appendix I)
$\psi, \phi$	Stream functions
$\psi$	Angle deviation on plume surface
$\lambda$	Kawamura lambda parameter
$\Lambda$	Total temperature ratio, $\frac{RT_f}{R_a T_{t_a}}$
$\mu$	Dynamic viscosity
$\nu$	Kinematic viscosity, $\mu/\rho$ or Prandtl-Meyer angle
$\theta$	Total enthalpy ratio, $H/H_e$
$\rho$	Density
$\sigma$	Turbulent spreading parameter, $12 + 2.758 M$
$\phi$	Velocity ratio, $u/u_e$

### Subscripts

a	Reference state
aw	Adiabatic wall condition
B	Base or separation region
C	Combustion chamber condition
e	Outer-edge condition or stream-side shear layer
ex	Nozzle exit condition
j	Dividing streamline or plume-side shear layer
l	Leeside flow region
o	Local freestream condition or reference state



p	Plateau pressure
s	Discriminating streamline
t	Stagnation flow condition
w	Wake or recompression condition or windside flow region
$\infty$	Freestream condition
0, 1, 2 . . .	Zero-, first-, second-order solutions, etc.

## **Section I INTRODUCTION**

When a lifting reentry vehicle (LRV) undertakes aerodynamic maneuvering to effect orbital plane changes (synergetic maneuvering), two modes of operation are possible: aeroglide turn and aerocruise turn. Aeroglide turn refers to the maneuver using the aerodynamic turning capability of the vehicle in a normal unpowered glide; propulsion is required only for the initial deorbit impulse and for achieving the desired orbit or flight condition following completion of the turning maneuver. Aerocruise turn refers to the orbital change maneuver achieved by varying the vehicle aerodynamic forces through propulsive thrust manipulation. From the viewpoint of heating restraints, the aerocruise maneuver is superior to its aeroglide counterpart for synergetic plane changes (Ref. 1).

However, the presence of propulsive thrust, and an associated jet plume issuing from the rocket nozzle during the aerocruise maneuver can produce surface flow separation and, consequently, undesirable effects on vehicle aerodynamics. This separated flow phenomenon occurs because at high altitudes the expanded rocket exhaust plume would resemble a large hemisphere-cylinder afterbody which may induce an adverse pressure gradient too great for the boundary layer to remain attached on the vehicle surface. Experimental studies conducted by NASA (Refs. 2 through 5) and Mithras (Refs. 6 and 7) have revealed that jet pluming can indeed incur flow separation on the body surface under simulated high altitude flight conditions.

For sufficiently extensive plume-induced flow separation, the attendant local pressure elevation could result in significant losses in lift, stability, and control of the lifting reentry vehicle. Such losses in performance would seriously reduce the synergetic maneuvering potential of the vehicle, and the high L/D features brought forth by the aerocruise maneuver would be greatly compromised.

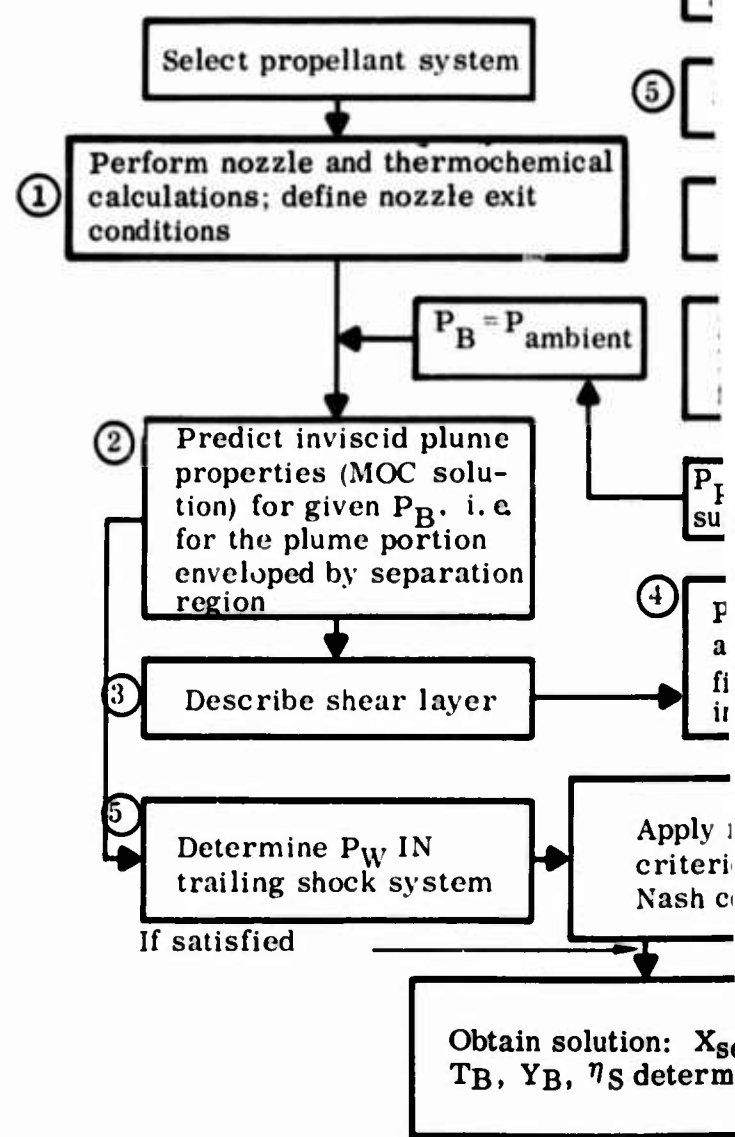
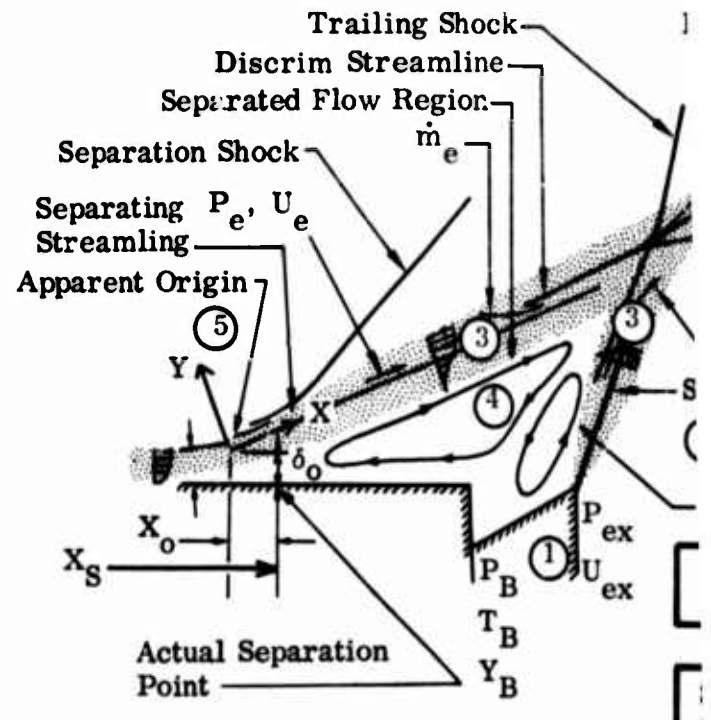
An efficient design of high-performance lifting reentry vehicles thus entails configuration development as well as a careful study of the exhaust plume effects on vehicle aerodynamic characteristics under realistic operating conditions. The present study is concerned exclusively with the latter aspect and encompasses the following objectives:

- Development of an analytical scheme to predict the overall flow characteristics in the plume-induced separation region on lifting reentry vehicles for a wide spectrum of flight variables
- Estimation of the effects of plume-induced separation on the aerodynamic characteristics of lifting surfaces
- Identification of important physical parameters which require further experimental information so that a meaningful and proficient wind tunnel test program for the follow-on study can be formulated

Specific tasks and various disciplines involved in the theory development are delineated in the text. For convenience and for order of discussion, these tasks are classified in terms of several flow regions, each essentially embracing a particular discipline. Figure 1 depicts these flow regions along with the analytical scheme, in flow-diagram form, for predicting the overall propulsion effects on LRV aerodynamic characteristics. Basic assumptions and salient features associated with each flow region are listed in Table I to provide a clear perspective of the analytical tasks performed during this study.

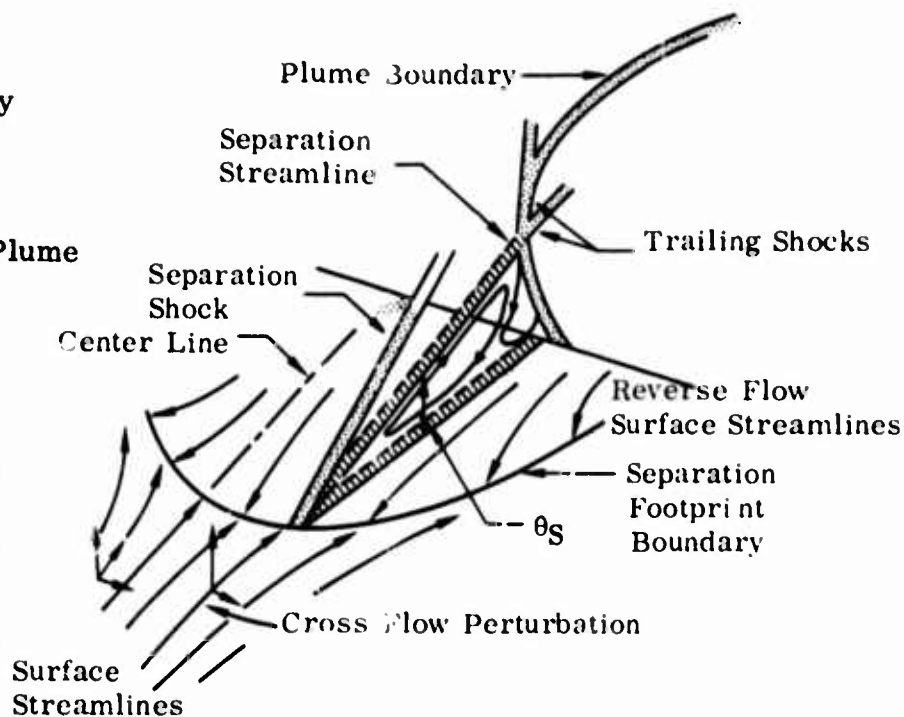
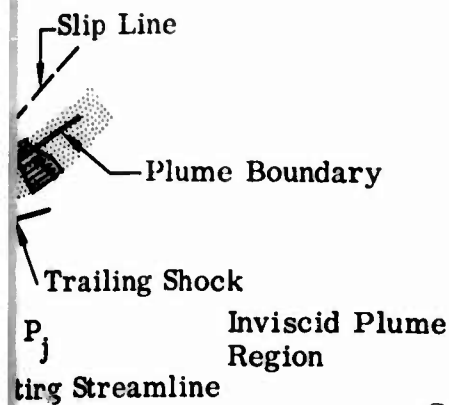
For completeness, detailed derivations of the pseudo-two-dimensional separated flow theory and the cross-flow perturbation theory developed during the study are included in the Appendixes. Also reviewed are the degree of approximation and limitations of the prediction method as a result of the lack of relevant data. Finally, the analytical model is demonstrated by means of a detailed analysis of a simple lifting body configuration with a delta planform and triangular cross section for a wide range of flight conditions. Appropriate design charts and easy-to-use semiempirical formulas are included.

# PLUME & SEPARATED FL



# THREE-DIMENSIONAL FLOW EFFECTS

PREDICTIONS



im Streamline

sign flow conditions:  
,  $\alpha$ , alt. etc.

particular pseudo-2-D  
region; e.g., plane of  
metry

ribe attached flow field

Assume location of  
separation point

rmine plateau pressure  
with semiempirical  
ula

$P_B$  const. base pres-  
dead-air model)

rm plume-induced sep-  
d flow analysis (modi-  
Chapman-Korst model.  
ding  $T_B$ ,  $Y_B$ ,  $\eta_s$  iteration)

achment  
including  
ection factor

$P_B$ ,

If not satisfied

Iterate

Perform separated flow  
analysis for other streamlines

Employ simplified analysis  
(strip method)

Consider  $P_B$  and  $P_W$  invariant  
for different strips (dead-air),  
therby defining local separa-  
tion wedge angle,  $\theta_s$

Define "local" plume bound-  
aries corresponding to dif-  
ferent 2-D strips

Determine local separation  
points using local plume con-  
tours and corresponding  $\theta_s$

Describe 3-D boundary layers  
with streamline coord system

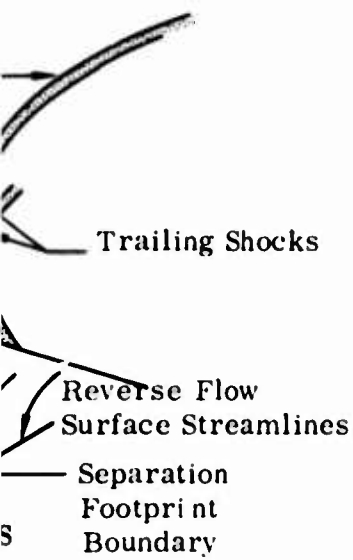
Perform cross-flow perturba-  
tion analysis

Determine local outer edge  
streamline from surface oil  
flow data

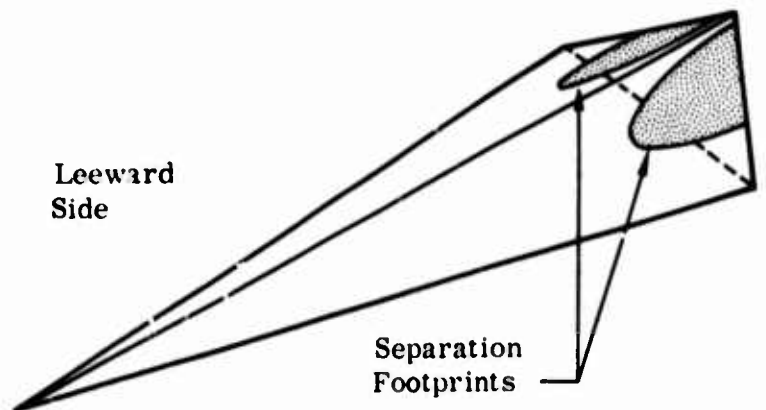
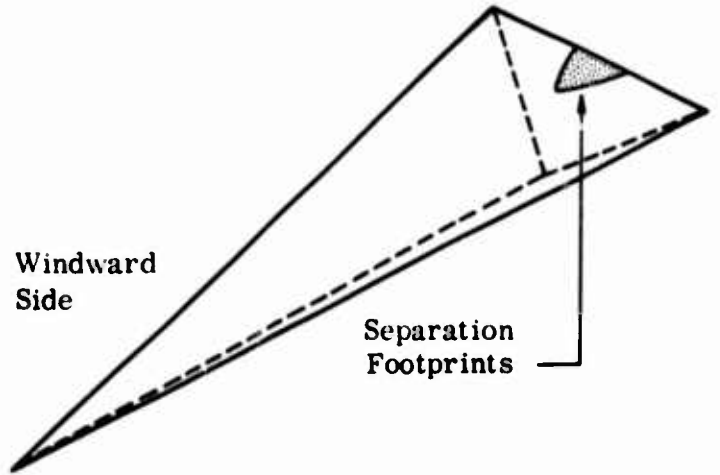
Compare with strip method;  
make necessary correction  
or establsih limitations of  
strip method

Obtain separation footprint

# DETERMINATION OF PLUME-INDUCED SEPARATION EFFECTS ON LRV AERODYNAMIC CHARACTERISTICS



bation



- Remarks: a. ① ② ③ ④ ⑤  
Represent main flow regions
- b. Further descriptions of flow regions presented in Table I

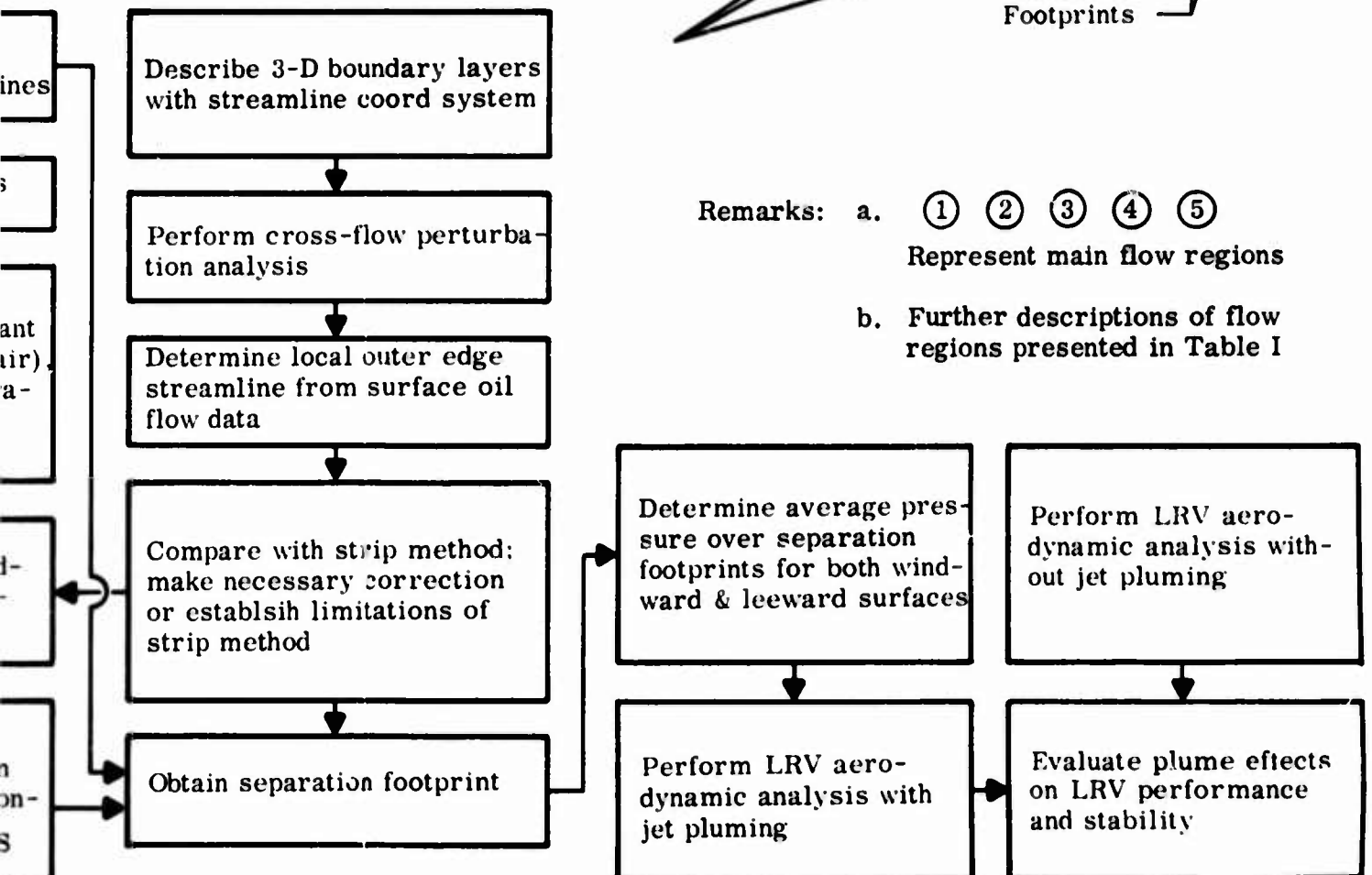


Figure 1 Analytical Model for Plume-Induced Separated Flow Prediction

Table I Summary of Problem So

Flow Region	Main Task	Basic Assumptions
① Propulsion system and nozzle flow	Coupling of fluid dynamics with thermochemistry	<ul style="list-style-type: none"> <li>Thermochemical equilibrium in chamber and base region</li> <li>1-D nozzle flow with constant <math>\gamma</math></li> </ul>
② Exhaust plume flow	Method-of-characteristics solution	<ul style="list-style-type: none"> <li>Perfect gas</li> <li>Inviscid, constant <math>\gamma</math>; steady-state, and axisymmetric</li> <li>Portion enveloped by separation region characterized by quiescent ambient condition (dead-air model discussed in ④)</li> <li>Pressure boundary condition alone to be satisfied for plumes in quiescent air (constant ambient pressure)</li> </ul>
③ Viscous mixing layer	Similarity solution for constant-pressure shear layer superimposed along inviscid plume boundary or emanating from separation point	<ul style="list-style-type: none"> <li>Perfect gas</li> <li>Zero longitudinal and lateral pressure gradients</li> <li>Chapman (laminar) and Korst (turbulent) models which lead to self-similar mixing layer profiles</li> <li>Linear viscosity-temperature relation</li> <li>Prandtl and Schmidt numbers equal to unity</li> <li>Equivalent-origin method to account for initial boundary-layer or disturbance effect</li> </ul>
④ Plume-induced boundary layer separation	Application of modified Chapman-Korst model with diffusion and equilibrium chemical reaction	<ul style="list-style-type: none"> <li>"Dead-air" in the plume-induced separated flow region in which all flow quantities are average values and the average flow velocity is zero</li> <li>Separation region describable by an equivalent solid wedge or conical flare</li> <li>Average separation pressure represented by plateau pressure</li> <li>Intersection of stream-side and plume-side shear layers resulting in a trailing shock system (see Fig. 1)</li> <li>Reattachment criterion - total pressure along discriminating streamline equal to static trailing shock pressure modified by a correction factor (Nash factor)</li> <li>Thermochemical equilibrium within the separation region</li> </ul>
⑤ Flow field surrounding the vehicle	Description of attached flow upstream of separation region, including 3-D boundary layer effects, for determining separation footprint and other properties	<ul style="list-style-type: none"> <li>Strip method for subdivision of narrow strips, each characterized by locally 2-D flow</li> <li>Base pressure and trailing shock pressure invariable from strip to strip</li> <li>Small cross-flow boundary layer</li> </ul>

A

## Solutions for Various Flow Regions

	Salient Features	Output Items
<p>d base</p>	<ul style="list-style-type: none"> <li>• <math>H_2-F_2</math> and <math>H_2-O_2</math> systems</li> <li>• Prediction of combustion temperatures for <math>P_c = 500</math> psi, <math>\gamma = 1.38</math> and <math>AR = 60</math></li> <li>• Constant <math>\gamma</math> selected to represent an average value during plume expansion</li> </ul>	<ul style="list-style-type: none"> <li>• Design charts for <math>H_2-F_2</math>/air and <math>H_2-O_2</math>/air systems for different altitudes and vehicle velocities, which can be incorporated in separate flow analysis for interpolating base temperature and base species concentration</li> </ul>
<p>rac- d-air</p>	<ul style="list-style-type: none"> <li>• Plume boundary being the outermost constant-property contour, i.e., constant temperature, pressure, Mach number, density, entropy, etc. (quiescent air)</li> <li>• MOC method for axisymmetric exhaust plumes</li> <li>• Simplified but more generalized plume prediction formulas based on MOC results</li> <li>• Latvala-Anderson 1-D model to determine initial plume boundary</li> </ul>	<ul style="list-style-type: none"> <li>• Design charts for axisymmetric plumes</li> <li>• Design charts for plume boundary properties</li> <li>• Simplified formulas for plume boundary prediction</li> </ul>
<p>lients models files y ltial</p>	<ul style="list-style-type: none"> <li>• Exponential-polynomial formula for Chapman laminar profile (from curve fitting scheme)</li> <li>• Error function formula for Korst turbulent profile</li> <li>• Generalized Crocco relation for correlating total enthalpy and concentration profiles with velocity profile</li> <li>• Mixing layer always turbulent on plume side but generally laminar on stream side</li> <li>• Superposition of mixing layer along inviscid plume boundary</li> <li>• Boundary shock imbedded in mixing layer ignored</li> </ul>	<ul style="list-style-type: none"> <li>• Similar solutions for laminar and turbulent shear layers</li> </ul>
<p>d flow rage o lent by le long rec-</p>	<ul style="list-style-type: none"> <li>• Plateau pressure formula in terms of jet-to-ambient pressure ratio</li> <li>• Iteration scheme for predicting separation length and other separated flow quantities with the aid of conservation requirements and equilibrium thermochemistry</li> </ul>	<ul style="list-style-type: none"> <li>• Analytical theory</li> <li>• Appropriate design charts to correlate separation length with Mach number and jet-to-ambient pressure ratio</li> </ul>
<p>rips, re</p>	<ul style="list-style-type: none"> <li>• Determination of separated flow properties for plane of symmetry with method discussed in ④</li> <li>• Utilization of strip method and constant base pressure concept to determine local separation distance</li> <li>• Establishment of limits of validity of strip method by means of small cross-flow boundary layer solution</li> <li>• Construction of separation footprint and other flow properties</li> <li>• Determination of aerodynamic characteristics and assessment of plume-induced separation effects on LRV performance and stability.</li> </ul>	<ul style="list-style-type: none"> <li>• Strip method for separation footprints</li> <li>• Cross-flow boundary layer solution</li> <li>• Design charts for aerodynamic characteristics for simple configuration with delta planform and triangular cross section with and without jet pluming.</li> </ul>



## Section II

### ANALYSIS AND DISCUSSION

This section presents a description of the analytical model for plume-induced flow separation. This model asserts that when the flow field on a LRV surface encounters a sufficiently strong adverse pressure gradient induced by the exhaust plume, a constant-pressure shear layer will emanate from some point on the vehicle surface and intersect with the corresponding shear layer along the plume boundary. A separated flow region and a trailing shock system are thus formed, accompanied by variation of local flow properties. Important flow regions, related phenomena, and the main tasks involved are listed in the Introduction. In this section, the discussion is devoted to detailed descriptions of these different flow regions, with emphasis on existing theories and unique features associated with this class of flow separation as well as simplifications and refinements underlying the present analytical approach.

#### 1. CANDIDATE PROPULSION SYSTEMS

Potential rocket engine candidates for representative lifting reentry vehicles were reviewed to determine typical propulsion system parameters. While the present study is not directed specifically to the analysis of a particular vehicle design, this approach was selected in order to limit the range of values to those which would bracket candidate systems. From this review, two propulsion systems have emerged as prime candidates, owing to their superior engine performance: hydrogen-fluorine ( $H_2-F_2$ ) and hydrogen-oxygen ( $H_2-O_2$ ). The important propulsion parameters for the hydrogen-fluorine system analyzed during a concurrent USAF study (Ref 8) and a similar hydrogen-oxygen system are presented in Tables II and III. Columns 1 and 2 in these tables present values for a small "throttleable" bell nozzle; and columns 3, 4, and 5 present values for a larger bell nozzle engine equivalent in rated thrust to the small engine. The two engines (large and small bells) can produce identical thrust for synergetic maneuvers as shown in Columns 2 and 3, although for considerably different chamber pressures and exit diameters. Variation of oxidizer-to-fuel ratio (O/F) for the particular oxidizer and fuel combinations are not expected to be significant within the limits of the present study. The remaining terms are the primary parameters which are to be varied over the indicated excursion range.

In the present study which is concerned with exhaust plume effects, a single set of representative propulsion parameters for both systems was selected for detailed analysis. The parameters include: chamber pressure of 500 psi, area ratio of 60, and nozzle half-angle of 9.5 degrees with O/F = 12 and 6 for the hydrogen-fluorine system and the hydrogen-oxygen system, respectively. Emphasis on exhaust plume description also attaches prominence to the prediction of propellant thermochemical properties discussed in the next section.

Table II Propulsion Parameters ( $H_2$ - $F_2$  System)

	Small Engine		Equivalent Large Engine			Excursions
	1	2	3	4	5	
Condition						
Thrust	2320	3330	3330	5000	15,000	
Throttle (%)	70	100	11.1	16.7	50	
Rated thrust (lb)	3330	3330	30,000	30,000	30,000	
$P_c$ (lb)	525	750	77.8	110	325	77.8-750
O/F	12	12	12	12	12	
Oxidizer	$F_2$	$F_2$	$F_2$	$F_2$	$F_2$	
Fuel	$H_2$	$H_2$	$H_2$	$H_2$	$H_2$	
AR	60	60	60	60	60	40-100
Nozzle lip angle (deg)	9.5	9.5	9.5	9.5	9.5	8-12
Exit diameter (in.)	13.60	13.60	43.82	43.82	43.82	12-50

Table III Propulsion Parameters ( $H_2-O_2$  System)

Condition	Small Engine		Equivalent Large Engine			Excursions
	1	2	3	4	5	
Thrust	2320	3330	3330	5000	15,000	
Throttle (%)	70	100	11.1	16.7	50	
Rated thrust (lb)	3330	3330	30,000	30,000	30,000	
$P_c$ (lb)	630	900	166	250	1,500	166-1500
O/F	6	6	6	6	6	
Oxidizer	$LO_2$	$LO_2$	$LO_2$	$LO_2$	$LO_2$	
Fuel	$LH_2$	$LH_2$	$LH_2$	$LH_2$	$LH_2$	
AR	60:1	60:1	60:1	60:1	60:1	40-100
Nozzle lib angle (deg)	9.5	9.5	9.5	9.5	9.5	8-12
Exit diameter (in.)	12.5	12.5	29.0	29.0	29.0	11-35

## 2. THERMOCHEMISTRY IN NOZZLE AND IN PLUME FLOW FIELD

### a. Propellant Combustion and Nozzle Flow

The overall thermodynamic properties in the nozzle and the exhaust plume flow fields associated with the candidate propulsion systems can be predicted by coupling thermochemistry with fluid flow analysis. In the combustion chamber, where the fluid motion is slow, equilibrium chemical calculations can be performed to ascertain the basic thermochemical parameters, such as gas temperature, species concentration, and specific heat ratio,  $\gamma$ . In recent years, calculation schemes to determine these quantities have been standardized and continuously improved by NASA-Lewis. As a result, a versatile equilibrium thermochemical computer program is now available for universal use (Ref 9). A complete listing of the NASA-Lewis program and the proper input format are included in Reference 9, which can be duplicated by anyone interested in full use of this program. In this report, however, calculated thermochemical results for the candidate propellant systems are presented in design chart form to permit temperature interpolation in connection with separated flow computations.

During nozzle expansion, nonequilibrium reactions prevail over a portion of the nozzle for which tedious computations and uncertain information on important reaction rates are frequently encountered. An expedient alternative is to implement Bray's "sudden freezing" criterion (Ref 10), in that the final flow is assumed to be initially characterized by "shifting" equilibrium (infinite reaction rates), but at some distance downstream of the throat, a "composition freeze" takes place suddenly. This model essentially postulates an infinitely thin nonequilibrium or transition zone and is valid if three-body recombination constitutes the controlling reaction process. By circumventing the nonequilibrium consideration, the relatively easy equilibrium or frozen flow calculations can be carried out to determine the thermochemical quantities in the chamber and in the nozzle. In most applications, sudden freezing leads to reasonable thermochemical estimates and occurs at area ratio less than 5. For the candidate propulsion systems considered in this analysis, the large area ratio (40 to 150) implies that species concentrations will have been frozen long before the flow reaches the nozzle exit.

In this study, the thermochemical problem in connection with the nozzle flow for a lifting reentry vehicle is treated as follows:

- In the combustion chamber, equilibrium chemical computations based on the NASA-Lewis program are performed to determine the thermochemical properties.
- In the nozzle portion, a one-dimensional inviscid flow field is assumed to exist. For most applications, low critical area ratios for sudden freezing are observed; hence, the assumption of composition freezing in the chamber is expected to result in valid first approximation. For simplicity, this chamber freezing model is postulated along with a constant  $\gamma$  value of 1.38 as an average "frozen" value. Selection of this relatively large  $\gamma$  value is consistent with the continual increase in  $\gamma$  and decrease in  $c_p$  during nozzle expansion under frozen flow conditions. The wall boundary layer effect is not expected to affect the nozzle flow significantly; its effect on plume properties will be discussed later.

Table IV presents typical thermochemical results for the candidate hydrogen-fluorine and hydrogen-oxygen systems, including equilibrium and frozen temperatures at different pressure ratios (or area ratios) that correspond to different nozzle locations.

Once the nozzle exit thermochemical properties are properly defined, the entire exhaust plume flow field can be described by means of inviscid flow analysis and gas-dynamic-thermochemical coupling.

#### b. Thermochemistry in Plume Flow Field

Beyond the nozzle exit, the thermochemical effects are of importance to LRV applications in two aspects:

- Plume geometry and other physical features are influenced by the thermochemical properties of the flow field, e.g., the specific heat ratio,  $\gamma$ , thereby affecting the plume-induced separation mechanism.
- Diffusion of the generally fuel-rich exhaust products may occur in the shear layer as well as in the base and plume-induced separation region. The ensuing mixing between the exhaust gas and the ambient air may initiate chemical reactions, causing an elevated base temperature\* and possible overheating of the vehicle surface. Deleterious by-products arising from chemical reactions, if existing, may lead to surface corrosion after prolonged exposure.

In view of the constant  $\gamma$  model for plume description adopted in the present analysis, this section focuses attention on establishing conditions where afterburning occurs and preparing appropriate temperature charts useful to plume-induced separated flow predictions.

As already mentioned in the Introduction and as will be further elaborated in a later section, the generalized Crocco relation is rendered valid as a result of the assumptions of unit Prandtl and Schmidt numbers and equilibrium chemical reactions. The local temperature and local exhaust-gas/ambient-air mixture ratio within the shear layer, including the plume-induced separation region, can then be ascertained. Based on the "flame sheet" concept, the afterburning properties along any shear layer streamlines can be estimated also. However, from the results of Reference 11, the reaction time and the ignition delay time vary inversely with ambient pressure, which render afterburning in a high-speed stream or shear layer almost impossible at altitudes near 100,000 feet. On the other hand, the plume-induced separation problem is an exception. In this case, the base region is characterized by a "dead-air" zone where the exhaust gas and the ambient air will diffuse, mix, and become stagnated. Therefore, a short characteristic ignition length is ensured despite the long reaction and ignition times, and the chemical equilibrium model is generally valid.

\*Base temperature and pressure refer to either base or plume-induced separation region.

Table IV Equilibrium Thermochemical Calculations for  $H_2-F_2$  and  $H_2-O_2$  Systems

(A) $H_2-F_2$	Cham	$X_1$		$X_2$		$X_3$		$X_4$		$X_5$	
		equil	frozen	equil	frozen	equil	frozen	equil	frozen	equil	frozen
$P_c/P$	1.00	12.5	12.5	39.6	39.6	91.5	91.5	236	236	381	381
$P$ (atm)	34.02	2.72	2.72	0.86	0.86	0.372	0.372	0.144	0.144	0.09	0.09
$T$ ( $^{\circ}K$ )	4459	3296	2369	2825	1740	2477	1377	2056	1045	1841	907
AR	-----	2.67	2.3	6.13	4.72	11.39	8.16	22.81	15.3	32.13	21.04

(B) $H_2-O_2$	Cham	$X_1$		$X_2$		$X_3$		$X_4$		$X_5$	
		equil	frozen	equil	frozen	equil	frozen	equil	frozen	equil	frozen
$P_c/P$	1.00	12.5	12.5	39.6	39.6	91.5	91.5	236	236	381	381
$P$ (atm)	34.02	2.72	2.72	0.86	0.86	0.372	0.372	0.144	0.144	0.09	0.09
$T$ ( $^{\circ}K$ )	3506	2739	2252	2382	1813	2105	1536	1792	1262	1643	1138
AR	-----	2.82	2.58	6.55	5.71	12.33	10.44	25.35	20.92	36.49	29.74

NOTE: Cham represents chamber conditions.  
 $X_1$ ,  $X_2$ , etc. refer to different nozzle locations.

For the present LRV application, only the dead-air case is considered for afterburning calculations. The equilibrium model is adopted and design curves are prepared which correlate equilibrium base temperature with exhaust-gas mixture ratio, CR (ratio of exhaust mass to total mass of exhaust gas and air), for various ambient pressures (or altitudes) and equivalent heat of formation,  $\Delta h_f$ . The latter quantity is defined as the enthalpy in calories per mole of air converted from the kinetic energy of the high-speed stream. In other words, when the free stream is stagnated in a dead-air region, the chemical system within this region will experience an increase in internal energy arising from the kinetic energy conversion. Thermochemical calculations are therefore performed by incorporating this heat of formation term which depends on Mach number and altitudes, as shown in Figure 2. Figures 3 through 19 depict the appropriate temperature design curves. It should be remarked that the temperature and CR values on these graphs are synonymous to  $T_B$  and  $Y_B$  used in conjunction with the plume-induced separated flow iteration scheme described in Section 5 and Appendix I.

### 3. EXHAUST PLUME DESCRIPTION

For a balanced exhaust jet (nozzle exit pressure equal to ambient pressure), the flow field can be successfully described by means of a viscous shear layer model shown in Figure 20a. Analytical solutions have been obtained not only for laminar jets but also for turbulent jets with diffusion and chemical reactions (Refs 12 to 15). However, in most high-altitude applications, the rocket exhaust plume is under-expanded (nozzle exit pressure greater than ambient pressure) for which its basic structure is illustrated in Figure 20b. A comparatively simple method of treating underexpanded plume problems is to combine the solution of the inviscid exhaust plume with that of a viscous mixing layer (shear layer) which is assumed to grow continuously along the plume boundary. The near-field region, which features an extensive inviscid flow field and a thin shear layer, is particularly amenable to this approach. Inasmuch as plume-induced flow separation extends within the near-field region only, the phenomena of Mach disc, shock reflection, and turbulent wake occurring in the intermediate and far-field regions are neglected in the present analysis. Only the inviscid portion of the exhaust plume is considered here; the shear layer problem is discussed subsequently.

#### a. Inviscid Plume Prediction

The inviscid plume contour and its internal properties can be described accurately by employing the method of characteristics. The basic principles underlying the method-of-characteristics (MOC) solution for axisymmetric exhaust plumes and formulation of a computation scheme are discussed in detail in Reference 16. To proceed with the computation, the one-dimensional or axisymmetric MOC solution for the nozzle flow is first obtained to establish the nozzle exit conditions which represent the initial conditions for the exhaust plume. Then, step-by-step MOC numerical computation is carried out for the plume flow field until the free boundary or ambient pressure condition is satisfied. One computation scheme is to construct the left-running characteristics from point to point over the entire flow field to determine the local flow properties, including the locus for the ambient pressure points or the free boundary. A boundary shock is also formed downstream of the nozzle exit as a result of coalescing compression waves reflected from the boundary.



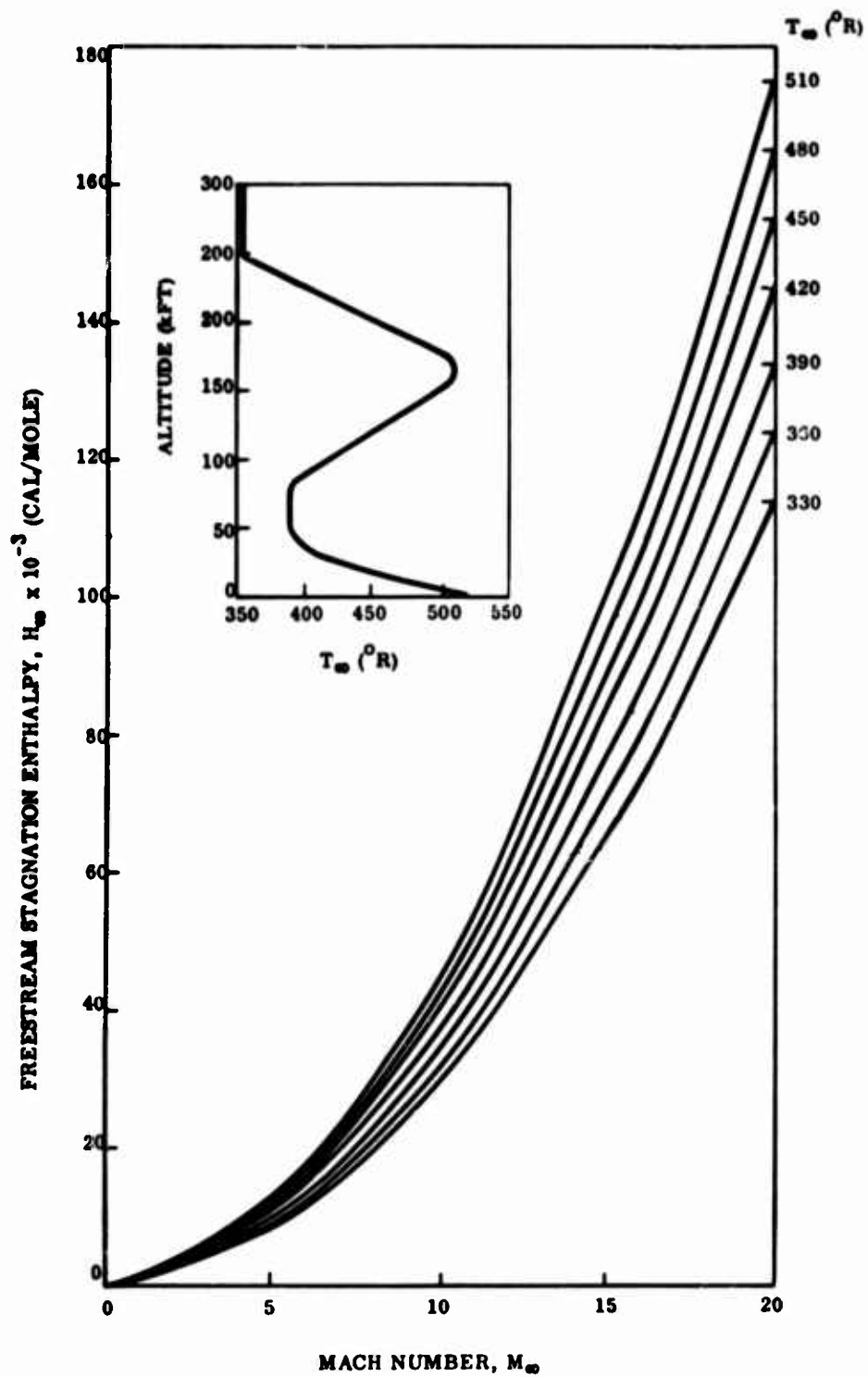


Figure 2 Freestream Stagnation Enthalpy Versus Mach Number for Various Atmospheric Conditions



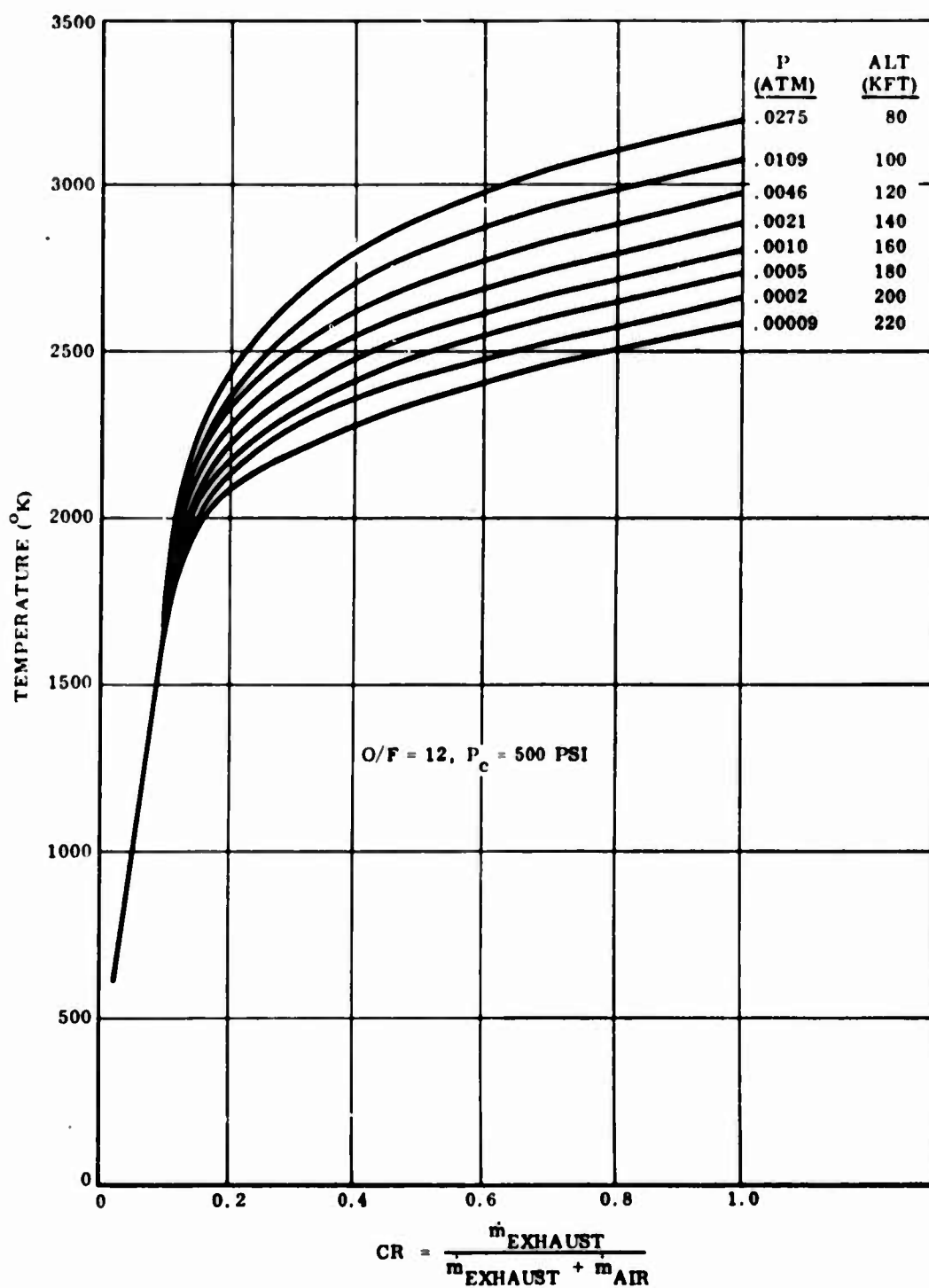


Figure 3 Hydrogen-Fluorine/Air Equilibrium Temperatures for  $\Delta h_f = 0$

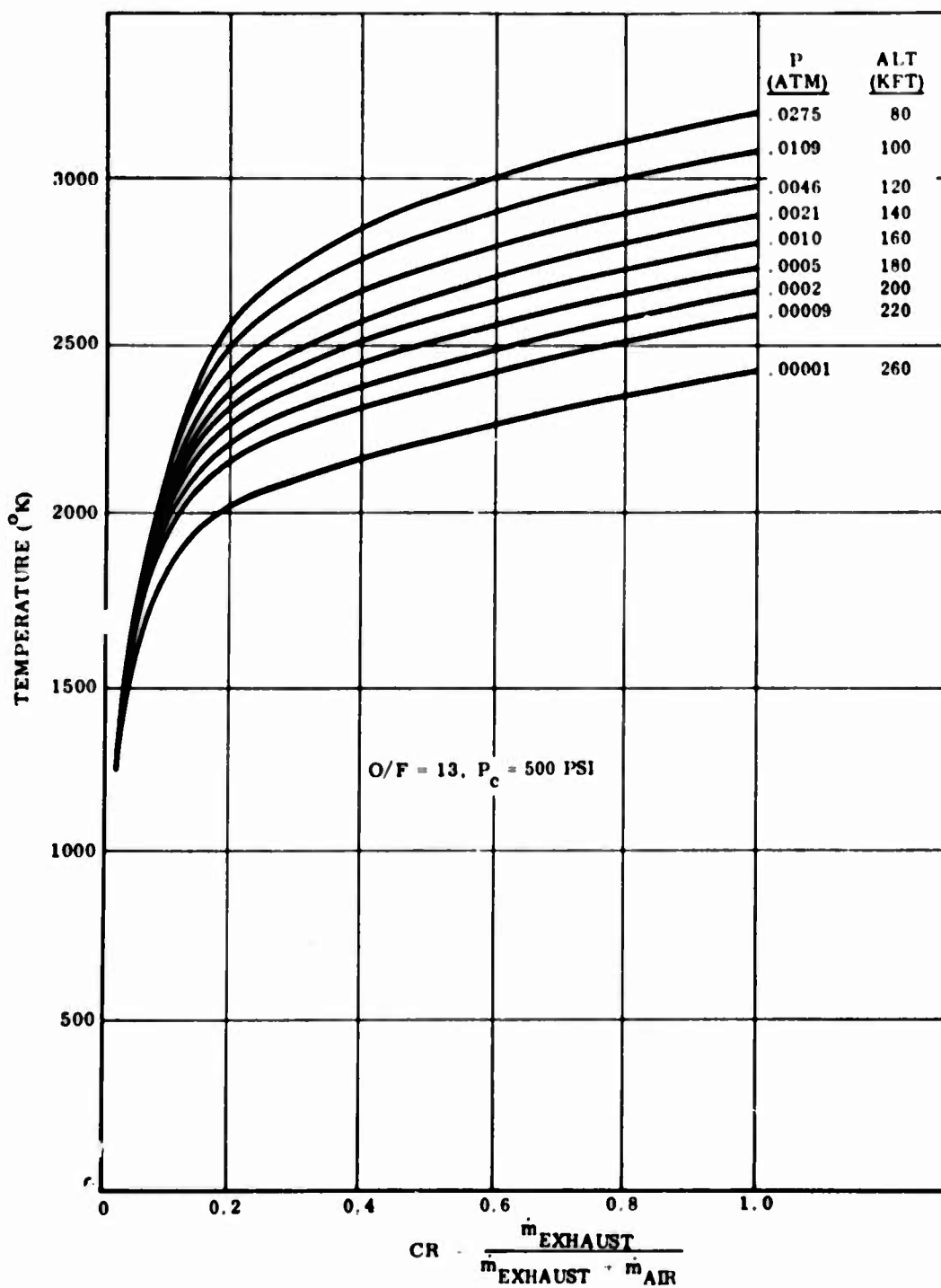


Figure 4 Hydrogen-Fluorine/Air Equilibrium Temperatures for  $\Delta h_f = 5000$  Cal/Mole

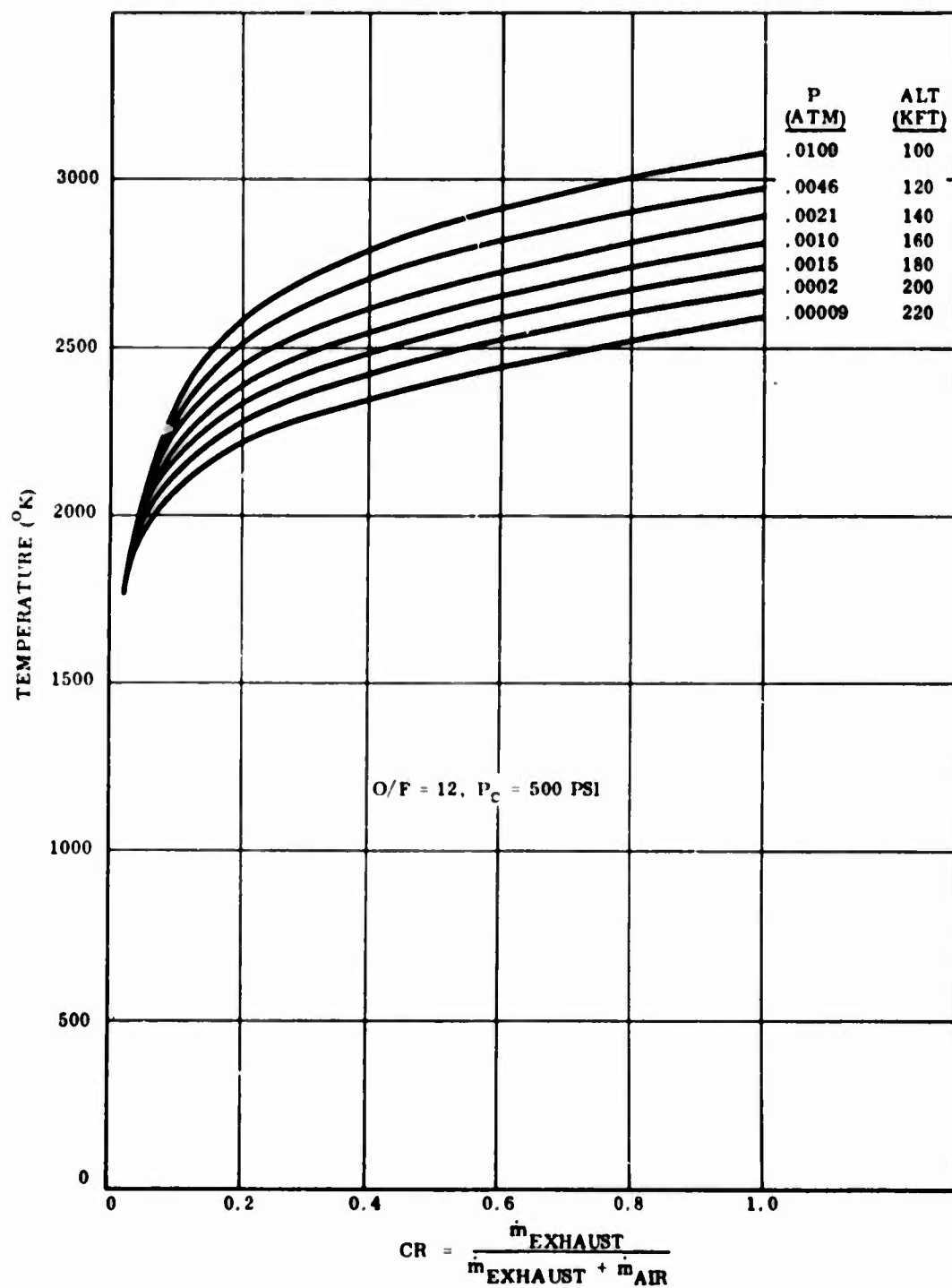


Figure 5 Hydrogen-Fluorine/Air Equilibrium Temperatures for  $\Delta h_f = 10,000$  Cal/Mole

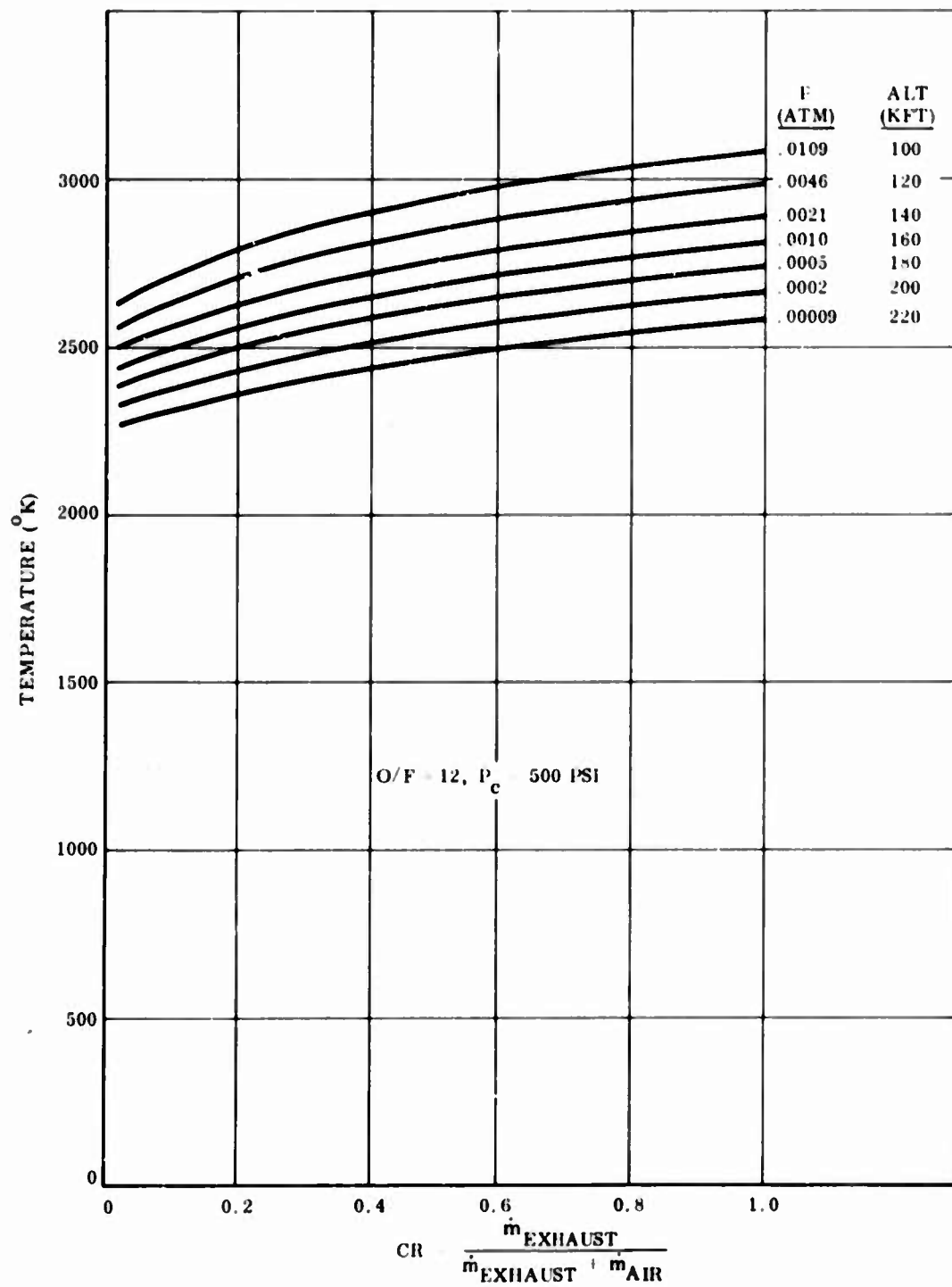


Figure 6 Hydrogen-Fluorine/Air Equilibrium Temperatures for  $\Delta h_f = 25,000$  Cal/Mole

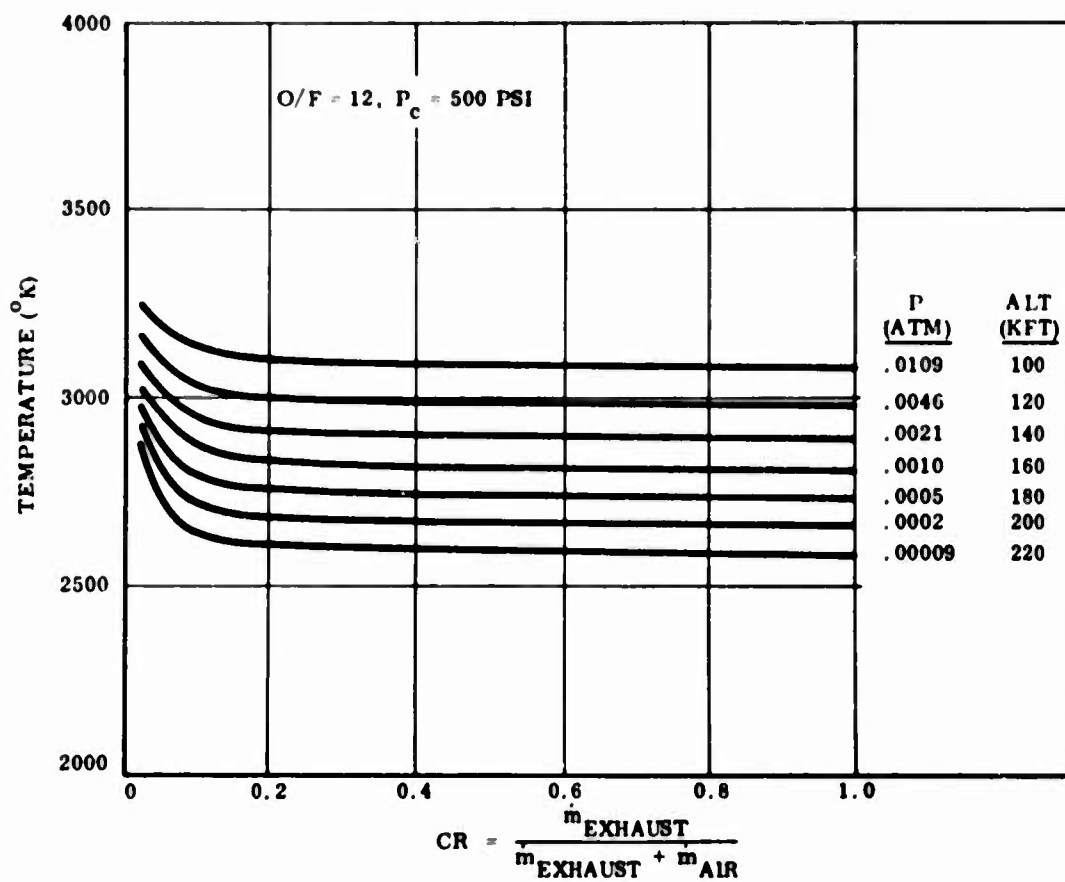


Figure 7 Hydrogen-Fluorine/Air Equilibrium Temperatures for  $\Delta h_f = 50,000 \text{ Cal/Mole}$

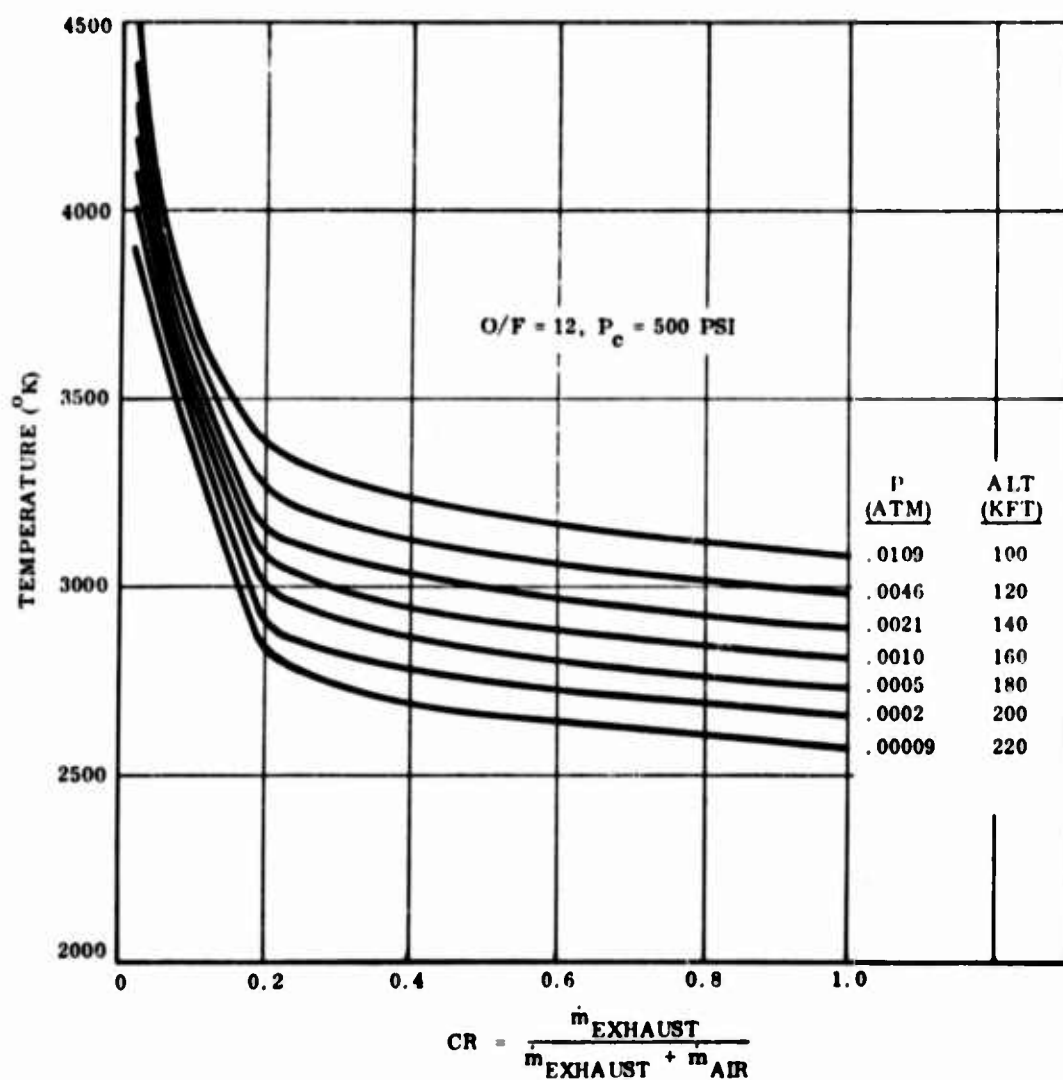


Figure 8 Hydrogen-Fluorine/Air Equilibrium Temperatures for  $\Delta h_f = 75,000 \text{ Cal/Mole}$

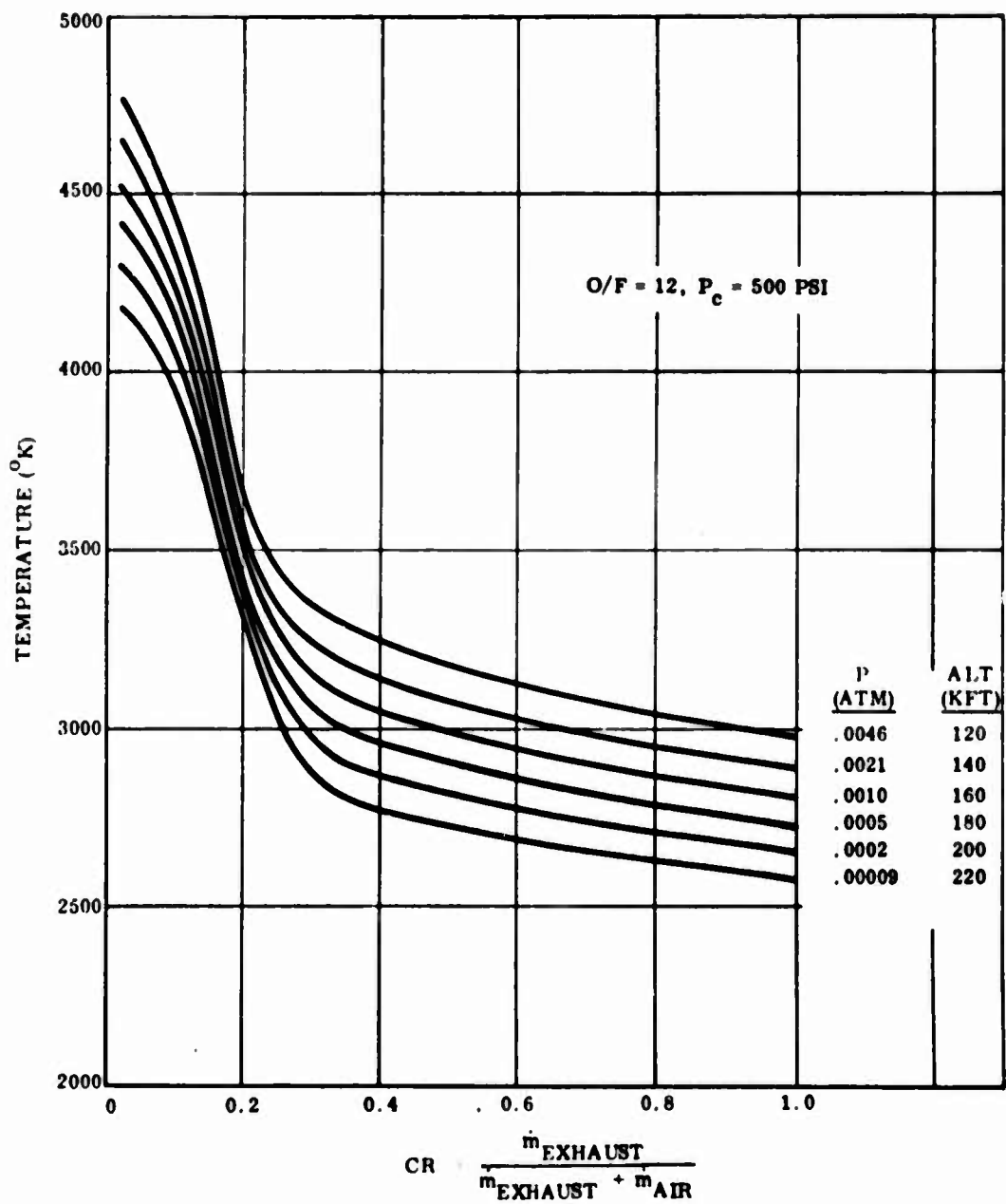


Figure 9 Hydrogen-Fluorine/Air Equilibrium Temperatures for  $\Delta h_f = 100,000 \text{ Cal/Mole}$

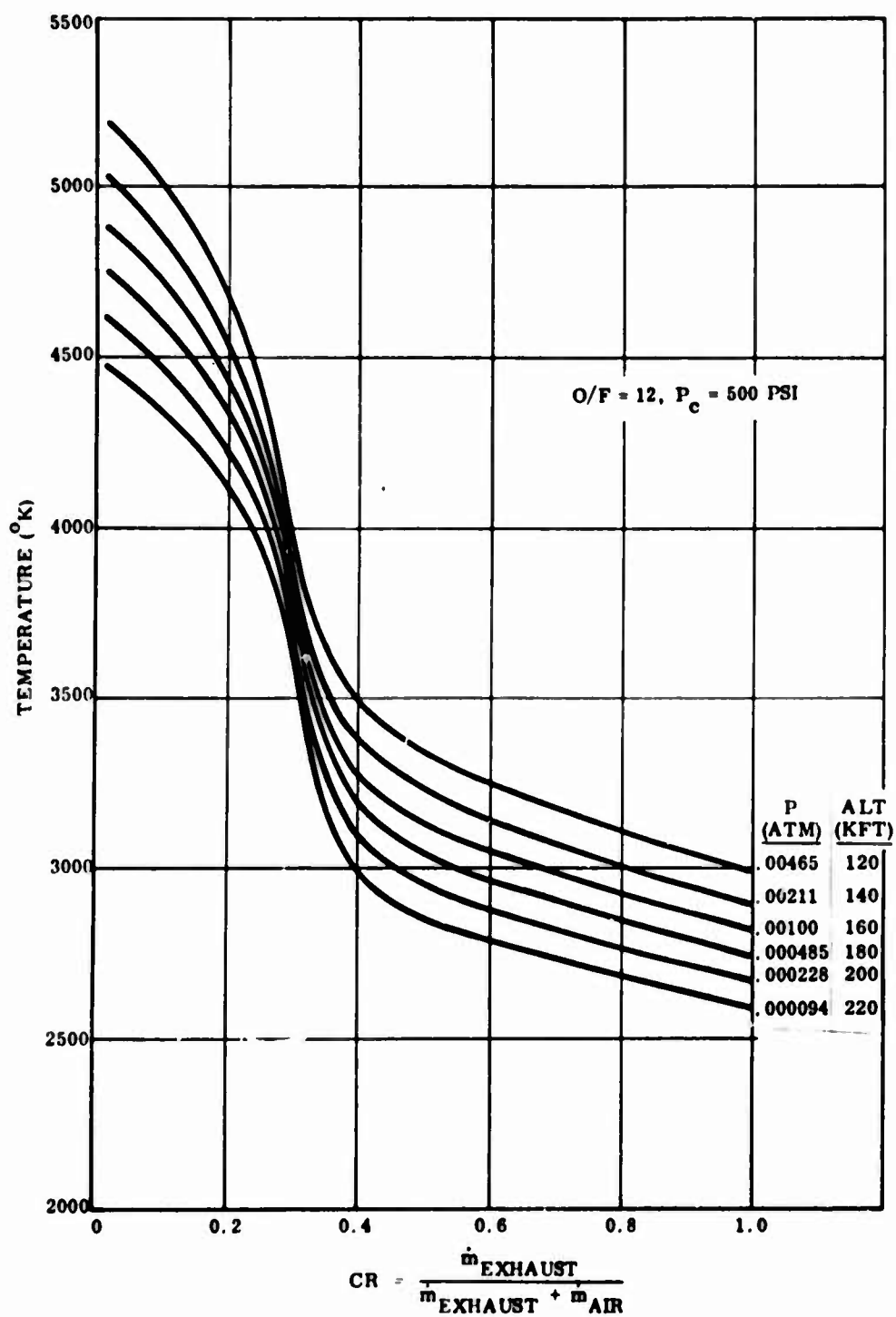


Figure 10 Hydrogen-Fluorine/Air Equilibrium Temperatures for  $\Delta h_f = 149,000 \text{ Cal/Mole}$



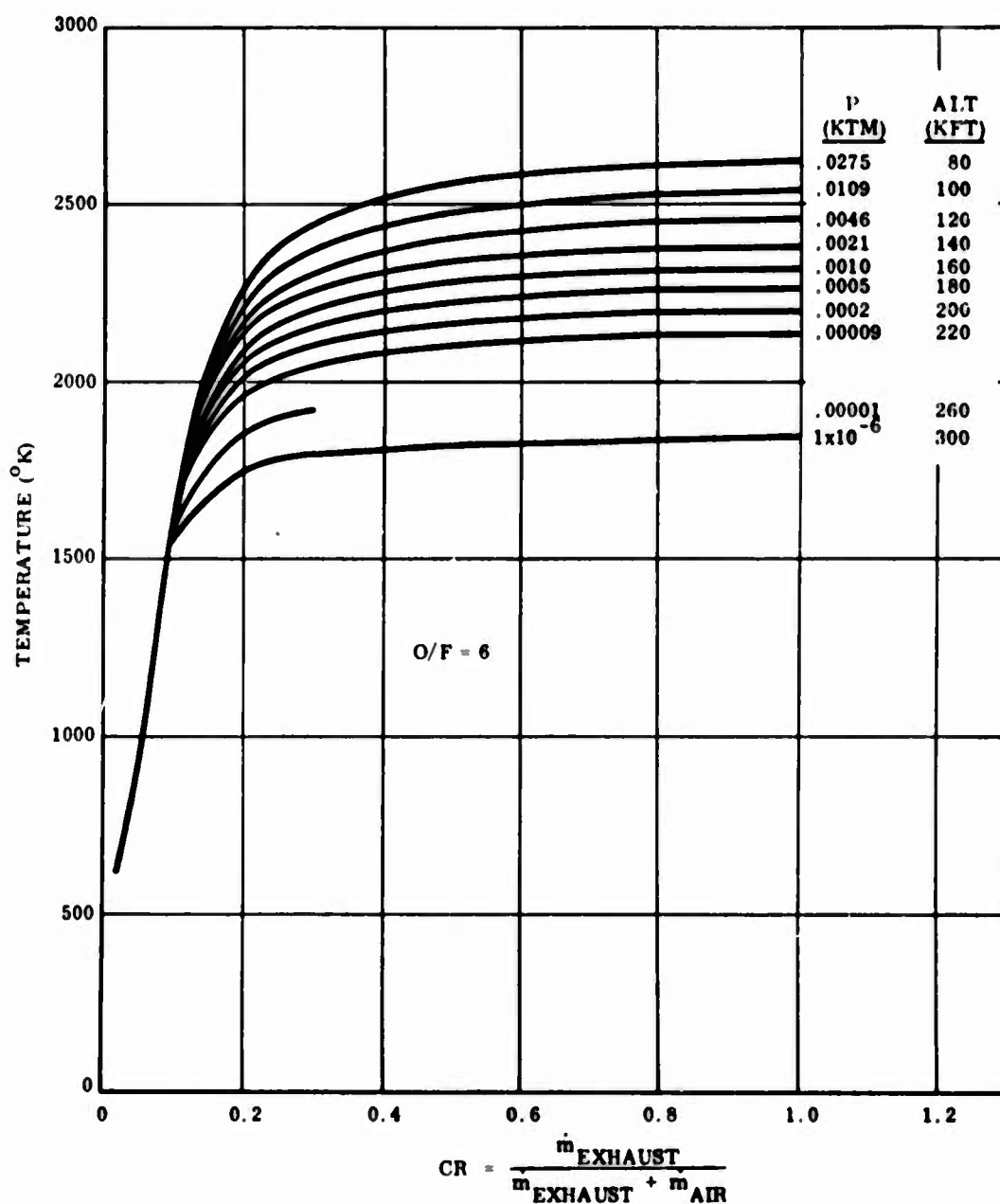


Figure 11 Hydrogen-Oxygen/Air Equilibrium Temperatures for  $\Delta h_f = 0$

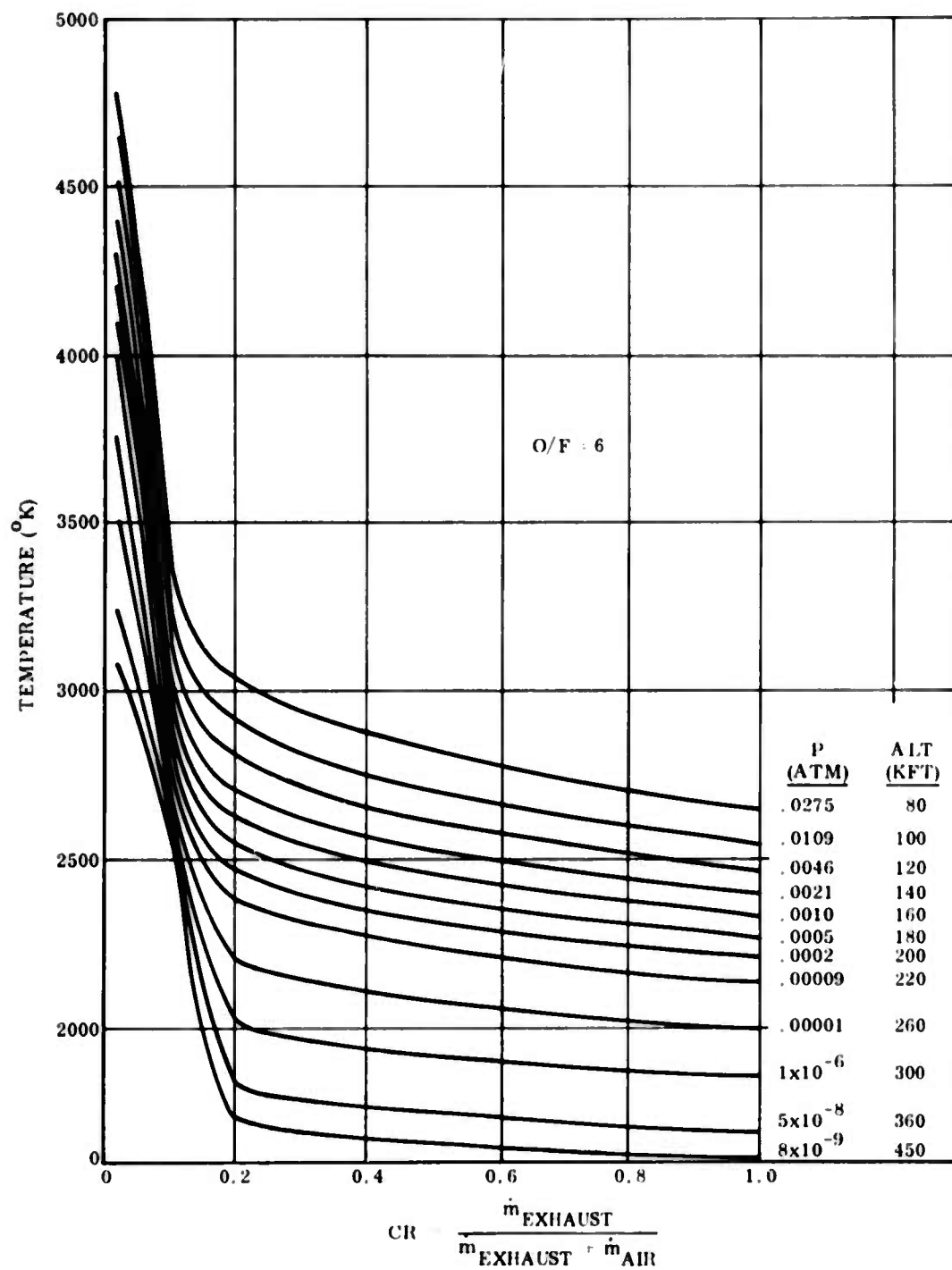


Figure 12 Hydrogen-Oxygen/Air Equilibrium Temperatures for  $\Delta h_f = 86,000$  Cal/Mole

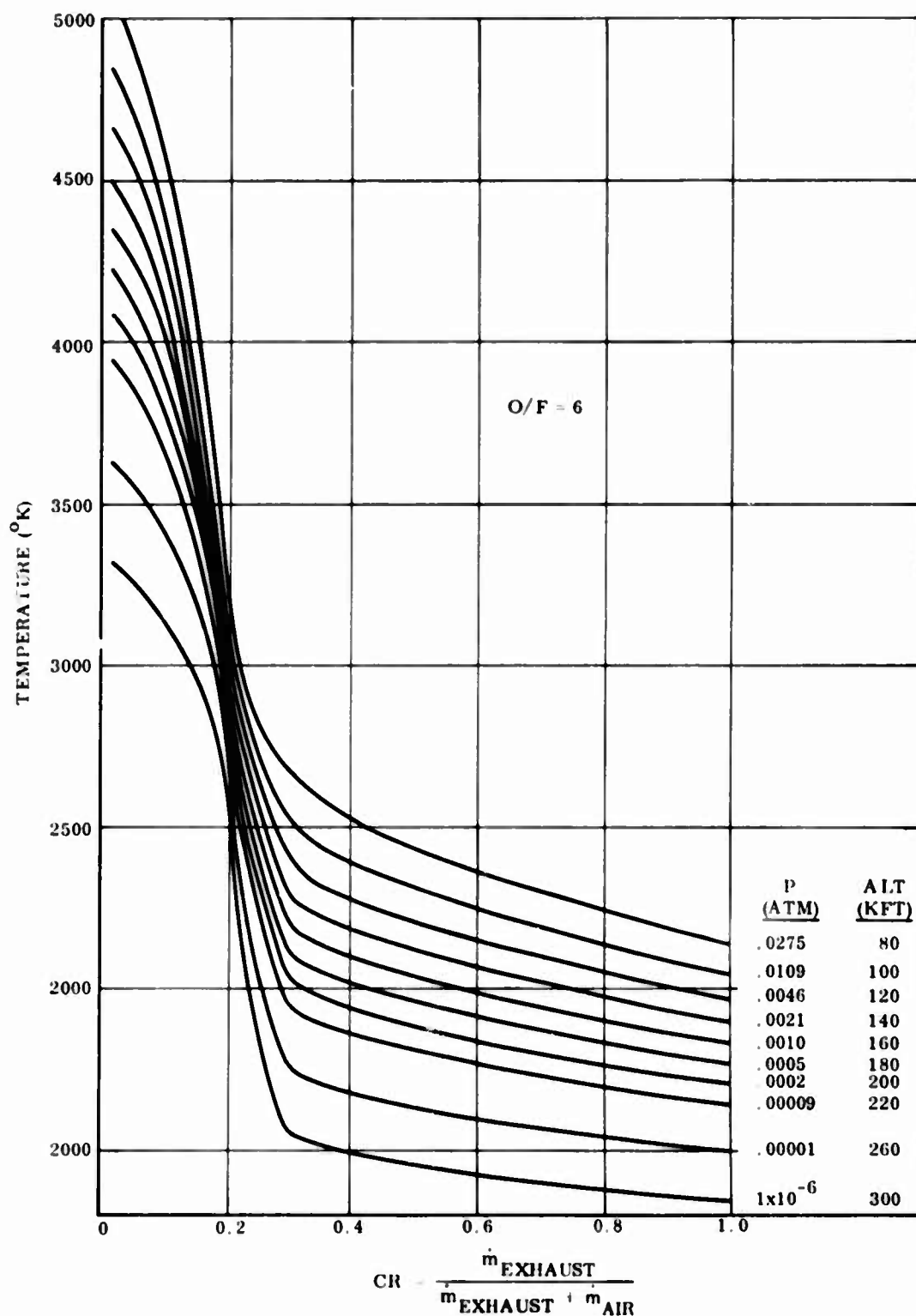


Figure 13 Hydrogen-Oxygen/Air Equilibrium Temperatures for  $h_f = 149,000$  Cal/Mole

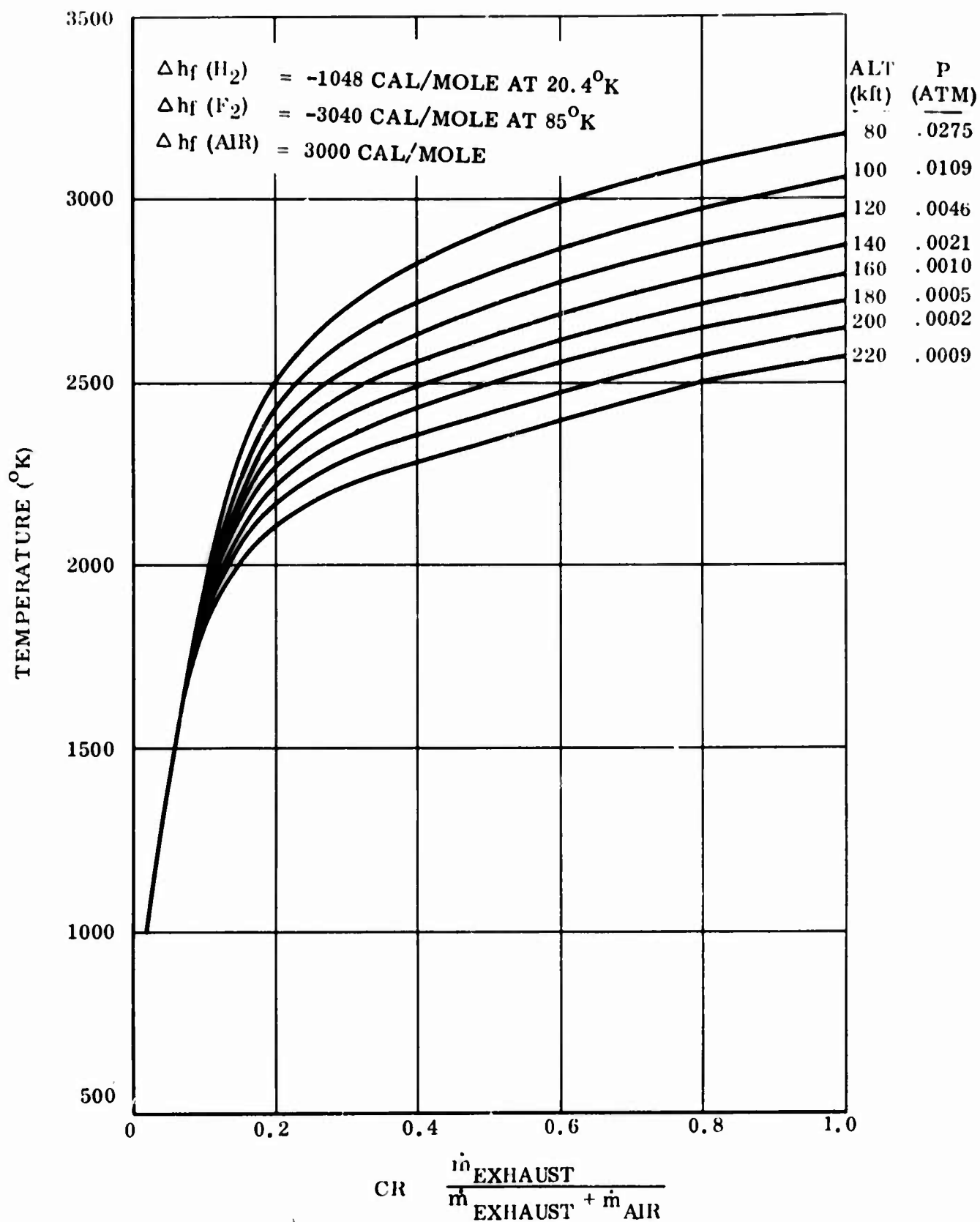


Figure 14 Liquid Hydrogen/Liquid Fluorine/Air Equilibrium Temperatures for  
 $O/F = 12$ ,  $P_c = 500 \text{ psi}$

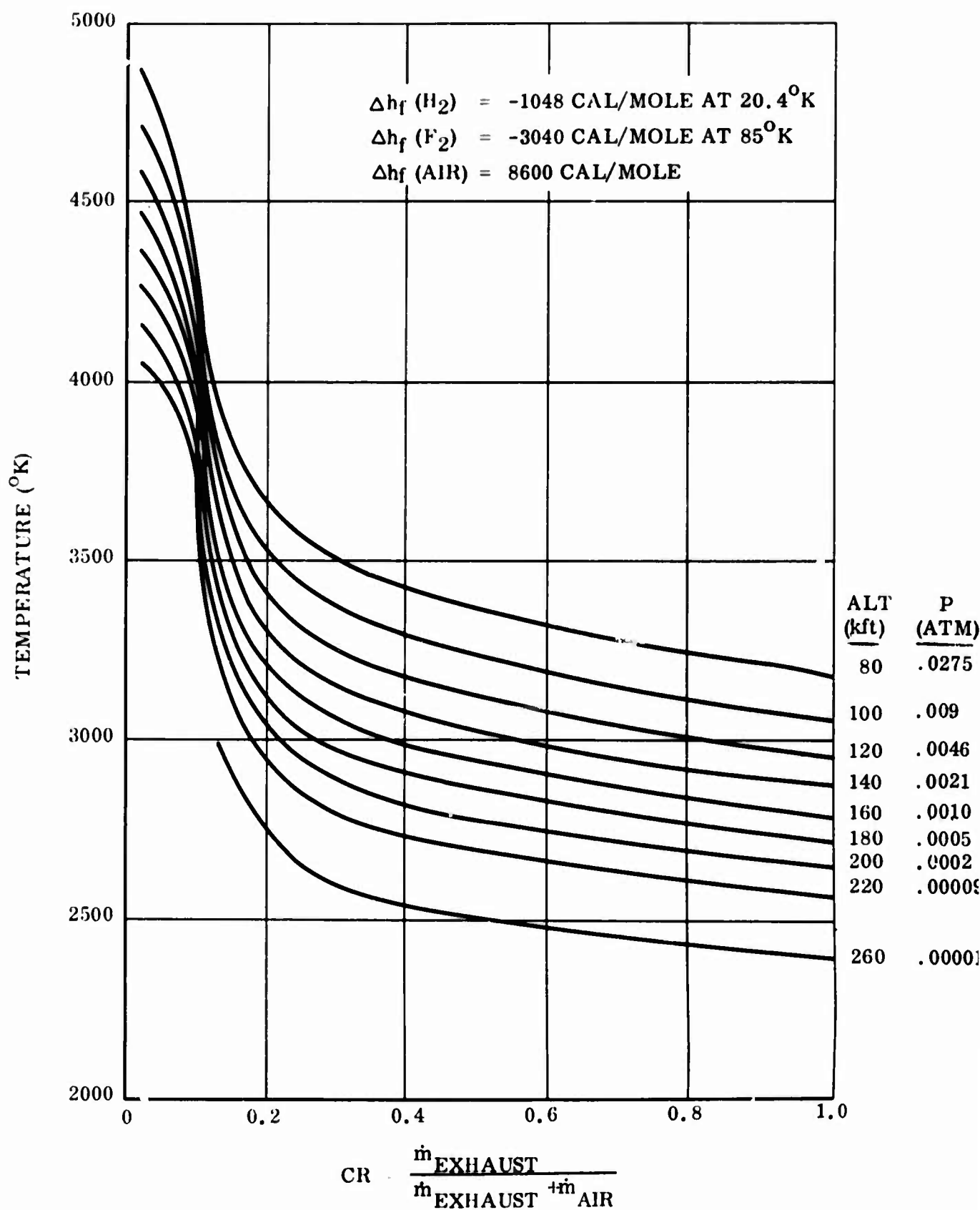


Figure 15 Liquid Hydrogen/Liquid Fluorine/Air Equilibrium Temperatures for  
 $O/F = 12$ ,  $P_c = 500 \text{ psi}$

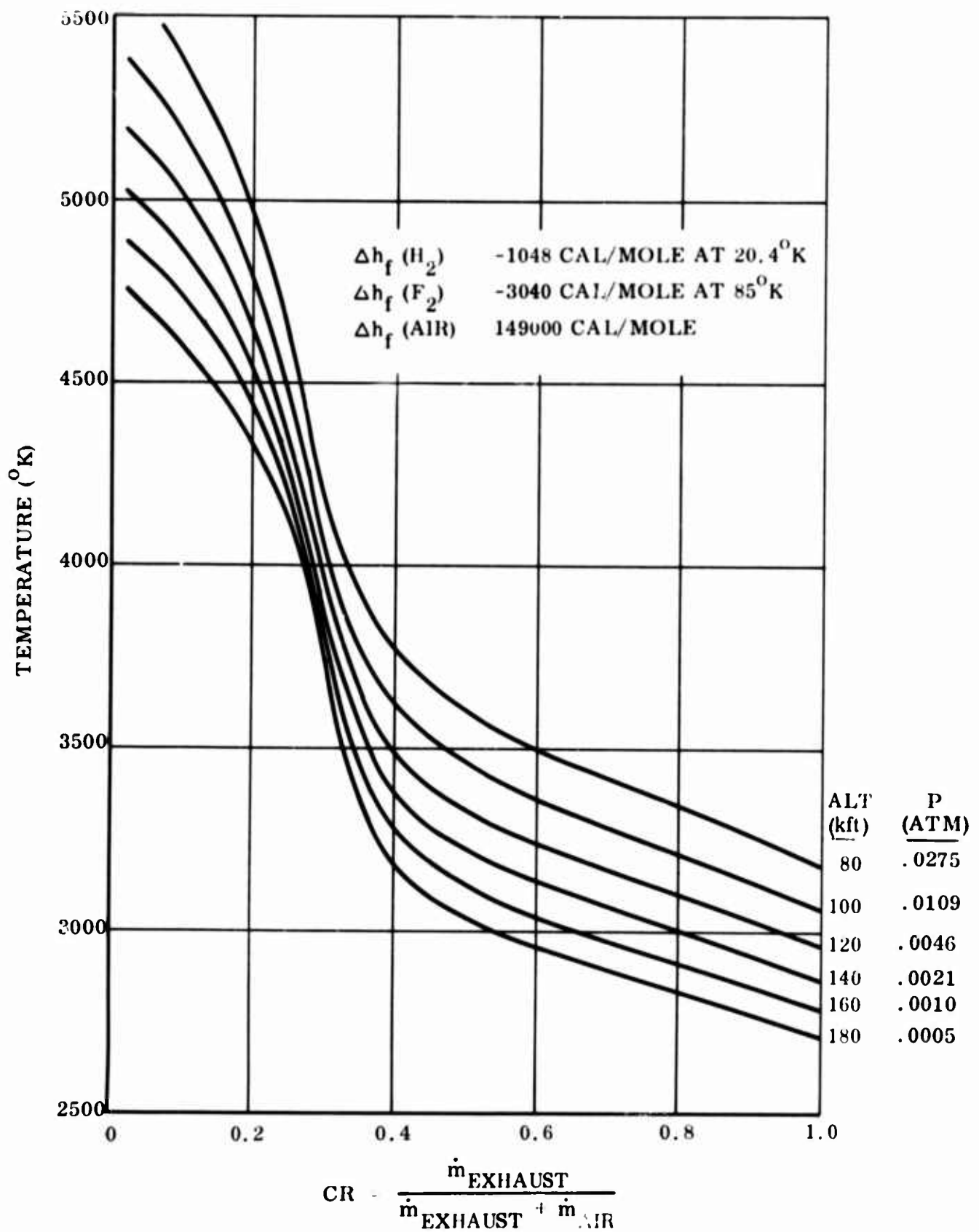


Figure 16 Liquid Hydrogen/Liquid Fluorine/Air Equilibrium Temperatures for  
 O/F = 12,  $P_c$  = 500 psi

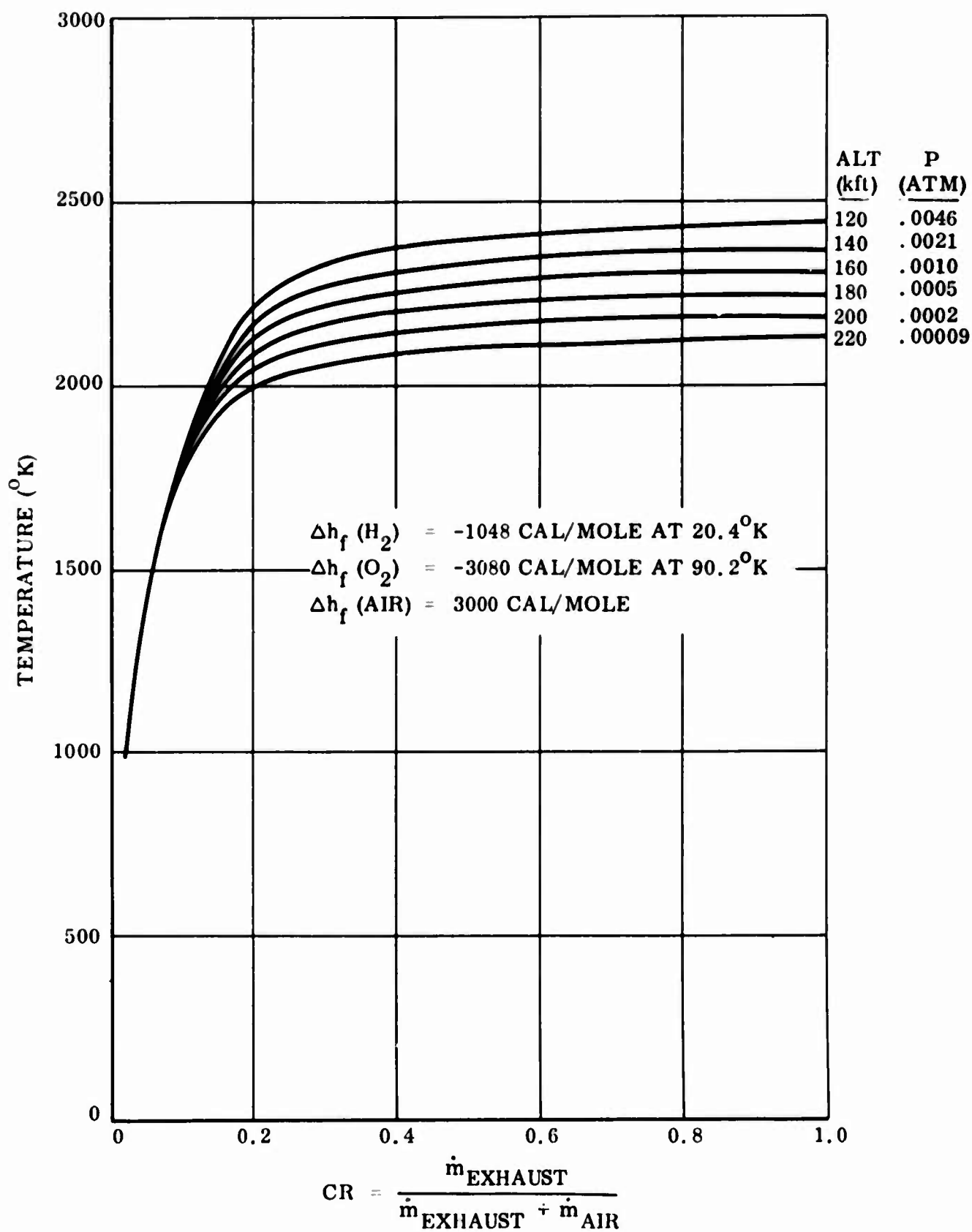


Figure 17 Liquid Hydrogen/Liquid Oxygen/Air Equilibrium Temperatures for  $\text{O/F} = 6$ ,  $P_c = 500 \text{ psi}$

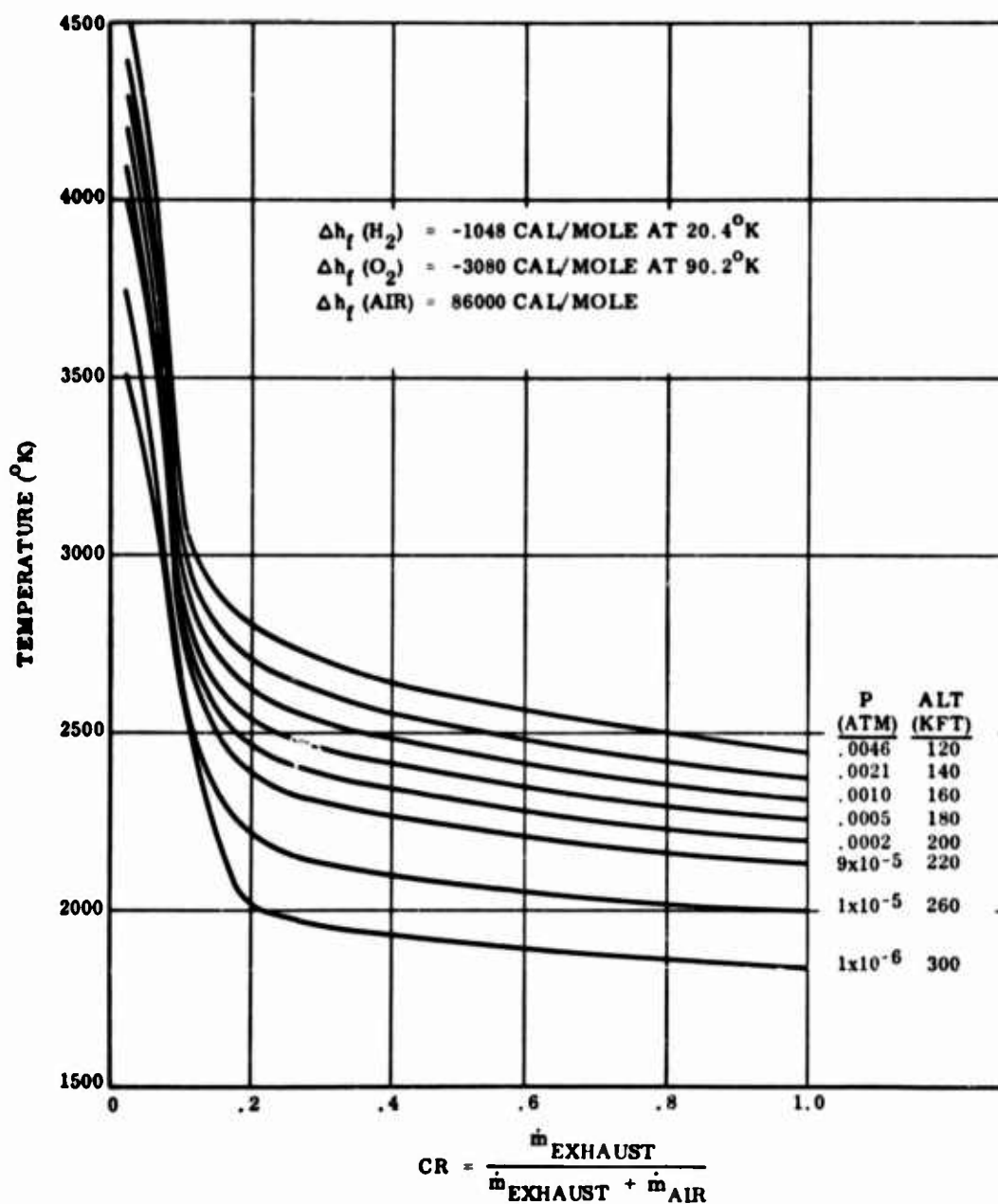


Figure 18 Liquid Hydrogen/Liquid Oxygen/Air Equilibrium Temperatures for  
 $O/F = 6$ ,  $P_c = 500 \text{ psi}$



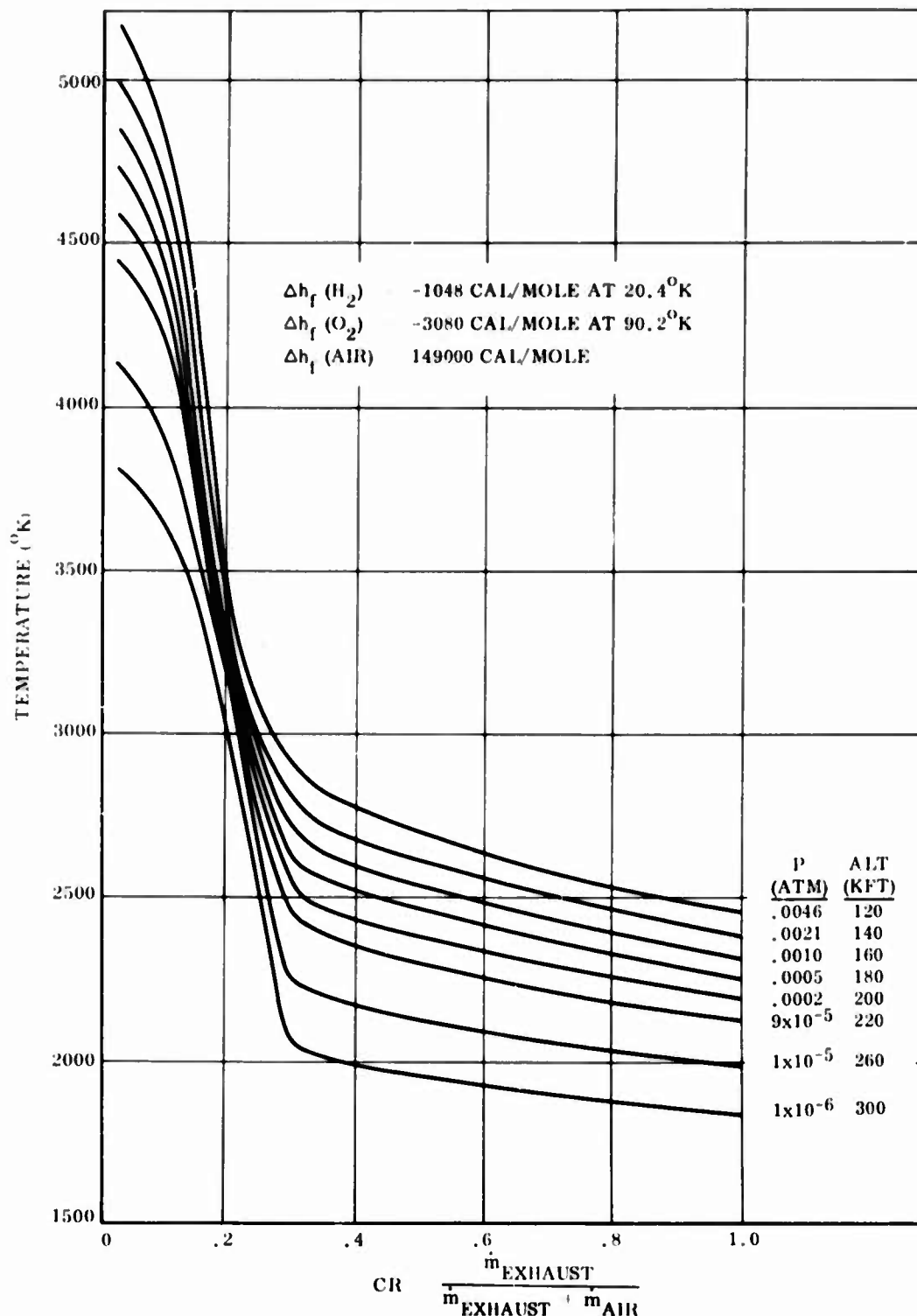


Figure 19 Liquid Hydrogen/Liquid Oxygen/Air Equilibrium Temperatures for  $O/F = 6$ ,  $P_c = 500 \text{ psi}$

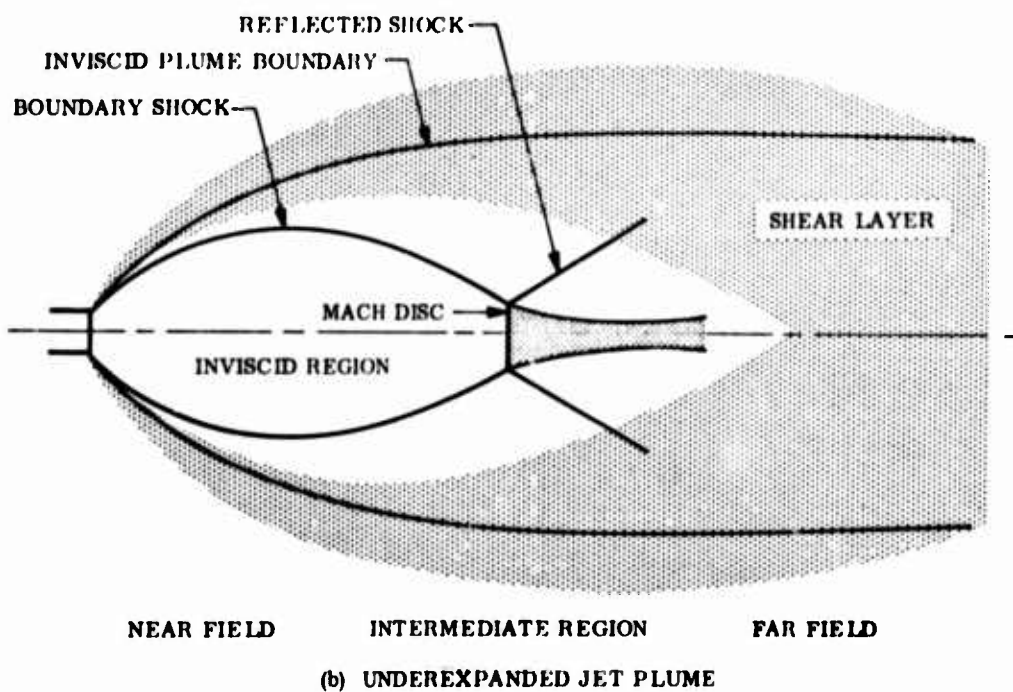
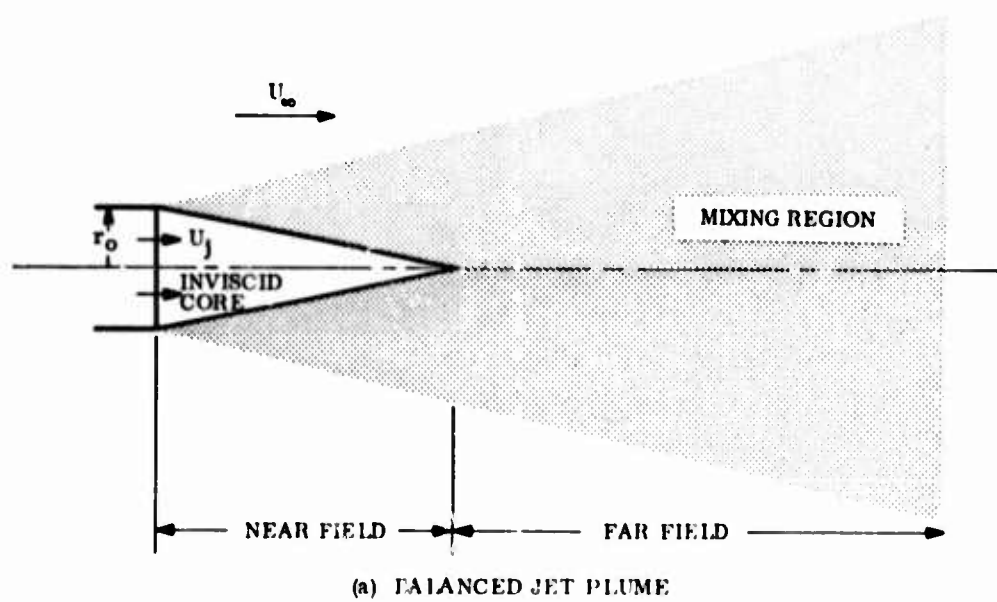


Figure 20 Sketches of Plume Structure

In general, two types of MOC problems in terms of boundary conditions can be classified:

- Quiescent ambient condition. The only boundary condition to be satisfied is that the ambient pressure must be matched at the free boundary. Furthermore, according to the MOC model, all other thermodynamic quantities are constant along the plume contour. Figure 21 illustrates a typical plume boundary under quiescent ambient condition and several constant-Mach contours in the interior. Figure 22 depicts several important plume boundary parameters versus ambient pressure, each being constant along the entire plume contour for a given ambient pressure.
- High-speed freestream condition. Because of external stream impinging on the plume, the thermodynamic properties along the plume boundary will vary from point to point. The "local" plume contour can be determined iteratively with the aid of the oblique shock or Newtonian concept with which the boundary pressure of the characteristic mesh must match the impact pressure. Figure 23 shows typical contours under high-speed freestream conditions.

A computer program based on this MOC solution currently in use at LMSC has been proven efficient and commands a wide applicability. Satisfactory comparisons with air plume data for a number of sample problems have also been demonstrated (Refs 17 and 18). In addition to frozen flow and constant  $\gamma$ , the program also accommodates equilibrium chemistry in each characteristic mesh as well as an option to estimate the boundary layer effects during nozzle expansion. However, chemical kinetics, phase transition, and three-dimensional plume effects cannot be accurately predicted with the LMSC MOC plume program in its present version.

While the MOC solution has been extensively applied during this study, relevant design charts and simplified formulas for exhaust plume description have been developed so that important plume properties for the candidate propellant systems can be determined quickly. In this respect, the following two postulates were made:

- Consistent with the dead-air hypothesis, the plume surface enshrouded by the separated flow region can be regarded as being exposed to zero ambient air velocity. As this plume portion is pertinent to the trailing shock determination and the separated flow solution (to be discussed in a later section), design curves are constructed only on the basis of the quiescent environment.
- From the discussion on thermochemistry in the preceding section, it is quite certain that frozen chemical composition would be established within a short distance from the nozzle throat. However, because of continuous flow expansion, the  $\gamma$  value would increase with decreasing temperature. A large  $\gamma$  value in the plume flow field is thus anticipated (likely to be of the order 1.4) even if the equilibrium  $\gamma$  value were as low as 1.1 in the combustion chamber. As already indicated in the preceding section, a constant  $\gamma$  of 1.38 is selected in the present analysis. The typical effect of  $\gamma$  on plume contour is depicted in Figure 24.

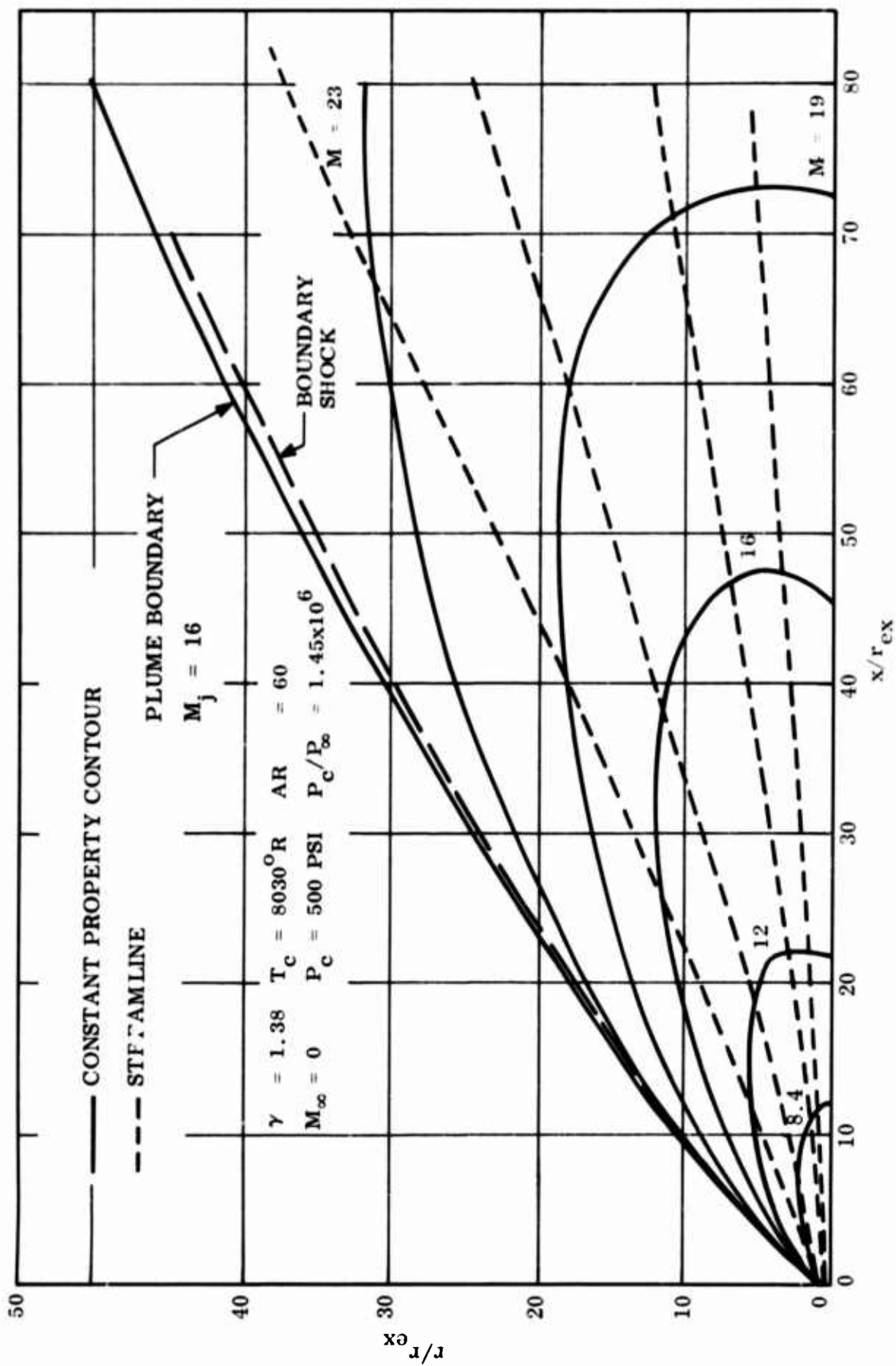


Figure 21 MOC Jet Plume in Quiescent Air

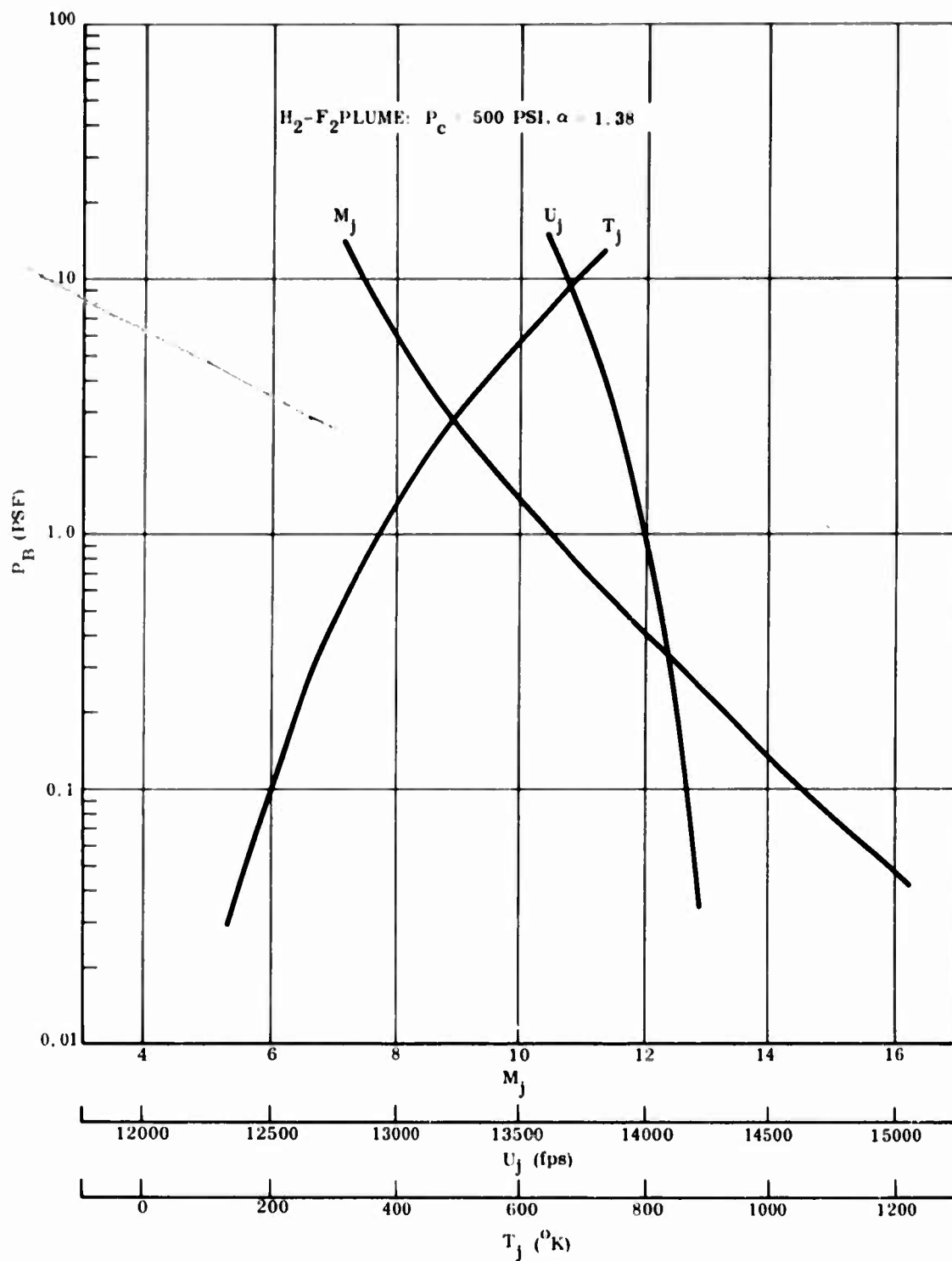


Figure 22 Plume Boundary Properties

— CONSTANT-PROPERTY CONTOUR

--- STREAMLINE

REMARKS: NEWTONIAN FLOW;  
VARIABLE BOUNDARY  
PROPERTIES

$\gamma = 1.38, M_\infty = 10$

$T_c = 8030^\circ R, P_c = 500 \text{ PSI}$

$AR = 60, P_c/P_\infty = 1.45 \times 10^6$

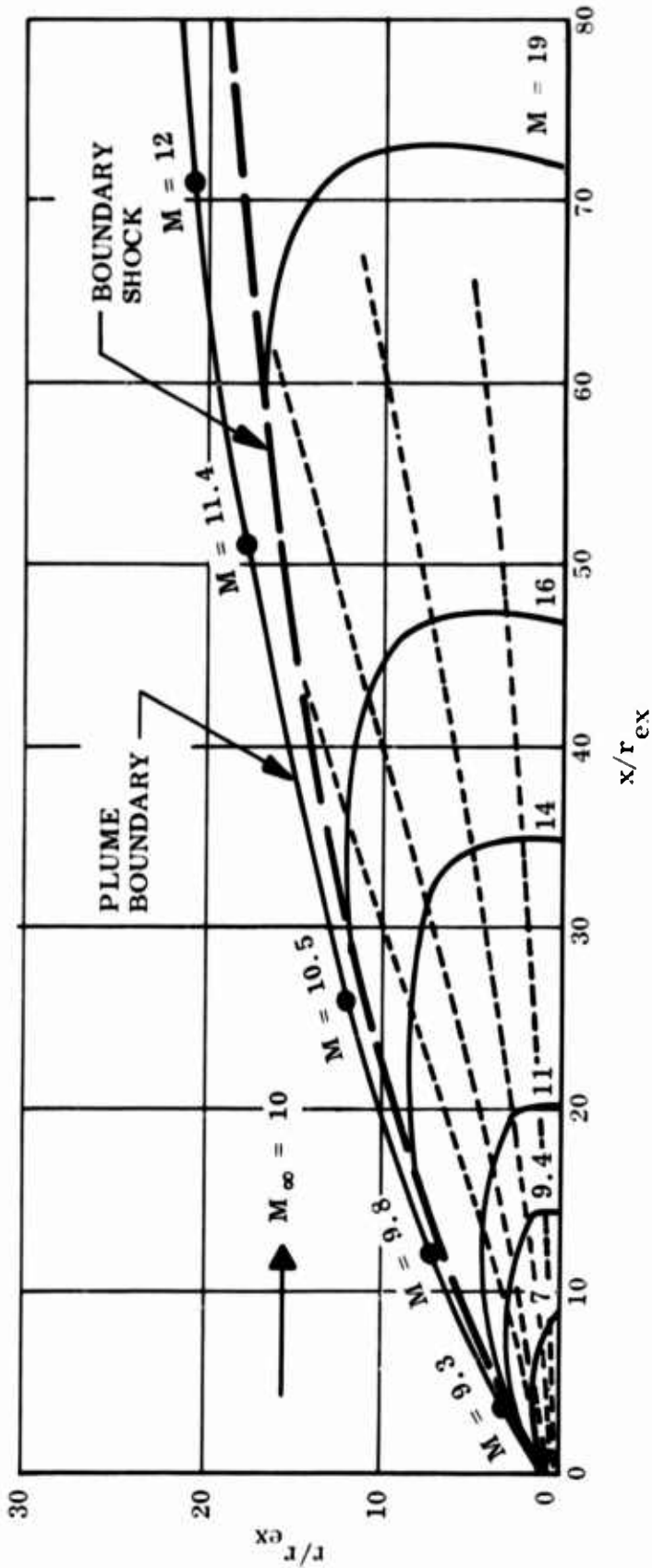


Figure 23 MOC Jet Plume at  $M_\infty = 10$

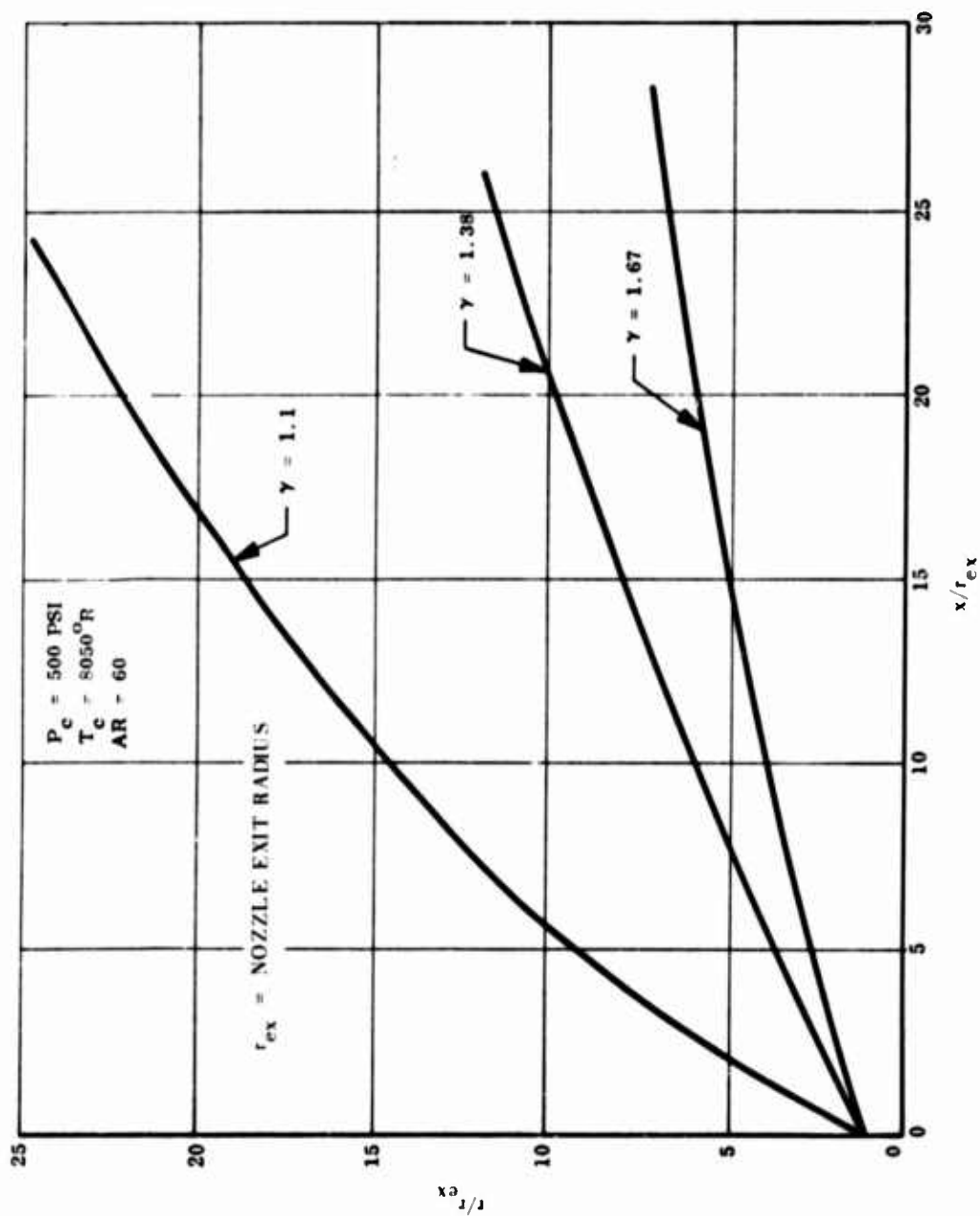


Figure 24 Effect of  $\gamma$  on Exhaust Plume Contour

With the plume model selected, the exhaust plume properties for hydrogen-fluorine and hydrogen-oxygen mixtures are obtained by carrying out the MOC computations together with the following assumptions:

- Axisymmetric with zero angle of attack
- Area ratio = 60
- Ambient air velocity = .0
- Chamber pressure = 500 psi
- Chamber temperature = 8050°R
- $\gamma = 1.38$
- Nozzle half-angle = 9.5 degrees
- Frozen species concentrations

By selecting a particular  $\gamma$ , the propulsion system is not explicitly identifiable except by implication of the chamber temperature value. However, the exhaust plume contour is affected by the chamber temperature primarily through the nozzle exit Mach number. According to calculated results presented in Ref 19, this effect is not a strong one. Furthermore, the assumed chamber pressure of 500 psi would lead to no loss of generality since the design curves were constructed in terms of jet-to-ambient pressure ratio, as depicted in Figure 25.

For development of simplified prediction formulas, two methods are proposed herein: (1) Formulas to predict five boundary points based on the MOC solution, and (2) The Latvala-Anderson model to predict plume contour in the vicinity of the nozzle exit.

- (1) The Five-Point Method. On the basis of the MOC solutions, prediction formulas have also been developed which permit estimates of plume contours involving the effects of freestream Mach number, area ratio, nozzle half-angle, etc.

$$X_{\max} = 1.076 f_1^{-0.563} \quad (1)$$

$$r_{\max} = 0.65 f_2^{0.91} \quad (2)$$

$$r_{1/4} = 0.686 (r_{\max})^{0.963} \text{ for } x = 1/4 x_{\max} \quad (3)$$

$$r_{1/2} = 0.871 (r_{\max})^{0.992} \text{ for } x = 1/2 x_{\max} \quad (4)$$

$$r_{3/4} = 0.969 r_{\max} \text{ for } x = 3/4 x_{\max} \quad (5)$$



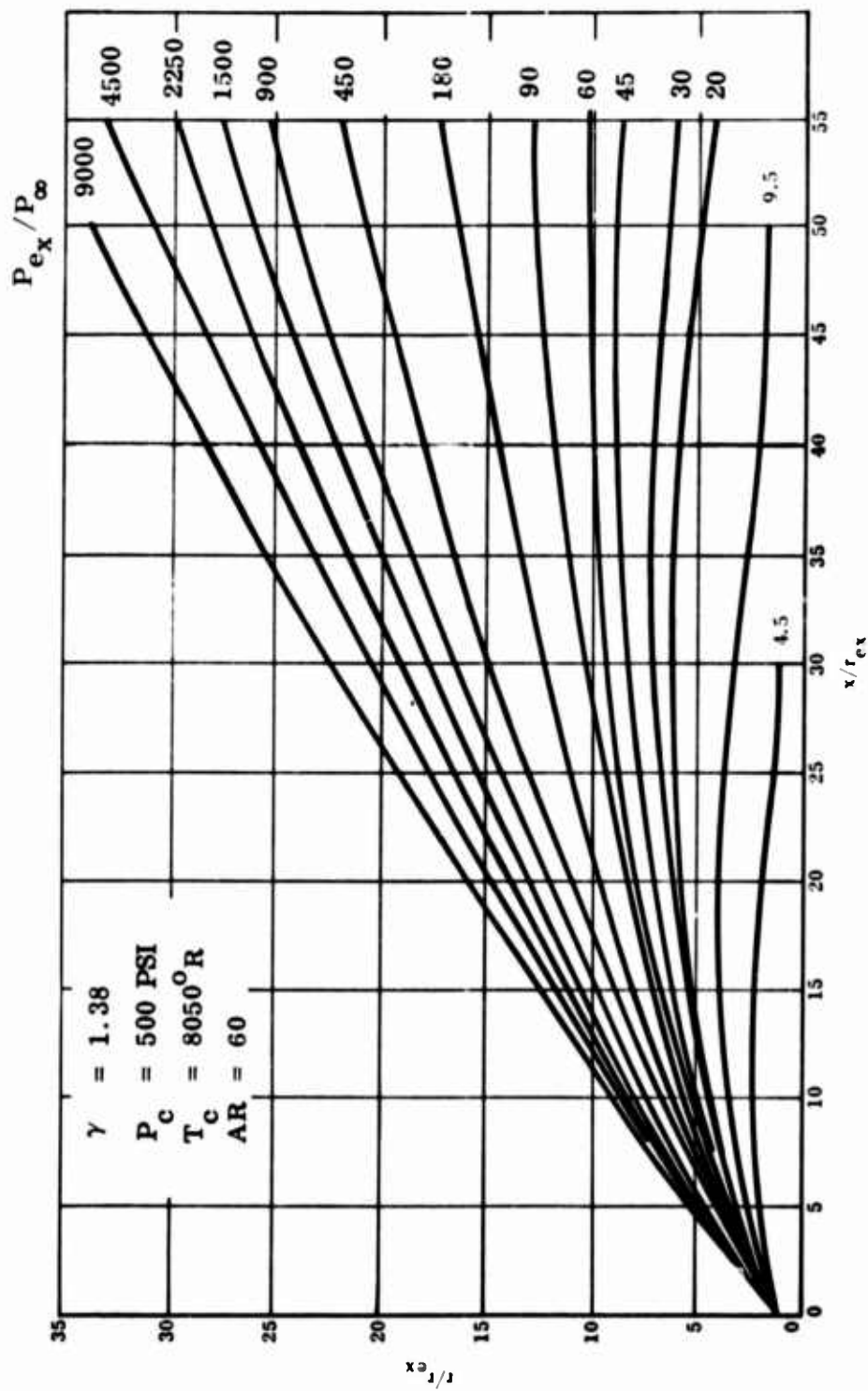


Figure 25 Exhaust Plume Contours for Various Ambient Pressures

where

$$f_1 = \frac{A}{A^*} \frac{P_o}{P_c} (1 + \gamma_o M_o^2)^{1/4} \frac{1}{1 - \sin \theta_N} \quad (6)$$

and

$$f_2 = \left[ \left( \frac{A}{A^*} \right)^{1/4} (1 + \gamma_o M_o^2)^{1/8} (1 - \sin \theta_N) \right]^{-1} x_{\max} \quad (7)$$

The corresponding prediction curves are presented in Figures 26 through 28. It should be mentioned that these formulas are valid for non-zero freestream Mach number also, but they are based on  $\gamma = 1.38$  and zero angle of attack for the plume.

- (2) The Latvala-Anderson Method. The Latvala-Anderson Method (Refs 20 and 21) provides a simplified scheme to predict the initial portion of a highly underexpanded jet boundary. The basic hypothesis underlying the method is that the jet boundary is composed of a series of connecting circular arcs, each being describable by the following "length" formulas (Fig. 29)

$$\frac{r_{n+1}}{r_{ex}} = \left[ \frac{(1 + \cos \alpha_{n+1}) \left( \frac{A}{A^*} \right)_{n+1}}{(1 + \cos \alpha_n) \left( \frac{A}{A^*} \right)_n} \right]^{1/2} \quad (8)$$

$$\frac{\Delta x / r_{ex}}{r_n / r_{ex}} = \left( \frac{r_{n+1} / r_{ex}}{r_n / r_{ex}} - 1 \right) \cot \left( \alpha_n - \frac{\Delta \alpha}{2} \right) \quad (9)$$

The initial wave angle is determined from the Prandtl-Meyer expression

$$\nu = \int \sqrt{M^2 - 1} \frac{d \left( M \sqrt{\left[ \frac{a_t^2}{1 + \frac{1}{2} (\gamma - 1) M^2} \right]} \right)}{\left( M \sqrt{\left[ \frac{a_t^2}{1 + \frac{1}{2} (\gamma - 1) M^2} \right]} \right)} \quad (10)$$

where  $\nu$  is the Prandtl-Meyer angle, and  $M$  is the average Mach number. The corresponding turning angle is then determined from

$$\alpha_1 = \nu_1 - \nu_{ex} + \theta_N \quad (11)$$

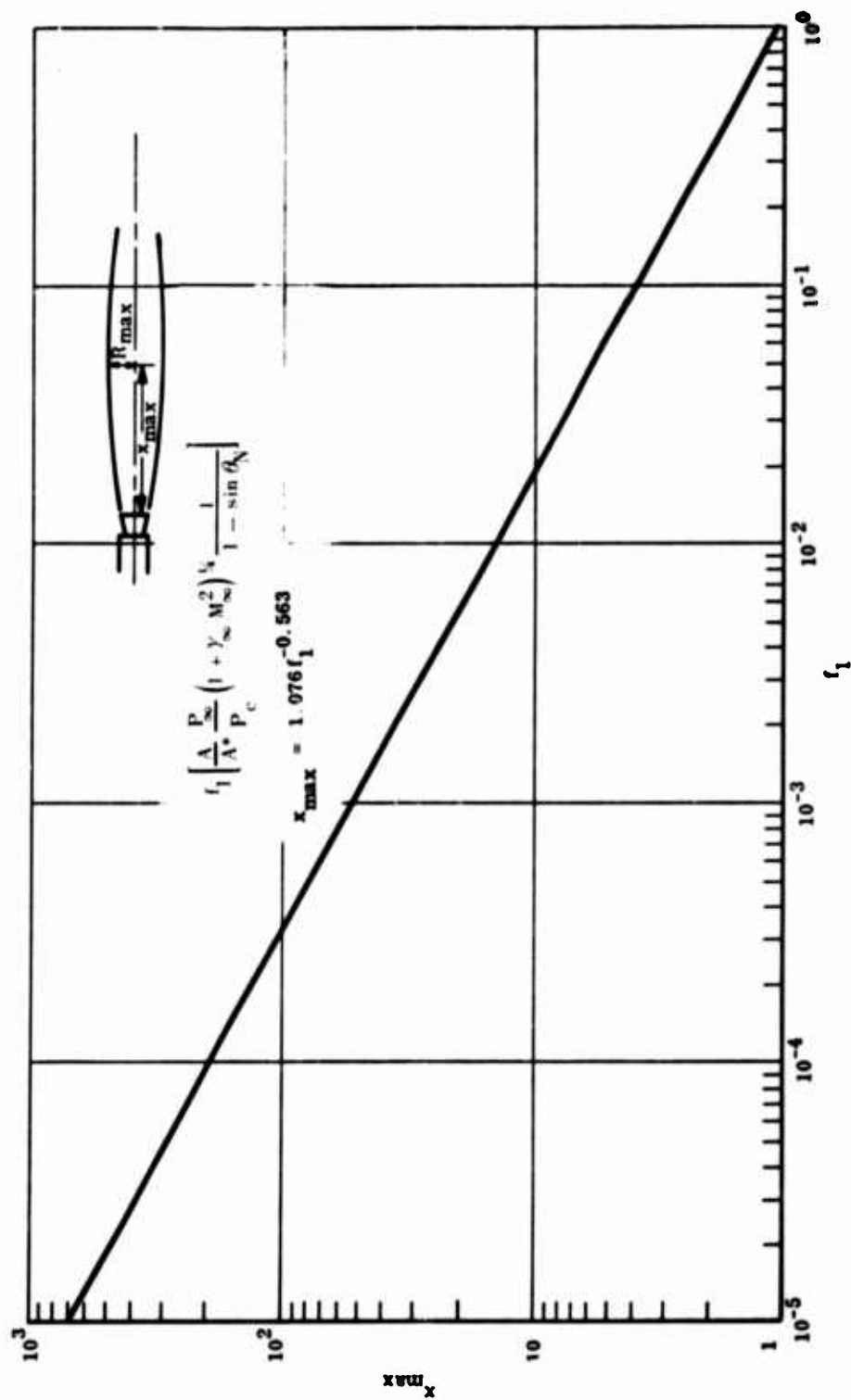


Figure 26 Prediction of Distance to Maximum Plume Radius

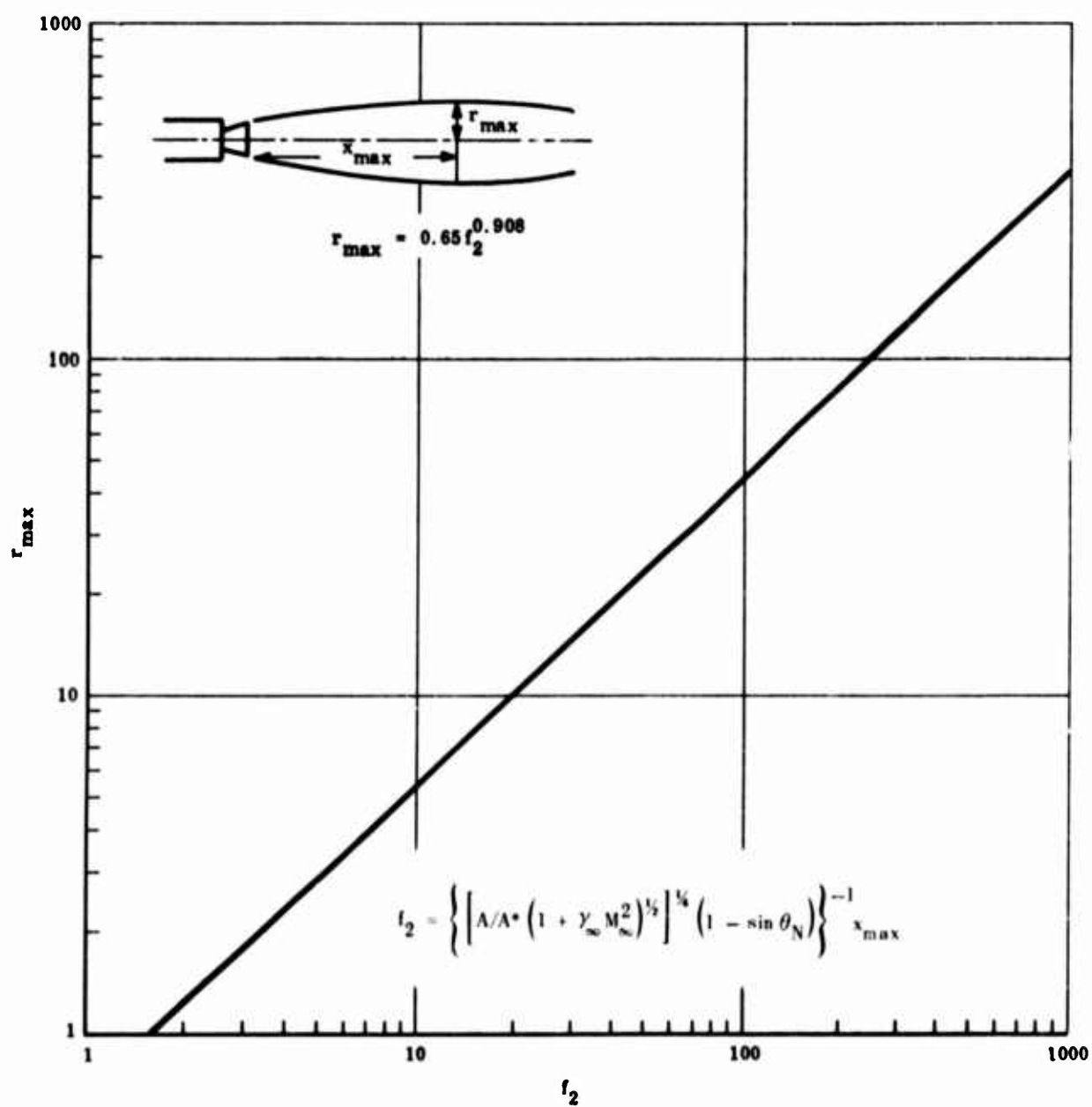


Figure 27 Prediction of Maximum Plume Radius

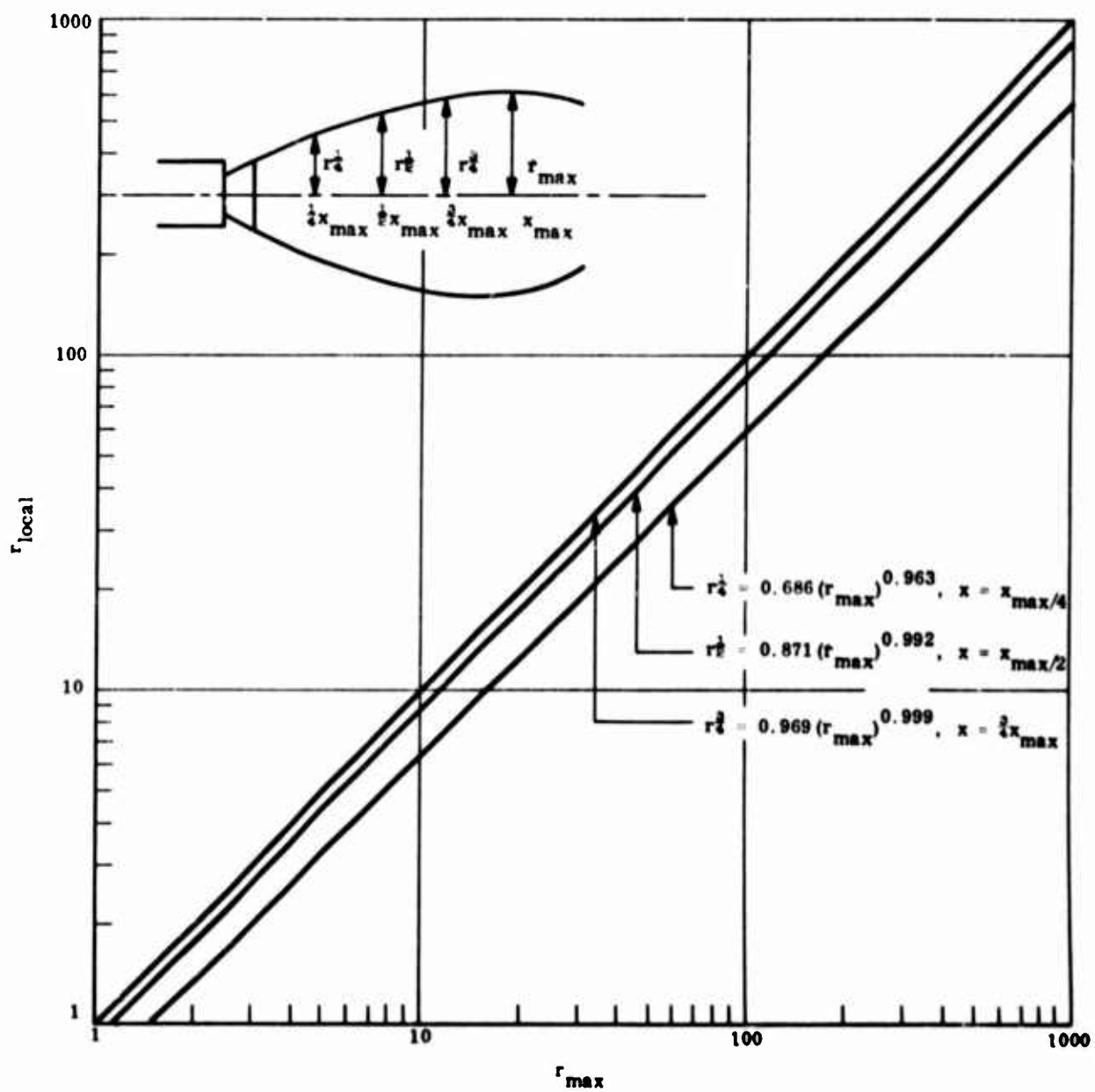


Figure 28 Local Plume Radius as a Function of Maximum Plume Radius

(Reproduced from Reference 20)

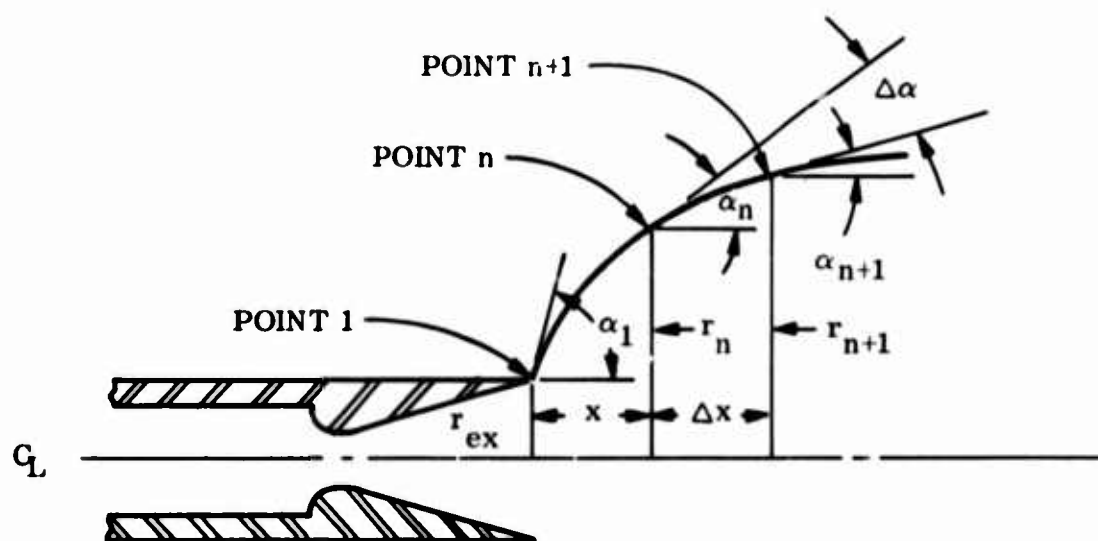


Figure 29 Jet Boundary Coordinate System

Continuing the forward integration using local Prandtl-Meyer angle, average Mach number, and isentropic area ratio, the entire spherical-arc jet boundary surface for the fore part of the plume can be ascertained. Figure 30 depicts the comparison between the Latvala-Anderson solution and the MOC solution for several typical air plumes which show excellent agreement for the region investigated.

For further approximation, graphical construction of the circular-arc initial jet plume boundary can be made. Figure 31 shows the variation of the radius as a function of nozzle Mach number,  $M_{ex}$ , for an air plume. The curve can also be represented by the following simple formula:

$$\frac{R}{r_{ex}} = \frac{15.25}{M_{ex} - 0.377} + 13.78 \quad (12)$$

Although the Latvala-Anderson method is merited with simplicity in execution, its one-dimensional model admits only an average Mach number and other average flow quantities across the plume for which the pressure boundary condition is not satisfied. Hence, aside from the plume contour near the nozzle exit, the important plume parameters along the jet boundary cannot be determined by this method. Additional information, such as the design curves presented in Figure 22, must be supplemented in order to pursue the plume-induced separated flow prediction.

#### b. $\gamma$ Variation in Exhaust Plume

As mentioned previously, rapid high-altitude plume expansion under frozen flow conditions would result in a decrease in gas temperature and a corresponding rise in the  $\gamma$  value. A rigorous approach to plume prediction entails a continuous adjustment of the  $\gamma$  value in the characteristic mesh. On the other hand, a simplified model, as adopted herein, is to select a constant  $\gamma$  corresponding to anticipated boundary temperatures. Although somewhat arbitrary, a constant  $\gamma$  of 1.38 has been chosen on the basis of observing a number of MOC plumes with various  $\gamma$  values for the nozzle exit conditions. Evidently, the Latvala-Anderson method with  $\gamma = 1.4$  would lead to practically the same answer.

#### c. Nozzle Boundary Layer Effects

The growth of boundary layer in the rocket nozzle affects the exhaust plume properties in two ways:

- Modification of the nozzle shape and area ratio due to the growth of displacement thickness along the wall
- Change in plume contour due to the presence of low-speed boundary layer at the nozzle exit

(Reproduced from Reference 20)

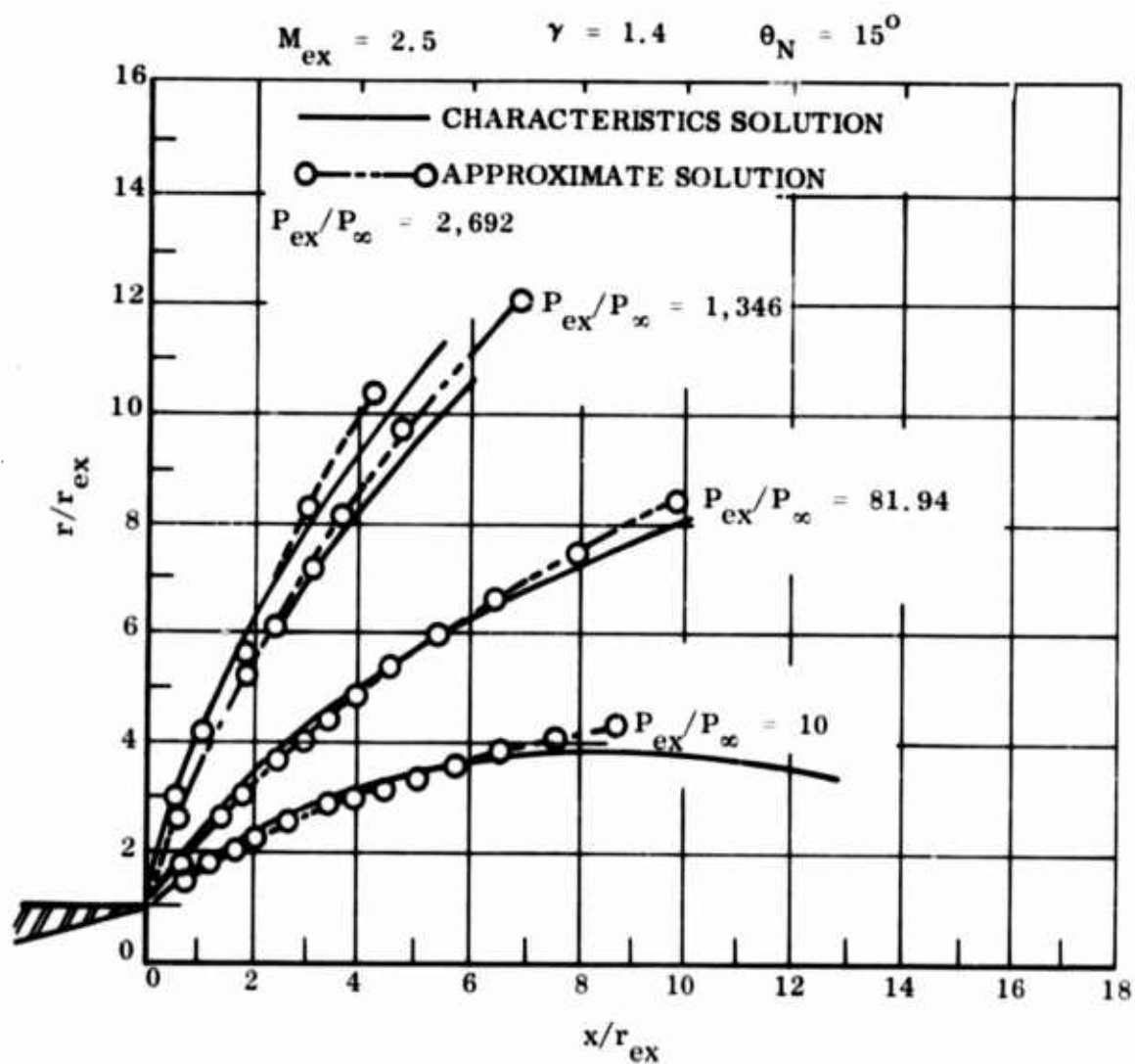


Figure 30 Jet Boundaries Calculated by Approximate Method Compared With Method of Characteristics Solution from NASA TRR-6



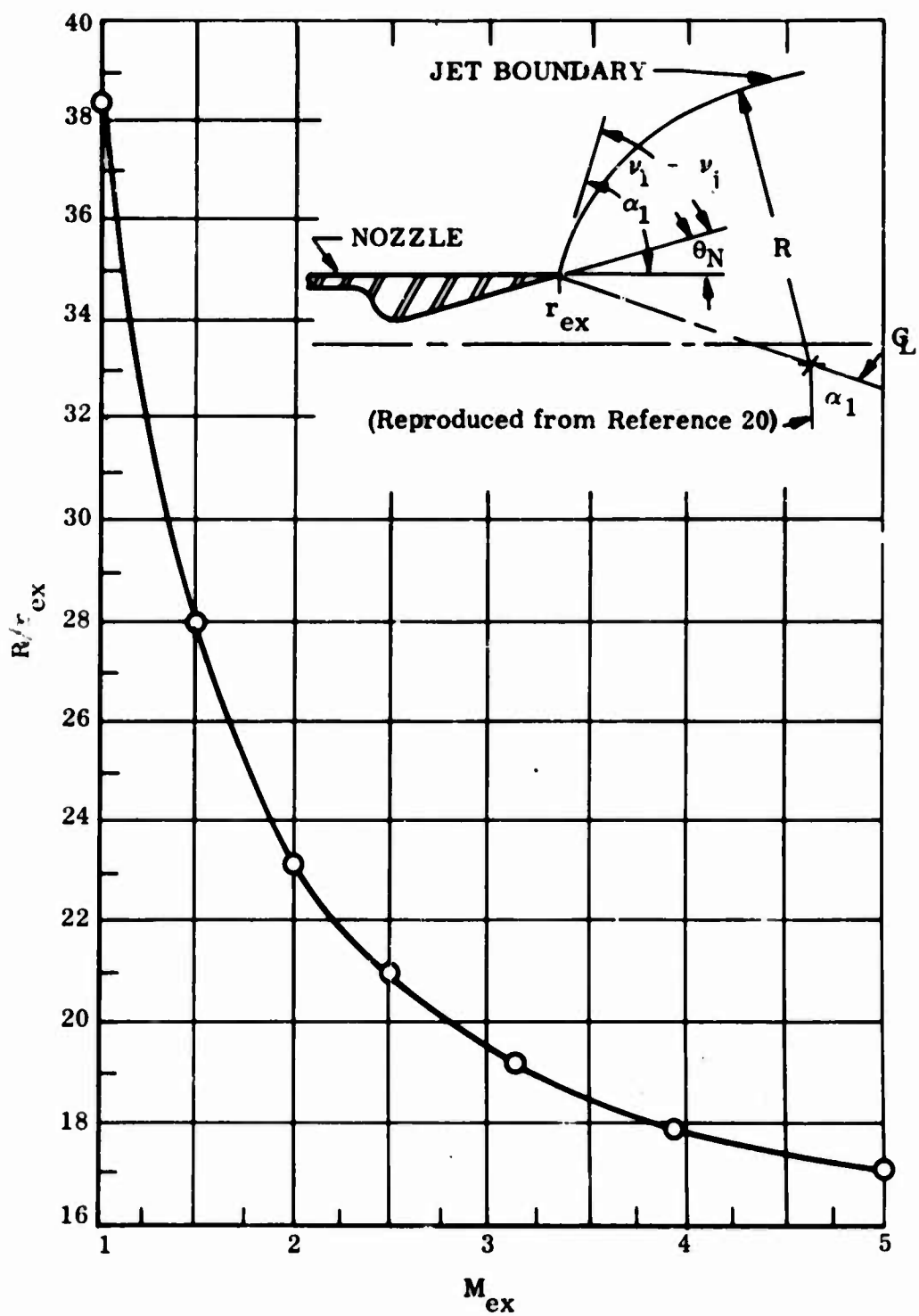


Figure 31 Radius Ratio of Jet Boundary for  $\gamma = 1.4$

The first problem has been investigated quite extensively, particularly by Bartz et al (Refs. 22 and 23) in conjunction with the evaluation of rocket nozzle heat transfer characteristics and possible degradation of performance as a result of boundary layer formation. By employing the turbulent nozzle flow model discussed in Reference 22, the displacement thickness at the nozzle exit for the hydrogen-fluorine plume considered here ( $AR=60$ ) was found to be approximately 2 percent of the exit radius. With this magnitude of displacement thickness growth, the nozzle geometry will be modified only slightly, for which any significant change in plume configuration is not expected to be incurred.

However, upon leaving the nozzle exit, the low-speed wall boundary layer must undergo greater expansion than its high-speed counterpart in the center core so as to satisfy the pressure boundary condition. As a result, the plume boundary would become enlarged, particularly in the near-field region (Ref. 24). To assess this effect, the boundary layer option of the LMSC MOC plume program was utilized which calculates the boundary layer profile in the nozzle and, using  $M=1$  as the lowest Mach number, subsequently computes the Prandtl-Meyer expansion at the nozzle exit corner. The program also computes the exit Reynolds number and selects laminar or turbulent profile accordingly.

Using the hydrogen-fluorine system once again, the plume contours showing the boundary layer effects were obtained (Fig. 32). While a laminar profile has been predicted based on a transitional Reynolds number of  $10^6$ , the turbulent case is also included, since in rocket nozzles, the flow is almost always turbulent. The comparison presented in Figure 32 shows a considerable enlargement in plume size when the boundary layer effect is considered. Other parameters, such as internal shock location, boundary Mach number, etc., will also change accordingly. These changes will strongly affect the ensuing plume-induced separation prediction and must be understood thoroughly. Discrepancy between inviscid plume prediction and schlieren observation for selected cases obtained from recent NASA-Langley plume-induced separation study (Ref. 25) seems to indicate the boundary layer effect qualitatively. However, data available are not sufficiently copious to draw a final conclusion at this time.

#### d. Effect of Sting Support Concentric to the Nozzle

Some attention was accorded to this problem because a sting support concentric to the jet nozzle was used in all the NASA-Langley tests (Ref. 25). By considering the same area ratio and nozzle angle, it was found that the sting would not yield any effect on the inviscid plume properties (Fig. 32).

#### e. Three-Dimensional Plume Effect

Although only an axisymmetric nozzle is considered in this analysis, the exhaust plume will become three-dimensional when the vehicle is at angle of attack or yaw. A rigorous analysis for describing three-dimensional plumes requires tedious numerical computations. However, for a reasonable estimate of the three-dimensional plume characteristics which are coupled with the separated flow analysis, a simple patching of solutions

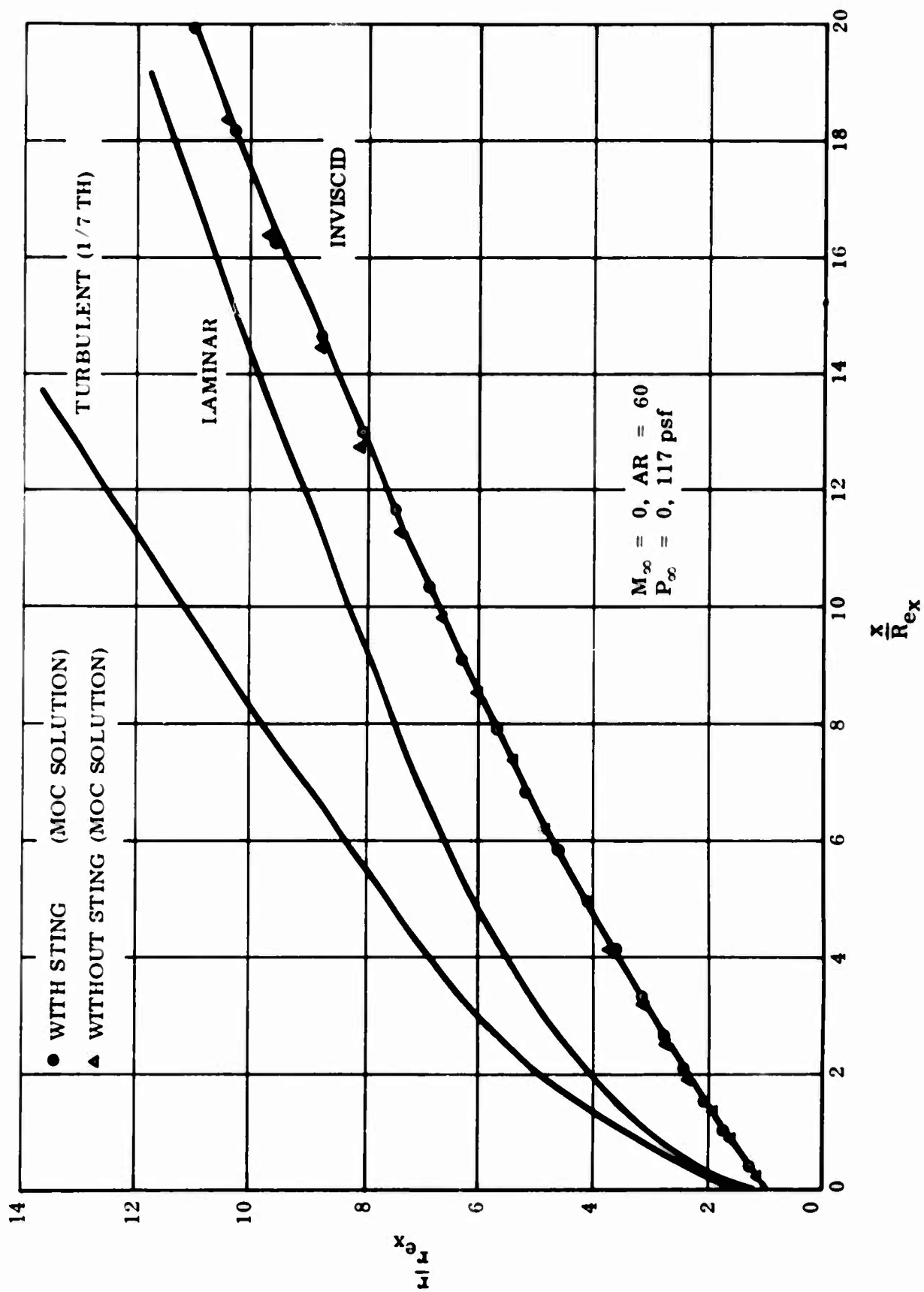


Figure 32 Hydrogen-Fluorine Plume Boundary:  $M_\infty = 0, AR = 60, P_\infty = 0.117 \text{ psf}$

would suffice. For example, the flow fields on the windward side and the leeward side of a pitching lifting reentry vehicle can be treated separately, each being exposed to its own local surrounding. The exhaust plume properties in each main region are, therefore, governed by the local freestream conditions. On the compression side, the plume would become more slender, whereas on the expansion side the plume would be enlarged. The validity of this model encompassing these two distinct regions is shown in Figure 33 wherein predicted and observed plume contours at angle of attack are compared. This simple three-dimensional plume model is chosen in this analysis in carrying out the plume and separated flow predictions.

#### 4. VISCOUS MIXING LAYER.

The inviscid-viscous plume model adopted in the present analysis is composed of an inviscid plume and a relatively thin viscous mixing layer (shear layer) superimposed along the plume boundary (Region (3) in Fig. 1). The shear layer is assumed to be describable by the Prandtl boundary layer equations for which the pressure gradient across the shear layer is zero. In view of the hypothesis of an average pressure within the dead-air separated flow region, the shear layer is essentially of the flat-plate type with zero streamwise pressure gradient, and its solution is self-similar except in cases where finite boundary layer thickness or disturbance occurs at the initial point of the shear layer (Fig. 1). Aside from the plume boundary, the separation region induced by the enlarged plume is also characterized by a shear layer emanating from the separation point. In general, on the plume side, the shear layer is fully developed turbulent because of the turbulent boundary layer prevailing in the nozzle. On the other hand, under high-altitude conditions in most LRV applications, the shear layer on the stream-side is generally pure laminar (Fig. 1). In this study, the flow separation and plume shear layer are assumed to be either pure laminar or fully developed turbulent; transitional shear layer is excluded entirely. Salient features of the shear layer solutions are discussed in the following paragraphs.

##### a. Laminar Shear Layer

A constant-pressure laminar shear layer can be described by a set of partial differential equations identical with those for a flat-plate boundary layer but with different boundary conditions. As discussed by Chapman (Ref. 26) the shear-layer momentum equation with zero initial boundary layer thickness in terms of a similarity velocity function,  $f$ , reduces to the familiar Blasius equation

$$f''' + ff'' = 0 \quad (13)$$

where

$$f'(\eta) = u/u_e \quad \text{and the boundary conditions are}$$

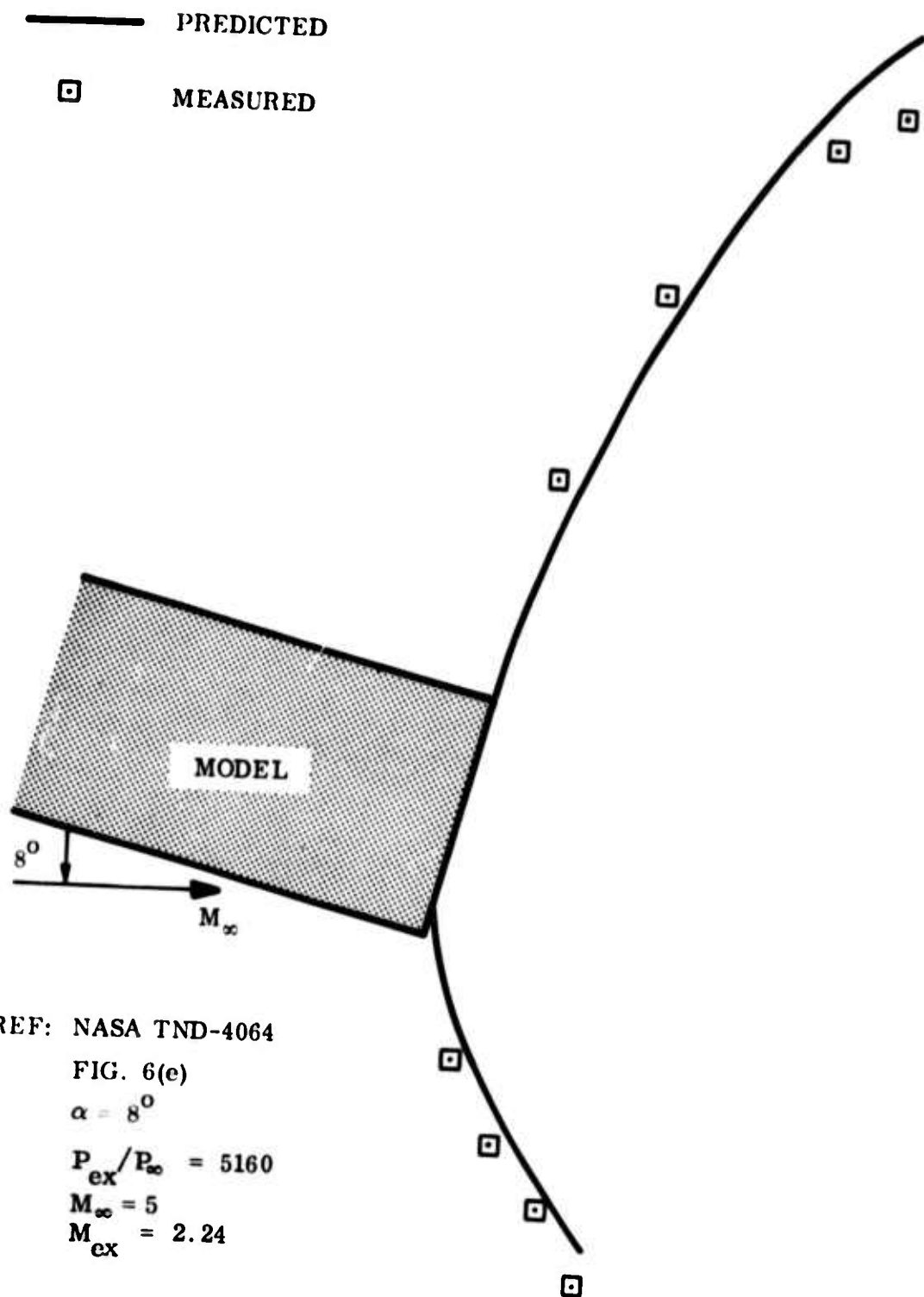


Figure 33 Comparison of Predicted and Measured Exhaust Plume Boundary at Angle of Attack

$$f'(\infty) = 1, f(0) = 0, \text{ and } f(-\infty) = \frac{u_B}{u_e} = 0 \quad (14)$$

The last boundary condition indicates that the average velocity in the separated flow or base region,  $u_B$ , is very low, as compatible with the dead-air assumption. Numerical solution to equation (13) yields the similarity profile illustrated in Figure 34.

To incorporate the laminar profile in the separated flow computer program, it was found more expedient to describe the profile numerically. Based on a curve fitting scheme, the velocity profile formula is obtained as follows:

$$f'(\eta) = \frac{u}{u_e} = \exp(-0.5613 + 0.4549\eta - 0.08868\eta^2 - 0.00106\eta^3) \quad (15)$$

where  $\eta = -7.4$  and  $3.6$  are the practical lower and upper limits for the width of the shear layer.

#### b. Turbulent Shear Layer

The shear layer initiated at the rocket nozzle exit and growing continuously along the plume boundary can be represented approximately by a constant-pressure turbulent shear layer. For simplicity, the Korst model is adopted to describe this shear layer for which the governing differential equation is linearized and the resulting self-similar velocity profile can be represented by an error function (Ref. 27). If the shear layer is exposed to a dead-air region, a simple error function formula for velocity profile description is obtained (Fig. 35):

$$\frac{u}{u_e} = \frac{1}{2} (1 + \operatorname{erf} \frac{y\sigma}{x}) \quad (16)$$

where  $x, y$  are the intrinsic coordinates oriented along the plume boundary and  $\sigma$  is a similarity spreading parameter to provide a macroscopic description of the turbulent shear layer. An approximate prediction formula for  $\sigma$ , either for a compressible free jet (Ref. 27) or for parallel streams (Ref. 28), can be expressed in the following form:

$$\sigma = 12 + 2.758 M. \quad (17)$$

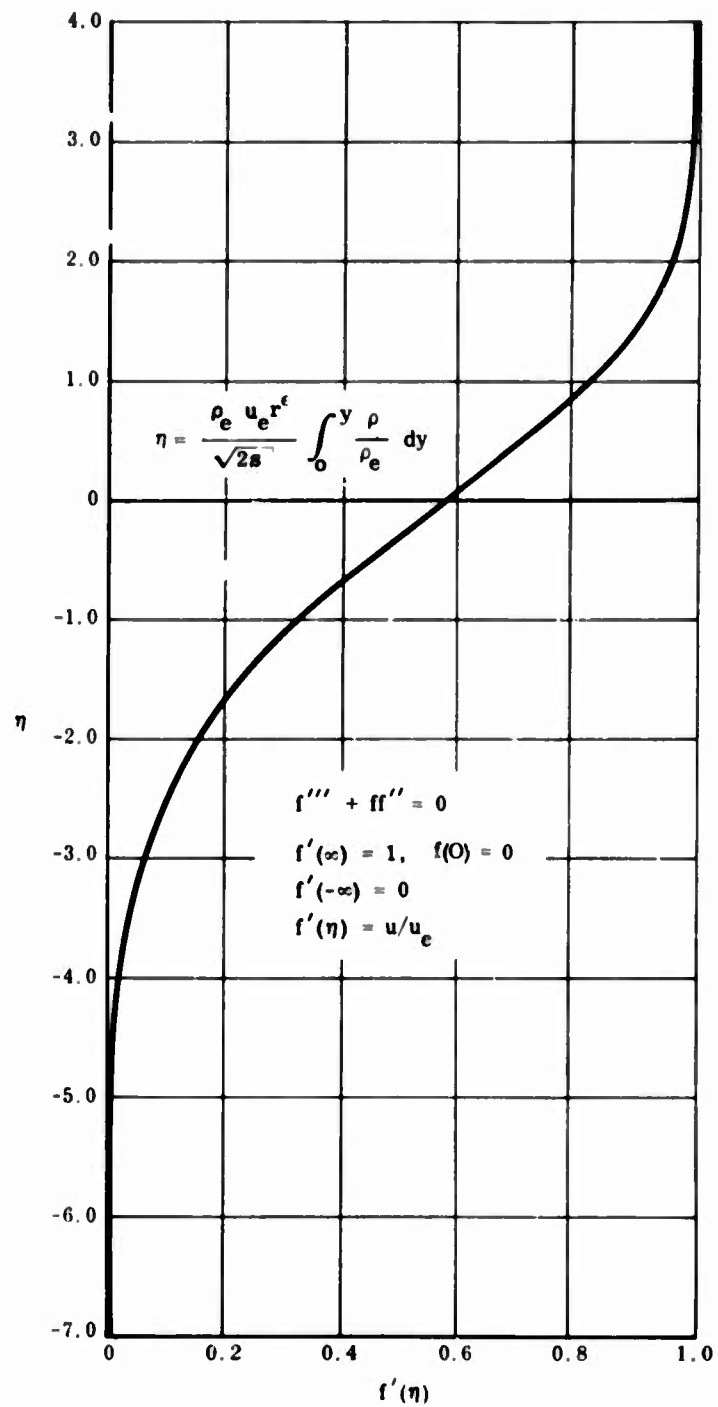


Figure 34 Velocity Function vs Distance Function for Constant Pressure Laminar Mixing Layer

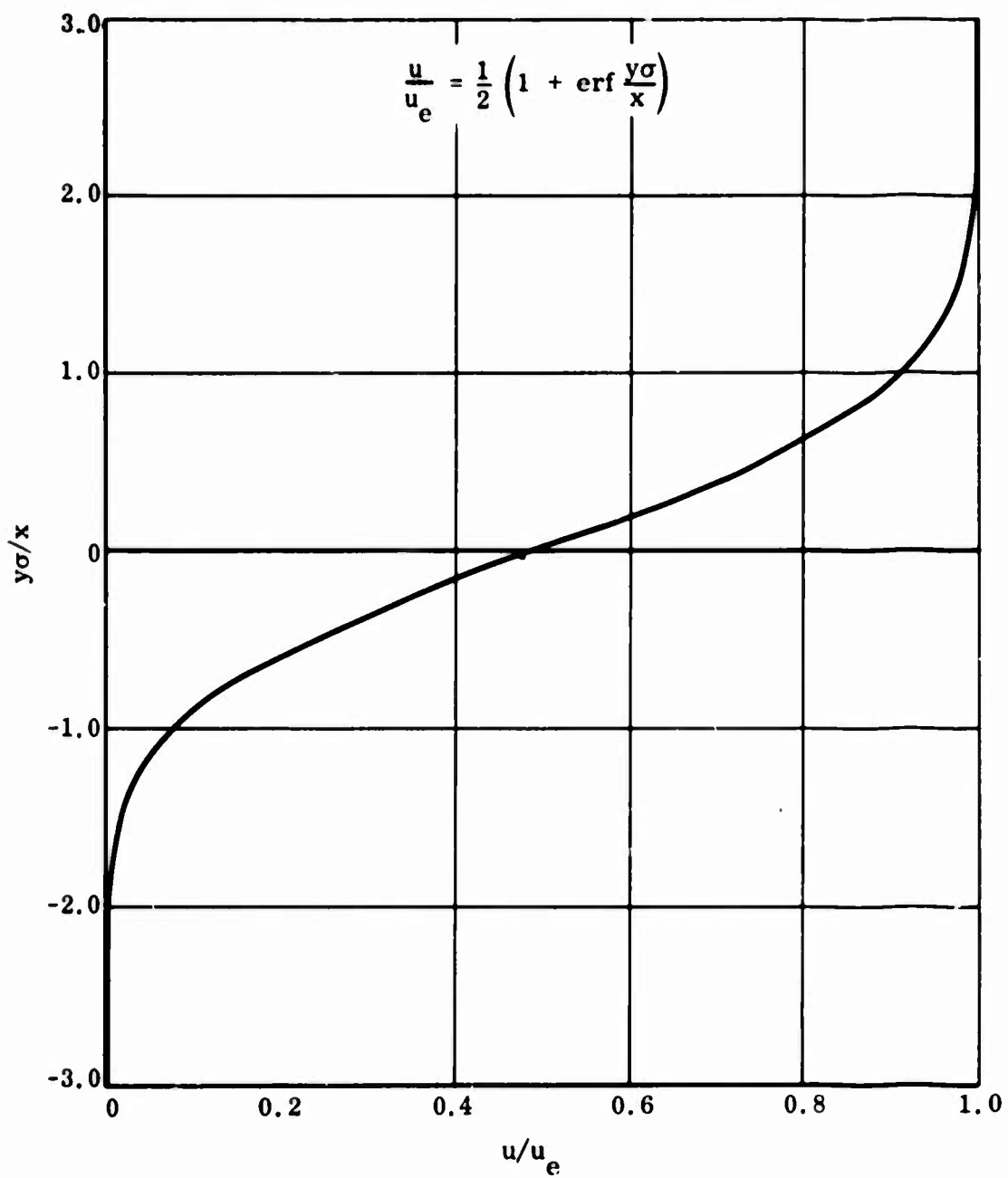


Figure 35 Error Function Velocity Profile for Constant Pressure Turbulent Mixing Layer



where  $M_0$  is the freestream Mach number for either a single stream or, in the case of two parallel streams, an equivalent single stream. A summary of experimentally obtained  $\sigma$  values (Ref. 29) is presented in Figure 36, including a comparison with the Maydew-Reed semiempirical estimates (Ref. 30). Data scattering shown in the figure clearly indicates the need for extensive experimental study and statistical analysis.

### c. Generalized Crocco Relation

A well known particular solution for determining the total enthalpy profile across a boundary layer or shear layer is by means of the Crocco relation. The main hypothesis underlying this approach is unit Prandtl number whereby the solution of the energy equation exhibits a linear relation between the local total enthalpy and the local stream-wise velocity, viz.,

$$H = Au + B \quad (18)$$

where  $A$  and  $B$  are constants depending on the appropriate boundary conditions. Thus, the relatively complicated energy equation is now decoupled from the momentum equation and can be solved by employing a simple scheme, once the velocity profile is determined. In the majority of cases, the unit Prandtl number provides satisfactory solutions, thus rendering the Crocco relation valid.

By the same token, the Crocco relation can be generalized to predict the species concentration profile across the boundary or shear layer if the corresponding Schmidt number (or Lewis number) is unity, viz.,

$$Y_i = A'u + B' \quad (19)$$

where  $Y_i$  is the mass concentration for species  $i$  and  $A'$ ,  $B'$  are the integration constants.

In short, incorporation of the generalized Crocco relation in the Chapman-Korst model permits a complete determination of the velocity, temperature, and concentration profiles across the shear layer separating the exhaust plume from the surrounding air.

### d. Afterburning in Mixing Layer

By virtue of the generalized Crocco relation, the species concentration profile across the mixing layer is defined, which encompasses an entire range of mixture ratios of the fuel-rich exhaust gas and the ambient air. Combustion or afterburning will occur if the local temperature is above the ignition temperature and the total reaction delay time is short. In the analysis the flame sheet concept is invoked for which local combustion is assumed to take place in each layer that characterizes a particular exhaust gas/air mixture ratio. This model can easily accommodate equilibrium chemistry and permits construction of design curves showing afterburning characteristics.

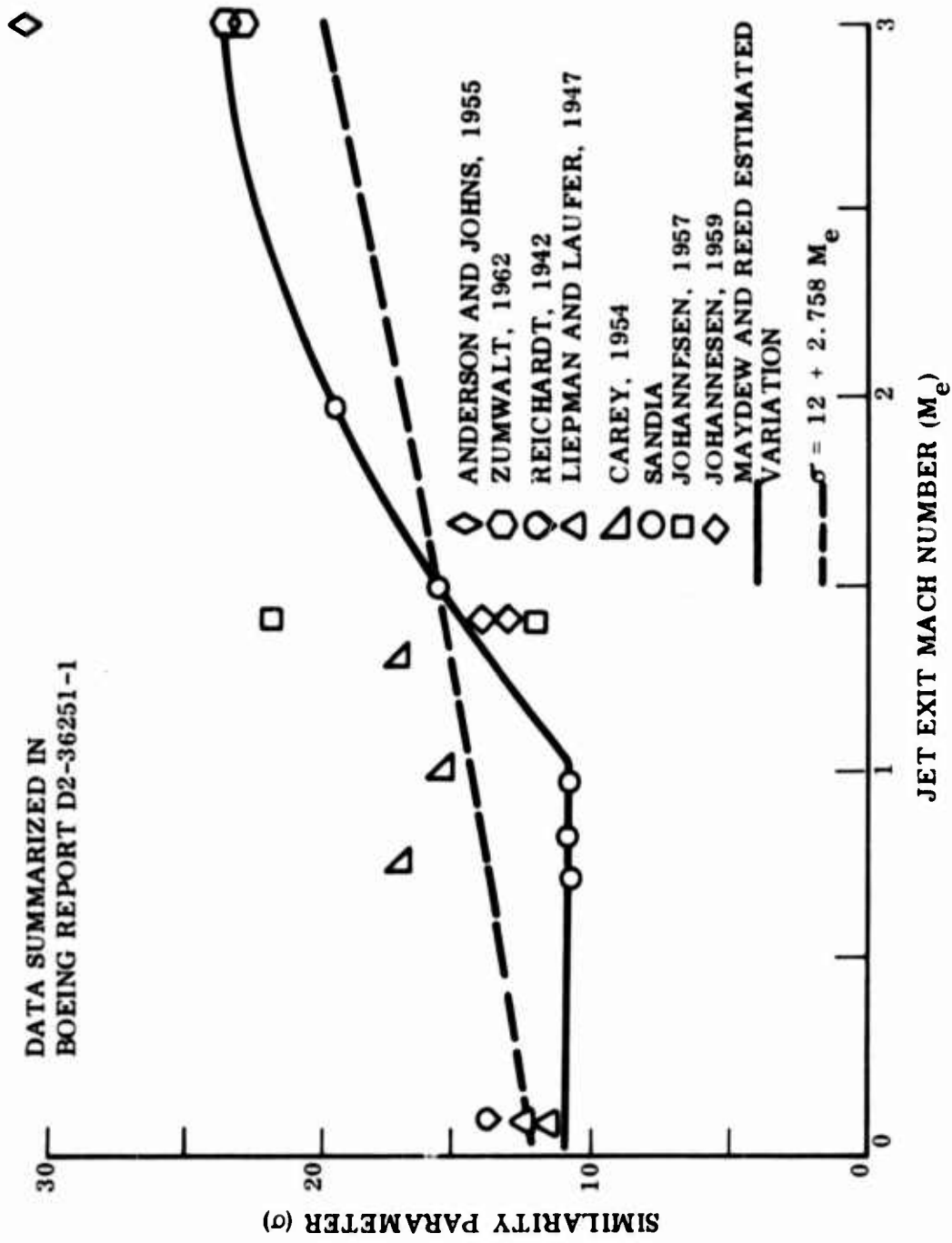


Figure 36 Experimental and Theoretical Sigma Values for Free Jets

However, in the shear layer the energy of the chemical system is partially converted into kinetic energy, resulting in a reduction of the local static enthalpy and temperature. The temperature reduction and the attendant high gas velocity render the shear layer susceptible to nonequilibrium chemical effects. As a matter of fact, in the present LRV application involving altitudes above 200,000 feet, afterburning within the shear layer is not likely to occur, at least not in the equilibrium sense. This aspect is therefore not pursued except for the base or plume-induced separation region which can be regarded as a special mixing layer featuring a single mixture ratio, zero kinetic energy, and short characteristic length.

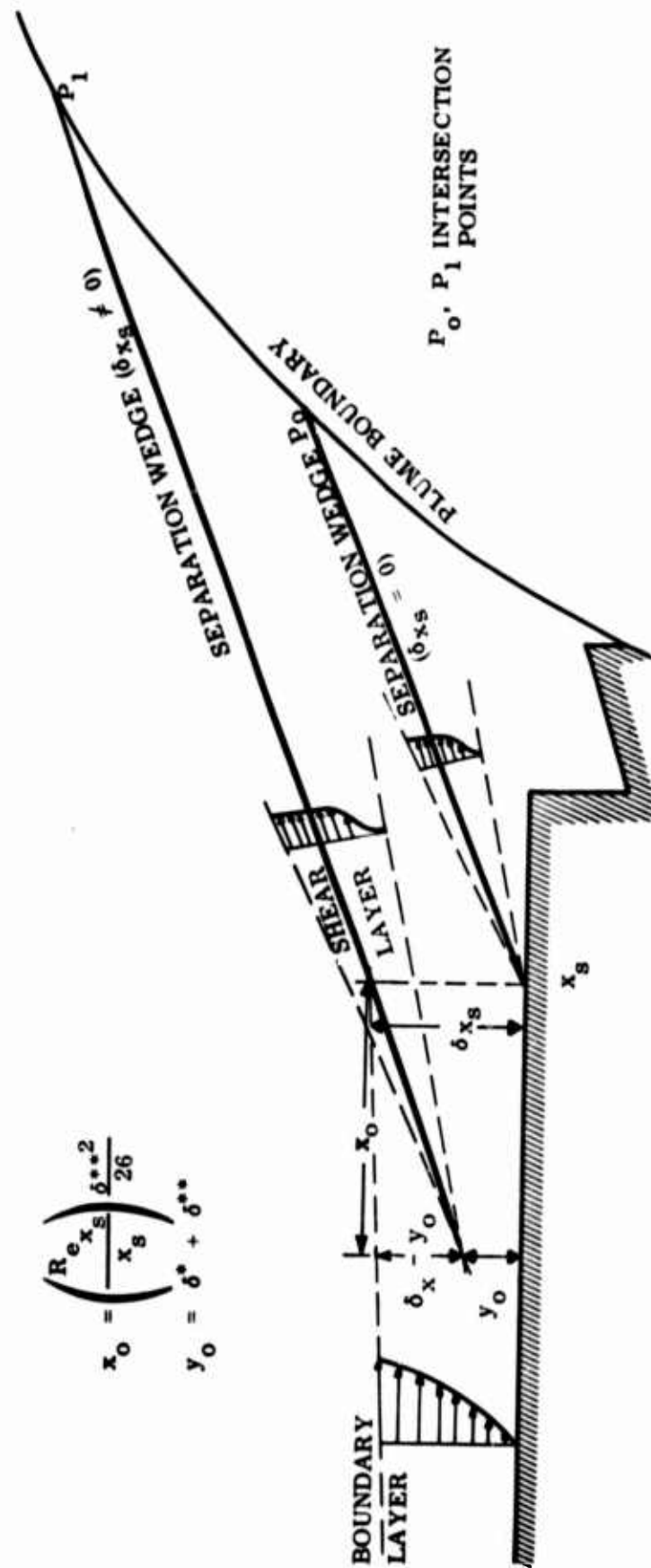
#### e. Initial Boundary Layer Effects

The Chapman and Korst profiles presented in Equations 15 and 16 are applicable only to the case where zero boundary layer thickness or flow disturbance prevails at the separation point from which the shear layer emanates. If the initial boundary layer is finite, then the self-similar feature of the Chapman-Korst profile will no longer be valid. To emphasize this, the laminar flat-plate case is considered. In this case, the flow field is characterized initially by a self-similar Blasius profile but is later replaced by a different self-similar Chapman profile. The presence of two distinct velocity profiles violates the similarity requirement and suggests the existence of a transition region linking these two distinct similar flow regions. A sufficient understanding of the transition region thus constitutes the prerequisite for a reliable assessment of the initial boundary layer effect.

On the plume side, the boundary layer thickness at the nozzle exit (initial point for the shear layer) is considered to be insignificant for the present LRV application; therefore, the initial boundary layer effect is excluded. However, on the stream side, the local environment may be highly rarefied as a result of high altitude and/or large angle of attack (leeside). The boundary layer thickness concomitant with the typical low Reynolds number in such a rarefied gas medium may be quite substantial; hence, its effect must be considered.

A rigorous approach to the transition problem requires a separate solution (Ref. 31) and/or empirical data, particularly for the turbulent case. An alternate approach is to introduce certain transformation variables so that the resulting equivalent shear layer will retain the self-similarity features while implicitly taking account of the initial boundary layer effect. One such method is that based on the equivalent bleed concept discussed in Reference 28. With this model, the governing integral equations involving the initial boundary layer effect are expressed in a form identical with that involving mass bleed with zero initial disturbances. However, as pointed out in Reference 32, a singularity is present at the separation point.

A different method to resolve the initial disturbance dilemma is that based on the origin shift model discussed in References 32 through 36. According to this model, which is adopted in this analysis, an apparent or equivalent origin is defined at a distance  $(x_0, y_0)$  upstream of the actual initial point satisfying the following criteria (Fig. 37):



$$x_0 = \left( \frac{Re_{x_s} \delta^{*2}}{x_s} \right) \frac{26}{26}$$

$$y_0 = \delta^* + \delta^{**}$$

Figure 37 Initial Boundary Layer Effect on Plume-Induced Flow Separation

- The initial boundary layer thickness at the apparent origin is zero
- The mass and momentum fluxes are the same as those at the actual initial point.

Predicted velocity profiles based on the origin shift method were found to agree quite satisfactorily with data, whereas those based on the equivalent bleed model have been less successful (Ref. 35).

The origin-shift model is applicable to laminar and turbulent shear layers alike, although it was developed originally for turbulent flows. Recently, this method has also been applied to the two-stream mixing problem (Ref. 35).

Applying the total mass and momentum flux balances between the actual and the apparent origins, the origin-shift coordinates are found to be (Fig. 37):

laminar case

$$x_o = \frac{\rho_e u_e}{2 \mu_e} \left\{ \frac{\delta^{**}}{f(\delta) - f(-\infty)} \right\}^2 \quad (20)$$

$$y_o = \delta^* + \delta^{**} \quad (21)$$

turbulent case

$$x_o = \sigma \delta^{**} \left[ I_1(\infty) - I_2(\infty) \right]^{-1} \quad (22)$$

$$y_o = \delta^* + \delta^{**} \quad (23)$$

where all these symbols are defined in the Nomenclature section. Since the initial disturbance problem is encountered primarily on the stream side in LRV applications, only the laminar Equations 20 and 21 are used in this analysis. After some manipulation, Equation 20 can be simplified as follows:

$$x_o = \frac{\delta^{**2}}{26} \left( \frac{u_e}{\nu_e} \right) \quad (24)$$

where the constant value 26 is based on  $\eta = 3.6$  for the shear layer thickness above the plume boundary (Fig. 34).

Equations (21) and (24) represent the final form used in conjunction with the separated flow analysis in this report. The local boundary layer thickness is determined by means of the approximate formula presented in Reference 37

$$\delta = \frac{5.2 x}{\sqrt{\frac{P_w}{P_a} Re}} \left( 0.28 + 0.5 \frac{T_w}{T_a} + 0.22 \frac{T_{aw}}{T_a} \right)^{0.88} \quad (25)$$

where subscript  $a$  represents the local value at angle of attack  $\alpha$ . The corresponding  $\delta^*$  and  $\delta^{**}$  can then be evaluated from the definitions

$$\delta^* = \delta \int_0^1 \left( 1 - \frac{\rho}{\rho_e} f' \right) d\eta \quad (26)$$

$$\delta^{**} = \delta \int_0^1 \frac{\rho}{\rho_e} f' (1 - f') d\eta \quad (27)$$

The separation wedge based on the equivalent origin concept is then utilized in carrying out the separated flow analysis.

#### f. Shocks Imbedded in the Shear Layer

In the present model, a continuously spreading viscous shear layer is superimposed along the inviscid plume boundary. At some downstream location, it is quite possible that the calculated internal boundary shock would be imbedded in the shear layer. This occurrence will invalidate the Chapman-Korst shear layer model since normal pressure gradient and steep entropy rise are now present within the mixing layer. A coupled inviscid-viscous flow analysis is necessary to resolve this problem. Complex mathematical tasks are involved to reach a solution and, to date, quantitative results have not yet been obtained (Ref. 38).

### 5. PLUME-INDUCED BOUNDARY LAYER SEPARATION

The discussion presented in the foregoing sections describes the sequence of events that take place from the combustion chamber to the plume flow field as well as various important phenomena pertinent to the LRV jet pluming problem [flow regions (1), (2), (3) and (5)]. Because of high jet-to-ambient pressure ratios involved during the aerocruise maneuver, a relatively large equivalent plume body is frequently formed

which will, in turn, induce an adverse pressure gradient on the vehicle aft-surface. If the adverse pressure gradient is sufficiently strong, the boundary layer may not have enough kinetic energy to overcome the retarding force and is then forced to separate. Pressure elevation due to flow separation will affect the aerodynamic forces and moments over the vehicle surface. Serious stability problems may subsequently arise, which must be adequately resolved in order to ensure satisfactory flight characteristics.

This description shows that the mechanism of plume-induced flow separation is basically the same as that of separated flows upstream of a compression corner or an aft flare, except that mass exchange between the plume and the air stream is absent in the solid problem. Certain physical quantities between these two types of separation are expected to be at variance. Semiempirical formulas generated for the solid problem, such as plateau pressure prediction, may not be applicable to the plume problem without any modification.

To resolve the plume-induced separation problem, one approximate approach is to extend the Chapman-Korst shear layer model, originally developed for base pressure predictions (Refs 26, 27 and par. 4 of this section), to the case involving fluid compression, mass diffusion, and chemical reactions. This modified Chapman-Korst theory provides a scheme for predicting the overall properties within the separated flow region and is merited with relative simplicity.

For plume-induced flow separation, the separation point is also an unknown quantity whereas it is usually prescribed to occur at the base periphery for the base flow problem. Hence, an additional condition must be imposed. In this study, this condition is provided by introducing a semiempirical formula correlating the separation point with base pressure, initial Mach number, and initial Reynolds number. However, development of a versatile and satisfactory formula for separation length prediction still awaits the availability of pertinent data.

The modified Chapman-Korst model used in LRV application is described in the following section and Appendix I. Rigorously speaking, this model is valid only for two-dimensional or axisymmetric flows. Its applicability to the three-dimensional LRV plume problem in a pseudo-two-dimensional manner must be justified a posteriori. This facet and the incorporation of the small cross-flow concept in the analysis are discussed in par. 6 of this section. The present discussion is restricted to local two-dimensional flow separation with respect to a particular streamline.

#### a. The Modified Chapman-Korst Model

In accordance with the Chapman-Korst model (Figs. 1 and 38), the plume-induced separated flow structure can be elucidated in a phenomenological manner. When the flow encounters a strong plume-induced adverse pressure, it will leave the surface and create a dissipative layer which, along with the plume shear layer, will envelope a region of mass entrainment. Although recirculation occurs in this region, the

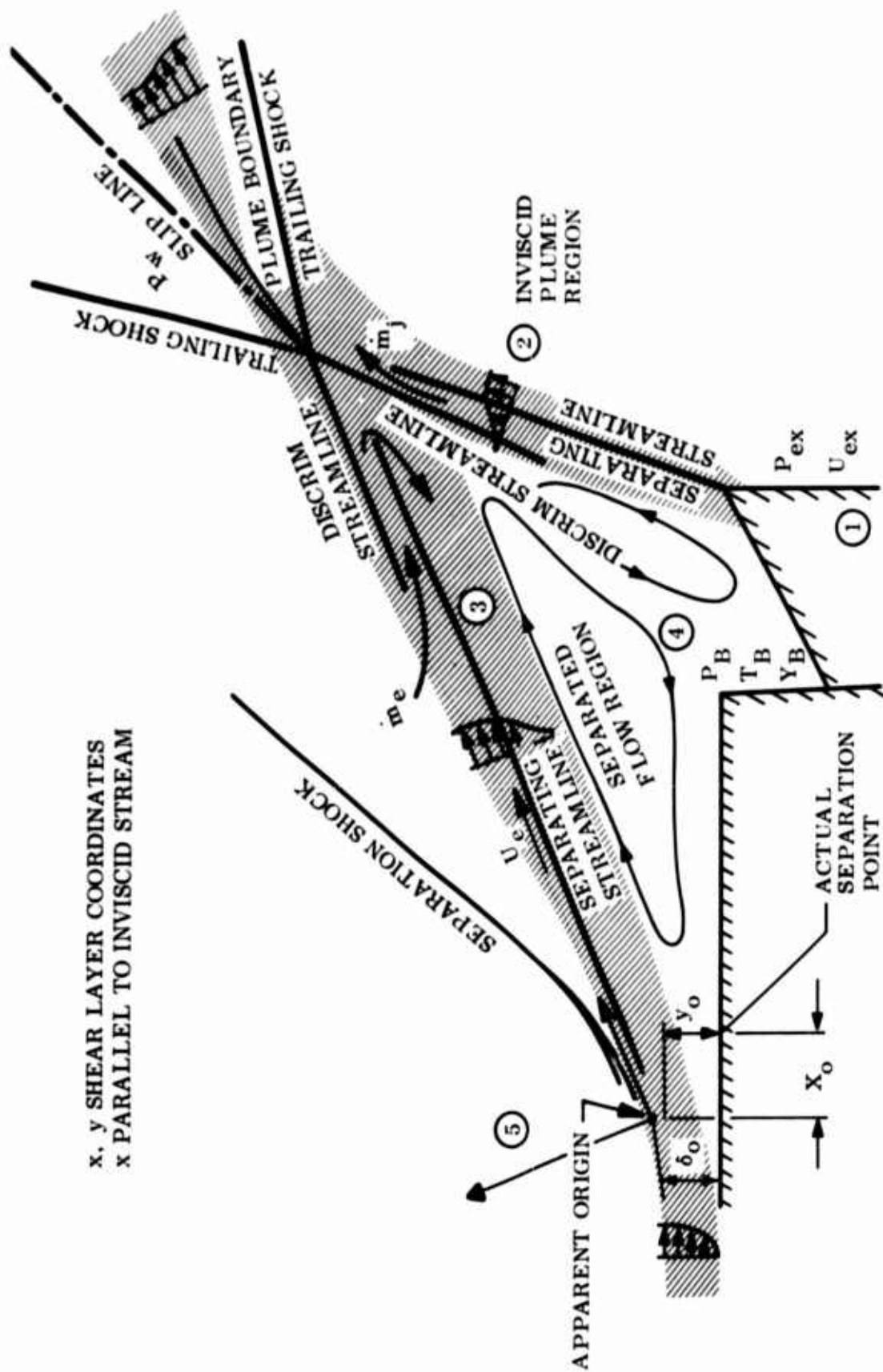


Figure 38 Plume-Induced Separation



average mean velocity therein can be regarded as very small (dead-air). Hence, the complex separated flow field is now replaced by a comparatively simple shear layer envelope. Implementation of mass and other flux conservations within the shear layer envelope as well as a proper reattachment criterion will then permit a steady-state solution describing the average separated flow characteristics.

The basic assumptions used in the present analysis are:

- Perfect gas
- Prandtl and Schmidt numbers are unity
- A linear viscosity-temperature relation
- Constant-pressure field

As already discussed in the Introduction and par. 4 of this section, as well as in References 26 and 27, these assumptions are introduced for both laminar and turbulent separations. Review and application of these shear layer theories are also included in References 39 to 41.

In evaluation of the separated flow properties, the main flow quantities to be ascertained are identified to be the following:

- Location of separation point,  $x_s$
- Average pressure in the plume-induced separation region (base pressure),  $P_B$
- Average gas temperature in the separation region (base temperature),  $T_B$
- Average species concentration in the separation region (base species concentration),  $Y_i$ , resulting from diffusion through the air and the plume shear layers
- The dividing (separating) streamline location measured from the shear layer coordinate,  $x$  (Fig. 38), defined as the streamline above which the total mass flux is equal to the total inviscid mass flux immediately upstream of the separation point. Although two dividing streamlines are present, i.e., one in the stream shear layer and the other in the plume shear layer, the constant-pressure condition permits a simple correlation between the two streamlines (see Appendix I).
- The discriminating (limiting) streamline location measured from the shear layer coordinate,  $X$  (Fig. 38), defined as the streamline which possesses just sufficient energy to overcome the overpressure in the trailing shock system created by the shear layer intersection. Analogous to the dividing streamline problem, the stream and plume discriminating streamlines are related in a simple manner.

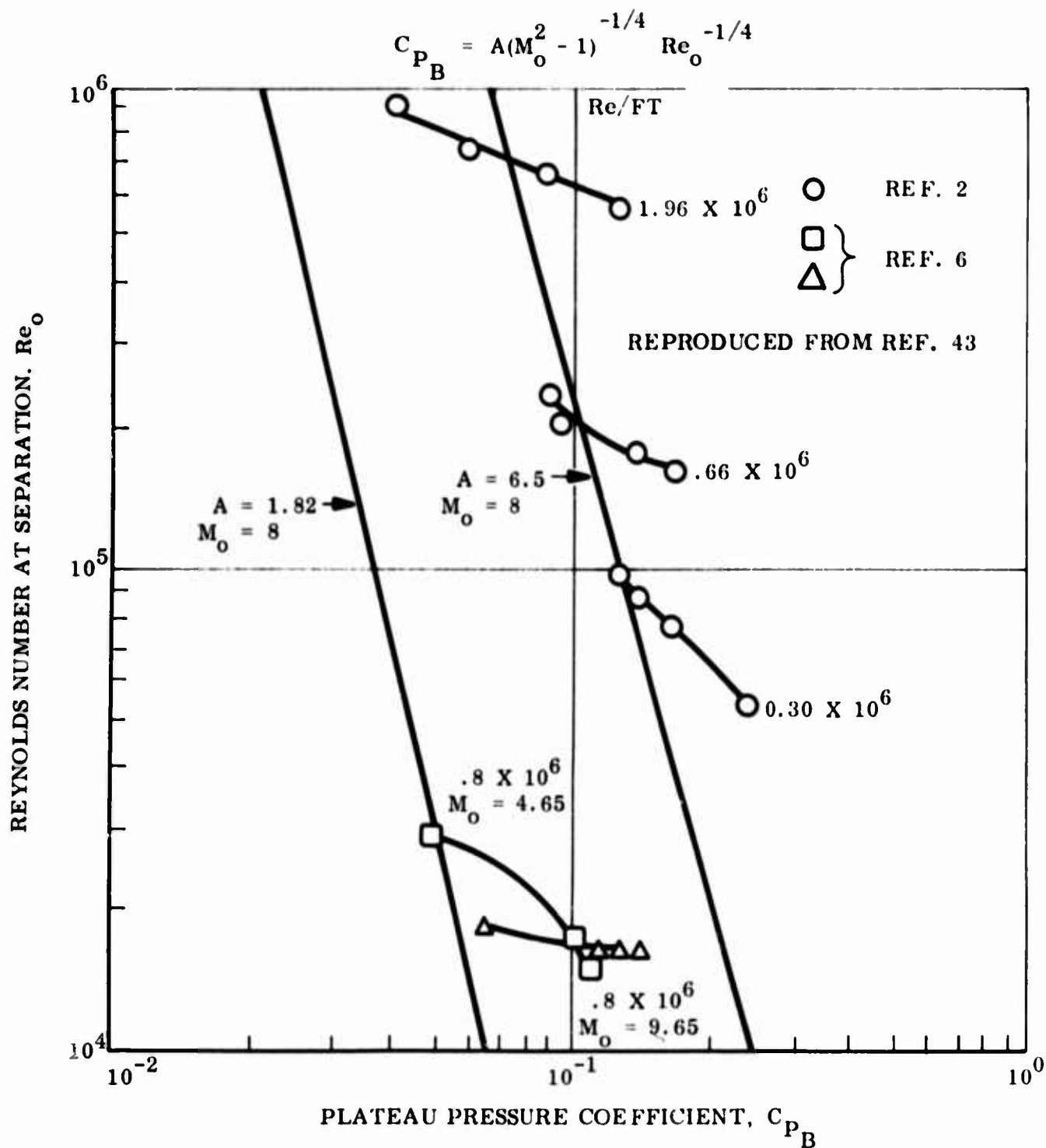


Figure 39 Reynolds Number Effect on Plateau Pressure Coefficient

$$A = 0.3 \left( \log \frac{P_{ex}}{P_o} \right)^3 - .88 \left( \log \frac{P_{ex}}{P_o} \right)^2 + .72 \left( \log \frac{P_{ex}}{P_o} \right)$$

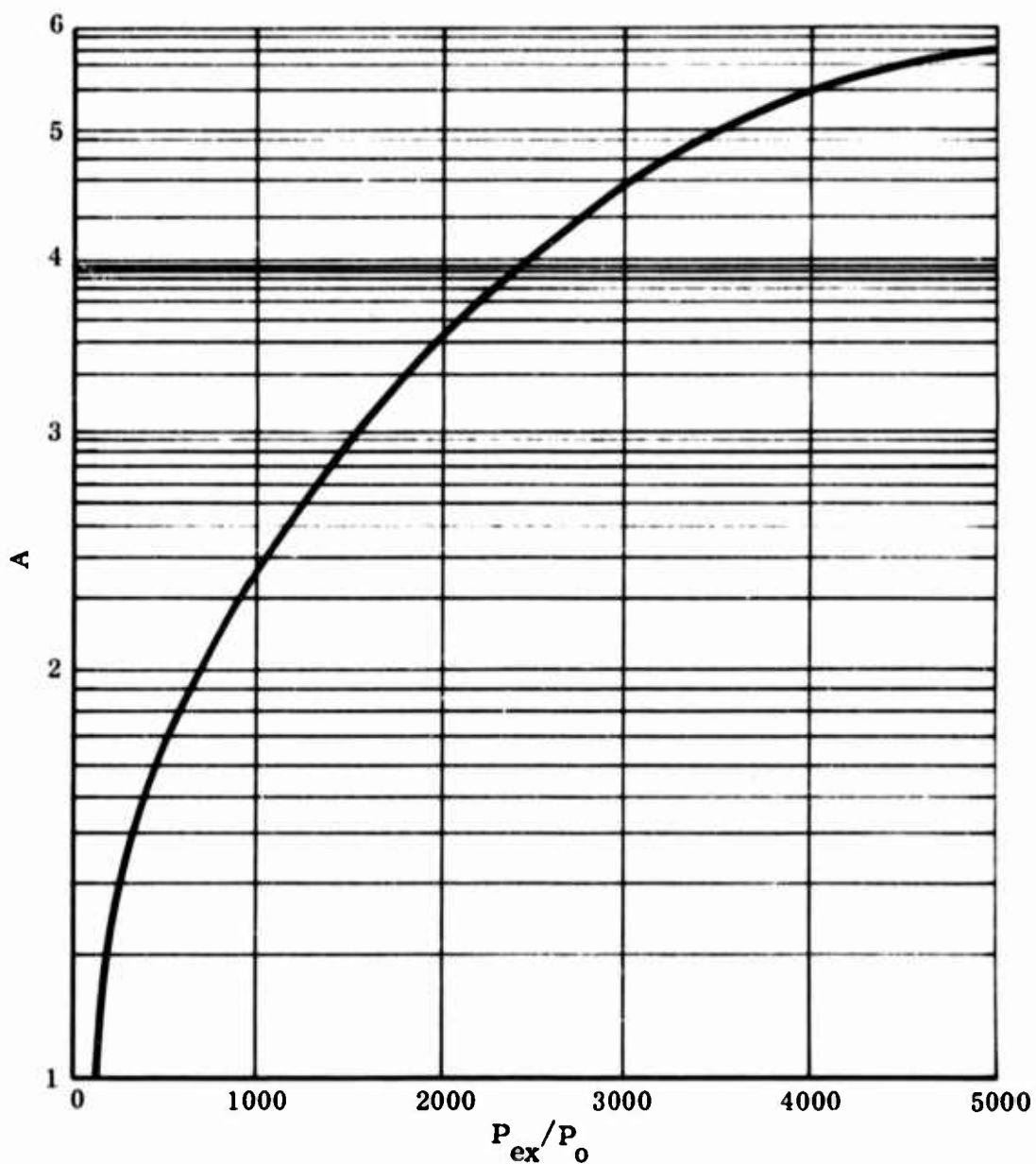


Figure 40 Variation of A With  $P_j/P_o$

In view of these six unknowns, six independent conditions are needed to obtain steady-state solutions. Mathematical details on formulation of these supplementary conditions are discussed in Appendix I, and this section places emphasis only on aspects that attach particular physical significance to the present LRV application:

- Semiempirical Relation Between  $X_s$  and  $P_B$ . Inasmuch as  $P_B$  represents an average quantity, it can be approximated by the average plateau pressure within a separated flow region. A simple correlation formula for  $P_B$  can then be expressed in the widely used form for laminar flows (Ref. 42):

$$C_{PB} = \frac{P_B - P_o}{\frac{1}{2} \rho_o u_o^2} = \frac{A}{(M_o^2 - 1)^{1/4} Re_o^{1/4}} \quad (28)$$

where  $C_{PB}$  is the base pressure coefficient,  $M_o$  and  $Re_o$  are the Mach number and Reynolds number at the separation point, and  $A$  is an empirically determined constant. From the various values of  $A$  summarized in Figure 39, a constant value  $A = 1.8$  has been proven adequate for solid compression corner flows and, from limited schlieren data (Refs. 2, 6, and 43),  $A = 6.5$  was found to be valid for plume-induced separated flow. However, recent cone-cylinder pressure data with an air plume at freestream Mach numbers of 4.5 and 6.0 (Ref. 25) have indicated that the  $A$  value should be much less than 6.5. Furthermore, the NASA-Langley data also show that  $A$  is strongly dependent on  $P_{ex}/P_o$  (jet-to-ambient pressure ratio) but not sensitive to Mach number for the moderate air speeds used in the tests. Based on these data, an empirical relation describing  $A$  is tentatively established and utilized in the present investigation:

$$A = 0.3 \left( \log \frac{P_{ex}}{P_o} \right)^3 - 0.88 \left( \log \frac{P_{ex}}{P_o} \right)^2 + 0.72 \left( \log \frac{P_{ex}}{P_o} \right) \quad (29)$$

which is graphically represented in Figure 40. The base pressure formula, Equation (28), essentially establishes a separation wedge from which important quantities, such as separation angle, and separation pressure coefficient, can be determined accordingly. For turbulent separation, a similar plateau pressure formula with different values of  $A$  and exponent for the denominators can be introduced. However, no data are available to verify this conjecture.

- Exhaust Plume Properties. For each set of  $X_s$  and  $P_B$  values, the inviscid exhaust plume properties based on the method-of-characteristics solution with  $P_B$  as the local ambient pressure and under quiescent air conditions (dead-air) can be determined (see par. 3 of this section).
- Conservation Requirements. Under steady-state conditions, the total mass flux, the mass flux for any particular species, and the energy flux within the separation region must be conserved. In particular, formulation of the species conservation requires that the total species flux at the separation point and the nozzle exit equal the total species flux at the intersection point of the shear

layers (Fig. 38). Instead of considering all the species that exist in the flow field, it is more convenient to select a particular species which occurs in the plume but not in the air stream, such as atomic hydrogen. By so doing, the species flux can be represented by the exhaust gas/air mixture ratio, and all other species can be determined subsequently from chemical equilibrium calculations. Derivations of the conservation equations and numerical computation schemes are included in Appendix I.

- **Thermochemical Compatibility Requirement.** The argument presented in par. 2.b of this section has established the validity of equilibrium chemistry in a dead-air separation region. Thus, for a particular set of base pressure,  $P_B$ , and base species concentration,  $Y_B$ , a corresponding base temperature,  $T_B$ , can be determined by using the NASA-Lewis equilibrium program. Furthermore, the uniqueness of  $T_B$  requires that the energy conservation utilizing the separated flow model be compatible with that considered thermochemically. For  $H_2 - F_2$  and  $H_2 - O_2$  systems with high-speed air flows, the design charts presented in Figures 2 through 19 can thus be used as an additional condition for energy conservation within the separation region. In application,  $T_B$ ,  $P_B$ , and  $Y_B$  refer to the temperature, pressure, and mixture ratio (CR) on these graphs.
- **Reattachment Criterion.** The reattachment criterion requires that the total pressure along the discriminating streamline,  $P_{t_{se}}$ , be equal to the static pressure in the trailing shock system,  $P_w$ , so that the flow can pass downstream. The trailing shock system is determined by the intersection characteristics between the separation wedge and the exhaust plume and, hence, is strongly dependent on the inviscid plume geometry and plume boundary properties. A simple two-dimensional shock polar intersection model (Ref. 44) is employed in this analysis to determine  $P_w$  as illustrated in Figure 41. From base pressure experiments, it has been found that the reattachment criterion is not always valid when employed in conjunction with the Chapman-Korst model. The difficulty is attributable to the over-simplified model which does not accurately describe the separated flow structure. To avert this problem, Nash (Ref. 45) introduced a correction factor to validate the predicted values:

$$N = \frac{P_{t_s} - P_B}{P_w - P_B} \quad (30)$$

where  $P_{t_s}$  is the total pressure along the discriminating streamline and  $P_w$  is the static pressure in the trailing shock system. The Nash factor is an experimentally determined parameter; its dependence on flow conditions requires further systematic study. Additional remarks concerning this correction factor are included in Reference 39.

#### b. Computation Scheme

With the supplementary conditions listed above, all the unknown parameters can be determined from the solutions of the conservation integral equations. Simultaneous

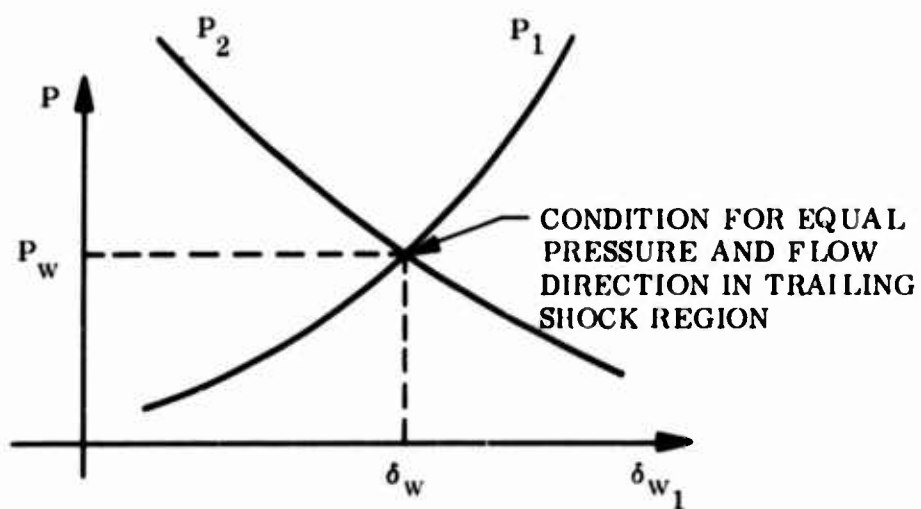
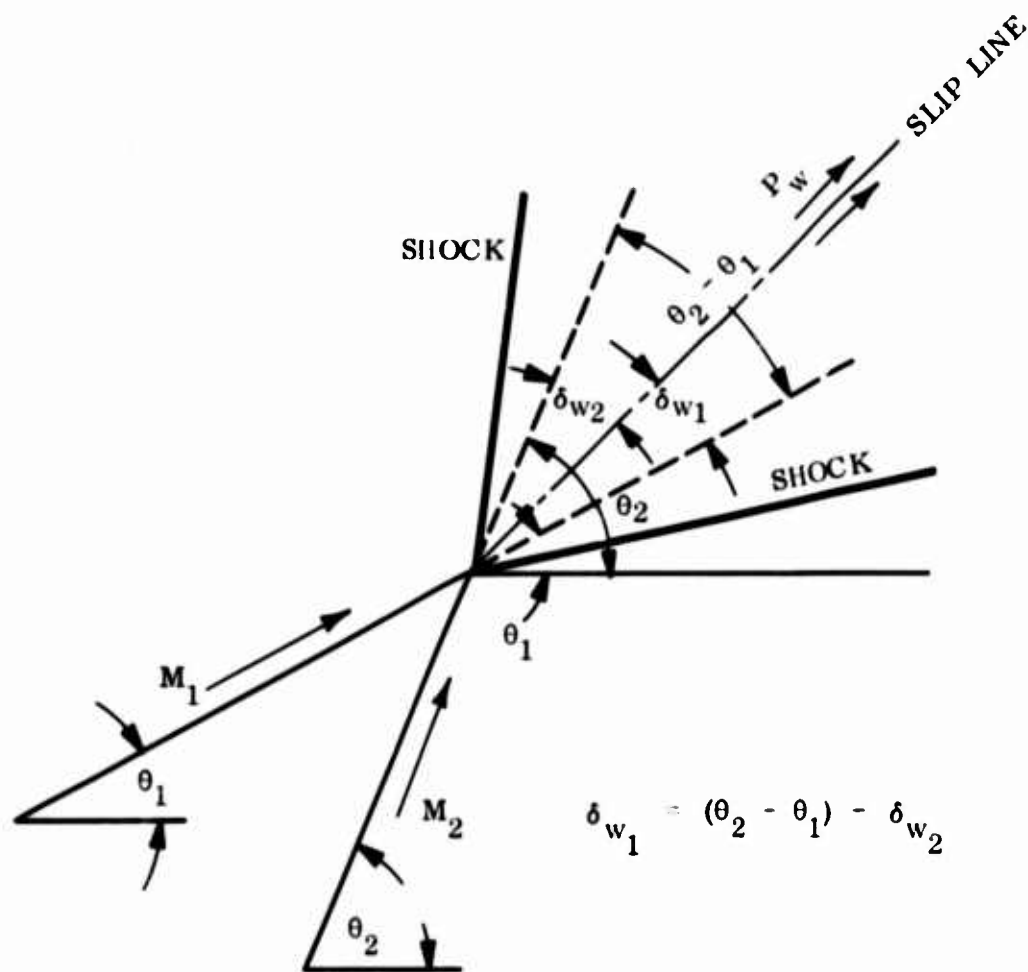


Figure 41 Determination of Trailing Shock Pressure

consideration of thermochemistry and cross-flow boundary layer would then permit complete determination of the plume-induced flow field associated with LRV synergetic maneuvers.

An iteration numerical procedure has been developed to ascertain these unknown parameters,  $T_B$ ,  $Y_B$ , etc., which constitute a part of the boundary conditions for the governing equations. The calculation procedure thus involves assigning a number of values for  $P_B$ ,  $Y_B$ ,  $T_B$ ,  $\eta_{se}$ , etc. and evaluating the integral equations until all the conservation and reattachment requirements are satisfied. In performing the analysis, several items are considered:

- To expedite the numerical iteration, the energy equation can be replaced by the thermochemical compatibility requirement; then the problem involves only the relatively simple mass and species iterations, and  $T_B$  is correlated with  $Y_B$  and  $P_B$  from the thermochemical design curves constructed independently.
- When the initial boundary layer thickness is finite, an apparent origin is defined based on the discussion of par. 4.3 of this section. Then, the corresponding separation wedge can be quite different from that without the initial disturbance (Fig. 37). The separation flow properties and the ensuing intersection with the plume are determined in accord with this apparent wedge.
- Because of flat surfaces involved in LRV applications, at least in the sample problem considered in this report, a separation wedge is postulated. It is quite conceivable, however, that the separation region may exhibit conical properties, particularly for slender or axisymmetric bodies (Ref. 43). Additional data are needed to clarify this problem.

For mathematical details of the iteration procedure, the reader is again referred to Appendix I. In this section, only the computer flow diagram for the accelerated procedure (mass and species iterations together with temperature design charts) is presented to provide an overview of the numerical analysis (Fig. 42). Although a computer program based on the modified Chapman-Korst model has been developed, it is not an indispensable item since sufficient graphical solutions have been obtained to permit prediction of important parameters, such as separation distance and base pressure, under a wide range of flow conditions. Application of the pseudo-two-dimensional separated flow analysis to the LRV plume problem will be further elaborated in Section III.

## 6. THREE-DIMENSIONAL BOUNDARY LAYER EFFECTS

The flow field over an LRV surface is three-dimensional in character because of its three-dimensional configuration and possible pitch, yaw, and roll motions during maneuvering. Three-dimensionality complicates the mathematical analysis because of the presence of the cross-flow component and its derivatives in the governing differential equations. For attached boundary layer flows, the three-dimensional equations are amenable to similarity transformation or other analytical treatments under special circumstances. Notable examples include laminar flow over an infinite yawed cylinder, the small cross flow problem, axisymmetric spinning-body flow, etc. However, their separated flow counterpart has not met with comparable success because of the lack of understanding of the three-dimensional separated flow mechanism.

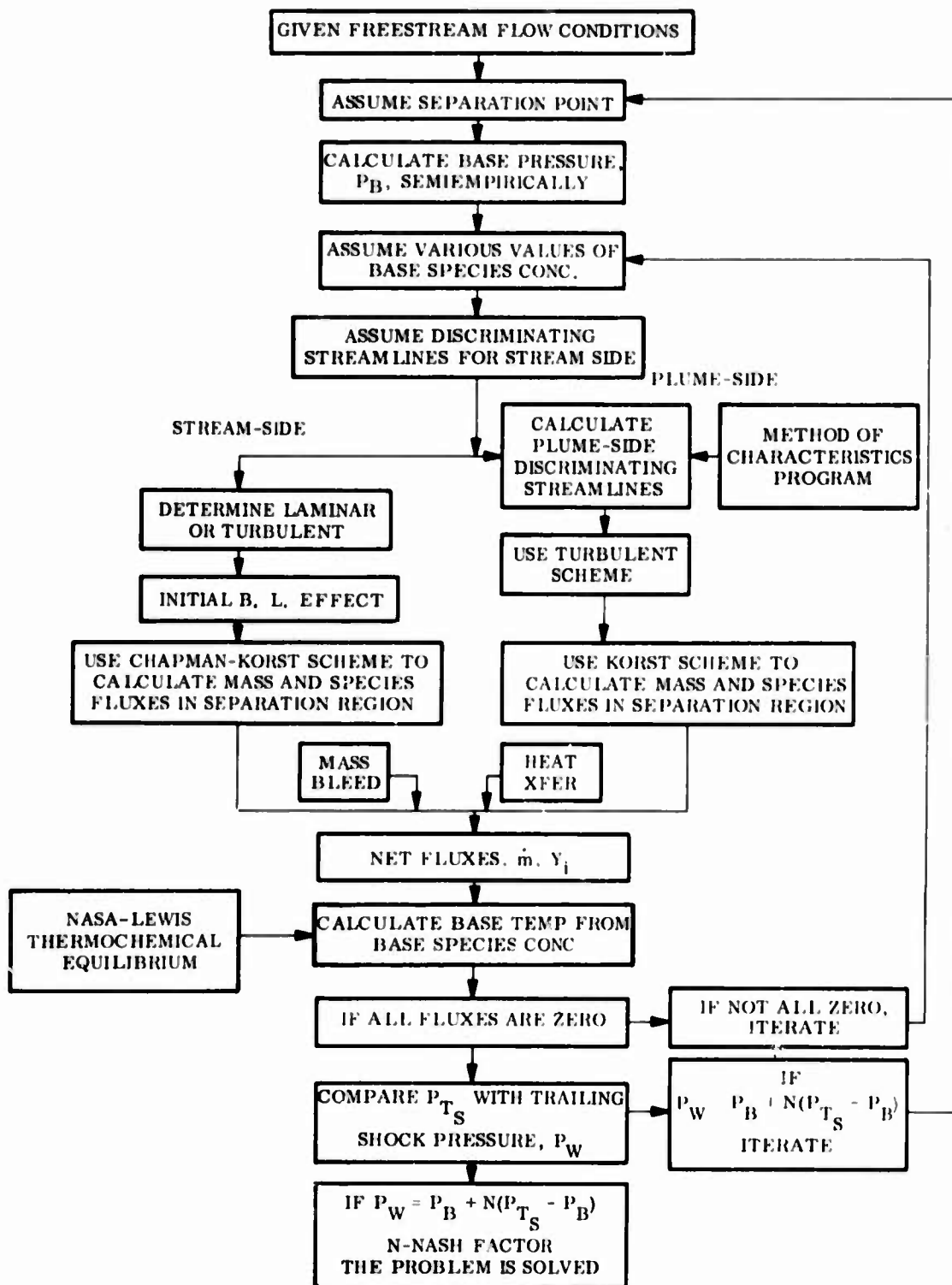


Figure 42 Computer Flow for Simplified Scheme



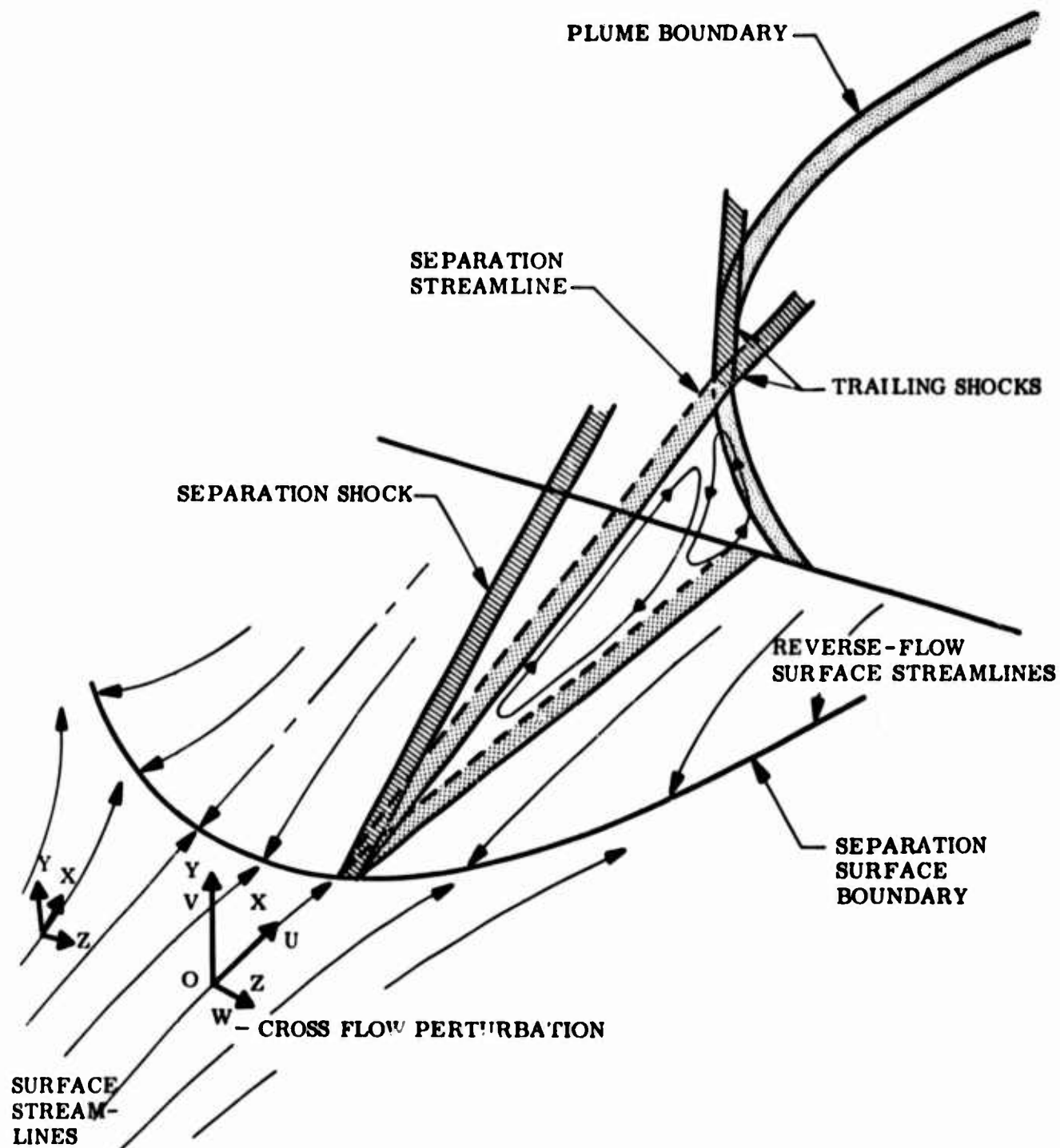


Figure 43 Streamline Coordinate System and Control Volume

During powered maneuver of a lifting reentry vehicle at orbital altitudes, the separated flow field generated from the three-dimensional attached flow by the enlarged exhaust plume would then be three-dimensional also. To predict the separated flow properties, two questions naturally arise:

- What are the limitations of the modified Chapman-Korst theory in application to this generalized problem?
- Whether a simplified analytical model is feasible, so that the three-dimensional separated flow properties can be predicted approximately.

In the course of this study, a cross-flow boundary layer solution has been obtained which not only answers these two questions but also allows rapid and realistic estimates of the flow characteristics associated with this type of flow separation.

The basic concept underlying this cross-flow theory is that of perturbation generation for laminar boundary layer flow oriented with respect to the streamline coordinate system (Fig. 43). Streamline coordinate system means that the x-coordinate is coincident with the external streamline so that the cross flow at the outer edge is zero. For a large class of boundary layer flows, implementation of the streamline coordinate system would indeed justify the perturbation approach for which the cross flow can be described by high-order linearized solutions. Inasmuch as in the current design of lifting reentry vehicles a large portion of the surface contour displays relatively small curvature, e.g. the HL-10 surface, the small cross-flow model is expected to be valid. Specifically, the present model evolves the following issues:

- It is rationalized that with the streamline coordinate system, the pseudo-two-dimensional separated flow solution is valid along each external streamline.
- In general, the external streamline is not directly measurable but accessible through surface oil flow observation. With the present analytic model, the external streamlines can be determined inversely from the small cross-flow solution together with relevant oil flow data. These external streamlines will correspond to the local streamlines upstream of the separation region discussed in the preceding paragraphs, which are needed for the separated flow analysis.
- A frequently used technique to treat three-dimensional boundary layer problems is the strip theory for which the vehicle surface is subdivided into a number of parallel strips, each exhibiting a local pseudo-two-dimensional flow field. While simple in principle and straight-forward in execution, its validity may be limited. The small cross-flow model developed herein would permit a critical evaluation of the strip theory.

In the following paragraphs, therefore, attention will be directed to two main topics:

- Determination of the external streamline from oil flow pattern and small cross-flow solution, including a comparison with the strip theory results, and
- An approximate scheme to determine the surface separated flow pattern under realistic three-dimensional flow conditions.

### a. Small Cross-Flow Solution

On the basis of the small cross-flow concept (Refs. 46 to 48), the governing partial differential equations describing a three-dimensional laminar boundary layer can be reduced to a system of ordinary differential equations, the zero-order equations representing the basic two-dimensional flow and higher-order equations describing the cross-flow effect. Mathematical details of the perturbation development are presented in Appendix II. It is appropriate to mention that since all higher-order equations are now linearized, the cross-flow solutions are comparatively easy to obtain. In this analysis, only the first-order equation has been solved for the cross-flow estimate.

Under hypersonic conditions, the first-order equation can be expressed in the following form:

$$g_1''' + f_0 g_1'' + \bar{\beta}_1^* (\theta_0 - f_0'^2) = 0 \quad (31)$$

where  $g_1$  is the cross flow velocity ratio,  $\bar{\beta}_1^*$  is the cross-flow pressure gradient parameter, ( )' indicates differentiation with respect to the similarity y-coordinate, and subscripts 0 and 1 represent the zero-order and first-order quantities, respectively. Since the zero-order values are already known, equation (31) is, in effect, a linear differential equation in  $g_1$ . The cross-flow solution provides information for flow distortion within a three-dimensional boundary layer. In the present case, this solution is utilized to ascertain the external streamlines with the aid of appropriate oil flow data. The following example demonstrates this inverse cross-flow application and compares with the predicted results using the strip theory.

Typical surface oil flow patterns in terms of angle of attack for a blunted delta slab under hypersonic flow conditions are depicted in Figure 44 (Ref. 49). It is seen that as the angle of attack increases, the surface streamlines will bend outward, and, eventually, the geometrical leading edge will behave like a trailing edge, hydrodynamically. However, the present concern is centered on interpretation of the surface three-dimensional flow behavior through the cross-flow boundary layer theory rather than evaluation of the angle-of-attack effect on cross-flow generation or the overall aerodynamic properties. As such, the zero angle-of-attack case illustrated in Figure 44 can be singled out for cross-flow analysis without any loss of generality.

For detailed considerations, the zero angle-of-attack oil flow pattern at Mach 6.8 is reproduced in Figure 45 in which three streamlines with azimuthal angles of 6, 10, and 14 degrees were selected for investigation. The corresponding  $\bar{\beta}_1^*$  values, where (see Appendix II)

$$\bar{\beta}_1^* = - \frac{2\xi}{\rho_e u_e^2} \frac{\partial p}{\partial \xi} \left( 1 + \frac{\gamma - 1}{2} M_e^2 \right) \quad (32)$$

were found to be 0.02, 0.035, and 0.05.

BASED ON NASA TN D-2708

$M_{\infty} = 6.8$

SWEEP ANGLE =  $80^{\circ}$

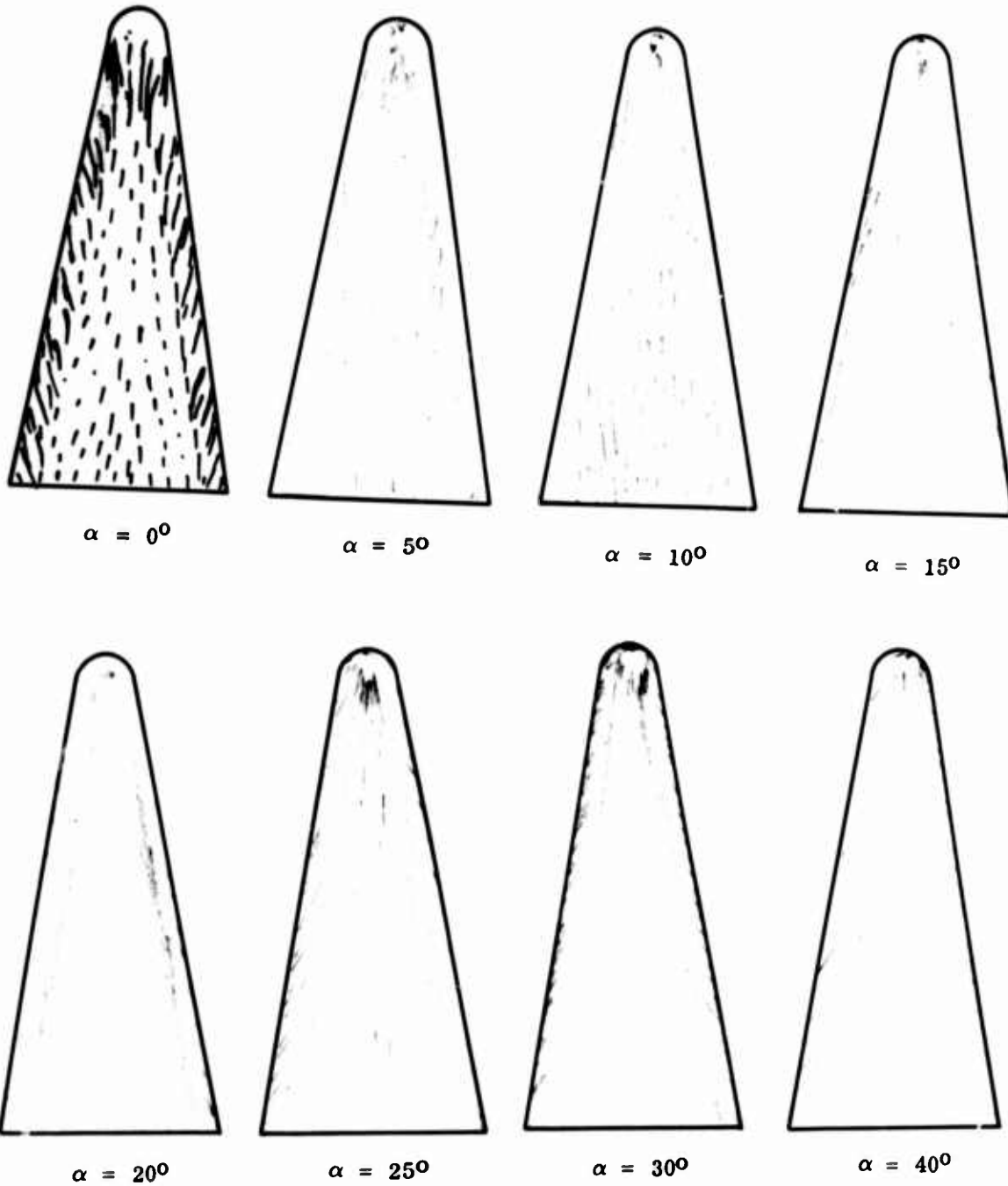


Figure 44 Surface Oil Flow Pattern on the Compression Side of a Blunted Delta Slab at Mach 6.8

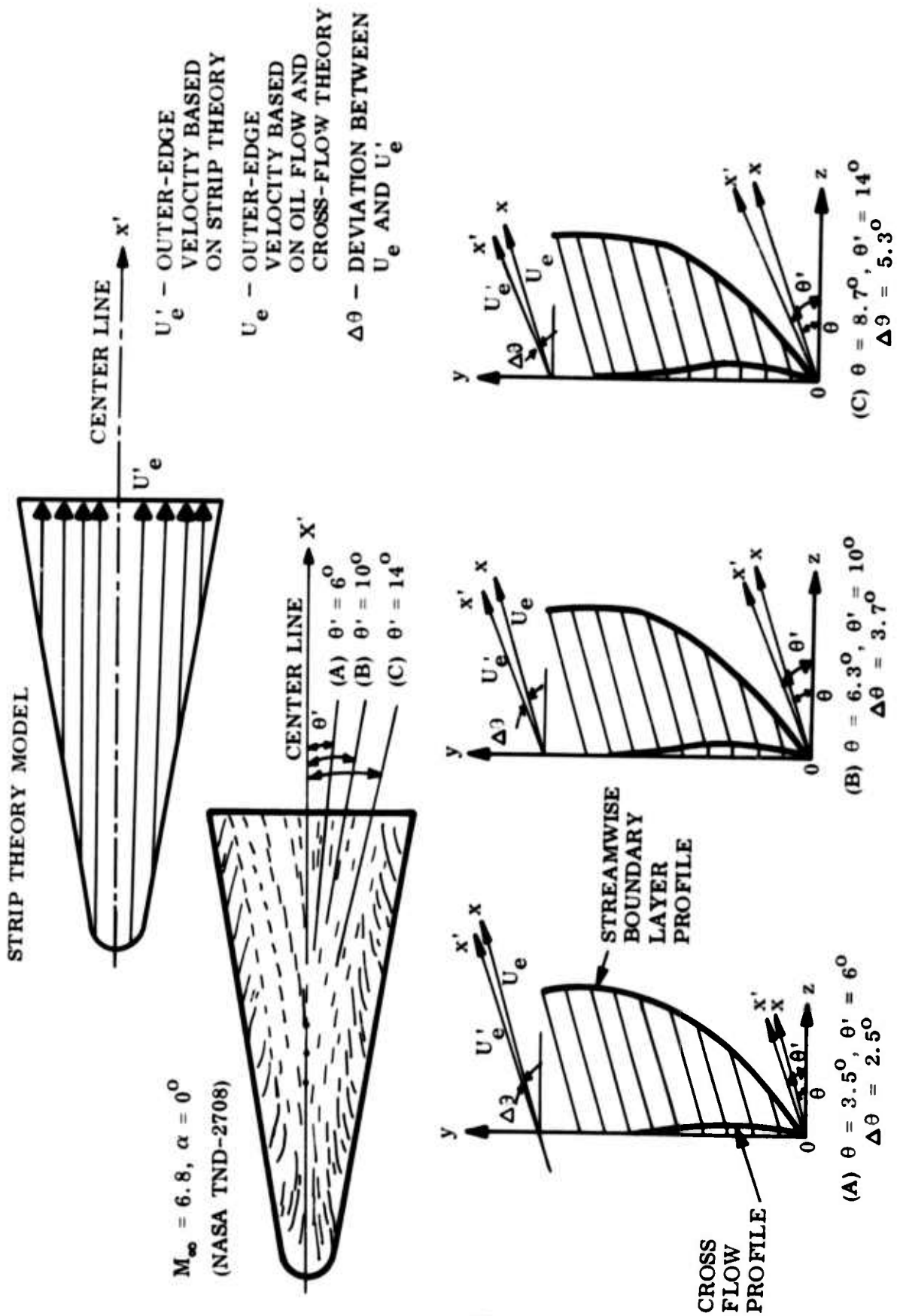


Figure 45 Comparison of Outer-Edge Velocities Based on Strip Theory and Small Cross-Flow Theory

The freestream flow was considered to be of the Blasius type and the cross-flow profiles were assumed to be approximately represented by those presented in Figure 46. Using the resultants of the streamwise and lateral velocity components at  $\eta = 0.5$  (boundary layer thickness = 9) to represent the surface streamlines, the inviscid streamline locations can be determined. The results are depicted in Figure 45 and are summarized below:\*

Streamline	(I)	(II)	(III)
	Surface streamline location (oil flow, deg)	Angle between surface and inviscid streamline (oil flow, deg)	Deviation of inviscid streamline from strip theory result (deg)
A	6	3.5	2.5
B	10	6.3	3.7
C	14	8.7	5.3

As a clarification of the tabulation above and Figure 45, prediction procedure for streamline A is exemplified below:

- (1) Identify the surface oil flow angle for streamline, i. e.,  $\theta' = 6^\circ$  measured from the center line, Column I of the table.
- (2) From the cross-flow solution and the oil-flow streamline, the streamwise flow direction is found to be  $\theta = 3.5^\circ$  measured from the oil-flow streamline (Column II). As mentioned above,  $\eta = 0.5$  is used in determining the surface streamline components. The streamwise flow direction also represents the local inviscid streamline direction in view of the streamline coordinate system employed here.
- (3) Since the outer-edge velocity,  $u_e'$ , based on the strip theory is 6 degrees measured from the center line, the discrepancy between the cross-flow method and the strip theory is 2.5 degrees (Column III).

Limited results have indicated that the discrepancy resulting from the strip theory model generally would not induce any significant effect on predicted surface separated flow patterns (less than 10 percent). This then justifies the strip theory model for a considerable latitude of separated flow applications. On the other hand, the anomalous flow behavior near the swept leading edge or over highly curved surfaces could conceivably incur serious inaccuracy. However, an in-depth study of this problem requires additional oil flow data which are not presently available.

---

\*The results are based on a Blasius profile with zero heat transfer. In the aft portion of the delta surface, experimental data have shown that these conditions are nearly attained (Ref. 49).

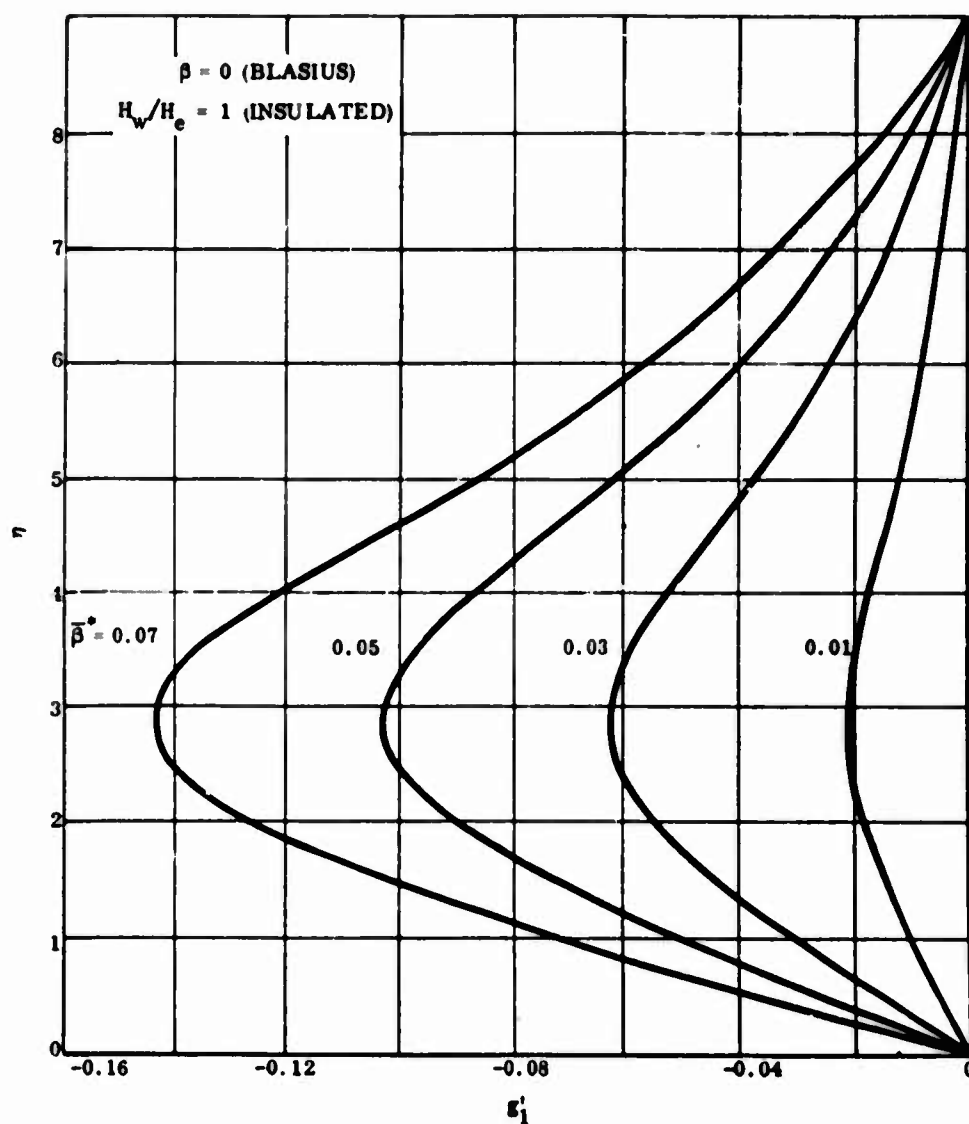


Figure 46 Typical Similar Cross-Flow Velocity Profile

#### **b. Surface Separated Flow Pattern**

The surface separated flow pattern or separation footprint induced by an LRV plume can be determined by the following simple scheme:

- Divide the vehicle surface into a number of parallel strips and consider each strip individually (Fig. 47).
- Use the strip that encloses the plane of symmetry as the reference strip and perform plume-induced separated flow predictions in accordance with the theory discussed in par. 5 of this section.
- Consider a particular strip away from the plane of symmetry and define the attached inviscid streamline,  $M_1$ , which is parallel to the reference streamline,  $M_0$ ; small cross-flow correction may be applied to obtain this component. For the simple configuration considered here,  $M_1$  is equal to  $M_0$ .
- Define the local plume boundary B. Because of the dead-air hypothesis, a uniform pressure prevails within the separation region; hence, the local separation pressure corresponding to boundary B is equal to that for the plane of symmetry. In other words, the separation wedges corresponding to different strips are geometrically similar.
- Assume the local trailing shock pressure to be equal to that with respect to the plane of symmetry. Based on this assumption and the plume boundary Mach number,  $M_j \cos \psi$ , the corresponding separation wedge can be determined. With this criterion and the geometrical similarity feature, the tip location and the size of the separation wedge can then be predicted.
- Repeat the process for other strips and obtain the parabolic separation footprint indicated in Figure 47. The computation procedure is also illustrated in Figure 48.



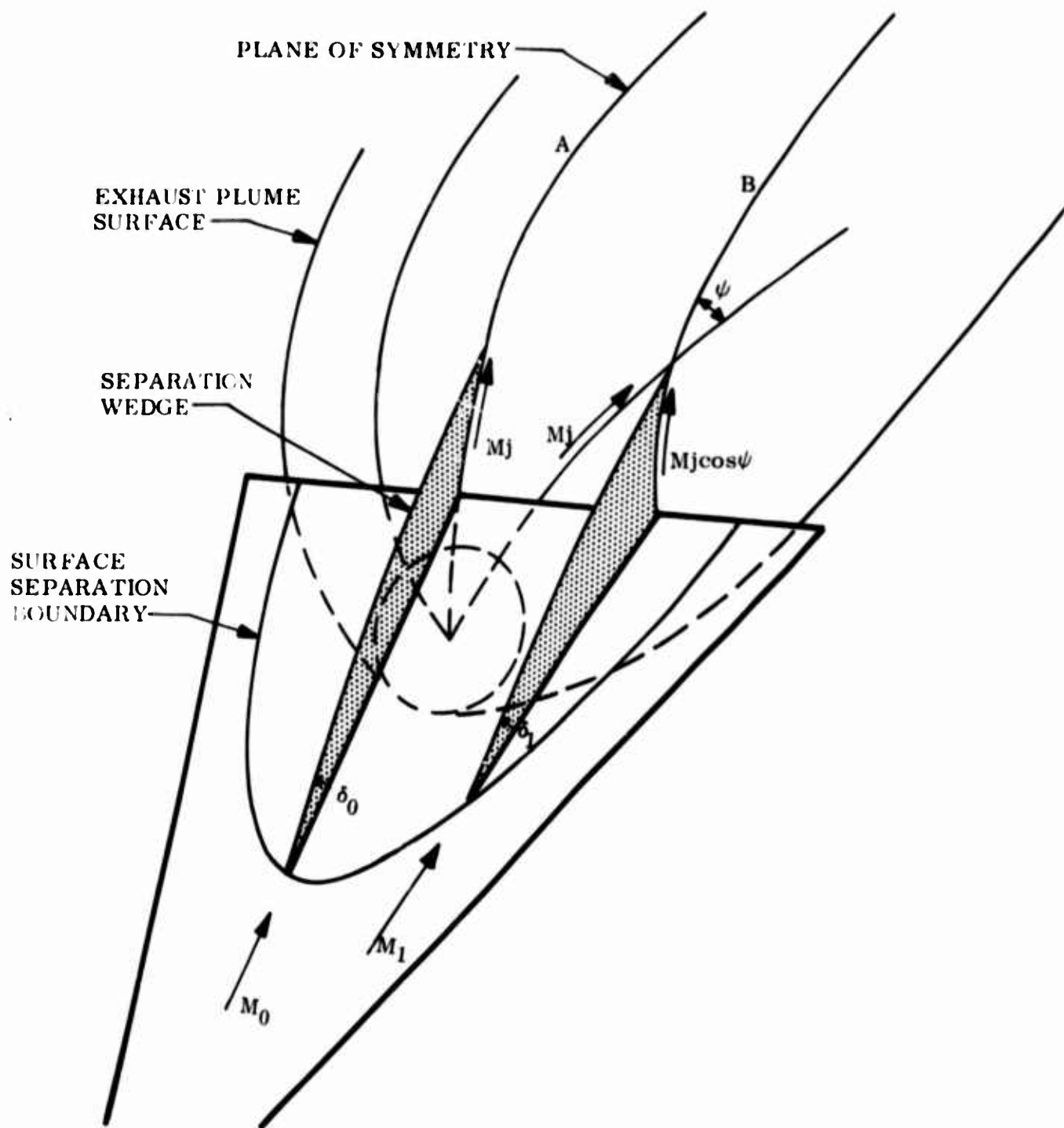


Figure 47 Separation Wedges and Surface Separation Contour

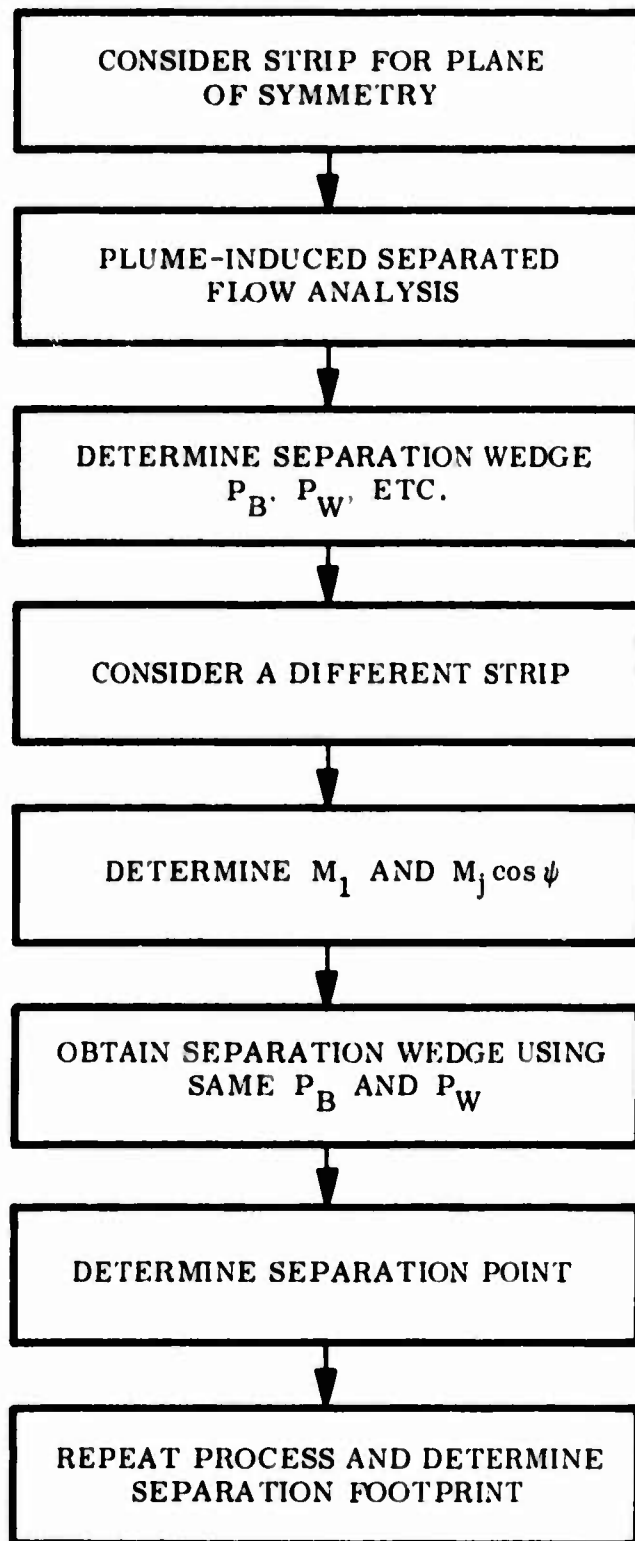


Figure 48 Computation Scheme for Determination of Separation Footprint

### Section III

#### APPLICATION TO A SIMPLE CONFIGURATION

Within the framework of the modified Chapman-Korst model development in the present study, the average plume-induced separated flow characteristics during synergetic maneuvering can be predicted. However, scarcity of relevant data has prevented full endorsement of predicted results on a quantitative scale. For this reason, no effort was made in this phase of the study to make predictions for actual LRV configurations. Instead, a simple lifting body configuration was thoroughly investigated for the twofold purpose of demonstrating the analytical model and acquiring a qualitative evaluation of aerodynamic performance changes when subjected to propulsion effects. The results will, of course, be updated when additional data become available.

The simple configuration consists of a delta planform with a triangular cross section, as illustrated in Figure 49. The delta flat plate is the bottom or windward surface whereas the slope sides constitute the leeward surfaces on which the most leeside ridge is at 10 degrees with the delta surface. For the windward surface, all elemental strips are assumed to be parallel to the center line, as indicated in Figure 45. For the leeward surfaces, it is posulated that the elemental surface strips are parallel to the most leeside ridge and are, therefore, also at 10 degrees with the bottom plate (Fig. 50). This leeside strip model is consistent with that proposed in Reference 50 and shown in Figure 51. Although curved surface streamlines near the leading edge are exhibited in Figure 51, straight parallel strips are adopted herein (Fig. 50) for two reasons:

- The aim of this study is to assess the plume effect on LRV aerodynamic characteristics. The lack of rigor for streamline determination near the leading edge is not expected to nullify the validity of this assessment, particularly if the separation footprint is located in the aft portion of the surface.
- In predicting the average pressures over these flat surfaces, the Newtonian flow is employed, which is compatible with the "straight" strip model.

The ensuing paragraphs encompass a detailed analysis of the plume-induced separation phenomena associated with this simple delta-slab LRV configuration as well as a critical evaluation of the present analytical model so that a guideline for future studies on plume-induced separation and related disciplines can be outlined.

#### 1. PREDICTION OF PLUME-INDUCED FLOW SEPARATION

The freestream conditions under which the exhaust plume effects were studied are:

$M_\infty$	= 6, 10, 15 and 20
Altitude	= 140,000, 200,000, 230,000, 250,000, and 280,000 feet
$\alpha$	= 0, 10, and 20 degrees

$$\begin{aligned} \ell &= 45 \text{ FT} & r &= 2.53 \text{ FT} \\ b &= 15.6 \text{ FT} & a &= 2.53 \text{ FT} \end{aligned}$$

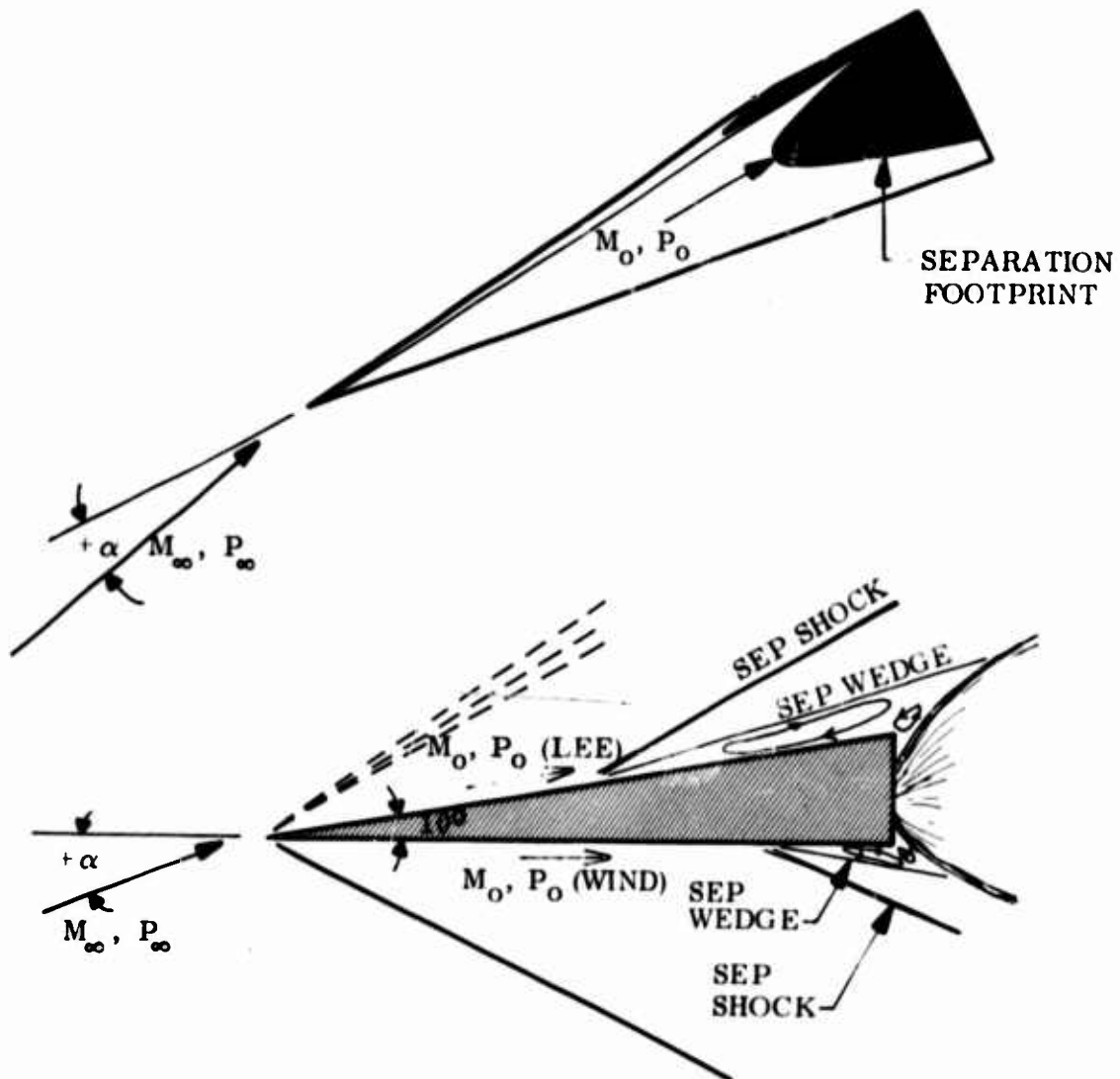
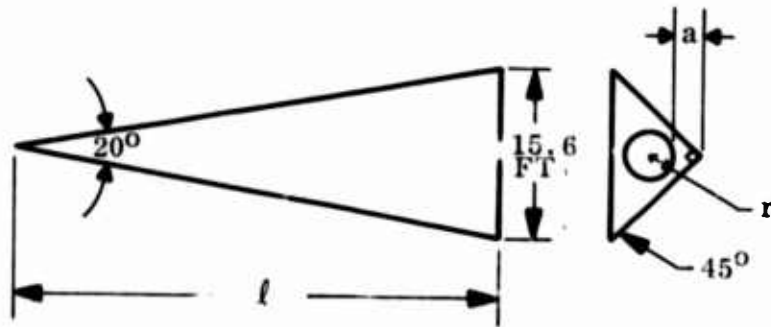
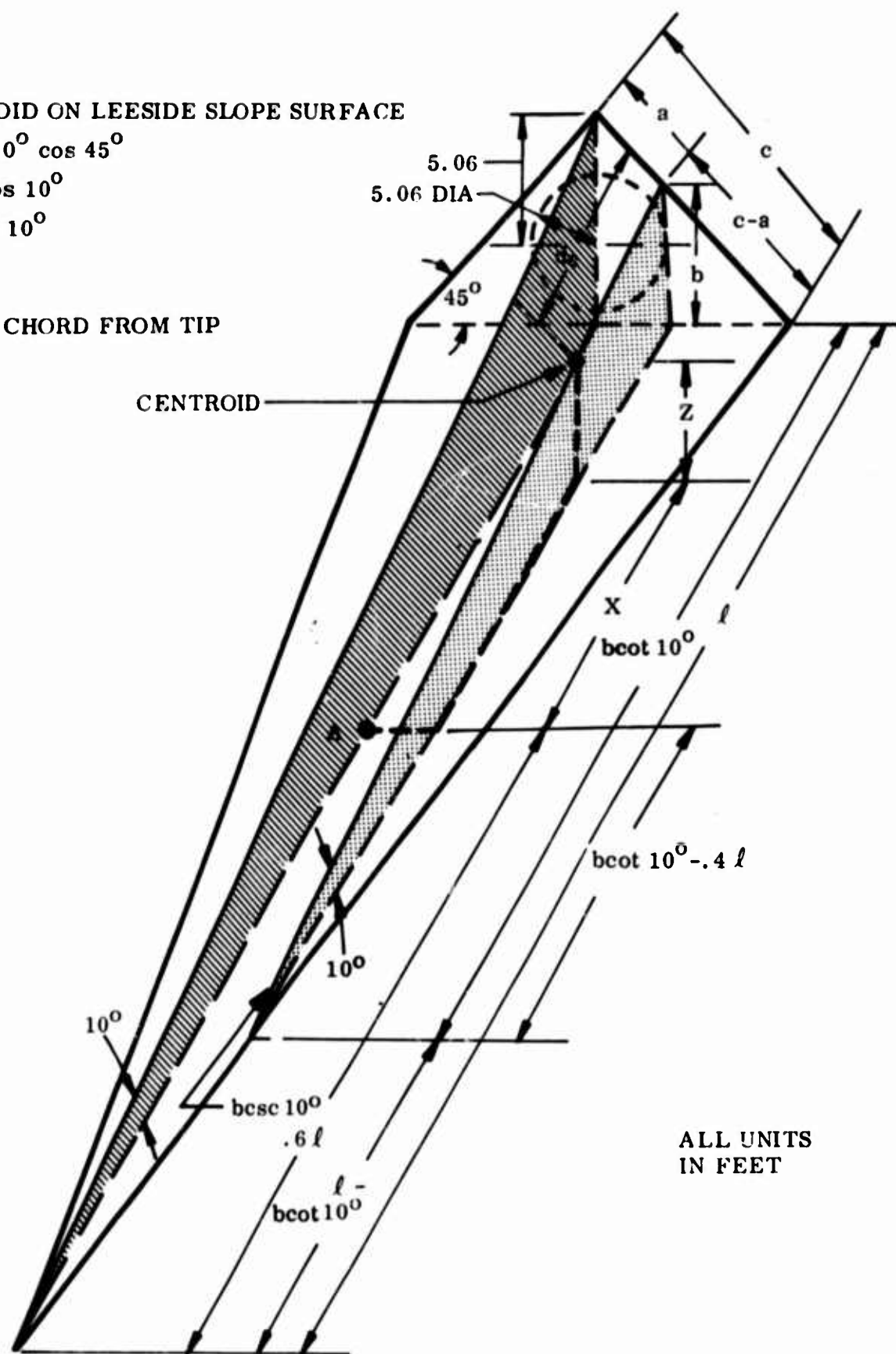


Figure 49 Plume-Induced Separation on Body with Delta Planform and Triangular Cross Section

- $d_c$  - CENTROID ON LEESIDE SLOPE SURFACE  
 $c = 4 \sin 10^\circ \cos 45^\circ$   
 $x = 18 - d_c \cos 10^\circ$
- $z = b - d_c \sin 10^\circ$   
 $l = 45 \text{ FT}$

A - 60% CHORD FROM TIP



ALL UNITS  
IN FEET

Figure 50 Moment Arms from Leeward Centroid to Point at 60-Percent Chord

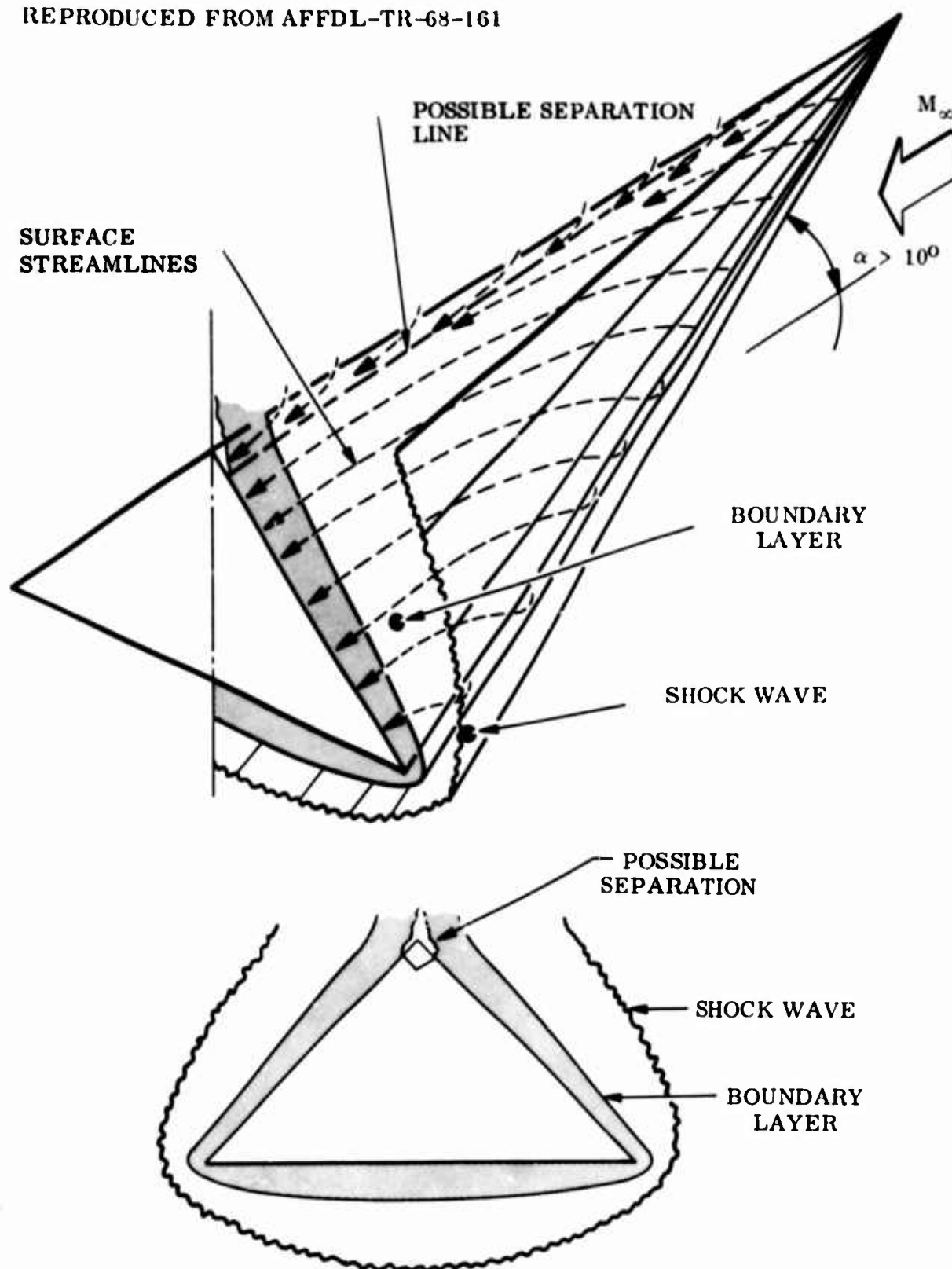


Figure 51 Suggested Upper Surface Flow Model

The basic step-by-step analytical procedure to carry out the separated flow prediction is summarized below:

- Define local freestream conditions for given Mach number, altitude, and angle of attack
- Perform plume-induced separation predictions iteratively, based on methods discussed in Section II and Appendixes I and II. The base pressure is defined by the plateau pressure formula, Equation (28). In addition to the empirical Equation (29) to determine the plateau pressure coefficient, the Nash factor for the reattachment criterion was also determined empirically. Data available comprise a number of schlieren photographs by McGhee (Ref. 25) using the same body configuration as that selected in this study. It was ascertained that the Nash factor should be  $N = 0.56$  to obtain steady-state separated flow solutions. This  $N$  value was used for a wide range of Mach numbers and altitudes, but because of limited Mach numbers ( $M_\infty = 4.5$  and  $6.0$ ) used in this test, extensive applicability for this particular  $N$  value needs further verification.
- Determine separation footprints on vehicle surfaces with the aid of the small cross flow solution, thus defining surface areas in which pressure elevation occurs
- Calculate pertinent aerodynamic parameters and estimate plume effects on vehicle performance and stability

#### a. Important Features of Problem Solution

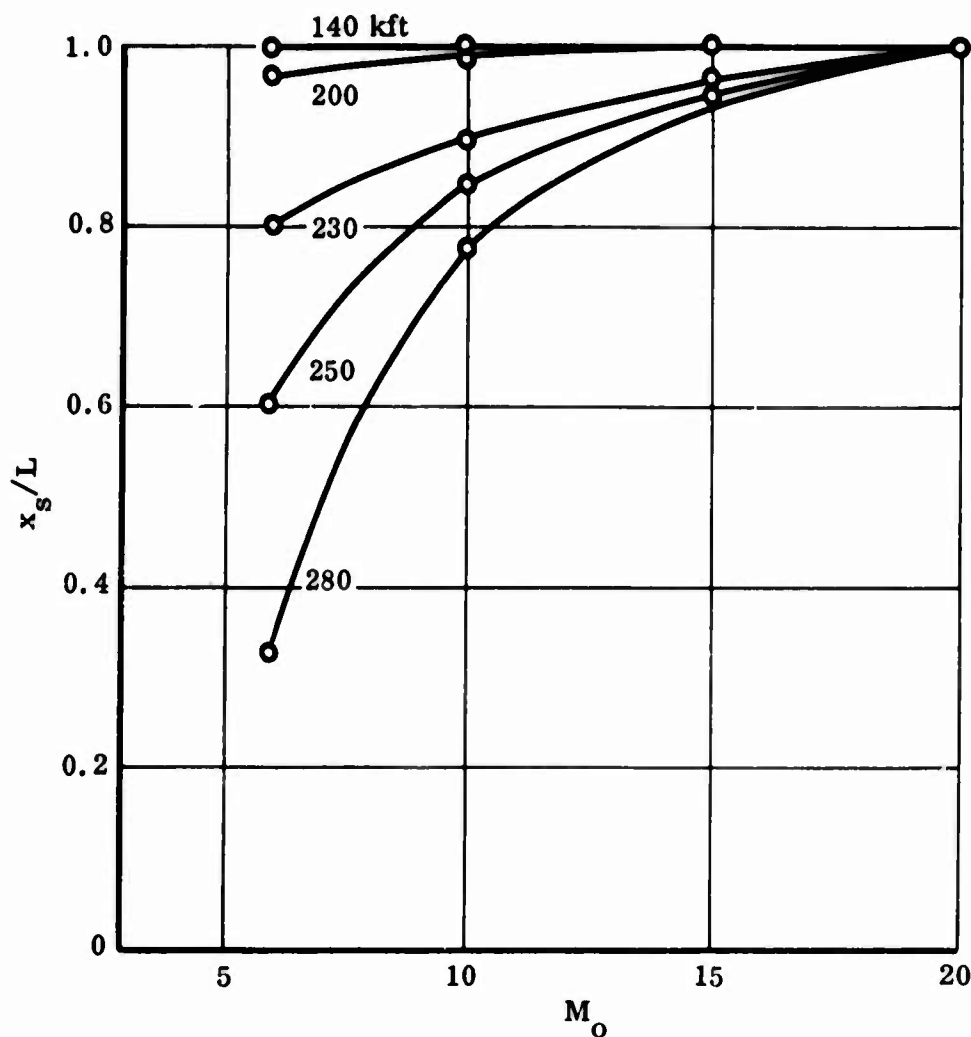
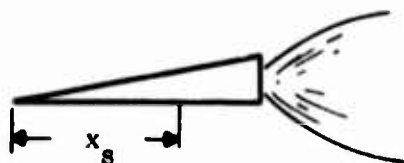
In carrying out the analysis, a number of problems were encountered and certain features of the problem solutions were exhibited, as follows:

- Because of the 10-degree vertex angle of the body, the leeside surfaces undergo a 10-degree compression at zero angle of attack. However, at 10-degree angle of attack, the leeside surfaces are effectively parallel to the free stream.
- Results presented in Figure 52 show predicted dimensionless separation length,  $X_g/L$ , versus Mach number for various  $P_{ex}/P_0$  values or local altitudes. In the figure, it is clearly manifested that the separation region is enhanced by an increasing  $P_{ex}/P_0$  but diminishes with increasing Mach number. These qualitative trends are consistent with the theories discussed in Section II. Because of "local" altitudes used, the angle-of-attack effect is considered implicitly. The curves are re-plotted in Figure 53 in terms of  $X_g/L$  versus  $P_{ex}/P_0$ . Pertinent results are also compiled in Tables V, VI, and VII.
- It should be mentioned that for  $P_{ex}/P_0 = 4030$  or at 280,000 feet (Figs. 52 and 53), no steady-state solution was obtained based on  $N = 0.56$ . From schlieren observation (Ref. 25), however, a new  $N$  value of 1.5 was ascertained, and the results are depicted in Figures 52 and 53. For altitudes above 280,000 feet and/or Mach numbers higher than 20, the separation distance was estimated by extrapolation, as indicated in Figure 53.
- For leeside problems involving high angles of attack, extrapolation was necessary to predict the plateau pressure coefficient and, subsequently, the base pressure. Furthermore, a thick boundary layer frequently accompanied the leeside expansion and necessitated additional extrapolation in order to reach a solution. This then rendered the solution less certain and open to speculation.

$$C_{P_B} = \frac{A}{(M_o^2 - 1)^{1/4} R_{e_o}^{1/4}}$$

$$A = 0.3 \left( \log \frac{P_{ex}}{P_o} \right)^3 - 0.88 \left( \log \frac{P_{ex}}{P_o} \right)^2 + 0.72 \left( \log \frac{P_{ex}}{P_o} \right)$$

$$L = 45 \text{ FT}$$



ALT (kft)	$P_{ex}/P_o$
140	9.4
200	88
230	321
250	860
280	4030

Figure 52 Separation Distance as a Function of Mach Number at Various Altitudes



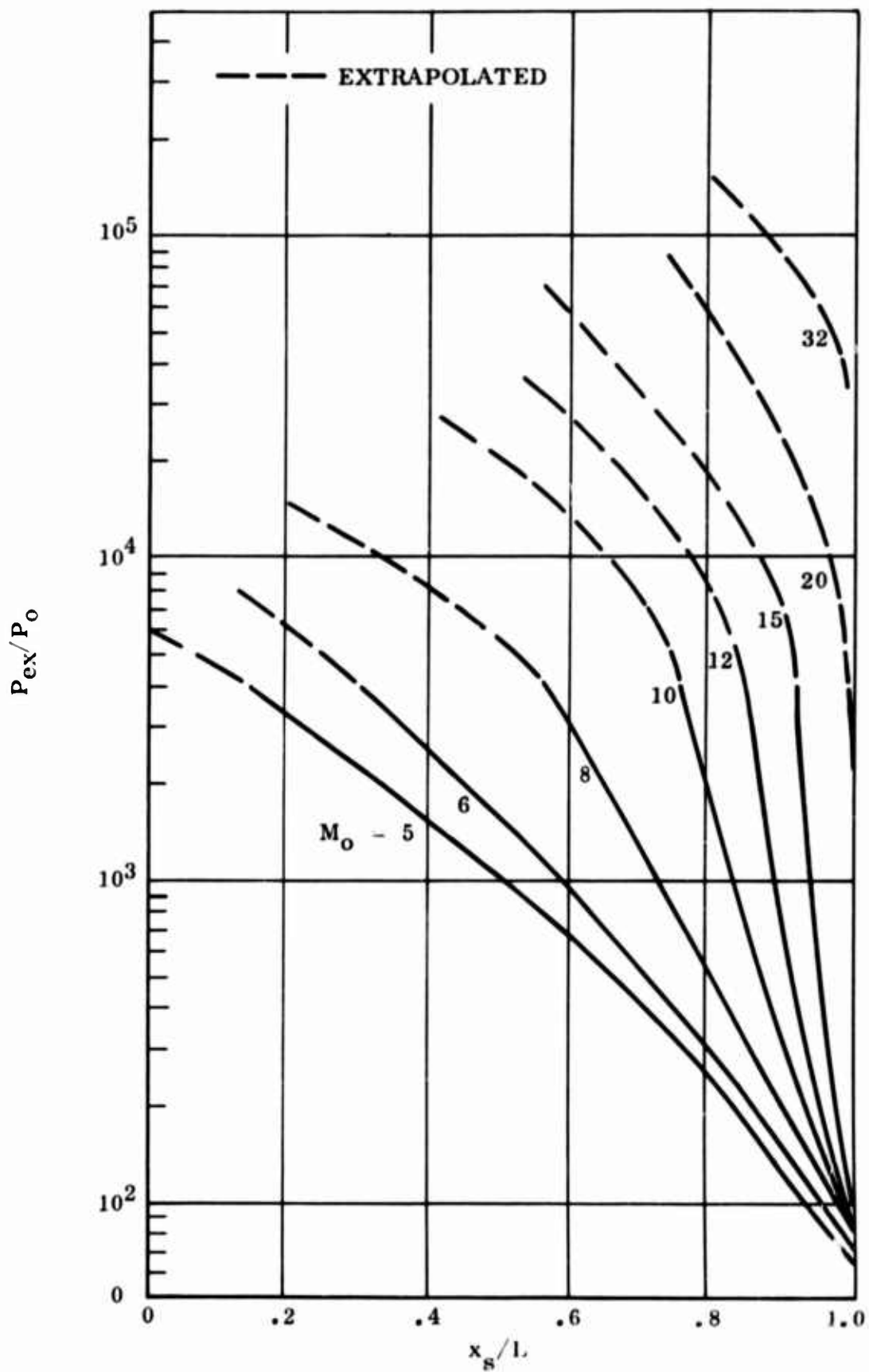


Figure 53 Separation Distance vs Pressure Ratio for Various Mach Numbers

Table V Problem Solution Summary,  $\alpha = 0$  Degree

No.	$\alpha$ (deg)	$M_\infty$	Alt (kft)	$P_\infty$ (psf)	Wind	Lee	$P_o$ (psf)	$M_o$	$P_{ex}/P_o$	$X_s$ (ft)	$P_B$ (psf)	Remarks
1	0	6	230	0.1299	✓		0.1299	6	321	36.0	0.242	
2		6	230	0.1299		✓	0.457	4.6	91.3	41.5	0.49	10° Compression
3		6	250	0.0486	✓		0.0486	6	860	27.2	0.117	
4		6	250	0.0486		✓	0.171	4.6	244	34.5	0.21	
5		6	280	0.01035	✓		0.01035	6	4030	15.5	0.078	
6		6	280	0.01035		✓	0.0354	4.6	1150	18.0	0.067	
7		10	230	0.1299	✓		0.1299	10	321	40.5	0.28	
8		10	230	0.1299		✓	0.904	6.67	41			No Separation
9		10	250	0.0486	✓		0.0486	10	860	38.5	0.185	
10		10	250	0.0486		✓	0.338	6.67	124	42.5	0.394	
11		10	280	0.01035	✓		0.01035	10	4030	35	0.137	
12		10	280	0.01035		✓	0.072	6.67	580	32.5	0.132	
13		15	230	0.1299	✓		0.1299	15	321	43.7	0.482	
14		15	230	0.1299		✓	1.77	11.5	23.6			No Separation
15		15	250	0.0486	✓		0.0486	15	860	43.0	0.274	
16		15	250	0.0486		✓	0.66	11.5	63			No Separation
17		15	280	0.01035	✓		0.01035	15	4030	41.5	0.23	
18		15	280	0.01035		✓	0.141	11.5	296	41.5	0.314	

Subscript o refers to local freestream conditions upstream of separation point.

Table VI Problem Solution Summary,  $\alpha = 10$  Degrees

No.	$\alpha$ (deg)	$M_\infty$	Alt (kft)	$P_\infty$ (psf)	Wind	Lee	$P_o$ (psf)	$M_o$	$P_{ex}/P_o$	$X_s$ (ft)	$P_B$ (psf)	Remarks
19	+10	6	230	0.1299	✓		0.457	4.6	91.3	41.5	0.49	10° Compression
20		6	230	0.1299		✓	0.1299	6	321	36.0	0.242	Eff. $\alpha = 0^\circ$
21		6	250	0.0486	✓		0.171	4.6	244	34.5	0.21	
22		6	250	0.0486		✓	0.0486	6	860	27.2	0.117	
23		6	280	0.01035	✓		0.0354	4.6	1150	18.0	0.067	
24		6	280	0.01035		✓	0.01035	6	4030	15.5	0.078	
25		10	230	0.1299	✓		0.904	6.67	41			No Separation
26		10	230	0.1299		✓	0.1299	10	321	40.5	0.28	
27		10	250	0.0486	✓		0.338	6.67	124	42.5	0.394	
28		10	250	0.0486		✓	0.0486	10	860	38.5	0.185	
29		10	280	0.01035	✓		0.072	6.67	580	32.5	0.132	
30		10	280	0.01035		✓	0.01035	10	4030	35	0.137	
31		15	230	0.1299	✓		1.77	11.5	23.6			No Separation
32		15	230	0.1299		✓	0.1299	15	321	43.7	0.482	
33		15	250	0.0486	✓		0.66	11.5	63			No Separation
34		15	250	0.0486		✓	0.0486	15	860	43.0	0.274	
35		15	280	0.01035	✓		0.141	11.5	296	41.5	0.314	
36		15	280	0.01035		✓	0.01035	15	4030	41.5	0.23	

Subscript o refers to local freestream conditions upstream of separation point.

Note: Same as  $\alpha = 0^\circ$  case if windward and leeward values are interchanged.

Table VII Problem Solution Summary,  $\alpha = 20$  Degrees

No.	$\alpha$ (deg)	$M_\infty$	Alt (kft)	$P_\infty$ (psf)	Wind	Lee	$P_o$ (psf)	Mo	$P_{ex}/P_o$	$X_s$ (ft)	$P_B$ (psf)	Remarks
37	+20	6	230	0.1299	✓		1.21	3.33	34.5	(20° Compression)		No Separation
38		6	230	0.1299		✓	0.0239	7.84	1745	29	0.111	10° Expansion
39		6	250	0.0486	✓		0.452	3.33	92.5	40	0.48	
40		6	250	0.0486		✓	0.00895	7.84	4660	23	0.0605	
41		6	280	0.01035	✓		0.0963	3.33	435	25	0.146	
42		6	280	0.01035		✓	0.0019	7.84	21900	Tip Sep	0.0493	(Rough Est. $P_B$ )
43		10	230	0.1299	✓		2.86	4.16	14.6			No Separation
44		10	230	0.1299		✓	0.00617	15.68	6770	41.8	0.155	Expands more than $M_\infty = 6$
45		10	250	0.0486	✓		1.07	4.16	39			No Separation
46		10	250	0.0486		✓	$2.3 \times 10^{-3}$	15.68	18050	37.5	0.12	Estimated $X_s$
47		10	280	0.01035	✓		0.227	4.16	183	36.5	0.3	
48		10	280	0.01035		✓	$4.9 \times 10^{-4}$	15.68	85000	26	0.052	Estimated $X_s$
49		15	230	0.1299	✓		6.06	4.55	6.88			No Separation
50		15	230	0.1299		✓	$6.85 \times 10^{-4}$	32	60800	42.5	0.542	
51		15	250	0.0486	✓		2.27	4.55	18.4			No Separation
52		15	250	0.0486		✓	$2.56 \times 10^{-4}$	32	$1.63 \times 10^5$	33	0.304	Estimated $X_s$
53		15	280	0.01035	✓		0.483	4.55	86.5	42.5	0.54	
54		15	280	0.01035		✓	$5.46 \times 10^{-5}$	32	$7.66 \times 10^5$	15	0.405	Estimated $X_s$

Subscript o refers to local freestream conditions upstream of separation point.

Note: 20° compression on windward side/10° expansion on leeward side.

- The predicted separation footprints are presented in Appendix III. The simple body configuration permits aerodynamic predictions in a straightforward manner.

b. Plume Effects on Aerodynamic Characteristics

Without loss of generality, pertinent aerodynamic parameters are expressed in terms of the windward delta surface area and, for aerodynamic moments, an additional reference length of 60 percent chord from the tip of the delta surface (Fig. 50). However, for the present simple delta-triangle configuration, the force components for the lee-side or slope surfaces are dependent upon the geometrical angles and the pressure forces. In deriving a general expression for the force determination, pertinent geometrical parameters, such as illustrated in Figure 54, are used. The main objective here is to ascertain,  $\vec{N}$ , the unit vector normal to the slope surface at any point on the surface. From Figure 54, the side vectors can be expressed as

$$\vec{S}_1 = l\vec{i} + a\vec{k} = l(\vec{i} + \tan\beta\vec{k}) \quad (33)$$

$$\vec{S}_2 = l\vec{i} + h\vec{j} = l(\vec{i} + \tan\theta\vec{j}) \quad (34)$$

Then, the unit vector normal to the slope surface is simply the cross product of  $\vec{S}_1$  and  $\vec{S}_2$  as follows:

$$\vec{N} = \frac{\vec{S}_2 \times \vec{S}_1}{|\vec{S}_2 \times \vec{S}_1|} = \frac{l^2}{|\vec{S}_2 \times \vec{S}_1|} (\vec{i} \tan\theta \tan\beta - \vec{j} \tan\beta - \vec{k} \tan\theta) \quad (35)$$

where  $|\vec{S}_2 \times \vec{S}_1|$  represents the magnitude of the cross product and is equal to

$$|\vec{S}_2 \times \vec{S}_1| = l^2 (\tan^2\theta \tan^2\beta + \tan^2\beta + \tan^2\theta)^{1/2} \quad (36)$$

If the pressure force normal to the leeside surface is

$$F_k = \Delta P_k A_k \quad (37)$$

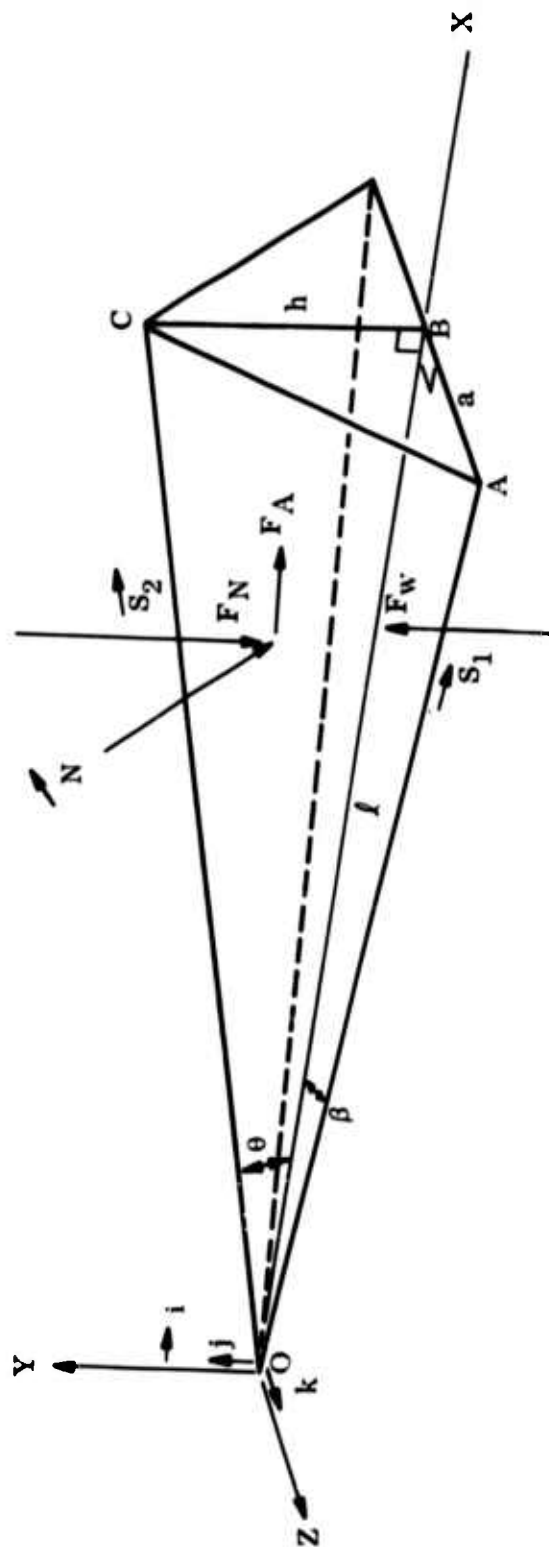
where the subscript k provides a general expression whether or not jet pluming occurs. Thus, normal pressure force with respect to the windward reference surface =

$$-F_k \tan\beta (\tan^2\theta \tan^2\beta + \tan^2\beta + \tan^2\theta)^{-1/2} \quad (38)$$

which is the  $\vec{j}$  component, and axial pressure force =

$$F_k \tan\theta \tan\beta (\tan^2\theta \tan^2\beta + \tan^2\beta + \tan^2\theta)^{-1/2} \quad (39)$$

which is the  $\vec{i}$  component.



- |       |                                     |       |                              |
|-------|-------------------------------------|-------|------------------------------|
| N     | UNIT VECTOR NORMAL TO SLOPE SURFACE | $F_w$ | WINDWARD NORMAL FORCE VECTOR |
| $S_1$ | LENGTH VECTOR REPRESENTING OA       | $F_N$ | LEEWARD NORMAL FORCE VECTOR  |
| $S_2$ | LENGTH VECTOR REPRESENTING OC       | $F_A$ | LEEWARD AXIAL FORCE VECTOR   |
- $AB = a, OB = l, BC = h, \angle AOB = \beta, \angle COB = \theta$   
 $\angle CCB = \text{PLANE OF SYMMETRY}$

Figure 54 Geometrical Parameters for Delta - Triangle Body

Two limiting cases are also immediately obvious:

$$\text{Normal pressure force} = \begin{cases} 0 & \text{for } \beta = 0 \\ -F_k & \text{for } \theta = 0 \end{cases} \quad (40)$$

In application to the present plume problem, these equations can be used for both the jet-on and jet-off cases. From Figures 49 and 54, it is apparent that  $\theta = \beta = -10^\circ$  for  $h = a$ . The main aerodynamic quantities are determined by the following equations:

(1) Jet-off

Windside normal force\*

$$F_{w_o} = (P_o - P_\infty)_w A_w \quad (41)$$

Leeside normal force\*

$$\begin{aligned} F_{n_o} &= (P_o - P_\infty)_l A_l \tan \beta (\tan^2 \theta \tan^2 \beta + \tan^2 \beta + \tan^2 \theta)^{-1/2} \\ &= (P_o - P_\infty)_l A_l (2 + \tan^2 10^\circ)^{-1/2} \\ &= 0.702 (P_o - P_\infty)_l A_l \end{aligned} \quad (42)$$

Axial force

$$\begin{aligned} F_{A_o} &= (P_o - P_\infty)_l A_l \tan \theta \tan \beta (\tan^2 \theta \tan^2 \beta + \tan^2 \beta + \tan^2 \theta)^{-1/2} \\ &= 0.702 \tan 10^\circ (P_o - P_\infty)_l A_l \\ &= 0.124 (P_o - P_\infty)_l A_l \end{aligned} \quad (43)$$

For completeness, the skin friction contribution to aerodynamic forces should be included in the foregoing equations. However, according to data reported in Reference 50 in which the same body configuration was tested, the skin friction effect on normal force component was not pronounced, and the frictional axial force was found to be of the same order of magnitude as the pressure axial force. Consideration of the skin friction contribution would not shed light on understanding the plume-induced separated flow

\*The normal forces are directed toward the respective surfaces vectorially.

mechanism but would introduce additional numerical integration and ambiguity, the latter referring to the problem of evaluating skin friction characteristics within a separation region for which no satisfactory simple theory is currently available. Inasmuch as the present analysis is concerned with determination of aerodynamic force differentials and other incremental quantities arising from jet pluming, it is doubtful if omission of the skin frictional forces would affect the results at all. Hence, the skin friction aspect is ignored in this analysis.

The corresponding aerodynamic coefficients can be expressed as follows:

Normal force coefficient

$$C_{N_o} = \frac{1}{q_\infty} (F_{w_o} - F_{N_o}) \quad (44)$$

Axial force coefficient

$$C_{A_o} = \frac{2}{q_\infty} F_{A_o} \quad (46)$$

Pitching moment coefficient

$$C_{M_o} = \frac{1}{q_\infty d_c} \left[ 2 F_{N_o} X - F_{w_o} X' + 2 F_{A_o} Z \right] \quad (46)$$

where  $d_c$  is the 60 percent chord location,  $X$ ,  $X'$  and  $Z$  are the moment arms from the different centroids to the 60 percent chord location,  $A_w$  is the bottom delta plate surface area,  $A_l$  is the leeside slope surface area, and  $q_\infty$  is the freestream dynamic pressure parameter with respect to the delta surface, i.e.,

$$q_\infty = \frac{1}{2} (\rho_\infty u_\infty^2 A_w) \quad (47)$$

According to the symbols used herein, subscript  $\infty$  means the freestream value, whereas subscript  $o$  refers to local freestream state upstream of the separated flow region with shock and flow expansion effects properly accounted for; subscripts  $w$  and  $l$  are the windward and leeward surfaces, respectively. Because of symmetry with respect to the central plane, i.e., plane OCB in Figure 54, all yaw and roll parameters are zero.

## (2) Jet-on

By the same token, the aerodynamic quantities showing plume-induced separation effects can be evaluated by using appropriate values for pressure force and wetted area.



Windside normal force increment

$$F_w = (P_B - P_o)_w A_{f_w} \quad (45)$$

Leeside normal force increment

$$\begin{aligned} F_N &= (P_B - P_o)_l A_{f_l} \tan \beta (\tan^2 \theta \tan^2 \beta + \tan^2 \beta + \tan^2 \theta)^{-1/2} \\ &= 0.702 (P_B - P_o)_l A_{f_l} \end{aligned} \quad (46)$$

Axial force increment

$$\begin{aligned} F_A &= (P_B - P_o)_l A_{f_l} \tan \theta \tan \beta (\tan^2 \theta \tan^2 \beta + \tan^2 \beta + \tan^2 \theta)^{-1/2} \\ &= 0.124 (P_B - P_o)_l A_{f_l} \end{aligned} \quad (47)$$

Incremental normal force coefficient

$$\Delta C_N = \frac{1}{q_\infty} (F_w - F_N) \quad (48)$$

Incremental axial force coefficient

$$\Delta C_A = \frac{2}{q_\infty} F_A \quad (49)$$

Incremental pitching moment coefficient

$$\Delta C_M = \frac{1}{q_\infty d_c} [2 F_N X_f - F_w X'_f + 2 F_A Z_f] \quad (50)$$

where  $A_{f_w}$  and  $A_f$  are the separation footprint areas on the windside and leeside plates, and  $X_f$ ,  $X'_f$  and  $Z_f$  are the moment arms.

The results are presented in Figures 55 through 70 and compiled in Table VIII. Important features of these results are as follows:

- The relatively small plumes for 230,000 and 250,000 feet altitudes have resulted in moderate changes in aerodynamic properties, as expected. However, at higher altitudes, say 280,000 feet, the large plume would induce more extensive flow separation and, therefore, greater changes in pressure coefficients and L/D.

- In general, exhaust plume results in a loss of  $L/D$ . The unexpected increase in  $L/D$  at low angle of attack at 280,000 feet shown in Figure 70 is an exception, since in the present example, the separated flow region on the windside surface is much greater than on the leeside surface at zero and low angles of attack, thus creating a strong overpressure and a higher  $L/D$ . The trend is reversed at high angles of attack, as seen in Figure 70. However, the erratic behavior exhibited for high-altitude plume problems may, in part, be attributed to the extrapolation procedure required in ascertaining the separation length (Fig. 53), which could significantly affect the ensuing separation footprint predictions.
- From Table VIII, it is seen that all the aerodynamic parameters are effectively independent of altitudes for the jet-off case. Hence, the exhaust plume effects can be demonstrated by comparing  $C_N$ ,  $C_A$ , and  $C_M$  values for different jet pressure ratios, where  $P_{ex}/P_\infty = 0$  refers to the jet-off case. These convenient design curves are illustrated in Figures 67, 68 and 69.
- The stability curves,  $C_N$  vs  $C_M$ , illustrated in Figures 64, 65 and 66 indicate that plume-induced flow separation affects the stability insignificantly at moderate altitudes (230,000 and 250,000 feet). However, severe changes in stability are evidenced at high altitudes (280,000 feet). The results presented in these figures show the anticipated qualitative trend and regions of instability under particular  $\alpha$  and  $M$  conditions.
- Because of angle-of-attack consideration alone and because of symmetry with the vertical plane (Fig. 54), the yaw and roll effects do not occur in this sample problem.
- The design curves presented in Figures 55 through 69 can be extrapolated, in a limited fashion, to predict aerodynamic characteristics at higher angle of attack and/or higher Mach number. For example, at Mach number 20, 250,000-foot altitude, and 30-degree angle of attack, the plume effects are estimated to be as follows:

$$C_N (\text{jet-on}) - C_N (\text{jet-off}) \approx 0$$

$$C_A (\text{jet-on}) - C_A (\text{jet-off}) \approx 0.002$$

$$C_M (\text{jet-on}) - C_M (\text{jet-off}) \approx -0.01$$

Because of lack of pertinent data, extensive effort has not been expended to investigate high angle of attack and Mach number cases further. Also, the validity of these design curves for more complex body shapes needs experimental verification.

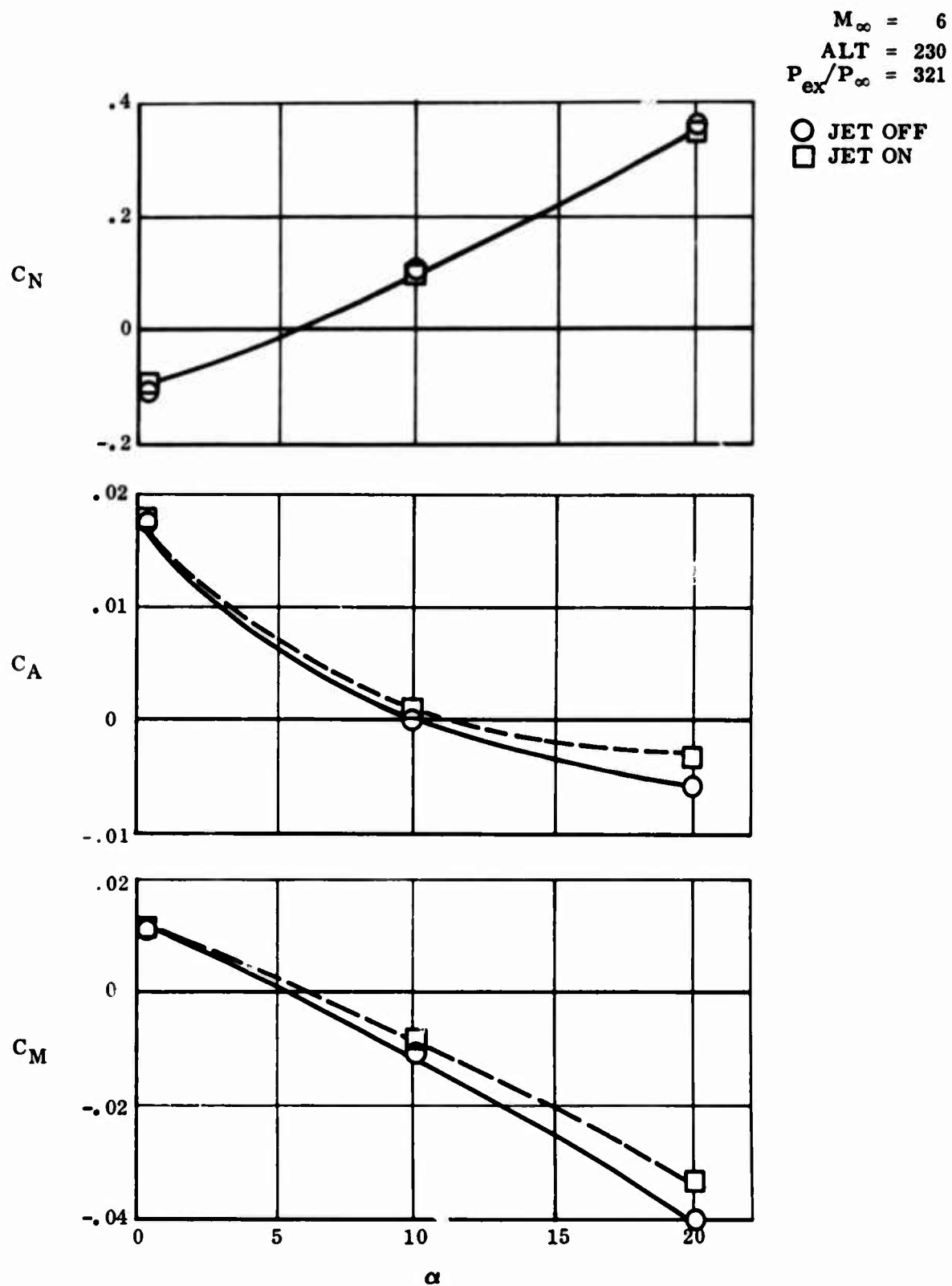


Figure 55  $C_N$ ,  $C_A$ , and  $C_M$  vs  $\alpha$  for  $M_\infty = 6$  at 230,000 Feet

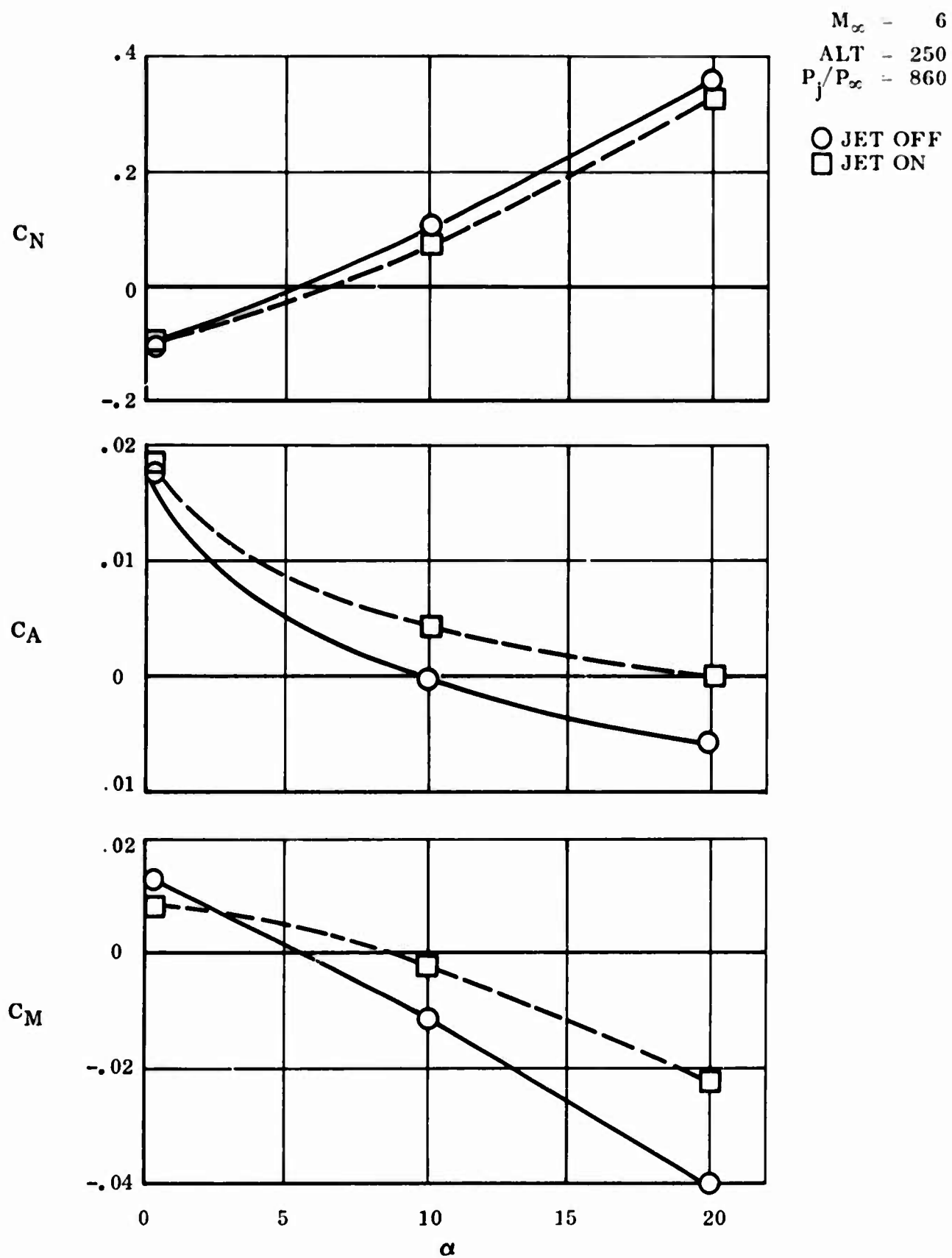


Figure 56  $C_N$ ,  $C_A$ , and  $C_M$  vs  $\alpha$  for  $M_\infty = 6$  at 250,000 Feet

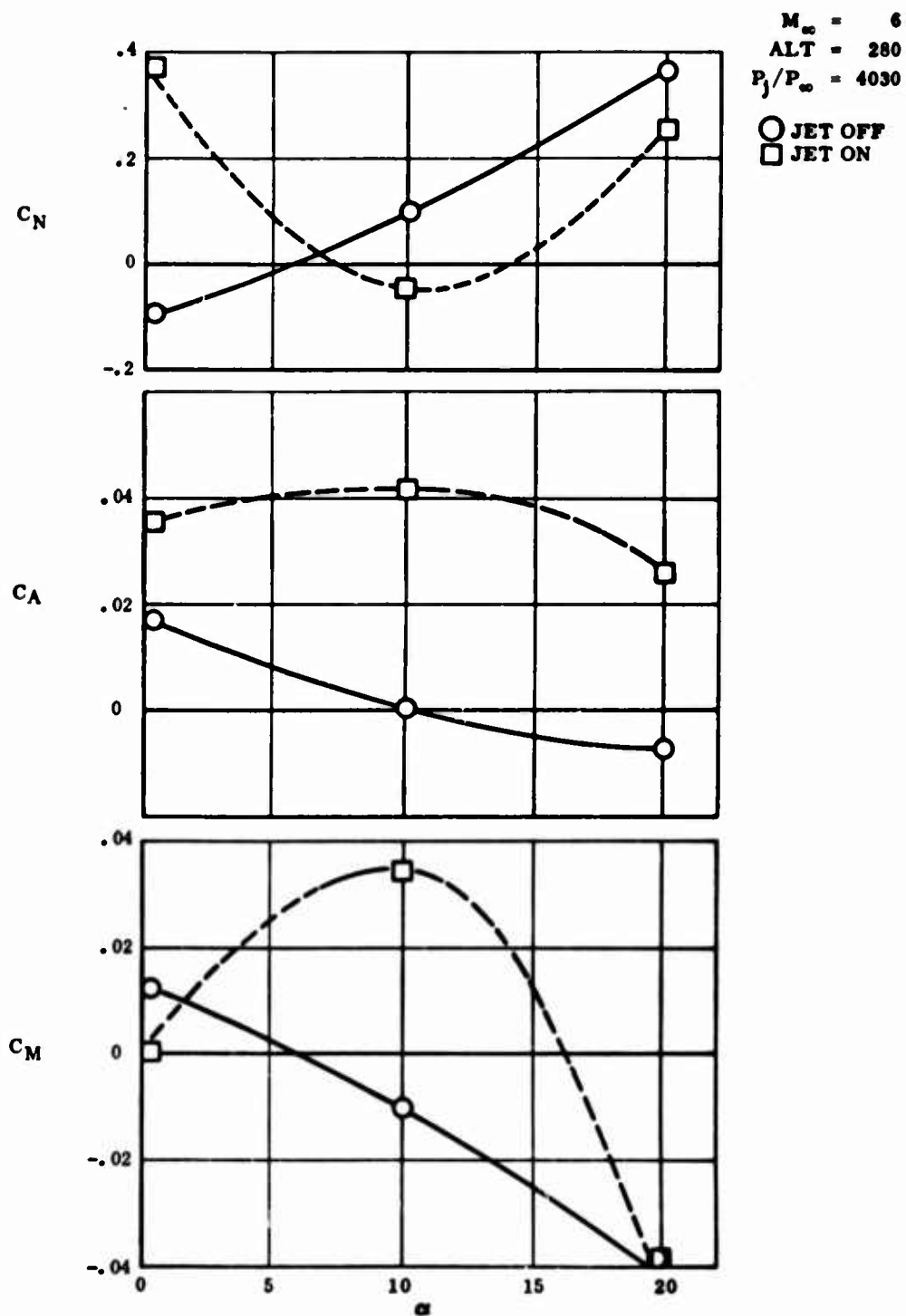


Figure 57  $C_N$ ,  $C_A$ , and  $C_M$  vs  $\alpha$  for  $M_\infty = 6$  at 280,000 Feet

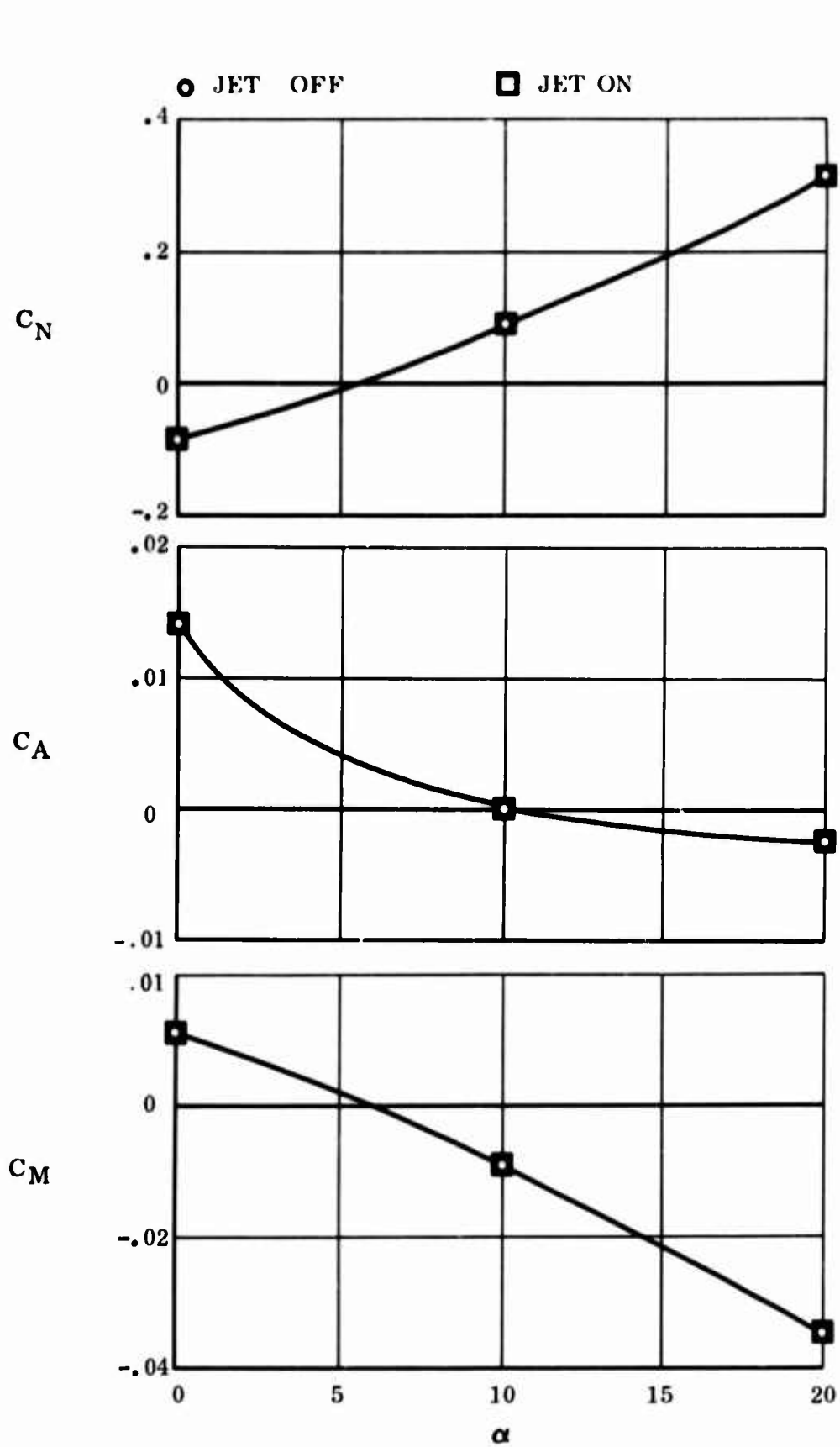


Figure 58  $C_N$ ,  $C_A$ , and  $C_M$  vs  $\alpha$  for  $M_\infty = 10$  at 230,000 Feet

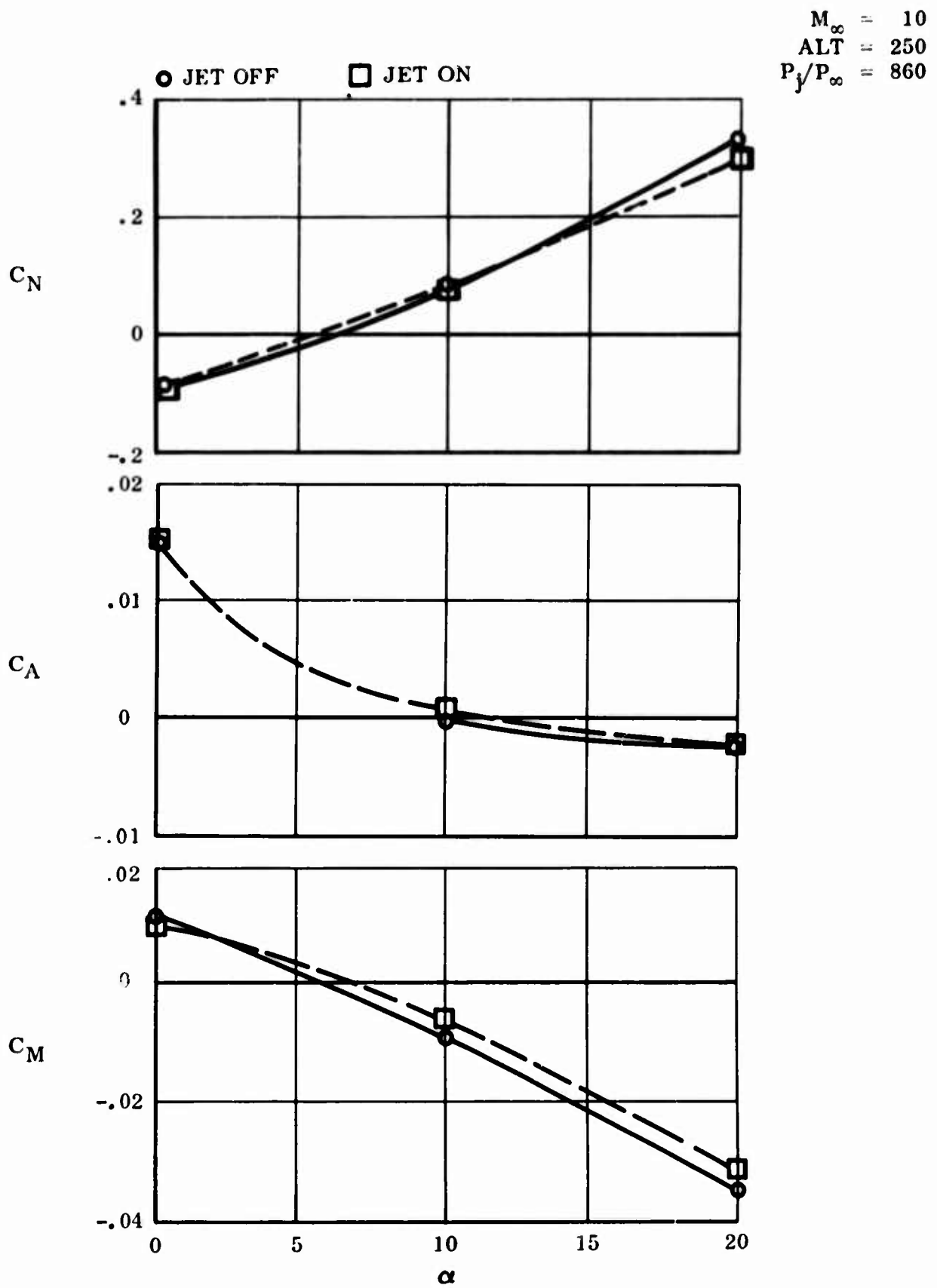


Figure 59  $C_N$ ,  $C_A$ , and  $C_M$  vs  $\alpha$  for  $M_\infty = 10$  at 250,000 Feet

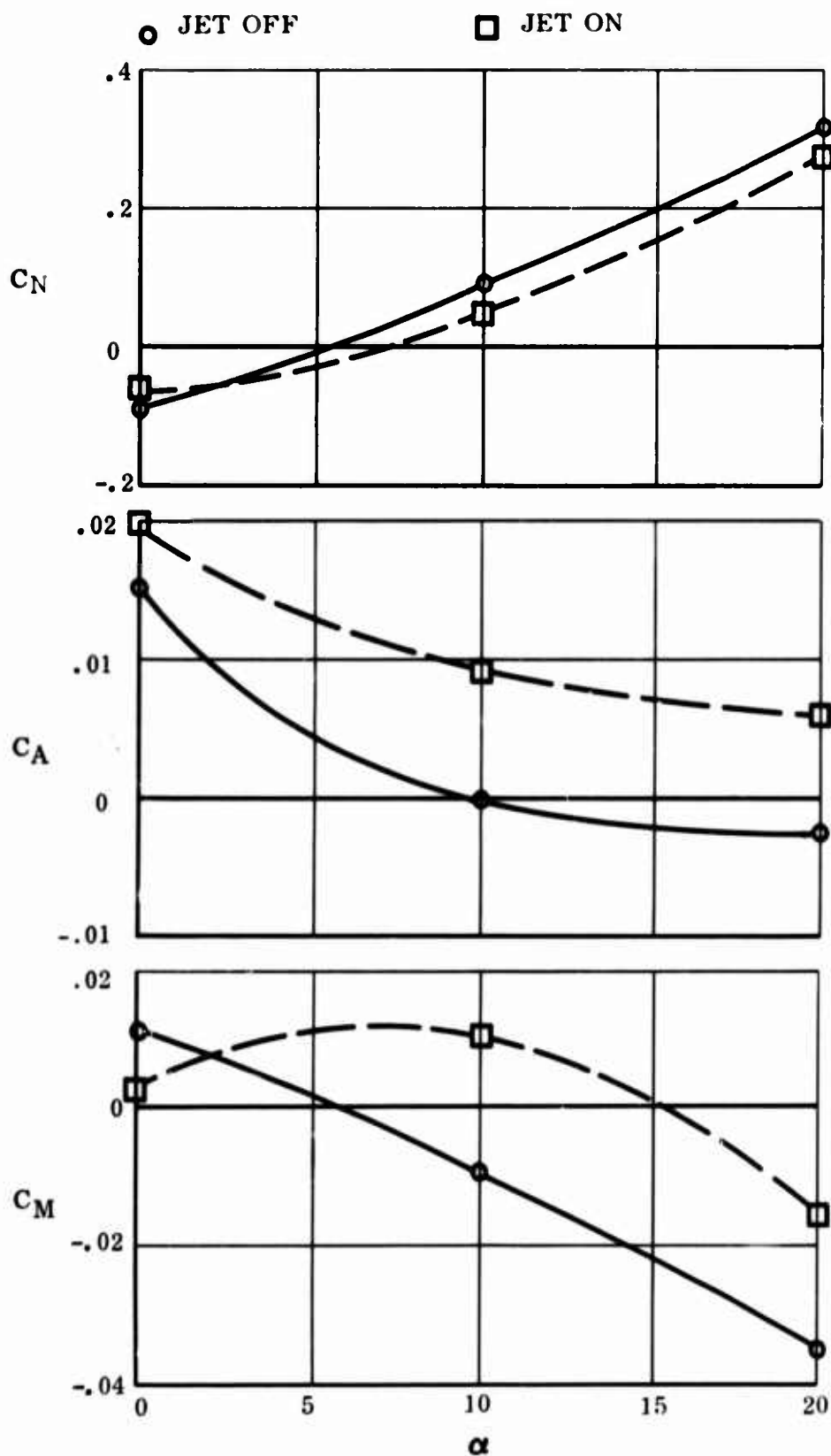


Figure 60  $C_N$ ,  $C_A$ , and  $C_M$  vs  $\alpha$  for  $M_\infty = 10$  at 280,000 Feet



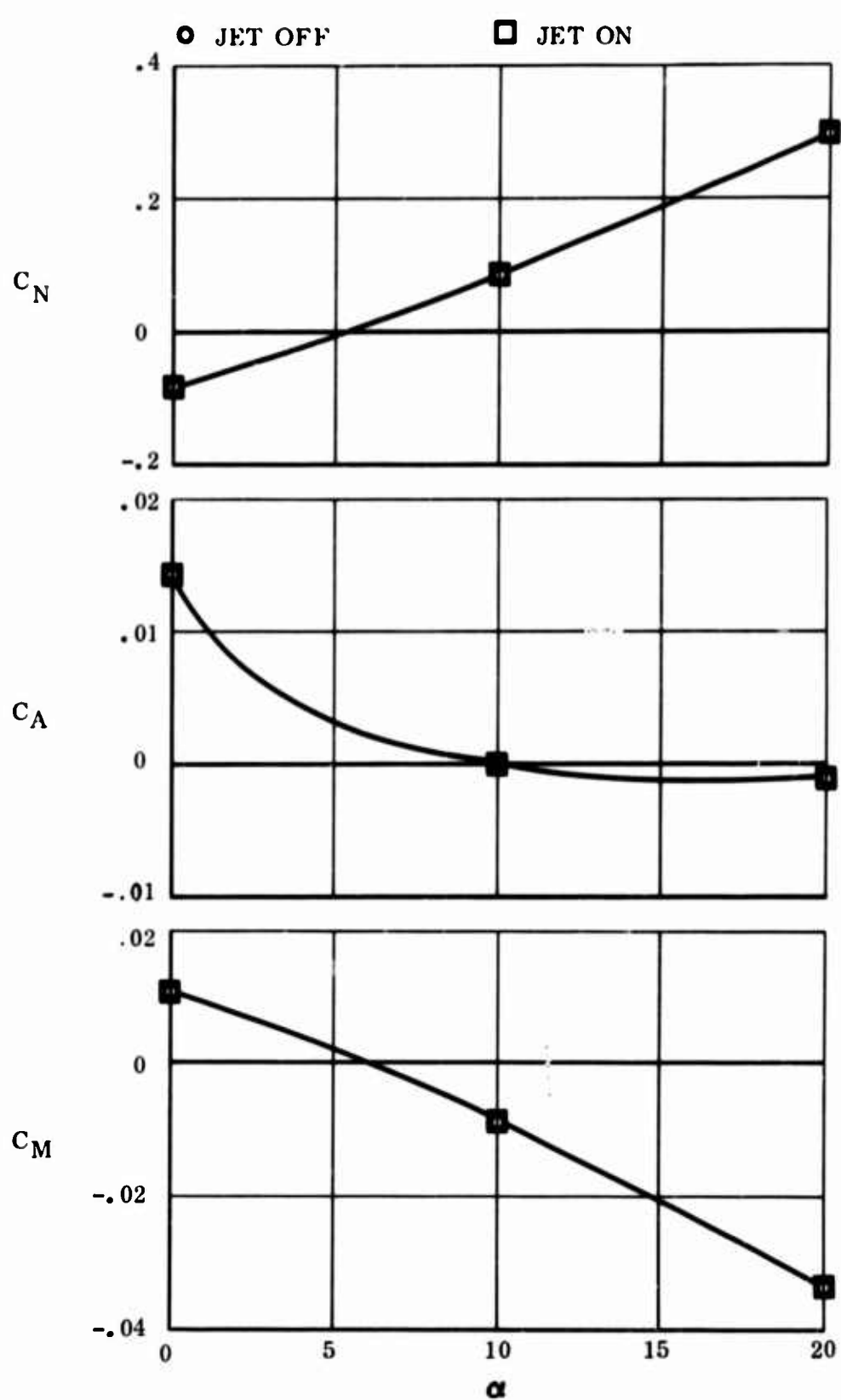


Figure 61  $C_N$ ,  $C_A$ , and  $C_M$  vs  $\alpha$  for  $M_\infty = 15$  at 230,000 Feet

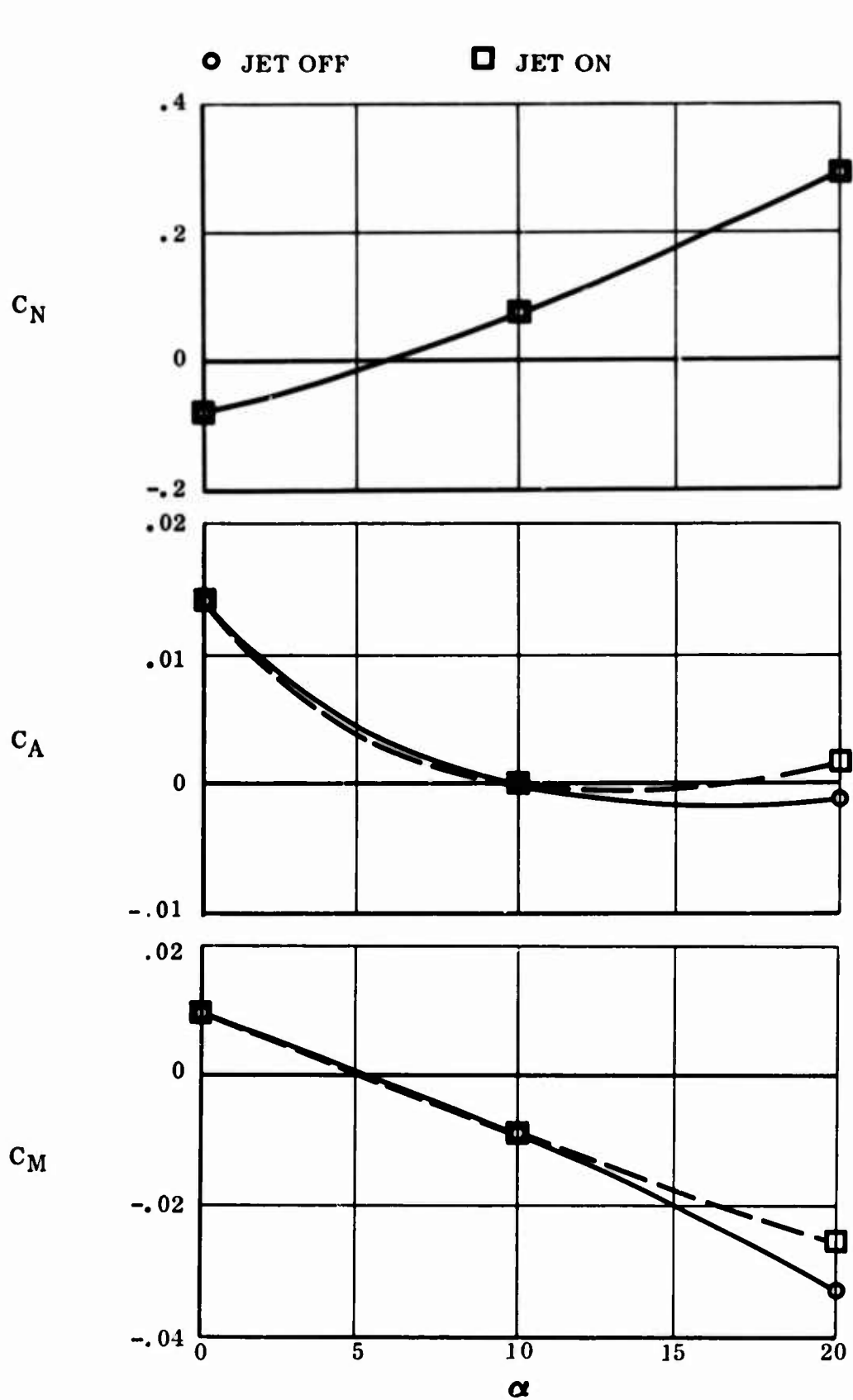


Figure 62  $C_N$ ,  $C_A$ , and  $C_M$  vs  $\alpha$  for  $M_\infty = 15$  at 250,000 Feet

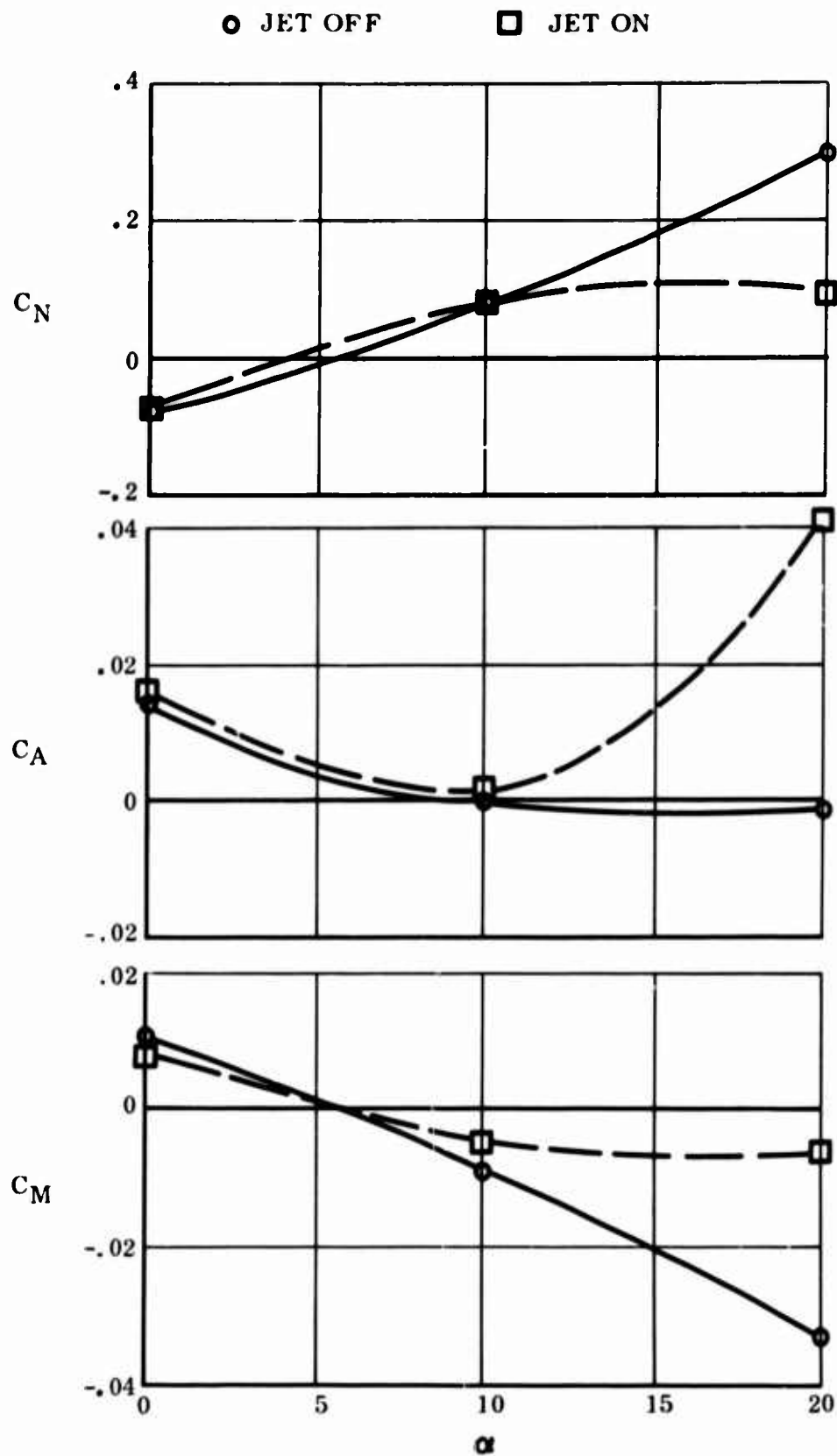


Figure 63  $C_N$ ,  $C_A$ , and  $C_M$  vs  $\alpha$  for  $M_\infty = 15$  at 280,000 Feet

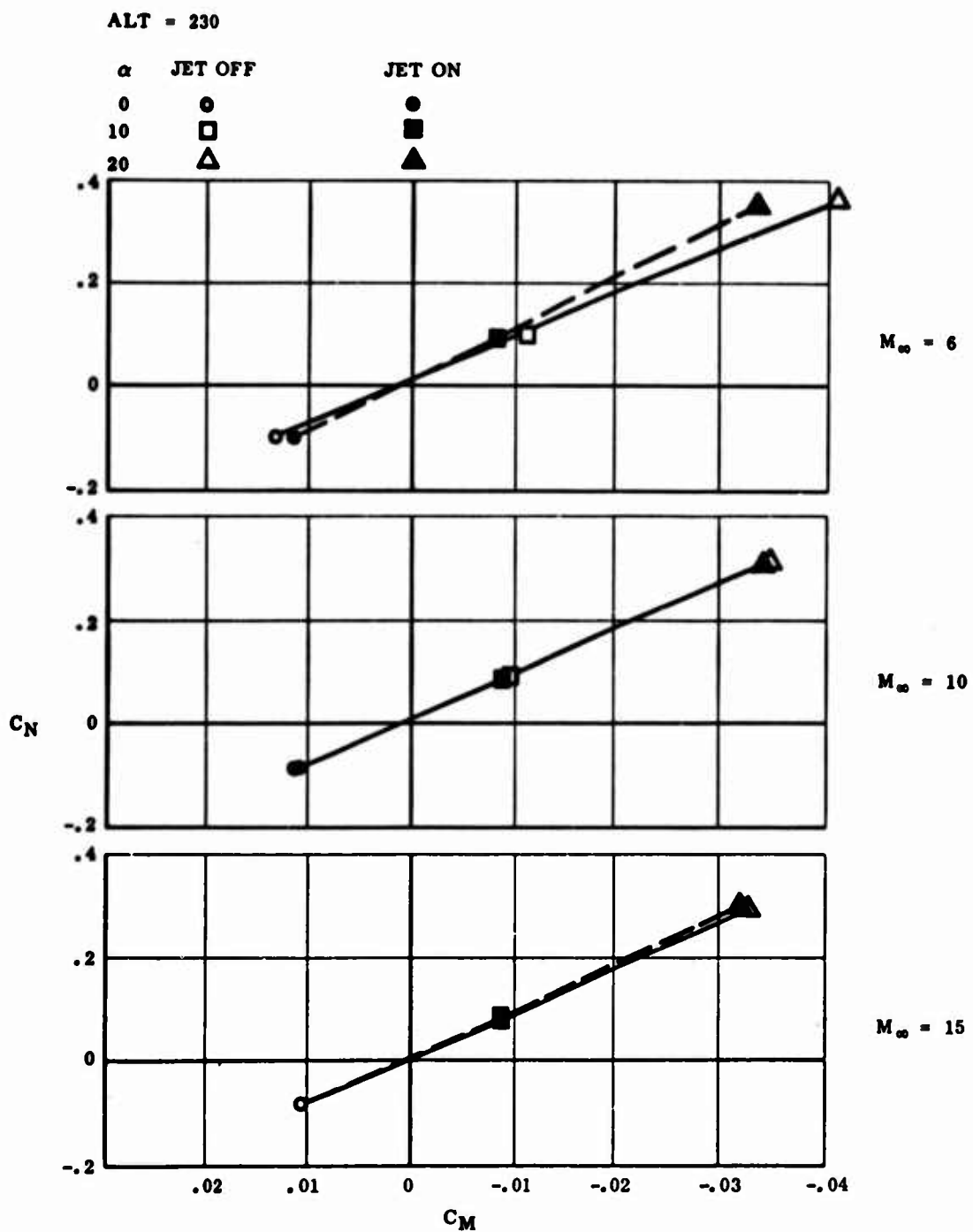


Figure 64  $C_N$  vs  $C_M$  for Various Mach Numbers at 230,000 Feet

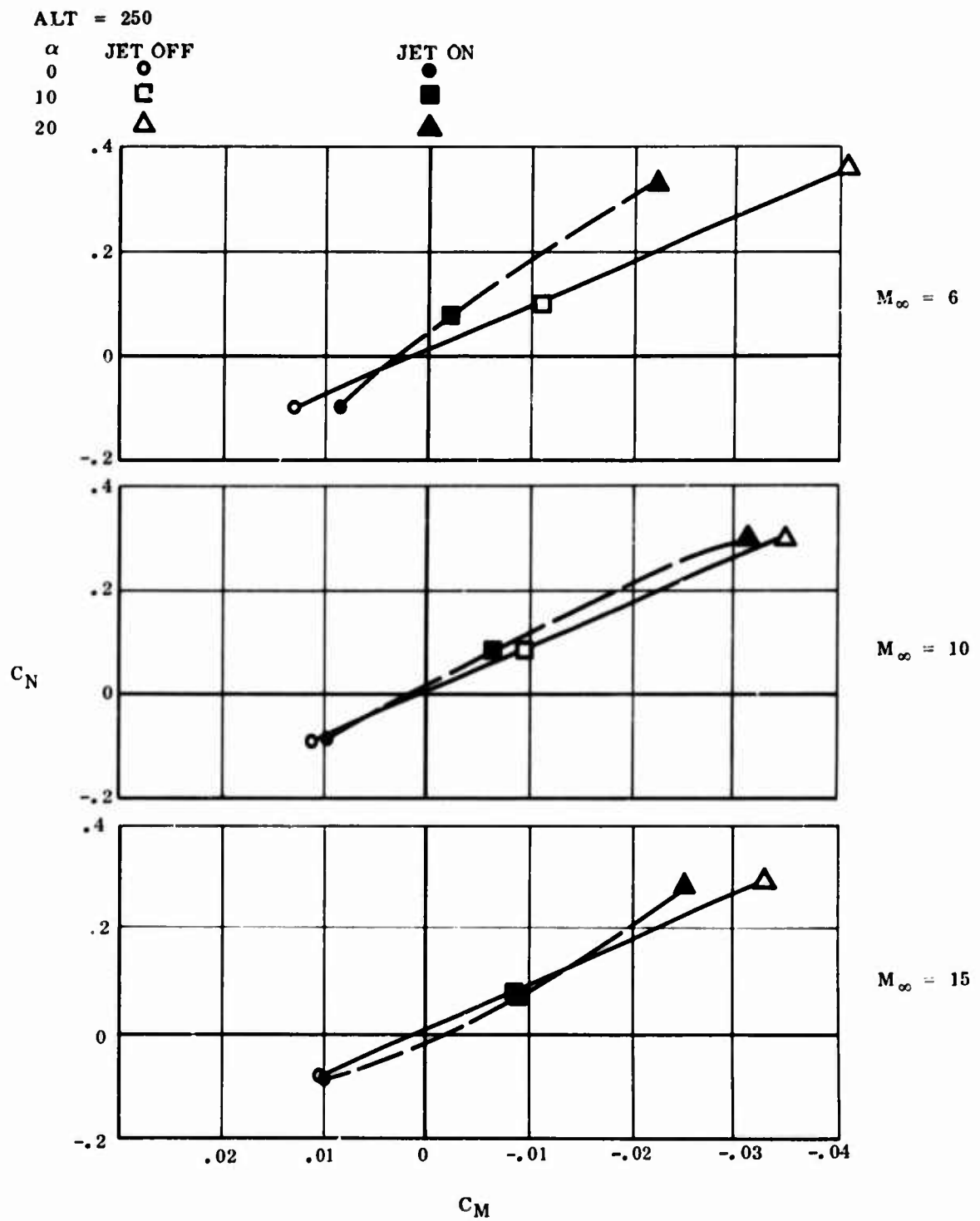


Figure 65  $C_N$  vs  $C_M$  for Various Mach Numbers at 250,000 Feet

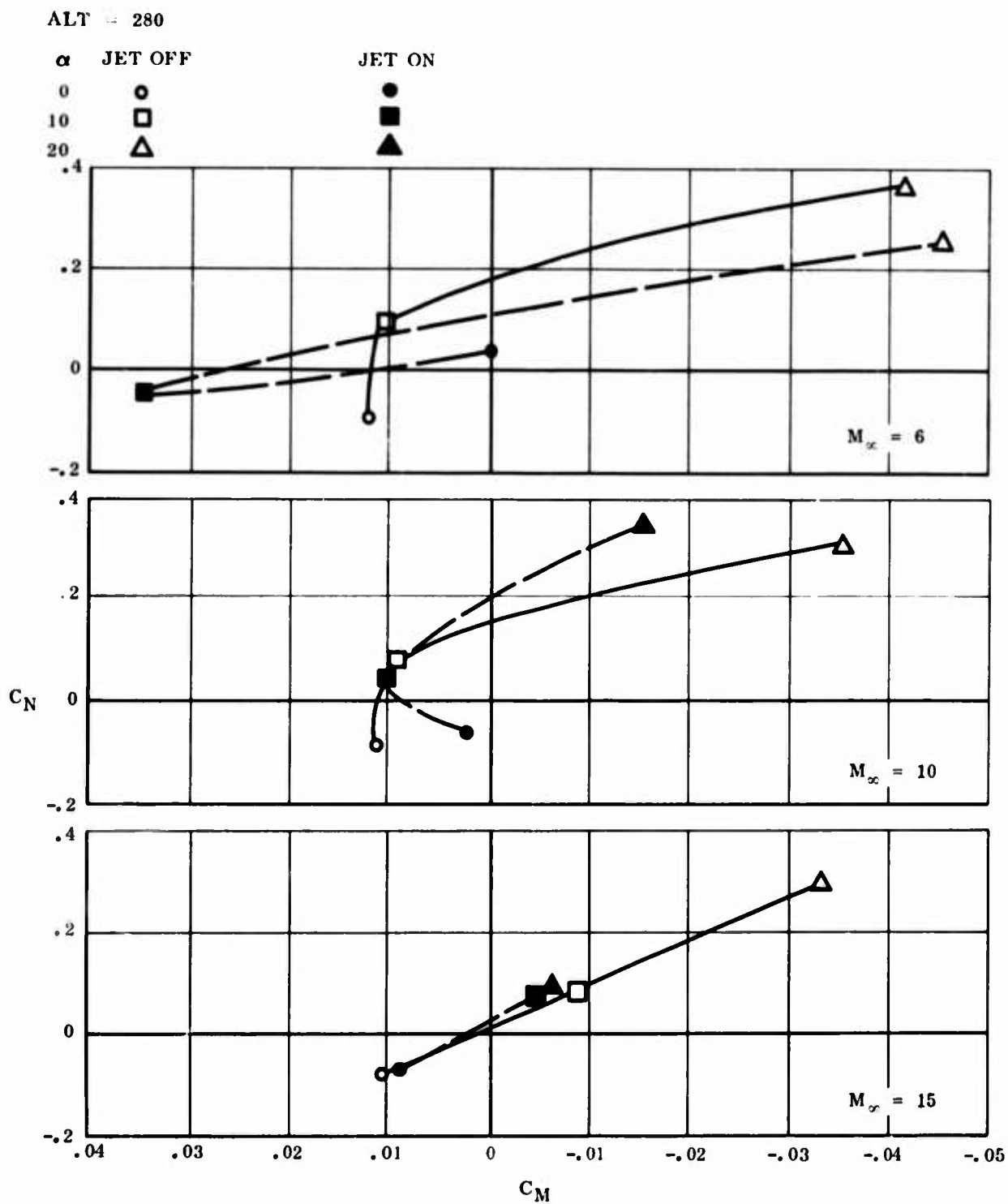


Figure 66  $C_N$  vs  $C_M$  for Various Mach Numbers at 280,000 Feet

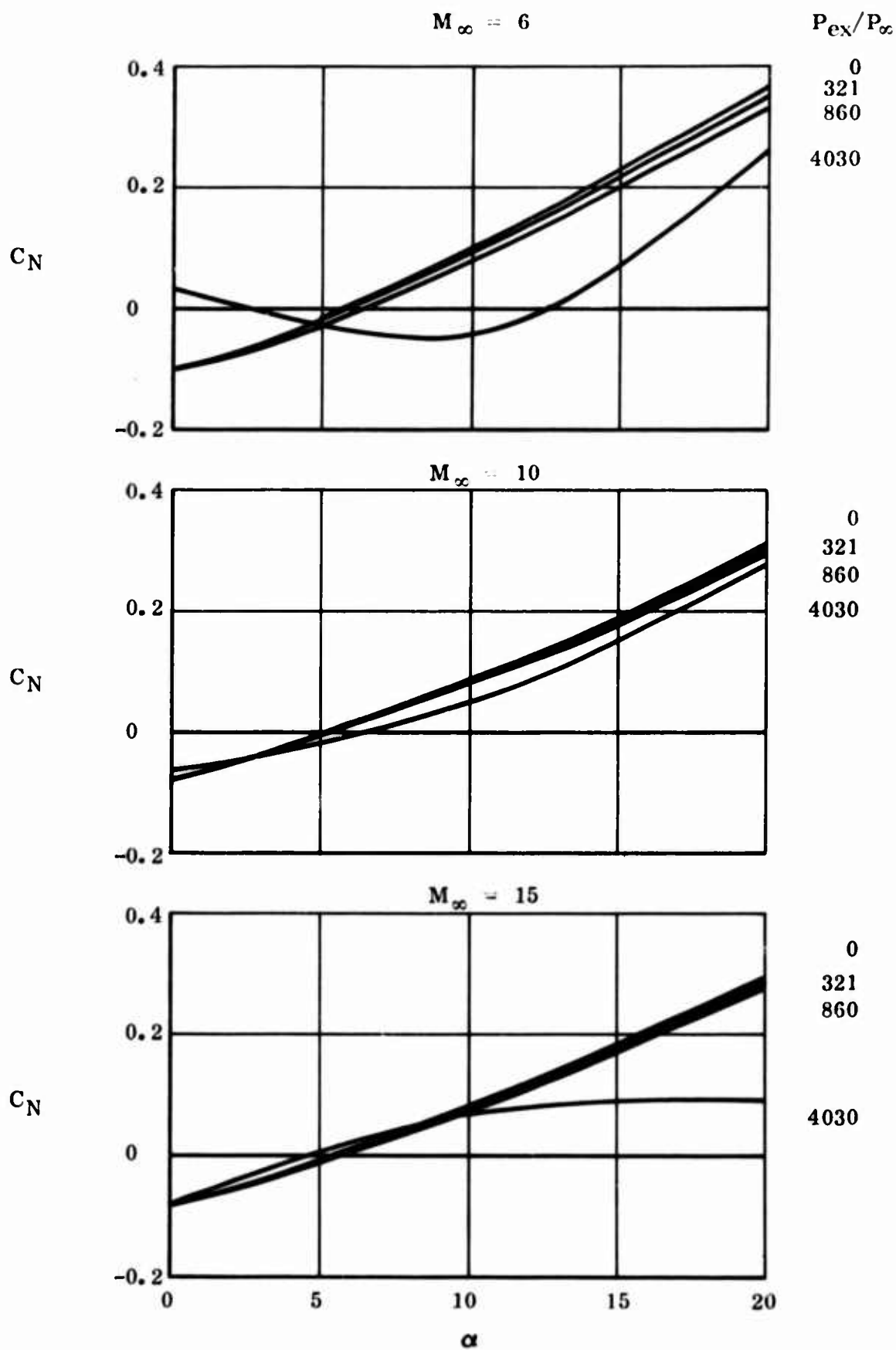


Figure 67  $C_N$  vs  $\alpha$  for Various Mach Numbers and Jet Pressure Ratios

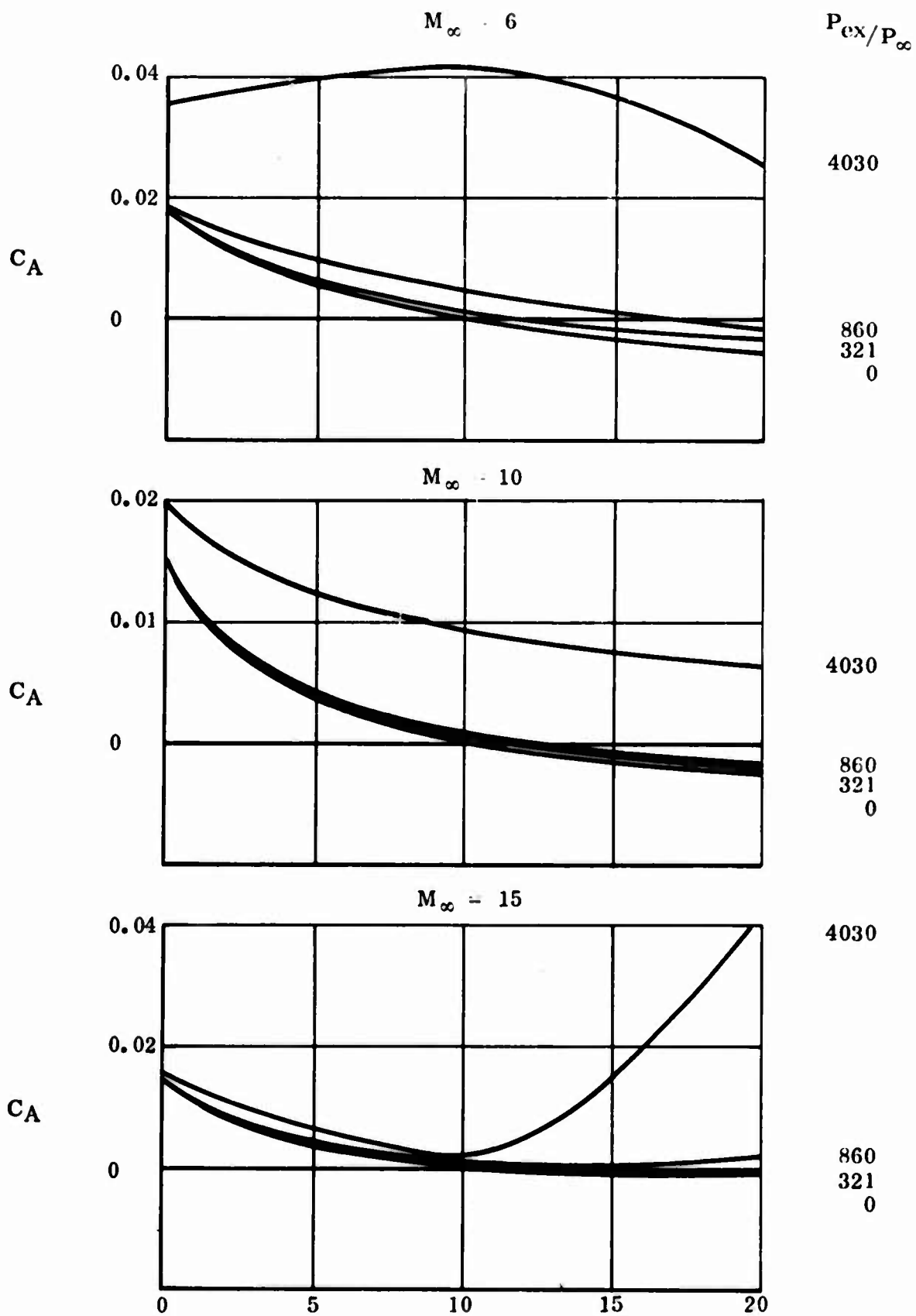


Figure 68  $C_A$  vs  $\alpha$  for Various Mach Numbers and Jet Pressure Ratios



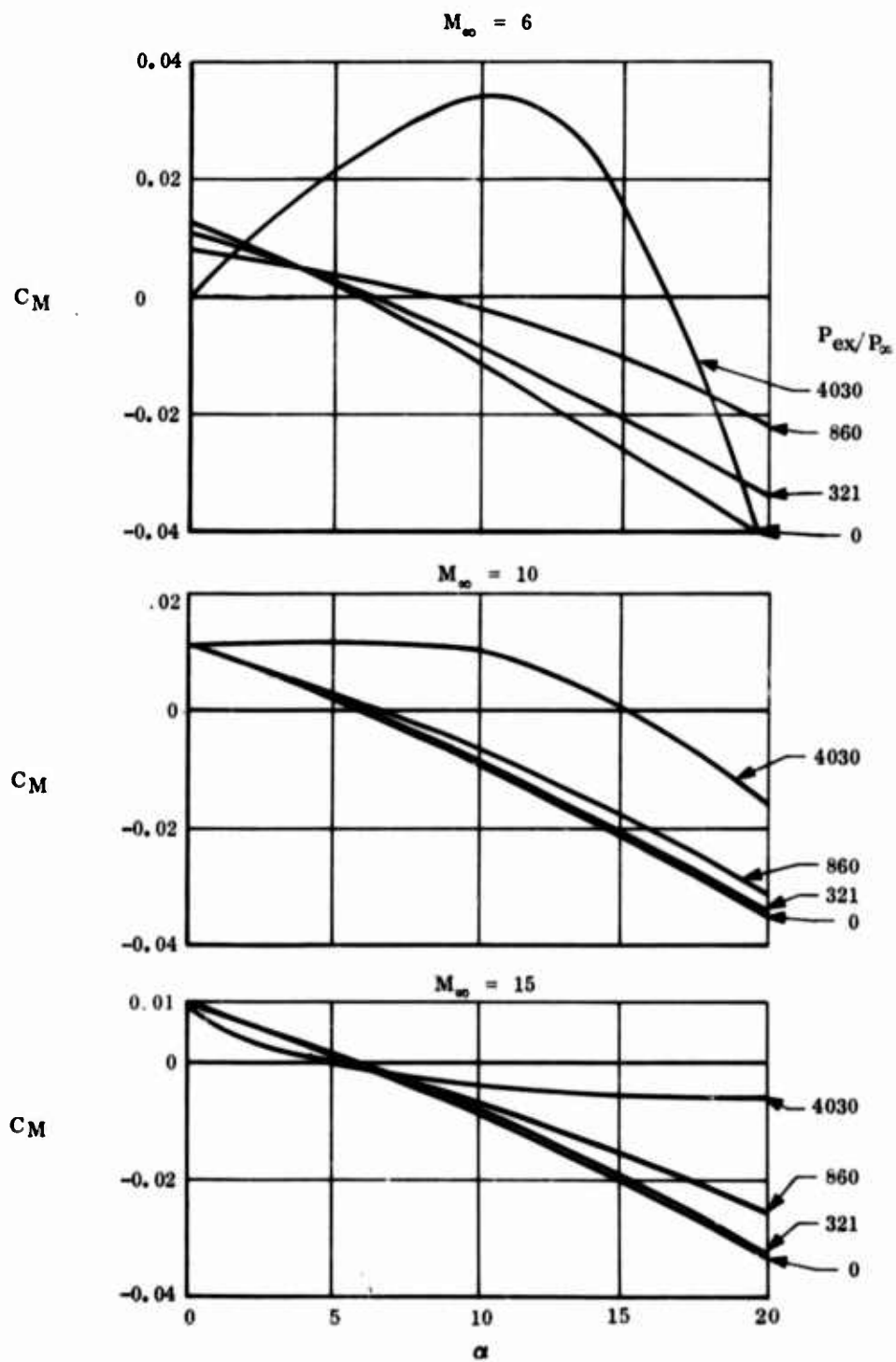
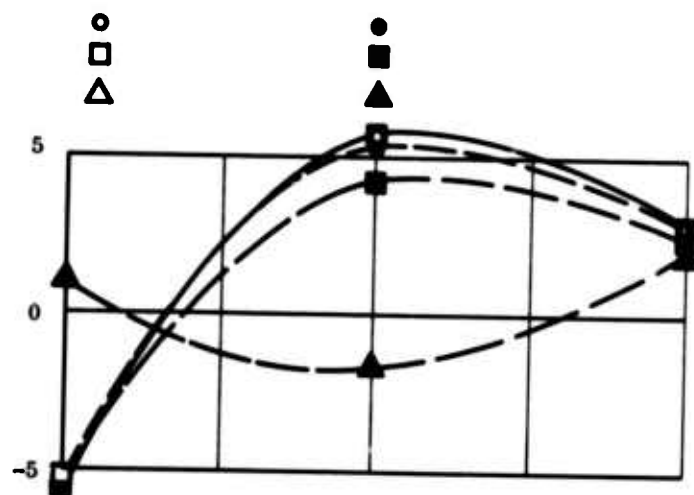


Figure 69  $C_M$  vs  $\alpha$  for Various Mach Numbers and Jet Pressure Ratios

ALT  
230  
250  
280

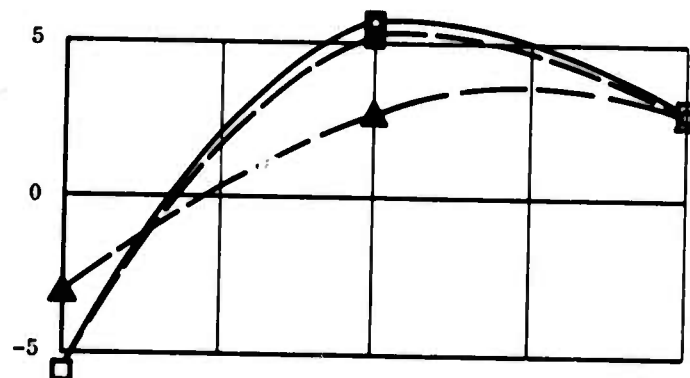
JET OFF

JET ON

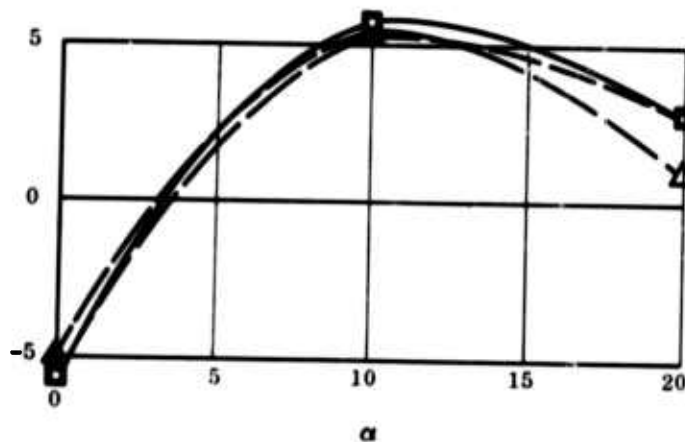


$M_\infty = 6$

$L/D$



$M_\infty = 10$



$M_\infty = 15$

Figure 70 Exhaust Plume Effect on  $L/D$

Table VIII Predicted Aerodynamic Characteristics for Simple Delta  
Slab Configuration With and Without Plume Effects

M	Alt (kft)	$\alpha$ (°)	Jet Off					Sep. Region					Jet On				
			C <sub>N</sub>	C <sub>A</sub>	C <sub>M</sub>	C <sub>L</sub>	C <sub>D</sub>	L/D	C <sub>N</sub>	C <sub>A</sub>	C <sub>M</sub>	C <sub>L</sub>	C <sub>D</sub>	L/D	C <sub>N</sub>	C <sub>A</sub>	C <sub>M</sub>
6	230	0	-0.1	0.0177	0.0131	-0.1	0.0177	-5.65	0.00317	0.00008	-0.00167	-0.0968	0.01778	0.01143	-0.0968	0.01778	-5.45
		10	0.0996	0	-0.0111	0.098	0.0173	5.67	-0.00505	0.00094	0.00288	0.9455	0.00094	-0.00822	0.09284	0.01733	5.36
		20	0.362	-0.00574	-0.041	0.342	0.119	2.88	-0.01488	0.00263	0.00764	0.3471	-0.00311	-0.03336	0.327	0.1161	2.81
		250	-0.1	0.0177	0.0131	-0.1	0.0177	-5.65	0.00131	0.00082	-0.00475	-0.0987	0.0185	0.00835	-0.0987	0.0185	-5.33
10	230	0	-0.1	0	-0.0111	0.09848	0.01736	5.67	-0.022	0.0044	0.0089	0.078	0.0044	-0.0022	0.07594	0.01785	4.25
		10	0.36	-0.00571	-0.0408	0.336	0.1176	2.86	-0.0304	0.0055	0.0185	0.3296	-0.0002	-0.0223	0.31	0.113	2.74
		20	-0.0957	0.017	0.0121	-0.0957	0.017	-5.65	0.133	0.0184	-0.0119	0.0373	0.0354	0.0002	0.0373	0.0354	1.052
		280	0	0.0957	0	-0.01062	0.0941	0.01659	5.67	-0.143	0.0415	0.0455	-0.0473	0.0415	0.03488	-0.0537	0.03261
10	230	0	0.364	-0.0064	-0.0412	0.3442	0.1183	2.915	-0.1058	0.0321	-0.00427	0.2582	0.0256	-0.04547	0.2334	0.1123	2.08
		10	-0.085	0.0151	0.0111	-0.085	0.0151	-5.63	0.00666	0	-0.00039	-0.0843	0.0151	0.01071	-0.0843	0.0151	-5.58
		20	0.0848	0	-0.00943	0.0835	0.01471	5.67	-0.0007	0.00012	0.00045	0.0841	0.00012	-0.00898	0.08268	0.01471	5.62
		250	0	0.3125	-0.0024	-0.035	0.2948	0.109	2.7	-0.00052	0.00009	0.00034	0.312	-0.00231	-0.03466	0.2938	0.1047
250	230	0	-0.085	0.015	0.0111	-0.085	0.015	-5.67	0.00268	0.00009	-0.00148	-0.0823	0.0151	0.00962	-0.0823	0.0151	-5.47
		10	0.0847	0	-0.00941	0.0833	0.0147	5.65	-0.0034	0.00066	0.00217	0.0813	0.00066	-0.0067	0.08	0.0148	5.4
		20	0.304	-0.0024	-0.035	0.2868	0.1017	2.82	-0.00597	0.00011	0.00342	0.298	-0.0023	-0.03158	0.281	0.1042	2.7
		280	0	-0.0852	0.0151	0.0111	-0.0852	0.0151	-5.65	0.0238	0.00444	-0.01355	-0.0614	0.01954	0.00245	-0.0614	0.01954
15	230	0	0.085	0	-0.00942	0.0836	0.01473	5.66	-0.0354	0.00904	0.0196	0.0496	0.00904	0.01018	0.04723	0.01757	2.69
		10	0.312	-0.0024	-0.0352	0.2948	0.1047	2.82	-0.0353	0.0085	0.0197	0.2767	0.0061	-0.0155	0.2679	0.0987	2.707
		20	-0.0805	0.0142	0.01053	-0.0805	0.0142	-5.66	0.00019	0	-0.00012	-0.0803	0.0142	0.01041	-0.0803	0.0142	-5.65
		250	0	0.0802	0	-0.00889	0.079	0.01393	5.66	-0.00024	0.00004	0.00016	0.7996	0.00004	-0.00873	0.0785	0.01399
250	230	0	0.296	-0.00112	-0.033	0.2784	0.1	2.784	-0.00096	0.00017	0.00064	0.295	-0.00095	-0.03236	0.2773	0.1	2.773
		10	-0.0798	0.0141	0.01043	-0.0798	0.0141	-5.65	0.00084	0	-0.00053	-0.079	0.0141	0.0099	-0.079	0.0141	-5.6
		20	0.0794	0	-0.00882	0.078	0.0138	5.66	-0.00108	0.00019	0.00071	0.783	0.00019	-0.00811	0.077	0.0145	5.3
		280	0	-0.00111	-0.033	0.2784	0.1	2.784	-0.015	0.00266	0.0074	0.281	0.00155	-0.0256	0.2635	0.09746	2.73
280	230	0	-0.0801	0.0142	0.01046	-0.0801	0.0142	-5.65	0.00277	0.00079	-0.00156	-0.07733	0.015	0.0089	-0.07733	0.015	-5.18
		10	0.08	0	-0.00888	0.0787	0.0139	5.66	-0.00586	0.00182	0.0042	0.7414	0.00182	-0.00468	0.0727	0.01306	5.57
		20	0.295	-0.00111	-0.033	0.2784	0.1	2.784	-0.204	0.0423	0.0269	0.091	0.0411	-0.0061	0.0714	0.0697	1.02
		250	0	-0.00111	-0.033	0.2784	0.1	2.784	-0.204	0.0423	0.0269	0.091	0.0411	-0.0061	0.0714	0.0697	1.02

Remark: Skin friction effects not considered

## 2. CRITICAL ANALYSIS

The main sources of error in the present simplified analysis to predict plume-induced flow separation are itemized as follows:

### a. Plateau Pressure Correlation

Lack of relevant pressure data constitutes the major source of analytical uncertainty. Deduced plateau pressures from preliminary NASA-Langley cone-cylinder data may be quite erroneous.

### b. Nash Factor

The Nash factor was introduced to reduce the discrepancy between theoretical and experimental results. In essence, it serves to rectify the over-simplification of the theoretical model. Additional data, particularly at high Mach numbers, are needed to establish whether this parameter is dependent upon the freestream flow conditions.

### c. Nozzle Wall Friction

Because of nozzle wall viscous effects, the plume contour may be much larger than the predicted inviscid plume; the flow properties along the plume contour are then modified accordingly. The plume/separation-wedge interaction characteristics may be substantially affected also. Using the case  $M_\infty = 6$ ,  $\alpha = 0$  degree, and altitude = 250,000 feet as an example, it was found that the Nash factor should be 0.3 instead of 0.56 if the "1/7th-power" plume was used (see Fig. 32). In view of uncertainty toward this problem, a careful experimental program is needed to reach a final conclusion.

### d. Chemical Kinetics in Nozzle and in Plume

The discrepancy in nozzle performance between a real nozzle involving chemical kinetics and a pseudo-ideal nozzle with an average constant  $\gamma$  of 1.38 could induce considerable difference in plume properties, thus affecting the plume-induced separated flow results. By the same token, the constant  $\gamma$  assumption for plume predictions beyond the nozzle exit could produce additional discrepancy with the real case. The cumulative effects of the constant  $\gamma$  idealization may be quite substantial and, therefore, warrant ample attention in carrying out exhaust plume analysis.

### e. Rarefied Gas Effect

At high altitudes or under locally low-pressure conditions, the rarefied gas effects should be incorporated in the analysis in two aspects: (a) the initial boundary layer prediction, and (b) hypersonic viscous-inviscid interaction near the leading edge. Both will influence the flow field upstream of the separated flow region and will, therefore, affect the predictions of the separation footprint and other quantities. However, at very high altitudes where the flow is of the free molecule type, plume-induced separation will not likely be of practical importance because of the very small aerodynamic forces experienced by the vehicle.

#### f. Three-Dimensional Flow Effect

Although it has been argued in par. 6 of this section that the three-dimensional boundary layer effect is not severe for the present sample problem, additional theoretical/experimental studies are needed to reach an irrefutable conclusion. Aside from this, two other factors will affect the analytical prediction:

- (1) At angle of attack, complicated cross-flow phenomena may create surface flow separation which is not easily tractable. For purpose of demonstration, a surface separation curve for a pitched delta slab is exemplified in Figure 71 (Ref. 37).
- (2) In carrying out the present analytical procedure, the assumption of wedge-like or cone-like separation will affect the laminar solution through the Mangler and Dorodnitsyn transformation variables but will not affect turbulent flows. As seen in Appendix I, a deviation factor of  $\sqrt{r}$  differentiates the wedge flow from the conical flow where  $r$  is a reference radial length. For the sample problems considered herein, it was found that insignificant error would be incurred if  $r$  is less than 3 feet.

#### g. Viscosity Parameter

Since Reynolds number is one of the parameters used in reaching a separated flow solution, an error in dynamic viscosity,  $\mu$ , would then lead to an erroneous solution. Again, from the viewpoint of numerical computation, the effect arises from the change in the transformation variables when different  $\mu$  values are used. Similar to the  $r$  problem discussed in the preceding paragraph, the square-root quantity,  $\sqrt{\mu}$ , constitutes the deviation factor.

#### h. Shear Layer Profiles

The idealized Chapman and Korst profiles are subject to further scrutiny, particularly if the shear layer contains shocks and other discontinuity surfaces.

#### i. Equivalent Origin

The hypothesis that the actual separation wedge coincides with that initiated at the equivalent origin must be verified experimentally. The equivalent origin is innovated to circumvent the mathematical dilemma encountered when the initial boundary layer thickness is finite. The analytical inaccuracy due to this hypothesis should be carefully assessed.

### 3. SIMULATION PARAMETERS

Based on the analytical results contained in this report and the critical comments summarized in the preceding section, a number of correlation parameters can be established to obtain similitude between actual LRV configuration and wind tunnel subscale model. A brief discussion of these parameters is presented below:

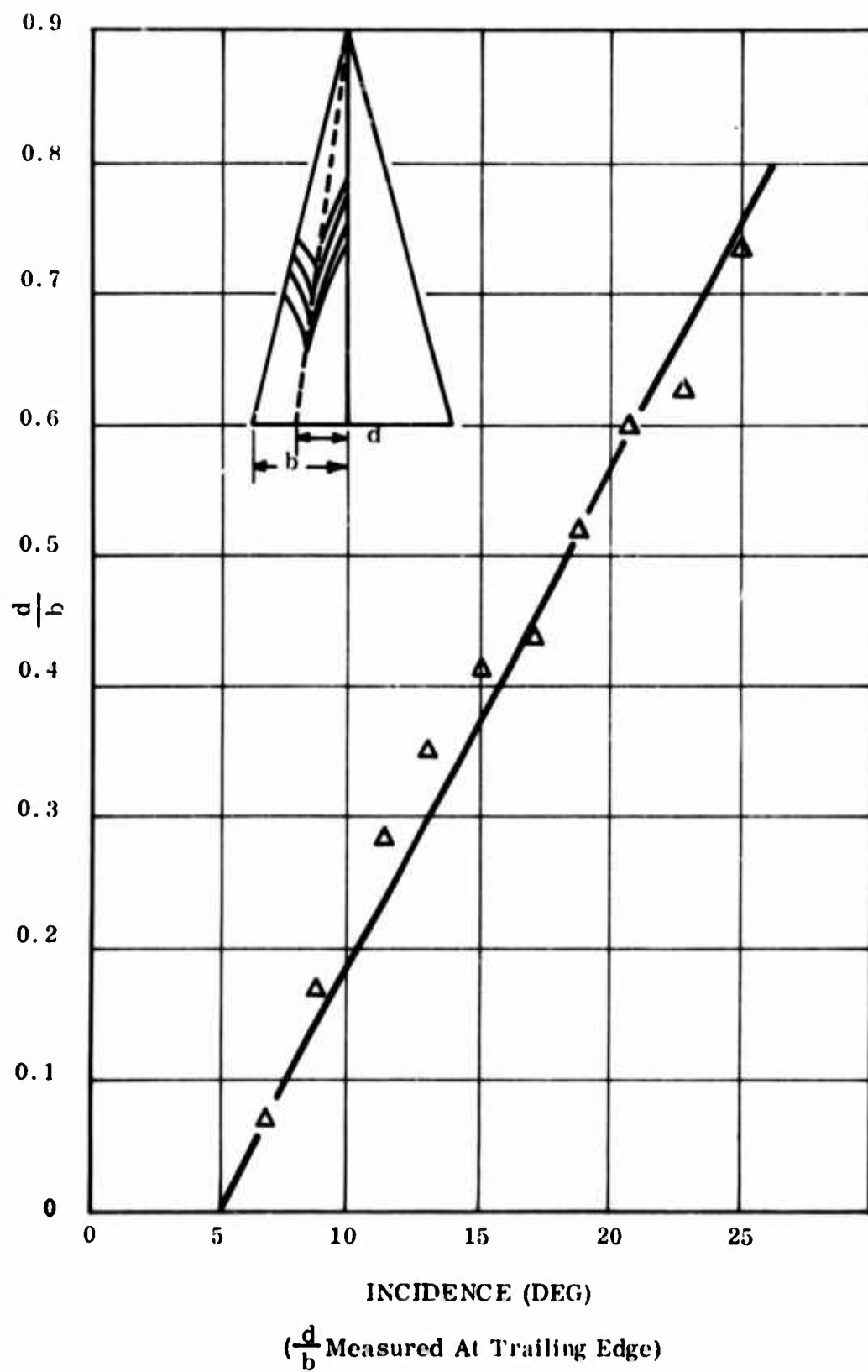


Figure 71 Position of Separation as a Function of Incidence

a. Mach Number

This parameter is limited by the tunnel capability, and a complete range of Mach number simulation is seldom possible. However, for a locally two-dimensional plume-induced separation model proposed herein, the flat-plate solution for determining separation length would be of practical use for a large number of problems. Under this circumstance, the Mach number simulation problem can be partially resolved by angle-of-attack manipulation of the test plate. For example, pitching can enhance the effective Mach number on the leeside of the test from which separation length and other parameters can be determined on the basis of the present theory.

b. Reynolds Number

Again tunnel limitations would govern the extent of Reynolds number simulation. In accordance with the present analysis, the Reynolds number correlation can best be implemented in the following manner:

$$\text{Re} (M^2-1) \big|_A = \text{Re} (M^2-1) \big|_S \quad (51)$$

where Re refers to that based on body length, and subscripts A and S indicate the actual and model geometry, respectively. This equivalence is compatible with the plateau pressure expression of equation (28).

From the discussion of the preceding section, viscosity and body length would affect the theoretical prediction of separation length through the Lees-Dorodnitsyn and Mangler transformation stated in Equation (I-5). Hence, another Reynolds number parameter can be obtained by combining the transformation variables of Equation (I-5) as follows:

$$\left( \frac{\rho_e U_e r^\epsilon}{\sqrt{\int_0^x \rho_e \mu_e U_e r^{2\epsilon} dx}} \right)_A = \left( \frac{\rho_e U_e r^\epsilon}{\sqrt{\int_0^x \rho_e \mu_e U_e r^{2\epsilon} dx}} \right)_S \quad (52)$$

or, approximately,

$$\left( \frac{\text{Re}}{r^2} \right)_A = \left( \frac{\text{Re}}{r^2} \right)_S \quad (53)$$

where Re is based on body length  $\ell$ , and the longitudinal distance,  $x$ , and the equivalent body radius,  $r$ , are assumed to be linearly proportional to  $\ell$ . Equation (53) primarily applies to the separation region where an equivalent separation wedge or cone can be defined.

### c. Jet-to-Ambient Pressure Ratio

For fixed nozzle geometry and  $\gamma$ , the jet-to-ambient pressure ratio,  $P_{ex}/P_{\infty}$ , is the main parameter that controls the similitude of the plume boundary characteristics, such as the geometric contour, boundary Mach number, etc. From the discussion and non dimensionalized plume contour curves presented in Section 2, this correlation parameter is clearly implied.

### d. Jet Initial Turning Angle

Again referring to the discussion of Section 2, the initial turning angle for jet plume would affect the initial plume contour. Hence, a convenient correlation parameter is the initial angle

$$\left( \nu_1 - \nu_{ex} + \theta_N \right)_A = \left( \nu_1 - \nu_{ex} + \theta_N \right)_S \quad (54)$$

### e. Jet Momentum Coefficient

In addition to the two correlation parameters cited above,  $\gamma$  provides an additional constraint, and its pronounced effect on plume geometry has been extensively discussed in Section 2. As a generalization, a jet momentum coefficient can be defined to obtain  $\gamma$  correlation as well as impingement force similitude:

$$\left( \frac{\gamma_{ex} P_{ex} A_{ex} M_{ex}^2}{\gamma_{\infty} P_{\infty} A_0 M_{\infty}^2} \right)_A = \left( \frac{\gamma_{ex} P_{ex} A_{ex} M_{ex}^2}{\gamma_{\infty} P_{\infty} A_0 M_{\infty}^2} \right)_S \quad (55)$$

where  $A_0$  is a reference area. However, momentum ratio is not a sufficient constraint in itself and the force similitude is assured only if the plume geometric similitude is obtained.

### f. The Kawamura Lambda Parameter

The Kawamura lambda parameter

$$\lambda = \left( \frac{M_{ex}^2 - 1}{\gamma_{ex} M_{ex}^2} \right)_A = \left( \frac{M_{ex}^2 - 1}{\gamma_{ex} M_{ex}^2} \right)_S \quad (56)$$

which was derived in Reference 51 based on the weak wave theory provides correlation with wave reflection at the plume boundary. This similitude is primarily applicable to weak wave problems and its validity for plumes involving large jet-to-ambient pressure ratio and strong shocks requires experimental verification.



g. Knudson Number

As discussed in Par. e of Section II, the present analytical prediction is significantly dependent on the initial boundary layer which is affected by the rarefied gas phenomena. Thus, a correlation based on the Knudson number can be introduced in the following form:

$$\left(\frac{M}{Re}\right)_A = \left(\frac{M}{Re}\right)_S \quad (57)$$

While the foregoing parameters would aid in establishing test simulation, a satisfactory scaling law has not been successful for two phenomena: chemical kinetics in the nozzle or plume flow field and particle flow effect although the latter is not relevant to the candidate liquid propellant systems discussed in this report.

## Section IV

### CONCLUSIONS AND RECOMMENDATIONS

The modified Chapman-Korst theory developed during this study provides a simplified numerical-interpolation scheme to predict local plume-induced separated flow properties within a narrow region along the chord of a lifting reentry vehicle surface during aerocruise maneuver. By coupling with cross-flow boundary layer analysis, the plume effects on LRV aerodynamic characteristics can be evaluated. Although sample calculations have disclosed results consistent with anticipated trends and in agreement with limited data, semiempiricism inherent in the analysis has precluded a wide applicability of this method due to the lack of sufficient data. Hence, in any future study the experimental aspect must receive the immediate attention after which further theoretical improvement can be instituted.

On the basis of the discussions concerning theory development and a critical assessment of the analytical model in the preceding sections, it is recommended that the following tasks constitute the bulwark of any future study on plume-induced flow separation:

#### a. Experimental Phase

- (1) Plateau Pressure. Perform systematic surface pressure measurements for a wide variety of freestream flow conditions so as to permit development of an adequate plateau pressure (or average separation pressure) formula.
- (2) Visual Observation. Employ the oil flow method to determine surface separation pattern; use schlieren and/or shadowgraph techniques to provide further observation of flow separation.
- (3) Temperature Measurement. Provide information for evaluation of temperature and surface heat transfer characteristics within the separation region.
- (4) Exhaust Plume Properties. Compare predicted and observed exhaust plume configurations in order to evaluate the validity of the simple constant  $\gamma$  model and to gain confidence in plume and nozzle flow, predictions involving flow separation upstream of base region. Different propellant systems (thus varying the combustion temperature, the specific-heat ratio, etc.) should be used to gain better insight.
- (5) Configuration Effect. Use different configurations, such as those with fins and flaps, to accrue knowledge on three-dimensional flow phenomena and to permit generalization of the theory.
- (6) Simulation Parameters. To aid in the experimental study, a set of simulation parameters can be defined to carry out a meaningful wind-tunnel test program. These parameters are discussed in the preceding section.

b. Theoretical Phase

- (1) Nash Factor. Evaluate this reattachment correction factor in terms of free-stream flow variables so that further mathematical refinement of the separated flow analysis need not be pursued. Introduction of the empirically determined Nash factor permits approximate description of the plume-induced separation phenomena by means of the pseudo-two-dimensional model. For example, Appendix I shows that the hypothesis of Nash factor of 0.56 is necessary to solve the delta slab problem. The non-unity Nash factor represents an overall correction of cross-flow mass diffusion and other complex flow phenomena that characterize the delta slab flow separation.
- (2) Rarefied Gas and Hypersonic Flow Effects. Perform a systematic analysis on the phenomena of boundary layer growth, its interaction with the inviscid stream, and the ensuing effects on plume-induced flow separation under hypersonic and/or rarefied gas conditions.
- (3) Vortex Generation. Determine the leading-edge vortex generation effect on plume-induced flow separation. The LRV vortex problem is three-dimensional in character, since it is strongly dependent on the angle of attack (also yaw or roll motion) and the leading edge geometry. Attention should be directed to engineering prediction, such as estimation of separation wedge angle and size upon encounter of vortex sheets in the flow field.

**Appendix I**  
**PLUME-INDUCED BOUNDARY LAYER SEPARATION\***  
**By M. C. Fong**

The basic assumptions for the modified Chapman-Korst model to predict plume-induced separated flow characteristics are recapitulated as follows:

- The inviscid flow properties upstream of the separation point are known a priori.
- The flow is two-dimensional or axisymmetric. On a lifting reentry vehicle surface, the flow is considered to be locally two-dimensional with respect to a particular streamline (pseudo-two-dimensional).
- The flow separation is either pure laminar (Chapman) or fully developed turbulent (Korst).
- The average flow velocity within the separation region is very low (dead air) and the average pressure therein can be represented by the plateau pressure.
- The Prandtl number and the Schmidt number are unity, thereby rendering the generalized Crocco relation valid.
- In the dead-air region, an average temperature and a fuel-to-air ratio can be defined.

---

\*The basic analytical model was developed during a Navy-sponsored study under Contract N0003066C0186 but modified and improved during the present study as well as during preparation of the technical proposal for this study contract. This appendix represents an improved version of Reference 41.

As described in considerable detail in the text, the unknown parameters associated with plume-induced flow separation are:

- Separation location,  $X_s$
- Base pressure,  $P_B$
- Base temperature,  $T_B$
- Base species concentration,  $Y_B$
- Dividing streamline location,  $\eta_{je}$
- Discriminating streamline location,  $\eta_{se}$

from which six conditions are required to ascertain these unknown functions. As proposed herein, the required conditions are provided by a set of integral equations representing conservation of fluxes within the separation region, supplemented by an appropriate plateau pressure correlation formula and a reattachment criterion, viz.,

- Semiempirical formula correlating  $P_B$  with  $X_s$
- Dividing streamline determination
- Conservation of total mass flux
- Conservation of energy flux
- Conservation of mass flux for individual species
- Reattachment criterion – Comparison of the total pressure along the discriminating streamline with the static pressure in the trailing shock system.

This appendix discusses these integral equations and supplementary conditions with emphasis on detailed mathematical formulation and calculated procedure.

## 1. ANALYTICAL PROCEDURE.

Before step-by-step calculation procedure is discussed, several useful concepts and definitions are summarized here for clarity and convenience of discussion:

- A dividing (separating) streamline is the streamline which separates the integrated mass flux upstream of the separation point from the mass entrained in the separation region (Fig. I-1).
- A discriminating (limiting) streamline is the streamline which contains just sufficient kinetic energy to overcome the trailing shock pressure and enters the compression zone.
- If the initial boundary layer thickness is finite, an equivalent origin based on the "origin shift" model for re-establishing self-similar shear layer is used. At the equivalent origin, the mass and momentum fluxes are the same as that at the actual separation point (Refs. 35 and 36). The origin shift coordinates are found to be

$$\left. \begin{aligned} x_o &= \frac{\delta^{**2}}{26} \frac{\rho_e u_e}{\mu_e} \\ y_o &= \delta^* + \delta^{**} \end{aligned} \right\} \text{(laminar)} \quad (\text{I-1})$$

$$\left. \begin{aligned} x_o &= \sigma \delta^{**} / \int_{-\infty}^{\eta} \left( \frac{\rho}{\rho_o} \right) \varphi(1 - \varphi) d\eta \\ y_o &= \delta^* + \delta^{**} \end{aligned} \right\} \text{(turbulent)} \quad (\text{I-2})$$

where  $\delta^*$  is the displacement thickness,  $\delta^{**}$  is the momentum thickness,  $\varphi$  is the turbulent velocity profile and  $\eta = \sigma y/x$  is a transformed  $y$  coordinate.

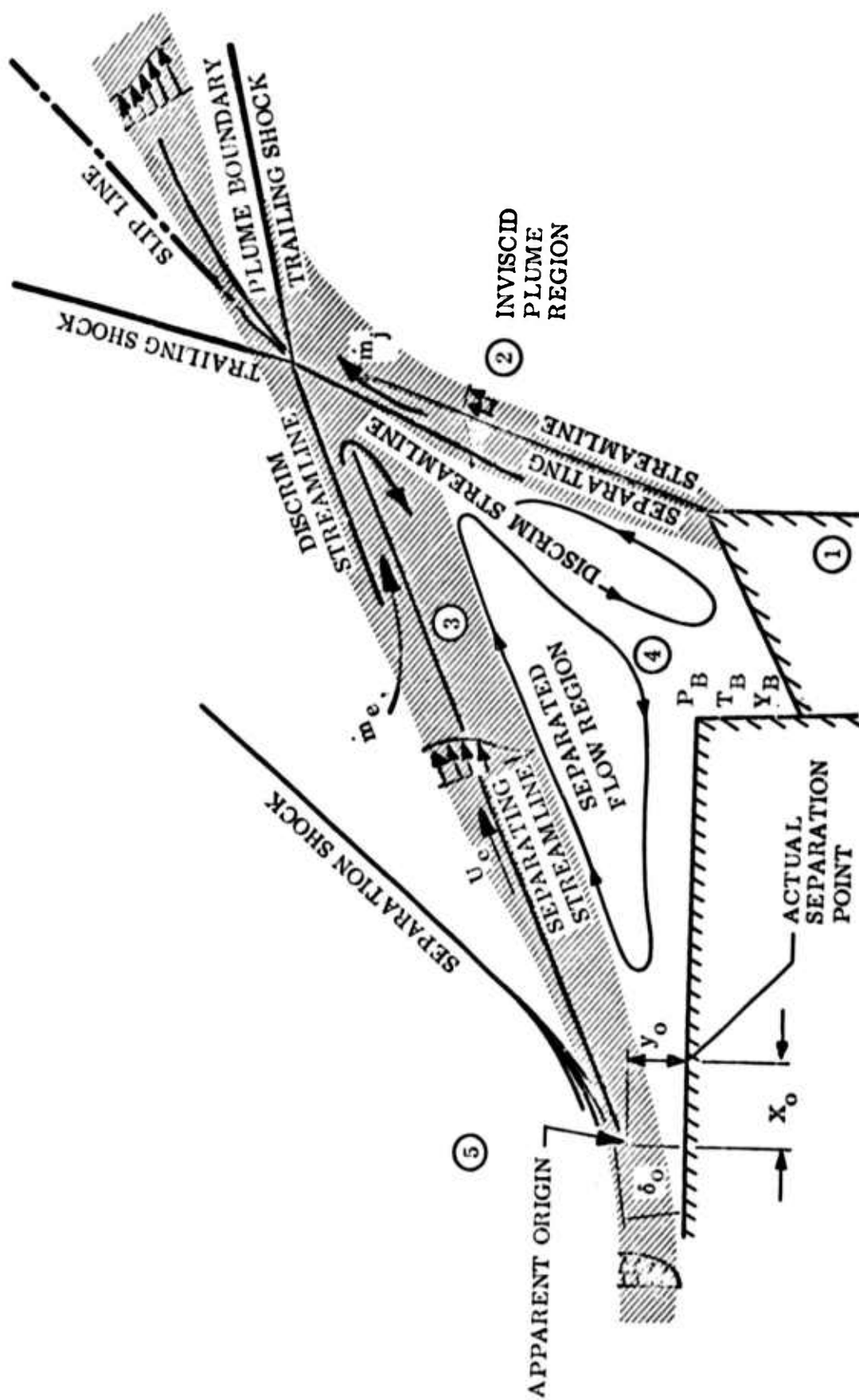


Figure I-1 Plume-Induced Separation

With the assumptions listed above, the complex flow field can be considerably simplified. A further simplification in this analysis requires that the separated flow field be either pure laminar or fully developed turbulent. Specifically, the shear layer on the plume side is assumed to be always fully developed turbulent; on the other hand, because of high-altitude cases under consideration, the streamside shear layer is regarded as invariably laminar.

For laminar separation, the governing momentum differential equation for the shear layer can be represented by a Blasius-type equation:

$$\rho \left( u \frac{\partial u}{\partial x} + v \frac{\partial u}{\partial y} \right) = \frac{\partial}{\partial y} \left( \mu \frac{\partial u}{\partial y} \right) \quad (\text{I-3})$$

where  $x$  and  $y$  are oriented along the separation wedge, and the boundary conditions are

$$u = u_e \quad \text{for } y = \infty \quad (\text{I-4})$$

$$\text{and } u = v = 0 \quad \text{for } y = -\infty$$

The Lees-Dorodnitsyn and Mangler transformations are employed to modify the governing differential equations, i.e.,\*

$$\left. \begin{aligned} s(x) &= \int_0^x \rho_e \mu_e u_e r^{2\epsilon} (x) dx \\ \zeta(s, y) &= \frac{\rho_e u_e r^\epsilon}{\sqrt{2s}} \int_0^y \frac{\rho}{\rho_e} dy \end{aligned} \right\} \quad (\text{I-5})$$

\*The symbol  $\zeta$  is introduced here to avoid confusion with the turbulent transformation variable,  $\eta$ . In the text, however,  $\eta$  is used for both laminar and turbulent cases.



Also, a similarity function is defined as follows:

$$f'(\xi) = \varphi = \frac{u}{u_e} \quad (\text{I-6})$$

where  $\epsilon = 0$  for two dimensional flow and  $\epsilon = 1$  for axisymmetric flow. The resulting equation is of the form

$$f''' + ff'' = 0 \quad (\text{I-7})$$

for which the solution is presented in Figure 34 and expressed in numerical form in Equation (15) in Section II.

For turbulent separation, the momentum equation is linearized in accordance with the Korst model (Ref. 27) to become

$$u \frac{\partial u}{\partial x} = E \frac{\partial^2 u}{\partial y^2} \quad (\text{I-8})$$

where  $E$  is an eddy viscosity parameter and boundary conditions similar to that of Equation (I-4) can be established.

For zero initial boundary layer thickness, an error function solution will result (Equation 16), i.e.,

$$\frac{u}{u_e} = \frac{1}{2} \left[ 1 + \operatorname{erf} \left( \frac{\sigma y}{x} \right) \right] \quad (\text{I-9})$$

Following the calculation procedures discussed in References 40 and 41, the plume-induced separated flow characteristics are determined by the following steps:

1. A separation point is assumed. From given initial flow conditions and by invoking the compression surface analogy, the plateau pressure within the

plume-induced separation region can be obtained from Equation 28 in the main text (laminar separation only), i.e.,

$$C_{P_B} = C_{P_P} = A (M_o^2 - 1)^{-1/4} Re_o^{-1/4} \quad (I-10)$$

where the appropriate "A" value, though not yet firmly established, is presented in Equation (21). Equation (I-10) correlates  $P_B$  with the Mach number and Reynolds number at the separation point. Because of the 1/4th power for the exponent,  $P_B$  is generally not sensitive to the different assumed values of  $X_S$ .

2. Based on the plateau (base) pressure, a separation wedge emanating from the equivalent origin can be defined from which the local outer-edge flow properties are determined (Fig. I-1). For example, the wedge angle, the separation shock, etc. can be evaluated. Tentatively, a wedge model is used; modifications will be made, should future data disclose contrary evidence.
3. The exhaust plume contour and pertinent flow properties are determined based on the plateau pressure (effective ambient pressure) and the MOC solution. The dead-air hypothesis permits the plume definition under quiescent flow conditions.
4. From the interaction between the separation wedge and the exhaust plume contour, a trailing shock system is established. The trailing shock characteristics can be ascertained by means of the usual compressible stream interaction considerations. Although viscous shear layers are assumed to develop along both the separation wedge and the plume contour, the intersection phenomenon refers to the inviscid stream interaction only.
5. Several values of the average base temperature,  $T_B$ , and overall fuel-air mixture ratios  $Y_B$ , in the separation region are next assumed.

6. In accordance with the generalized Crocco relation for  $Pr = 1$  and  $Sc = 1$ , the total enthalpy and species concentrations can be correlated with the velocity profile as follows:

Stream Side ( $0 < Y < Y_B$ )

$$H = (H_e - H_B) \frac{u}{u_e} + H_B \quad (I-11)$$

$$Y = Y_B \left(1 - \frac{u}{u_e}\right) \quad (I-12)$$

Plume Side ( $Y_B < Y < 1$ )

$$H = (H_j - H_B) \frac{u}{u_j} + H_B \quad (I-13)$$

$$Y = (1 - Y_B) \frac{u}{u_j} + Y_B \quad (I-14)$$

where the fuel-air mixture ratio,  $Y$ , has the same value as the hydrogen elemental mass fraction for the present problem, i.e.,  $Y_j = 1$  and  $Y_e = 0$ .

7. A number of gas properties needed for the iteration process are defined as follows:

$$c_p = Yc_{p_j} + (1 - Y) c_{p_e} \quad (I-15)$$

or

$$c_p = c_{p_B} + (c_{p_e} - c_{p_B}) \frac{u}{u_e} \quad (\text{Stream Side}) \quad (I-15a)$$

$$c_p = c_{p_B} + (c_{p_j} - c_{p_B}) \frac{u}{u_j} \quad (\text{Plume Side}) \quad (I-15b)$$

$$R = R \left( \frac{Y}{m_j} - \frac{1-Y}{m_e} \right) \quad (I-16)$$

where equivalence of Equations (I-15), (I-15a), and (I-15b) can be easily verified with the aid of Equations (I-12) and (I-14).

$$\frac{T}{T_e} = \frac{1 - \frac{c_{p_e}}{c_p} \varphi^2 C_{r_e}^2}{1 - C_{r_e}^2} + \frac{\left(\frac{T_{t_B}}{T_{t_e}} - 1\right) (1 - \varphi)}{1 - C_{r_e}^2} \quad (\text{I-17})$$

(Stream side)

$$\frac{T}{T_j} = \frac{1 - \frac{c_{p_j}}{c_p} \varphi^2 C_{r_j}^2}{1 - C_{r_j}^2} + \frac{\left(\frac{T_{t_B}}{T_{t_j}} - 1\right) (1 - \varphi)}{1 - C_{r_j}^2} \quad (\text{I-18})$$

(Plume side)

where  $c_{p_e}/c_p$  and  $c_{p_j}/c_p$  are obtained from Equations (I-15a) and (I-15b), and  $C_r$  is the Crocco number defined as

$$C_r^2 = \frac{\gamma - 1}{2} M^2 / \left(1 + \frac{\gamma - 1}{2} M^2\right) \quad (\text{I-19})$$

8. Several values of discriminating streamlines are then assumed. The Mach number along each external discriminating streamline is computed from

$$M_{s_e} = \frac{\varphi_{s_e} M_e}{\sqrt{\frac{\gamma_{s_e} R_{s_e} T_{s_e}}{\gamma_e R_e T_e}}} \quad (\text{I-20})$$

and the stagnation pressure ratio is determined by

$$\left(\frac{P_t}{P}\right)_{s_e} = \left(1 + \frac{\gamma_{s_e} - 1}{2} M_{s_e}^2\right)^{\gamma_{s_e}/(\gamma_{s_e} - 1)} \quad (\text{I-21})$$

Similarly, on the plume side, we have

$$M_{s_j} = \frac{\varphi_{s_j} M_j}{\sqrt{\frac{\gamma_{s_j} R_{s_j} T_{s_j}}{\gamma_j R_j T_j}}} \quad (I-22)$$

and

$$\left(\frac{P_t}{P}\right)_{s_j} = \left(1 + \frac{\gamma_{s_j} - 1}{2} M_{s_j}^2\right)^{\gamma_{s_j}/(\gamma_{s_j} - 1)} \quad (I-23)$$

Thus, for each value of assumed external discriminating streamline, there is a corresponding plume discriminating streamline where

$$\left(\frac{P_t}{P}\right)_{s_e} = \left(\frac{P_t}{P}\right)_{s_j} \quad (I-24)$$

Because of Equation (I-24), only one discriminating streamline, say the stream-side one, needs to be introduced explicitly.

9. To express the definition of dividing streamline mathematically, the total mass and momentum balances between the initial point and any downstream location (for zero initial boundary layer thickness) are:

$$\rho_e u_e y_o = \int_{y_{je}}^{\infty} \rho u dy \quad (I-25)$$

$$\rho_e u_e^2 y_o = \int_{-\infty}^{\infty} \rho u^2 dy \quad (I-26)$$

from which the following equation results

$$\int_{-\infty}^{y_j} \frac{\rho u^2}{\rho_e u_e^2} dy - \int_{y_j}^{\infty} \frac{\rho u}{\rho_e u_e} \left(1 - \frac{u}{u_e}\right) dy = 0 \quad (I-27)$$

Now consider an arbitrary streamline K, it is obtained that

$$\begin{aligned} \frac{\dot{m}_k}{r^\epsilon} &= \int_{y_j}^{y_k} \rho u dy = \rho_e u_e \left[ \int_{-\infty}^{y_k} \frac{\rho u}{\rho_e u_e} dy - \int_{-\infty}^{y_j} \frac{\rho u}{\rho_e u_e} dy \right] \\ &= \rho_e u_e \left[ \int_{-\infty}^{y_k} \frac{\rho u}{\rho_e u_e} dy - \int_{-\infty}^{y_j} \frac{\rho u}{\rho_e u_e} \left(1 - \frac{u}{u_e}\right) dy - \int_{-\infty}^{y_j} \frac{\rho u^2}{\rho_e u_e^2} dy \right] \\ &= \rho_e u_e \left[ \int_{-\infty}^{y_k} \frac{\rho u}{\rho_e u_e} dy - \int_{-\infty}^{\infty} \frac{\rho u}{\rho_e u_e} \left(1 - \frac{u}{u_e}\right) dy \right] \quad (I-28) \end{aligned}$$

Hence, along the dividing streamline,  $y_k = y_j$  and  $\dot{m}_k = 0$ , Equation (I-28) becomes

$$\frac{\dot{m}_j}{r^\epsilon} = \int_{-\infty}^{y_i} \frac{\rho u}{\rho_e u_e} dy = \int_{-\infty}^{\infty} \frac{\rho u}{\rho_e u_e} \left(1 - \frac{u}{u_e}\right) dy \quad (I-29)$$

Equation (I-29) is applicable to both laminar and turbulent flows. For a given problem where the velocity profile is known and proper coordinate transformation is implemented, the dividing streamline location  $y_j$  can be ascertained uniquely:

#### Laminar

$$\int_{-\infty}^{\xi_{je}} f'(\xi) d\xi = \int_{-\infty}^{\infty} f'(\xi) [1 - f'(\xi)] d\xi \quad (I-30)$$

#### Turbulent

$$\int_{-\infty}^{\eta_{jj}} \frac{\varphi}{\Lambda - C_{ra}^2 \varphi^2 \left( \frac{\gamma - 1}{\gamma_a - 1} \right)} d\eta = \int_{-\infty}^{\infty} \frac{\varphi - \varphi^2}{\Lambda - C_{ra}^2 \varphi^2 \left( \frac{\gamma - 1}{\gamma_a - 1} \right)} d\eta \quad (I-31)$$

in which the denominator contains the transformed density ratio as follows:

$$\frac{\rho}{\rho_a} = \frac{1 - C_{ra}^2}{\Lambda - C_{ra}^2 \varphi^2 \left( \frac{\gamma - 1}{\gamma_a - 1} \right)} \quad (I-32)$$

In deriving Equation (I-32), the definition of  $C_r$  (Eq. (I-19)) and the following supplementary expressions are used:

$$\frac{\gamma - 1}{2} M^2 = \frac{C_r^2}{1 - C_r^2}, \quad 1 + \frac{\gamma - 1}{2} M^2 = \frac{1}{1 - C_r^2}$$

and

$$1 + \frac{\gamma - 1}{2} M^2 = 1 + \frac{\gamma_a - 1}{2} M_a^2 \varphi^2 \left( \frac{\gamma - 1}{\gamma_a - 1} \right)$$



now

$$\begin{aligned}
 \frac{T_{ta}}{T_t} &= \frac{T_a}{T} \frac{1 + \frac{\gamma_a - 1}{2} M_a^2}{1 + \frac{\gamma - 1}{2} M^2} \\
 &= \frac{T_a}{T} (1 - C_{ra}^2)^{-1} \left[ 1 + \frac{\gamma_a - 1}{2} M_a^2 \varphi^2 \frac{R_a T_a}{RT} \left( \frac{\gamma - 1}{\gamma_a - 1} \right) \right]^{-1} \\
 &= \frac{T_a}{T} \left[ (1 - C_{ra}^2) + C_{ra}^2 \varphi^2 \frac{R_a T_a}{RT} \left( \frac{\gamma - 1}{\gamma_a - 1} \right) \right]^{-1}
 \end{aligned}$$

from which  $T_a/T$  can be expressed in terms of  $T_{ta}/T_t$  as follows:

$$\frac{T_a}{T} = (1 - C_{ra}^2) \frac{T_{ta}}{T_t} \left[ 1 - C_{ra}^2 \varphi^2 \frac{R_a T_{ta}}{RT_t} \left( \frac{\gamma - 1}{\gamma_a - 1} \right) \right]^{-1}$$

hence

$$\frac{\xi}{\xi_a} = \frac{R_a T_a}{RT} = \frac{\frac{R_a T_{ta}}{RT_t} (1 - C_{ra}^2)}{1 - C_{ra}^2 \varphi^2 \frac{R_a T_{ta}}{RT_t} \left( \frac{\gamma - 1}{\gamma_a - 1} \right)}$$

which leads to Equation (I-32) by substituting  $\Lambda = \frac{RT_t}{R_a T_{ta}}$

10. For conservation of mass flux per unit width, it is asserted that the mass flux above the discriminating streamline can enter the trailing shock system. For example, on the stream side, we obtain

$$\dot{m}_s' = r^\epsilon \int_{y_{se}}^{\infty} \rho u \, dy = r^\epsilon \left[ \int_{y_{se}}^{y_{je}} \rho u \, dy + \int_{y_{je}}^{\infty} \rho u \, dy \right] \quad (I-33)$$

Similarly, on the plume side

$$\dot{m}_j = \int_{y_{sj}}^{y_{jj}} \rho u \, dy + \int_{y_{jj}}^{\infty} \rho u \, dy \quad (\text{I-34})$$

For a steady-state solution, mass flux conservation requires that the sum of  $\dot{m}_s$  and  $\dot{m}_j$  be equal to the total flux entering the separation region plus mass bleed if it exists. In other words,

$$\dot{m}_s + \dot{m}_j = \dot{m}_{je} + \dot{m}_{jj} + \dot{m}_B = \sum \int_{y_s}^{y_j} \rho u \, dy + \dot{m}_{je} + \dot{m}_{jj}$$

which results in

$$r \epsilon \int_{y_{se}}^{y_{je}} \rho u \, dy + \int_{y_{sj}}^{y_{jj}} \rho u \, dy = \dot{m}_B \quad (\text{I-35})$$

This equation exhibits a mass corridor as if the flow were entering in and exiting from a corridor bounded by the dividing streamline and the discriminating streamline (Fig. I-1). As a corollary, it is seen that for the ordinary base flow problem (no jet plume and no base bleed),

$$\int_{y_{se}}^{y_{je}} \rho u \, dy = 0 \quad (\text{I-36})$$

indicating that the dividing streamline and the discriminating streamline are coincident.

In terms of transformed coordinates, the mass flux integrals can be expressed as:

• For the laminar stream shear layer

$$\begin{aligned} \frac{\dot{m}_{se}}{r^\epsilon} &= \int_{y_{je}}^{y_{se}} \rho u \, dy = \rho_e u_e \left[ \int_{-\infty}^{\infty} \frac{\rho u^2}{\rho_e u_e^2} \, dy - \int_{-\infty}^{y_{je}} \frac{\rho u}{\rho_e u_e} \, dy \right] \\ &= \rho_e u_e \left[ \int_{-\infty}^{y_{se}} \frac{\rho u}{\rho_e u_e} \, dy - \int_{-\infty}^{\infty} \frac{\rho u}{\rho_e u_e} \left(1 - \frac{u}{u_e}\right) \, dy \right] \end{aligned} \quad (I-29)$$

$$\begin{aligned} &= \rho_e u_e \left[ \int_{-\infty}^{\infty} \frac{\rho u^2}{\rho_e u_e^2} \, dy - \int_{y_s}^{\infty} \frac{\rho u}{\rho_e u_e} \, dy \right] \\ &= \frac{\sqrt{2s}}{r^\epsilon} F_1(\zeta_{je}, \zeta_{se}) = \frac{\sqrt{2s}}{r^\epsilon} \left[ \int_{-\infty}^{\infty} f'^2 \, d\zeta - \int_{\zeta_s}^{\infty} f' \, d\zeta \right] \end{aligned} \quad (I-37)$$

where

$$F_1(\zeta_{je}, \zeta_{se}) = \int_{\zeta_{je}}^{\zeta_{se}} f' \, d\zeta \quad (I-38)$$

• For the turbulent plume shear layer

$$\begin{aligned} \dot{m}_j &= \int_{y_{jj}}^{y_{sj}} \rho u \, dy = \frac{\rho_j u_j x_j}{\sigma_j} \int_{\eta_{jj}}^{\eta_{sj}} \frac{(1 - C_{rj})^2 \varphi}{\Lambda - C_{rj}^2 \varphi^2 \left( \frac{\gamma_j - 1}{\gamma_j - 1} \right)} \, d\eta \\ &= \frac{\rho_j u_j x_j}{\sigma_j} I_1(\eta_{ij}, \eta_{sj}) \end{aligned} \quad (I-39)$$

where  $\Lambda = (R T_t / R_a T_{t_a})$ ,  $\varphi = (u/u_e)$ , subscript a indicates some references state,\* and

$$I_1(\eta_a, \eta_b) = \int_{\eta_a}^{\eta_b} \frac{(1 - C_{r_a}^2)}{\Lambda - C_{r_a}^2 \varphi^2 \left( \frac{\gamma - 1}{\gamma_a - 1} \right)} d\eta \quad (I-40)$$

The total mass conservation then reads

$$\sum \dot{m} = \frac{2s}{r^\epsilon} F_1(\zeta_{je}, \zeta_{se}) + \frac{\rho_j u_j x_j}{\sigma_j} I_1(\eta_{jj}, \eta_{sj}) - \dot{m}_B = 0 \quad (I-41)$$

11. The total energy flux of the separation region consists of convection and conduction contributions: In the laminar case,

$$\begin{aligned} \frac{\dot{E}_e}{r^\epsilon} &= \frac{1}{r^\epsilon} (\dot{E}_{\text{conv}} + \dot{E}_{\text{cond}}) = \int_{y_{je}}^{y_{se}} \rho u H dy + \int_{y_j}^{\infty} \rho u (H_e - H) dy \\ &= \frac{\sqrt{2s}}{r^\epsilon} \left\{ \int_{\zeta_j}^{\zeta_s} f' \left[ (H_e - H_B) f' + H_B \right] d\zeta + (H_e - H_B) \int_{\zeta}^{\infty} f' (1 - f') d\zeta \right\} \quad (I-42) \end{aligned}$$

\*The same Korst velocity profile and spreading parameter are used for both two-dimensional and axisymmetric cases.

Or

$$\begin{aligned} \frac{\dot{E}_{t_e}}{r^\epsilon} = \frac{\sqrt{2s}}{r^\epsilon} & \left[ (H_e - H_B) F_2(\zeta_{j_e}, \zeta_{s_e}) + H_B F_1(\zeta_{j_e}, \zeta_{s_e}) \right. \\ & \left. + (H_e - H_B) F_1(\zeta_{j_e}, \infty) - (H_e - H_B) F_2(\zeta_{j_e}, \infty) \right] \end{aligned} \quad (I-43)$$

where the Crocco relation is used in the equations, and

$$F_2(\zeta_a, \zeta_b) = \int_{\zeta_a}^{\zeta_b} f'^2 d\zeta \quad (I-44)$$

Its turbulent counterpart is found to be

$$\begin{aligned} \dot{E}_{t_j} &= \dot{E}_{\text{conv}} + \dot{E}_{\text{cond}} \\ &= \frac{\rho_j u_j x_j}{\sigma_j} \left\{ H_B I_1(\eta_{ij}, \eta_{sj}) + (H_j - H_B) \left[ I_2(\eta_{jj}, \eta_{sj}) \right. \right. \\ &\quad \left. \left. + I_1(\eta_{jj}, \infty) - I_2(\eta_{jj}, \infty) \right] \right\} \end{aligned} \quad (I-45)$$

where

$$I_2(\eta_a, \eta_b) = \int_{\eta_a}^{\eta_b} \frac{(1 - C_{r_a}^2)}{\Lambda - C_{r_a}^2 \phi^2 \left( \frac{\gamma - 1}{\gamma_a - 1} \right)} d\eta \quad (I-46)$$

and

$$I_3(\eta_a, \eta_b) = \int_{\eta_a}^{\eta_b} \frac{(1 - C_{r_a}^2)}{\Lambda - C_{r_a}^2 \varphi^2 \left( \frac{\gamma - 1}{\gamma_a - 1} \right)} d\eta \quad (I-47)$$

The energy flux conservation thus is expressible as follows:

$$\begin{aligned} \sum \dot{E} = \frac{\sqrt{2s}}{r^\epsilon} & \left\{ H_B F_1(\zeta_{je}, \zeta_{se}) + (H_e - H_B) \left[ F_2(\zeta_{je}, \zeta_{se}) \right. \right. \\ & \left. \left. + F_1(\zeta_{je}, \infty) - F_2(\zeta_{je}, \infty) \right] \right\} \\ & + \frac{\rho_j u_j x_j}{\sigma_j} \left\{ H_B I_1(\eta_{jj}, \eta_{sj}) + (H_j - H_B) \left[ I_2(\eta_{jj}, \eta_{sj}) \right. \right. \\ & \left. \left. + I_1(\eta_{jj}, \infty) - I_2(\eta_{jj}, \infty) \right] \right\} - Q_B = 0 \quad (I-48) \end{aligned}$$

where  $Q_B$  is a base heat transfer parameter.

12. Similarly, the species conservation for laminar and turbulent shear layers are determined as follows:

$$\frac{\dot{Y}_e}{r^\epsilon} = \int_{y_{sj}}^{\infty} \rho u Y dy = \frac{\sqrt{2s}}{r^\epsilon} \left[ Y_B F_1(-\zeta_{se}, \infty) + (Y_e - Y_B) F_2(-\zeta_{se}, \infty) \right] \quad (I-49)$$

and

$$\dot{Y}_j = \int_{y_{sj}}^{\infty} \rho u Y dy = \frac{\rho_j u_j x_j}{\sigma_j} \left[ Y_B I_1 \left( -\eta_{sj}, \infty \right) + (1 - Y_B) I_2 \left( -\eta_{sj}, \infty \right) \right] \quad (I-50)$$

Inasmuch as the propellant gas/air ratio is used to represent  $Y$ , we have  $Y_e = 0$  and  $Y_j = 1$ . It follows that since the species flux at the initial stations must be equal to that flowing downstream, the following relation must be true

$$\dot{Y}_e = \dot{Y}_j = \int_{y_{sj}}^{\infty} \rho u Y_j dy = \int_{y_{sj}}^{\infty} \rho u dy = \dot{m}_j \quad (I-51)$$

In terms of transformed coordinates, we have

$$\begin{aligned} \sum \dot{Y} = \frac{\sqrt{2s}}{r^\epsilon} Y_B \left[ F_1 \left( -\xi_{se}, \infty \right) - F_2 \left( -\xi_{se}, \infty \right) \right] - \frac{\rho_j u_j x_j}{\sigma_j} I_1 \left( \eta_{jj}, \eta_{sj} \right) \\ + \frac{\rho_j u_j x_j}{\sigma_j} \left[ Y_B I_1 \left( -\infty, \eta_{sj} \right) + (1 - Y_B) I_2 \left( -\infty, \eta_{sj} \right) \right] = 0 \quad (I-52) \end{aligned}$$

In summary, equations (I-41), (I-48) and (I-52) are the conservation equations employed in this analysis for numerical computations. As stated earlier, these equations require laminar stream shear layer and turbulent plume shear layer. If both the stream side and the plume side are fully developed turbulent, the following system of integral equations are obtained:

### Mass Flux

$$\frac{\rho_e u_e x_e}{\sigma_e} I_1(\eta_{je}, \eta_{s_e}) + \frac{\rho_j u_j x_j}{\sigma_j} I_1(\eta_{jj}, \eta_{s_j}) - \dot{m}_B = 0 \quad (I-53)$$

### Energy Flux

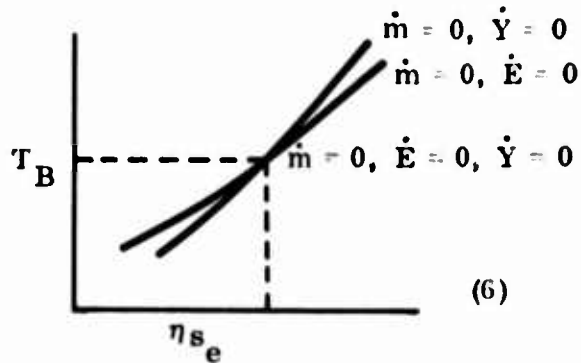
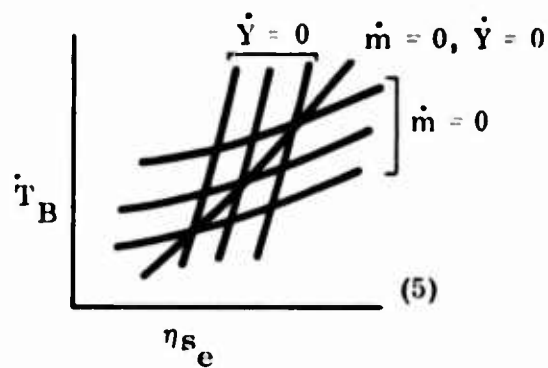
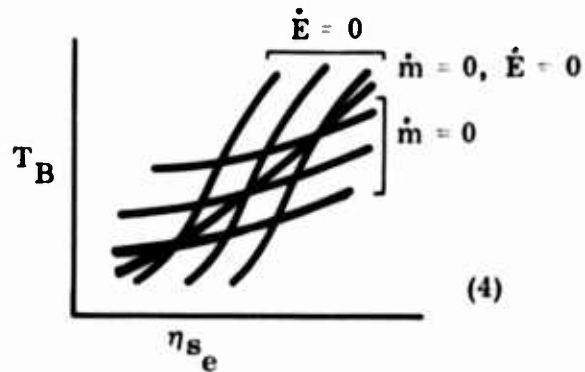
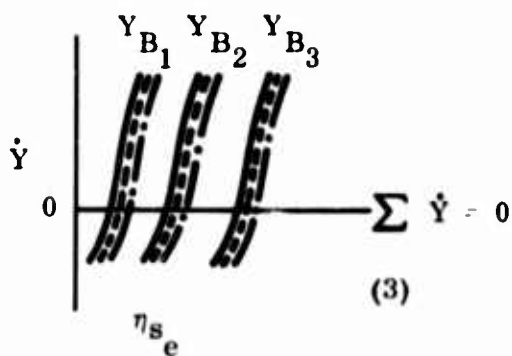
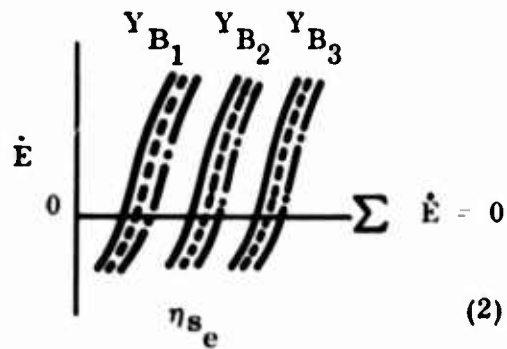
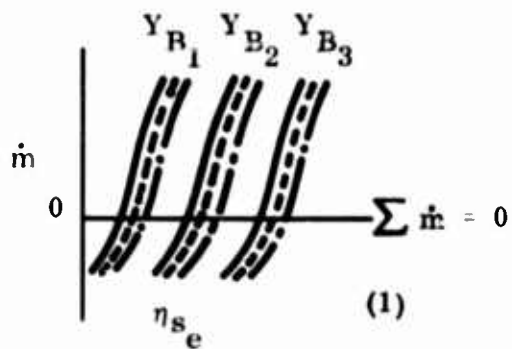
$$\begin{aligned} \sum \dot{E} = & \frac{\rho_e u_e x_e}{\sigma_e} \left\{ H_B I_1(\eta_{je}, \eta_{s_e}) + (H_e - H_B) \left[ I_2(\eta_{je}, \eta_{s_e}) + I_1(\eta_{je}, \infty) \right] \right\} \\ & + \frac{\rho_j u_j x_j}{\sigma_j} \left\{ H_B I_1(\eta_{jj}, \eta_{s_j}) + (H_j - H_B) \left[ I_2(\eta_{jj}, \eta_{s_j}) + I_1(\eta_{jj}, \infty) - I_2(\eta_{jj}, \infty) \right] \right\} - Q_B = 0 \end{aligned} \quad (I-54)$$

### Species Concentration

$$\begin{aligned} \sum \dot{Y} = & \frac{\rho_e u_e x_e}{\sigma_e} Y_B \left[ I_1(-\eta_{s_e}, \infty) - I_2(-\eta_{s_e}, \infty) \right] - \frac{\rho_j u_j x_j}{\sigma_j} I_1(\eta_{jj}, \eta_{s_j}) \\ & + \frac{\rho_j u_j x_j}{\sigma_j} \left[ Y_B I_1(-\infty, \eta_{s_j}) + (1 - Y_B) I_2(-\infty, \eta_{s_j}) \right] = 0 \end{aligned} \quad (I-55)$$

13. For a given  $P_B$  and several assumed values of  $T_B$  (or  $H_B$ ),  $Y_B$ , and  $\eta_{s_e}$ , the calculated results of mass flow, energy flux, and species concentration can be presented graphically, as depicted in Figure I-2. Cross-plotting the intersection points will permit interpolation of these results to ascertain the desired values of  $T_B$ ,  $Y_B$ , and  $\eta_{s_e}$  for which the conservation requirements,  $\sum \dot{m} = 0$ ,  $\sum \dot{E} = 0$ , and  $\sum \dot{Y} = 0$  are fulfilled; that is, Equations (I-41), (I-48), and (I-52) or Equations (I-53) through (I-55) are satisfied.





—  $T_{B1}; Y_{B1}, Y_{B2}, Y_{B3}$   
 - - -  $T_{B2}; Y_{B1}, Y_{B2}, Y_{B3}$   
 - · -  $T_{B3}; Y_{B1}, Y_{B2}, Y_{B3}$

NOTE:  $Y_B$  IS DETERMINED IN THE SAME MANNER

Figure I-2 Interpolation Scheme for Determination of  $T_B$  and  $Y_B$

Since the gas mixture in the separation region is chemically reacting, the separated flow parameters,  $T_B$ ,  $Y_B$ , etc., predicted by the foregoing procedure, must be compatible with the thermochemical results. For example, if chemical equilibrium prevails, then the predicted  $T_B$  and  $Y_B$  should, within the accuracy of the numerical method, agree with that by means of the NASA-Lewis equilibrium program. Under certain conditions, such as pronounced chemical kinetics effects, additional iteration parameters, e.g.,  $c_p$  or  $\gamma$ , may have to be introduced in order to determine all the pertinent flow quantities. However, this facet has not been sufficiently explored to permit any irrevocable conclusions.

14. Following the determination of  $T_B$ ,  $Y_B$ , and  $\eta_{se}$ , the stagnation pressure along the discriminating streamline,  $P_{ts}$ , is compared with the wake pressure in the trailing shock system,  $P_w$ . The method for determining  $P_w$  is discussed in Section II and an interpolation scheme is graphically represented in Figure 41. From recent studies (Refs. 39 and 45), it has been concluded that a semiempirically obtained Nash factor is generally necessary so as to establish a good pressure correlation. The Nash factor is defined as

$$N = \frac{P_{ts} - P_B}{P_w - P_B} \quad (I-56)$$

which ranges from 0.3 to 1.0 for most practical applications. For a delta plate with triangular cross section discussed in the text,  $N = 0.56$  was found to be valid, at least for moderate Mach numbers and altitudes. Essentially, the Nash factor is devised to improve the oversimplified model in an attempt to describe the very complex separated flow mechanism, and it provides a supplemental condition for an engineering estimate of plume-induced separated flow properties. Additional experimental information is needed to define the Nash factor adequately and to establish the influence of flow conditions on this parameter.

If  $P_{ts}$  does not correlate with  $P_w$ , then a new base pressure,  $P_B$ , will have to be assigned. The iteration process from Step (1) to Step (14) will then be repeated. Pressure compatibility thus provides the final step for prediction of the flow characteristics associated with plume-induced separation.

## 2. DISCUSSION.

A computer program for UNIVAC 1108 has been developed to carry out the iteration-interpolation process for the plume-induced separated flow solution discussed above. A flow diagram for the computer program is shown in Figure I-3, and a more expedient procedure using the thermochemical compatibility requirement in place of the energy iteration is presented in Figure 42. It should be emphasized that this computer program was used in generating proper design curves so that the reader can estimate the plume-induced separation effects on LRV aerodynamic performance and stability semi-graphically. These curves refer to the separation-distance curves depicted in Figures 52 and 53.

Nevertheless, in clarifying the analytical scheme, two sample problems are presented in this appendix. The first example is that of the solution for a cone-cylinder-flare problem is presented here to demonstrate the present analytical model. The problem is in accord with a particular NASA-Langley air plume test with  $M_\infty = 4.65$ ,  $Re = 346500$ , and zero angle of attack (Ref. 2). The plume boundary was traced from the schlieren photograph; base heating and diffusion effects were neglected. On the basis of unit Nash factor, the predicted results in terms of separation point locations are depicted in Figure I-4. Good agreement between predicted and measured values is clearly indicated.

In application to problems involving thermochemical considerations, the alternate scheme based on thermochemical compatibility (Fig. 42) is employed to avoid tedious cross-plotting. Here, appropriate equilibrium thermochemical design curves are constructed independent of the separated flow analysis but utilized in conjunction with the iteration scheme through the uniqueness of  $T_B$  and  $Y_B$  under equilibrium conditions. For further clarification another sample problem is included in this appendix to exemplify the alternate computation procedure. Selected for demonstration is the simple configuration discussed in the main text (delta planform with triangular cross

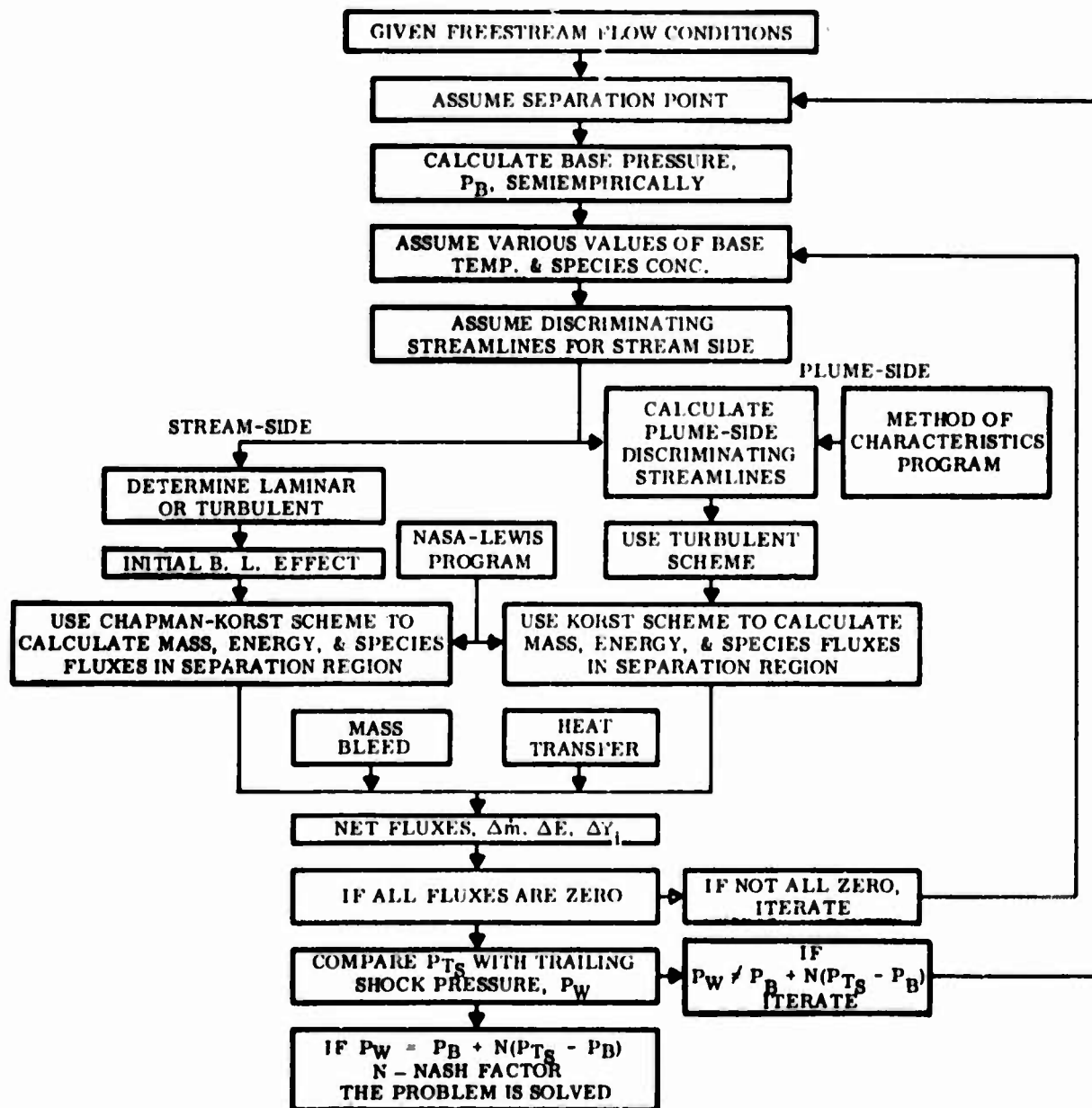


Figure I-3 Computer Flow

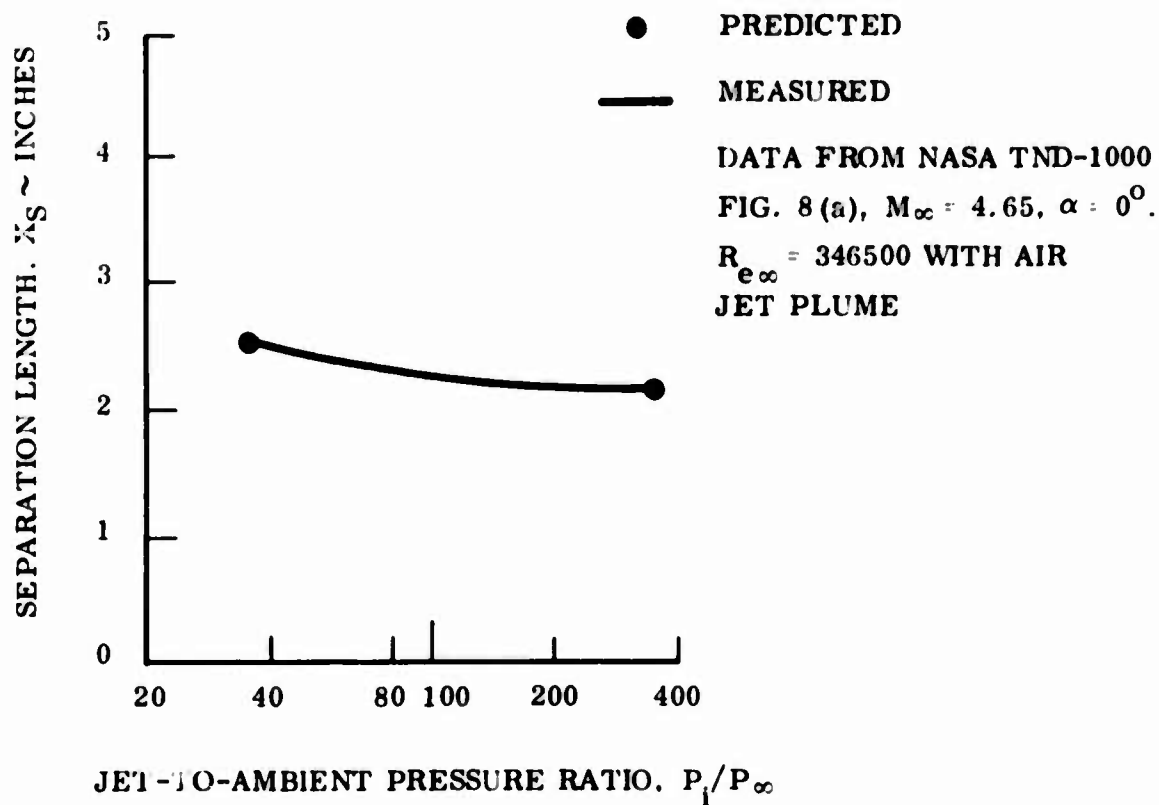
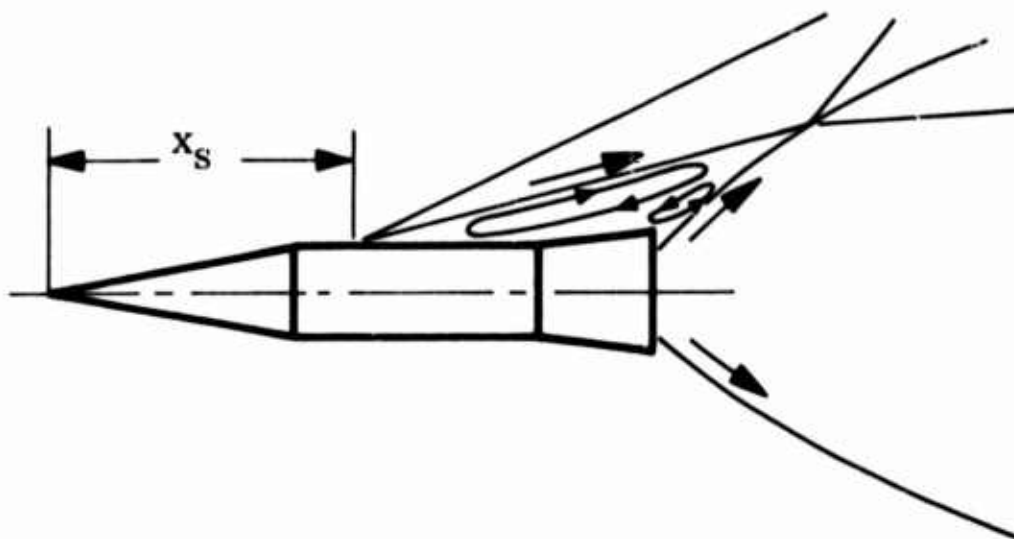


Figure I-4 Comparison of Predicted and Measured Plume-Induced Length for a Cone-Cylinder-Flare Body in Supersonic Stream

section with a length of 45 feet for the bottom delta plate), and the solution is only for that of a thin strip containing the plane of symmetry wherein the flow is assumed to be locally two-dimensional. Other requirements are:

- Windward Surface (bottom plate)
- Altitude = 250,000 feet,  $P_\infty = 0.0486$  psf
- Mach Number = 10
- Zero angle of attack;  $P_0 = P_\infty$
- Hydrogen-fluorine jet plume with  $P = 500$  psi, all other properties likewise being consistent with that discussed in the Section 2.3.1.

The step-by-step procedure with the aid of proper illustrations is as follows:

- (a) Select three separation points;  $X_g = 20, 30, \text{ and } 40$  ft from the tip
- (b) The resulting  $P_B$  based on Equations (28) and (29) in par. 5a of Section II was found to be 0.185 psf for  $x_g = 30$  ft. For simplicity, this  $P_B$  value was used for  $x_g = 20$  and 40 ft also. Because of the 1/4th-power for the denominator, no significant error would be incurred by this simplification.
- (c) Determine exhaust plume contour and other boundary properties using this  $P_B$  as the effective ambient pressure, and zero freestream velocity compatible with the dead-air hypothesis.
- (d) Assign three base temperatures:  $T_B = 3000, 5000, \text{ and } 8000^\circ\text{R}$
- (e) Carrying out plume-induced separated flow calculations. The resulting conservation equations for total mass and species fluxes for different  $X_g$  are illustrated in Figures I-5 through I-7. The intersection points satisfy both mass and species conservation requirements.
- (f) Cross-plotting  $T_B$  versus  $Y_B$  (indicated by BLSEP) and intersecting with the corresponding curve based on equilibrium thermochemical calculations (NASA-Lewis). The intersection points now satisfy mass, species, and energy conservation requirements (Fig. I-8). Thus, the proper  $Y_B$  values (fuel-air mixture ratios in the base region) are determined.

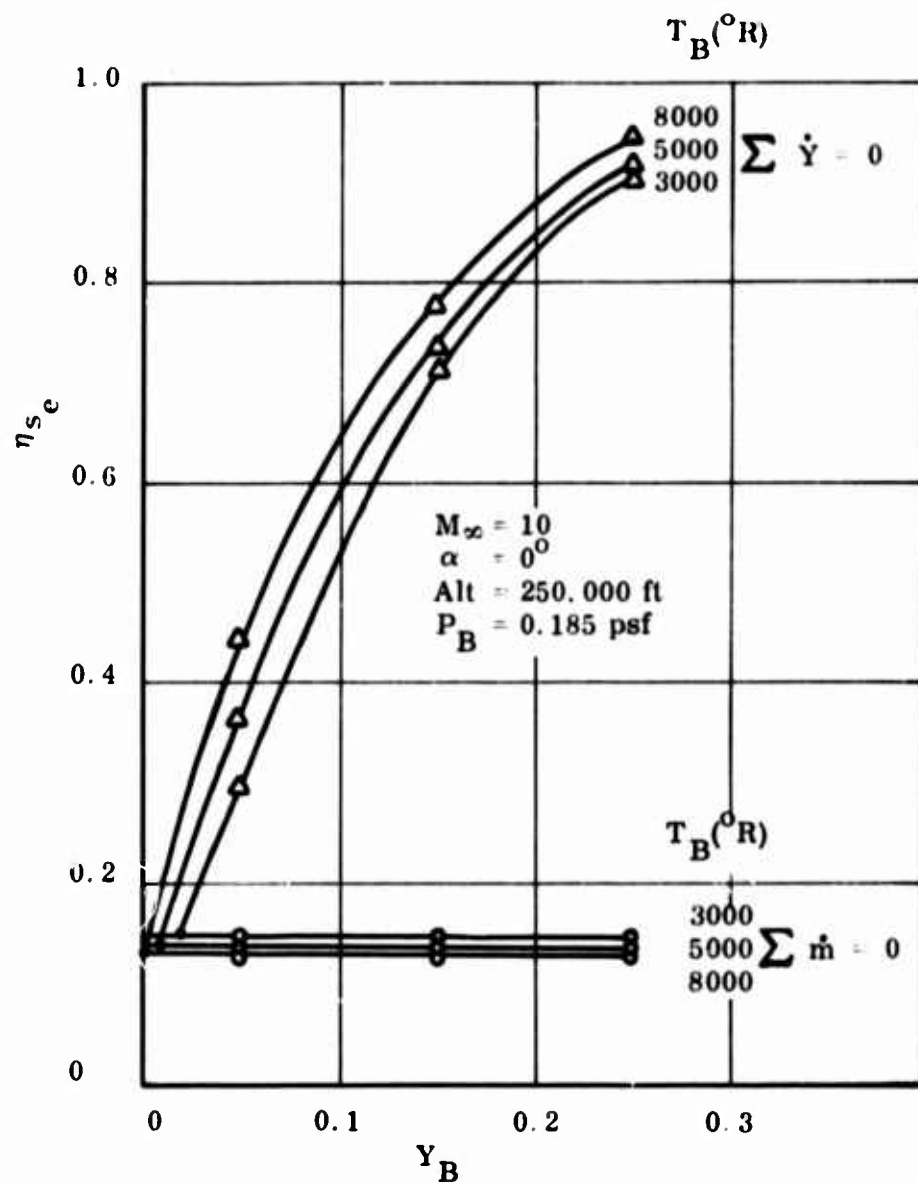


Figure I-5 Conservation of Mass and Species Fluxes for  $X_s = 20 \text{ ft}$

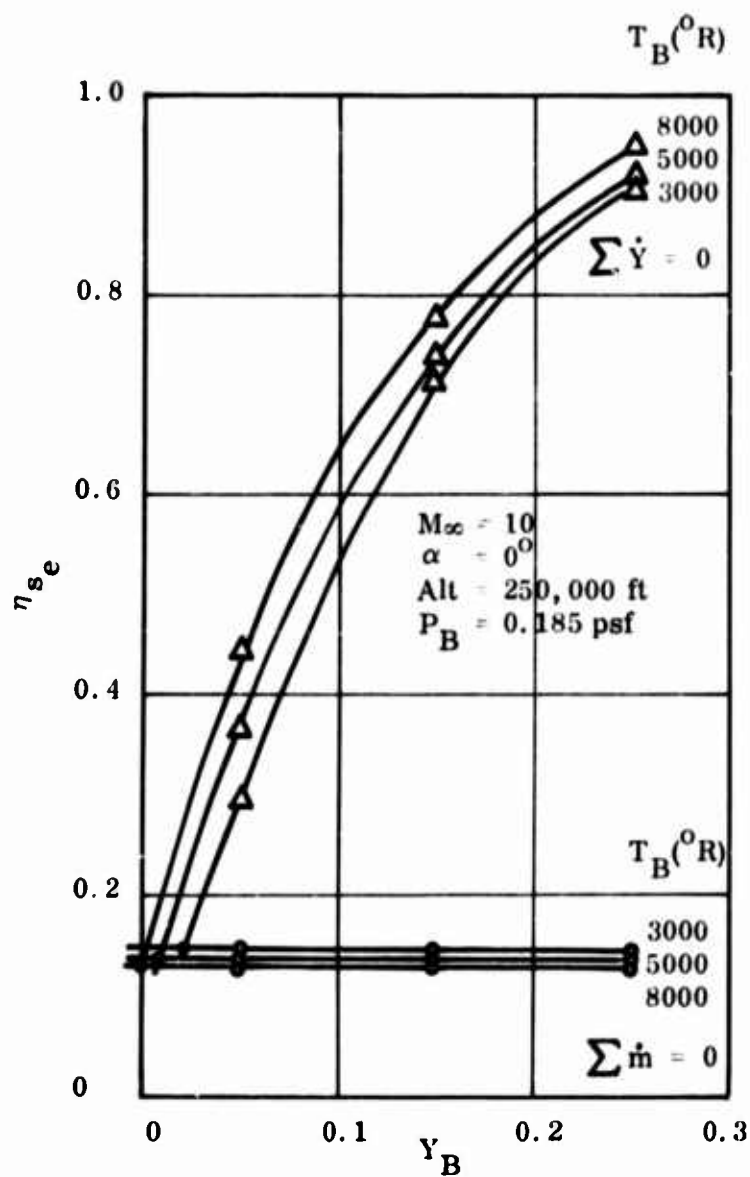


Figure I-6 Conservation of Mass and Species Fluxes for  $X_s = 30 \text{ ft}$



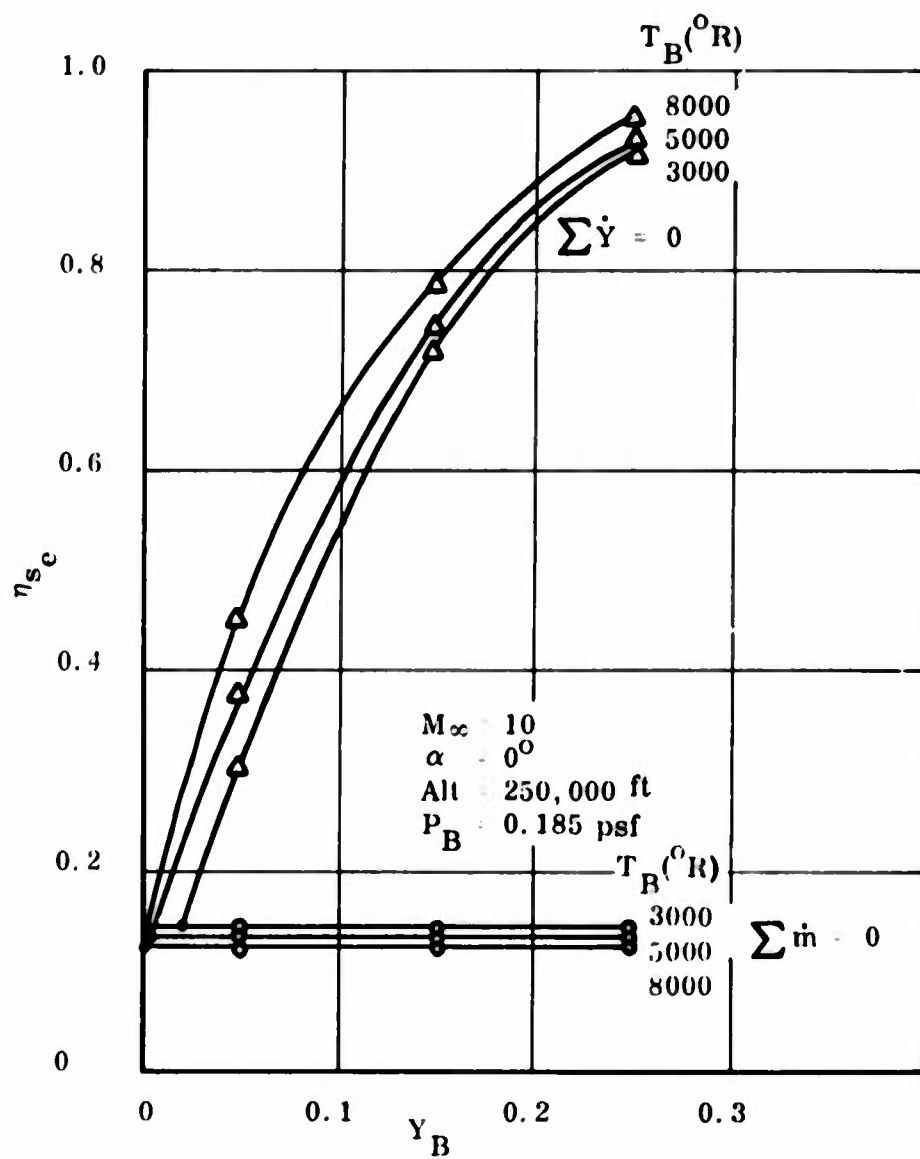


Figure I-7 Conservation of Mass and Species Fluxes for  $X_s = 40$  ft

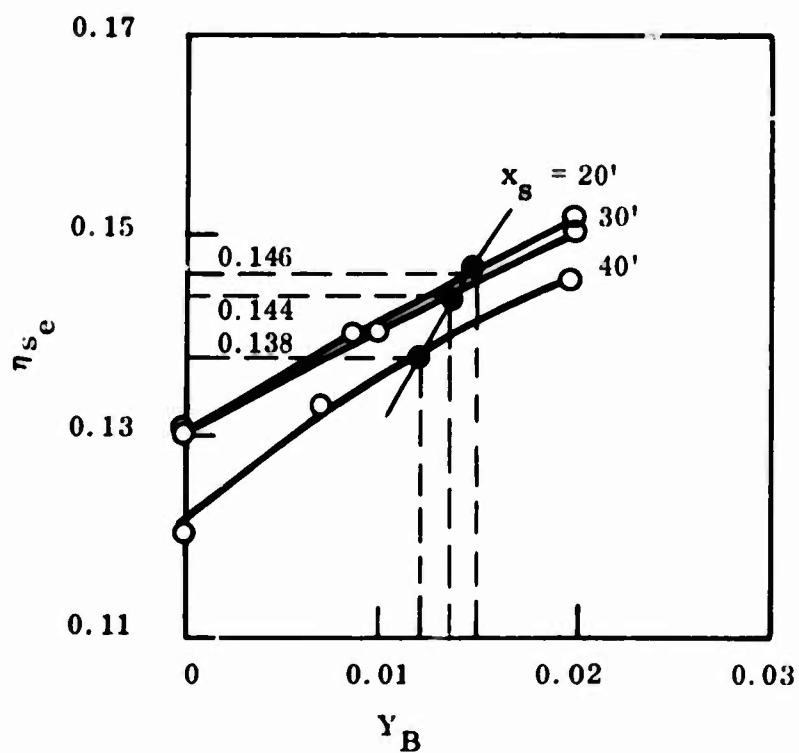
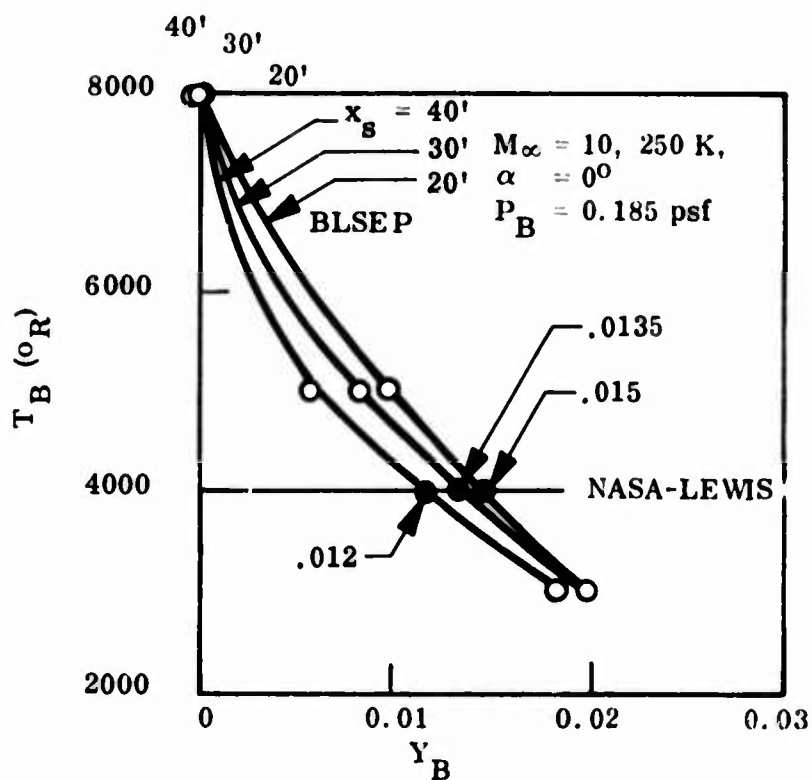


Figure I-8 Determination of  $Y_B$  and  $\eta_{s_e}$  Satisfying All Conservation Requirements

(g) The corresponding discriminating streamline locations,  $\eta_{se}$  are ascertained with additional cross-plot (Fig. I-8).

(h) Next, the discriminating streamline total pressures are plotted for various values of  $\eta_{se}$  and  $Y_B$  (Fig. I-9), resulting in the determination of the proper  $P_{ts}/P_B$  values for different  $x_s$ .

$x_s$ (ft)	$\frac{P_{ts}}{P_B}$
20	6.55
30	6.5
40	6.5

(i) Independent of the separated flow calculations, the trailing shock pressure,  $P_w$ , formed by the intersection between the stream shear layer and the plume shear layer can be determined on the basis of the classic wave interaction concept (Sec. II, Par. 5.a). The interpolation scheme and the resulting  $P_w$  for  $x_s = 20, 30$ , and 40 feet are depicted in Figure I-10. Using a Nash factor of 0.56, the following results are obtained:

$x_s$ (ft)	$\frac{P_w}{P_B}$	Calculated
		$\frac{P_{ts}}{P_B}$
20	9.6	5.8
30	10.2	6.15
40	10.9	6.55

(j) Now cross-plotting the  $P_{ts}/P_B$  values based on the shock interaction theory, a final  $P_{ts}/P_B$  is obtained. Inasmuch as this  $P_{ts}/P_B$  satisfies all the conservation requirements as well as the reattachment criterion, it represents the solution. The corresponding  $X_s$  is found to be 38.5 ft from the tip.

The plane-of-symmetry solution delineated above represents the basic plume-induced separated flow solution. Pseudo-two-dimensional solutions for other strips and a special technique to construct the separation footprint have been discussed in detail in par. 1 of Section III and will not be repeated here.

$M_\infty = 10, 250 \text{ K}, \alpha = 0^\circ$   
 $P_B = 0.185 \text{ PSF}$

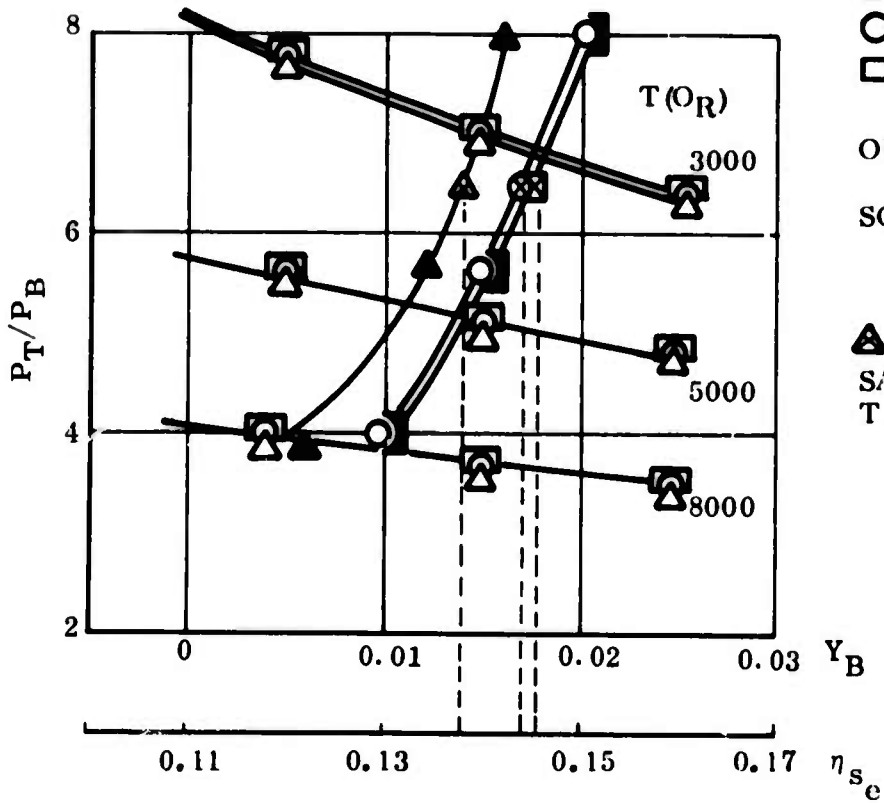
$X_S \text{ (FT)}$

$\triangle$  20  
 $\circ$  30  
 $\square$  40

OPEN SYMBOLS DENOTE  $Y_B$

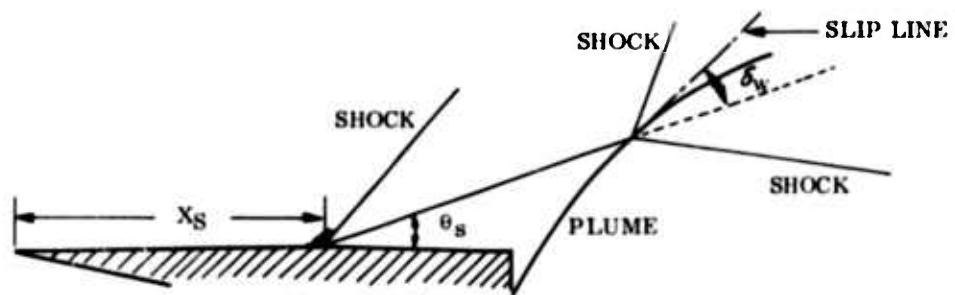
SOLID SYMBOLS DENOTE  $\eta_{s_c}$

$\triangle, \otimes, \boxtimes$  DENOTE RESULTS  
 SATISFYING ALL CONSERVA-  
 TION REQUIREMENTS

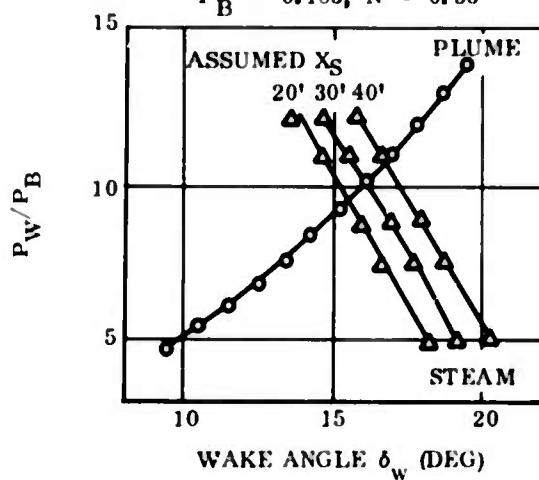


$X_S$	$P_T/P_B$
20	6.55
30	6.5
40	6.5

Figure I-9 Streamline Total Pressures for Various  $\eta_{s_c}$  and  $Y_B$

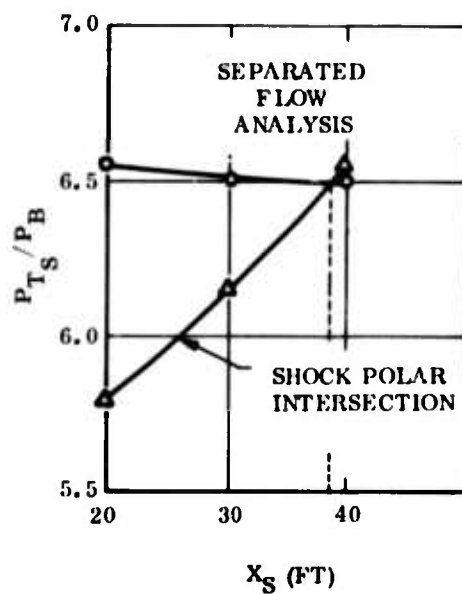


$M = 10, 250 \text{ K}$   
 $\alpha = 0^\circ$   
 $P_B = 0.185, N = 0.56$



$x_s$	$\frac{P_w}{P_B}$	$\frac{P_T}{P_B}$
20	9.6	5.8
30	10.2	6.15
40	10.9	6.55

(a) SHOCK POLAR INTERSECTION



$x_s = 38.5 \text{ FT}$

$\frac{P_{TS}}{P_B} = 6.5$

(b) DETERMINATION OF  $x_s$  AND  $\frac{P_{TS}}{P_B}$

Figure I-10 Determination of Trailing Shock Pressure and Separation Distance

Appendix II  
LAMINAR CROSS-FLOW BOUNDARY LAYER ANALYSIS  
by M. C. Fong

The flow field surrounding a maneuvering lifting reentry vehicle is three-dimensional not only due to the body geometry but also due to the attitude and orientation of the vehicle under hypersonic flight conditions. Peculiar surface streamline patterns have been observed (Refs. 37, 53, and 54) but analytical prediction of such streamline deviation behavior and the concomitant viscous flow properties has not reached beyond a semiempirical stage except for isolated instances (Ref. 55). However, the local inviscid and boundary layer flow properties must be well understood in order to obtain a satisfactory plume-induced separated flow solution presented in this analysis. Development of an analytical method to predict the attached flow properties under realistic LRV flight conditions thus constitutes the main goal of this appendix.

For expediency, a strip method has been adopted for both attached and separated boundary layer predictions in conjunction with the plume-induced separation problem. The strip method essentially rationalizes that the two-dimensional flat-plate solution within each narrow chordwise strip is approximately valid and any influence from the adjacent strip is of secondary importance. However, the streamline deviation cited above, which is generally attributable to inviscid-viscous interaction at hypersonic speeds, necessitates a re-examination of the strip method in application to the LRV maneuvering, or at least establishment of a set of criteria within which the strip method is satisfactory for predicting the exhaust plume effects.

In this analysis, an engineering method is proposed to resolve the streamline deviation problem, in that the cross-flow boundary flow in terms of the streamline coordinate system is treated with the small perturbation approach. Then, using an available surface oil flow pattern, the unknown inviscid streamline is determined which can be

compared with the corresponding streamline based on the strip method. This inverse approach avoids the displacement thickness growth problem and the subsequent inviscid-viscous flow interaction phenomenon and therefore, permits an assessment of the strip method. The predicted inviscid streamline, of course, provides an input for plume-induced separated flow prediction.

## 1. FORMULATION OF GOVERNING DIFFERENTIAL EQUATIONS.

The formidable task involved in the three-dimensional boundary layer problem lies in the cross-flow generation and streamline distortion within the boundary layer for which the high-order nonlinearity generally precludes any similarity treatment or other simplifications. However, by using the streamline coordinate system for which one of the coordinates is set to be coincident with the local outer-edge streamline projected in the tangent plane, it can be envisioned that the governing equations would be subject to small perturbation treatment except for large curvatures in the flow field. This analysis essentially follows the formulation presented in References 41 and 48, and places emphasis on development of a small cross-flow solution that can be easily incorporated in the plume-induced separated flow analysis.

Similar to the consideration by Beckwith (Ref. 47), a three-dimensional orthogonal streamline coordinate system  $(x, y, z)$  is introduced with corresponding velocity component  $u$  tangent to the external streamline,  $v$  normal to the body surface, and  $w$  the cross-flow velocity component normal to  $u$  in the tangent plane (Fig. II-1).<sup>\*</sup> The length elements are defined as:

$$\left. \begin{aligned} ds &= e_1(x, z) dx \\ dy &= dy \\ dn &= e_2(x, z) dz \end{aligned} \right\} \quad (\text{II-1})$$

<sup>\*</sup>The coordinate system is left-handed; the equations are identical to those by Beckwith (Ref. 47) if the coordinates  $y$  and  $z$  and the velocity components  $v$  and  $w$  are interchanged.

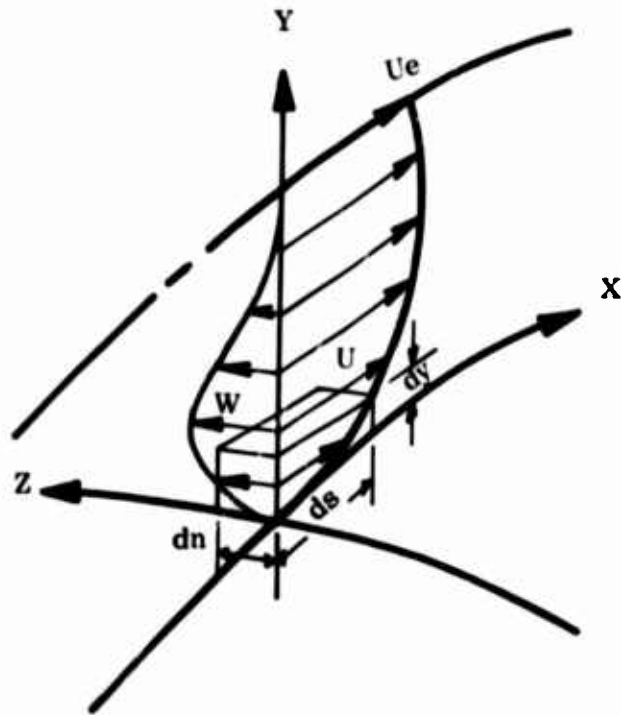


Figure II-1 Streamline Coordinate System

and the outer-edge conditions require that

$$\left. \begin{aligned} u &= u_e \\ w &= w_e = 0 \end{aligned} \right\} \quad (\text{II-2})$$

With the assumptions of perfect gas and the absence of diffusion and chemical reactions, the governing equations for a three-dimensional laminar compressible boundary layer are then expressible as



### Continuity

$$\frac{1}{e_1} \frac{\partial}{\partial x} (\rho u e_2) + \frac{\partial}{\partial y} (\rho v e_2) + \frac{1}{e_1} \frac{\partial}{\partial z} (\rho w e_1) = 0 \quad (\text{II-3})$$

### x-Momentum

$$\rho \frac{u}{e_1} \frac{\partial u}{\partial x} + \rho v \frac{\partial u}{\partial y} + \frac{\rho w}{e_2} \frac{\partial u}{\partial z} + \frac{\rho u w}{e_1 e_2} \frac{\partial e_1}{\partial z} - \frac{\rho w^2}{e_1 e_2} \frac{\partial e_2}{\partial x} = -\frac{1}{e_1} \frac{\partial p}{\partial x} + \frac{\partial}{\partial y} \left( \mu \frac{\partial u}{\partial y} \right) \quad (\text{II-4})$$

### y-Momentum

$$\frac{\partial p}{\partial y} = 0 \quad (\text{II-5})$$

### z-Momentum

$$\rho \frac{u}{e_1} \frac{\partial w}{\partial x} + \rho v \frac{\partial w}{\partial y} + \frac{\rho w}{e_2} \frac{\partial w}{\partial z} + \frac{\rho u w}{e_1 e_2} \frac{\partial e_2}{\partial x} - \frac{\rho u^2}{e_1 e_2} \frac{\partial e_1}{\partial z} = -\frac{1}{e_2} \frac{\partial p}{\partial z} + \frac{\partial}{\partial y} \left( \mu \frac{\partial w}{\partial y} \right) \quad (\text{II-6})$$

### Energy

$$\rho \frac{u}{e_1} \frac{\partial H}{\partial x} + \rho v \frac{\partial H}{\partial y} + \frac{\rho w}{e_2} \frac{\partial H}{\partial z} = \frac{\partial}{\partial y} \left[ \mu \left( \frac{\partial H}{\partial y} + \frac{1 - \text{Pr}}{\text{Pr}} \frac{\partial h}{\partial y} \right) \right] \quad (\text{II-7})$$

From the continuity equation, two stream functions  $\psi$  and  $\phi$  can be defined as follows:

$$\rho u e_2 = \frac{\partial \psi}{\partial y}, \quad \rho v e_2 = -\left( \frac{\partial \psi}{\partial x} + \frac{\partial \phi}{\partial z} \right) \frac{1}{e_1}, \quad \rho w e_1 = \frac{\partial \phi}{\partial y} \quad (\text{II-8})$$

Although for small perturbation approach, these partial differential equations can be simplified by examining the crossflow terms (Refs. 47 and 48), the present analysis

follows the scheme discussed in Reference 56 so that a system of similarity equations in successive order can be obtained. To accomplish this, the following transformation variables are introduced:

$$\left. \begin{aligned} \xi &= \int_0^x \rho_0 \mu_0 e_1 dx = \int_0^s \rho_0 \mu_0 ds \\ \eta &= \sqrt{\frac{u_e}{2\xi}} \int_0^y \rho dy \\ \zeta &= \int_0^z \rho_0 \mu_0 e_2 dz = \int_0^n \rho_0 \mu_0 dn \end{aligned} \right\} \quad (\text{II-9})$$

where subscript  $o$  denotes some reference value, such as that for local stagnation conditions. Furthermore, the stream functions are expressed in the following manner:

$$\begin{aligned} \psi &= \sqrt{2\xi u_e} e_2 f(\xi, \eta, \zeta) \\ \phi &= \sqrt{2\xi u_e} e_1 g(\xi, \eta, \zeta) \end{aligned} \quad (\text{II-10})$$

It follows that

$$u = u_e \frac{\partial f}{\partial \eta} \quad \text{and} \quad w = u_e \frac{\partial g}{\partial \eta} \quad (\text{II-11})$$

Also, at the outer edge of the boundary layer

$$\frac{\rho_e u_e}{e_1} \frac{\partial u_e}{\partial x} = - \frac{1}{e_1} \frac{\partial p}{\partial x} \quad (\text{II-12})$$

and

$$\frac{1}{e_1} \frac{\partial e_1}{\partial z} = -\frac{1}{u_e} \frac{\partial u_e}{\partial z} = \frac{1}{\rho_e u_e^2} \frac{\partial p}{\partial z} \quad (\text{II-13})$$

Substituting these transformation variables into the governing Equations (II-3) to (II-7) and after algebraic rearrangement, the following equations are obtained:

#### Streamwise Momentum

$$\begin{aligned} \frac{\partial}{\partial \eta} \left( N \frac{\partial^2 f}{\partial \eta^2} \right) + f \frac{\partial^2 f}{\partial \eta^2} + \frac{2\xi}{u_e} \frac{\partial u_e}{\partial \xi} \left[ \frac{\rho_e}{\rho} + \frac{f}{2} \frac{\partial^2 f}{\partial \eta^2} - \left( \frac{\partial f}{\partial \eta} \right)^2 \right] + \frac{2\xi}{u_e} \frac{\partial u_e}{\partial \xi} \\ \left[ \frac{g}{2} \frac{\partial^2 f}{\partial \eta^2} - \frac{\partial f}{\partial \eta} \frac{\partial g}{\partial \eta} \right] + 2\xi \left[ \left( \frac{\partial f}{\partial \xi} \frac{\partial^2 f}{\partial \eta^2} - \frac{\partial f}{\partial \eta} \frac{\partial^2 f}{\partial \xi \partial \eta} \right) + \left( \frac{\partial g}{\partial \xi} \frac{\partial^2 f}{\partial \eta^2} - \frac{\partial g}{\partial \eta} \frac{\partial^2 f}{\partial \xi \partial \eta} \right) \right] \\ + \frac{2\xi}{e_2} \frac{\partial e_1}{\partial \xi} \left[ f \frac{\partial^2 f}{\partial \eta^2} + \left( \frac{\partial g}{\partial \eta} \right)^2 \right] + \frac{2\xi}{e_1} \frac{\partial e_1}{\partial \xi} \left[ g \frac{\partial^2 f}{\partial \eta^2} - \frac{\partial f}{\partial \eta} \frac{\partial g}{\partial \eta} \right] = 0 \end{aligned} \quad (\text{II-14})$$

#### Cross-Flow Momentum

$$\begin{aligned} \frac{\partial}{\partial \eta} \left( N \frac{\partial^2 g}{\partial \eta^2} \right) + f \frac{\partial^2 g}{\partial \eta^2} + \frac{2\xi}{u_e} \frac{\partial u_e}{\partial \xi} \left[ \frac{\rho_e}{\rho} + \frac{g}{2} \frac{\partial^2 g}{\partial \eta^2} - \left( \frac{\partial g}{\partial \eta} \right)^2 \right] + \frac{2\xi}{u_e} \frac{\partial u_e}{\partial \xi} \left[ \frac{f}{2} \frac{\partial^2 g}{\partial \eta^2} - \frac{\partial f}{\partial \eta} \frac{\partial g}{\partial \eta} \right] \\ + 2\xi \left[ \left( \frac{\partial f}{\partial \xi} \frac{\partial^2 g}{\partial \eta^2} - \frac{\partial f}{\partial \eta} \frac{\partial^2 g}{\partial \xi \partial \eta} \right) + \left( \frac{\partial g}{\partial \xi} \frac{\partial^2 g}{\partial \eta^2} - \frac{\partial g}{\partial \eta} \frac{\partial^2 g}{\partial \xi \partial \eta} \right) \right] + \frac{2\xi}{e_2} \frac{\partial e_2}{\partial \xi} \left[ f \frac{\partial^2 g}{\partial \eta^2} - \frac{\partial f}{\partial \eta} \frac{\partial g}{\partial \eta} \right] \\ + \frac{2\xi}{e_1} \frac{\partial e_1}{\partial \xi} \left[ g \frac{\partial^2 g}{\partial \eta^2} + \left( \frac{\partial f}{\partial \eta} \right)^2 \right] = 0 \end{aligned} \quad (\text{II-15})$$

And with the definitions of the total enthalpy

$$\theta = \frac{H}{H_e} \quad (\text{II-16})$$

and

$$\frac{h}{H_e} = \theta - \frac{\frac{\gamma-1}{2} M_e^2}{1 + \frac{\gamma-1}{2} M_e^2} \left[ \left( \frac{\partial f}{\partial \eta} \right)^2 + \left( \frac{\partial g}{\partial \eta} \right)^2 \right] = \theta - Cr^2 \left[ \left( \frac{\partial f}{\partial \eta} \right)^2 + \left( \frac{\partial g}{\partial \eta} \right)^2 \right] \quad (\text{II-17})$$

the energy equation becomes:

$$\begin{aligned} \frac{1}{Pr} \frac{\partial}{\partial \eta} \left( N \frac{\partial \theta}{\partial \eta} \right) - \frac{1-Pr}{Pr} \frac{\frac{\gamma-1}{2} M_B^2}{1 + \frac{\gamma-1}{2} M_e^2} \frac{\partial}{\partial \eta} \left\{ N \frac{\partial}{\partial \eta} \left[ \left( \frac{\partial f}{\partial \eta} \right)^2 + \left( \frac{\partial g}{\partial \eta} \right)^2 \right] \right\} + f \frac{\partial \theta}{\partial \eta} + \frac{2\xi}{u_e} \frac{\partial u_e}{\partial \xi} \left( \frac{f}{2} \frac{\partial \theta}{\partial \eta} \right) \\ + \frac{2\xi}{u_e} \frac{\partial u_e}{\partial \xi} \left( \frac{g}{2} \frac{\partial \theta}{\partial \eta} \right) + 2\xi \left[ \left( \frac{\partial f}{\partial \xi} \frac{\partial \theta}{\partial \eta} - \frac{\partial f}{\partial \eta} \frac{\partial \theta}{\partial \xi} \right) + \left( \frac{\partial g}{\partial \xi} \frac{\partial \theta}{\partial \eta} - \frac{\partial g}{\partial \eta} \frac{\partial \theta}{\partial \xi} \right) \right] + \frac{2\xi}{e_2} \frac{\partial e_2}{\partial \xi} \left( f \frac{\partial \theta}{\partial \eta} \right) \\ + \frac{2\xi}{e_1} \frac{\partial e_1}{\partial \xi} \left( g \frac{\partial \theta}{\partial \eta} \right) = 0 \end{aligned} \quad (\text{II-18})$$

where  $N = \rho\mu/\rho_0\mu_0$  is a viscosity function which can be simplified to become a pressure ratio  $N = P/P_0$  if a linear viscosity-temperature relation holds.

The boundary conditions are:

At the wall,  $\eta = 0$

$$u = w = 0 : \frac{\partial f}{\partial \eta} = 0, \frac{\partial g}{\partial \eta} = 0$$

$$v = 0 : f = 0, g = 0$$

At the outer edge,  $\eta \rightarrow \infty$

$$u = u_e, w = w_e = 0, H = H_e$$

$$\text{or } \frac{\partial f}{\partial \eta} = 1, \frac{\partial g}{\partial \eta} = 1, \theta = 1$$

(II-19)

Introducing the following definitions:

$$\beta = \frac{2\xi}{u_e} \frac{\partial u_e}{\partial \xi} (\hat{m}) \quad \text{Streamline pressure gradient parameter}$$

$$K_1 = \frac{2\xi}{e_1} \frac{\partial e_1}{\partial \xi} \quad \text{Curvature parameter}$$

$$K_2 = \frac{2\xi}{e_2} \frac{\partial e_2}{\partial \xi} \quad \text{Dilatation parameter}$$

$$\beta^* = -\frac{2\xi}{\rho_e u_e^2} \frac{\partial p}{\partial \xi} \quad \text{Cross-flow pressure gradient}$$

$$\text{with } \hat{m} = 1 + \frac{\gamma - 1}{2} M_e^2 = 1 + m$$

(II-20)

Equations (II-15), (II-16), and (II-18) become (Ref. 56)

$$\begin{aligned}
& \frac{\partial}{\partial \eta} \left( N \frac{\partial^2 f}{\partial \eta^2} \right) + f \frac{\partial^2 f}{\partial \eta^2} \left[ 1 + \frac{\beta}{2\hat{M}} + K_2 \right] + \beta \left[ \theta - \left( \frac{\partial f}{\partial \eta} \right)^2 \right] + \left( \frac{\partial g}{\partial \eta} \right)^2 \left[ K_2 - \beta \frac{m}{\hat{M}} \right] \\
& + \frac{K_1}{2} g \frac{\partial^2 f}{\partial \eta^2} + 2\xi \left[ \frac{\partial f}{\partial \xi} \frac{\partial^2 f}{\partial \eta^2} - \frac{\partial f}{\partial \eta} \frac{\partial^2 f}{\partial \xi \partial \eta} \right] + 2\xi \left[ \frac{\partial g}{\partial \xi} \frac{\partial^2 f}{\partial \eta^2} - \frac{\partial g}{\partial \eta} \frac{\partial^2 f}{\partial \xi \partial \eta} \right] = 0
\end{aligned}
\tag{II-21}$$

$$\begin{aligned}
& \frac{\partial}{\partial \eta} \left( N \frac{\partial^2 g}{\partial \eta^2} \right) + f \frac{\partial^2 g}{\partial \eta^2} \left[ 1 + \frac{\beta}{2\hat{M}} + K_2 \right] + K_1 \left[ \left( \frac{\partial f}{\partial \eta} \right)^2 + \left( \frac{\partial g}{\partial \eta} \right)^2 + \frac{g}{2} \frac{\partial^2 g}{\partial \eta^2} \right] + \beta^* \left( \frac{\rho_e}{\rho} \right) \\
& - \left( \frac{\partial f}{\partial \eta} \frac{\partial g}{\partial \eta} \right) \left[ K_2 + \frac{\beta}{\hat{M}} \right] + 2\xi \left[ \frac{\partial f}{\partial \xi} \frac{\partial^2 g}{\partial \eta^2} - \frac{\partial f}{\partial \eta} \frac{\partial^2 g}{\partial \xi \partial \eta} \right] + 2\xi \left[ \frac{\partial g}{\partial \xi} \frac{\partial^2 g}{\partial \eta^2} - \frac{\partial g}{\partial \eta} \frac{\partial^2 g}{\partial \xi \partial \eta} \right] = 0
\end{aligned}
\tag{II-22}$$

$$\begin{aligned}
& \frac{1}{Pr} \frac{\partial}{\partial \eta} \left( N \frac{\partial \theta}{\partial \eta} \right) - \frac{1 - Pr}{Pr} \frac{m}{\hat{M}} \frac{\partial}{\partial \eta} \left\{ N \frac{\partial}{\partial \eta} \left[ \left( \frac{\partial f}{\partial \eta} \right)^2 + \left( \frac{\partial g}{\partial \eta} \right)^2 \right] \right\} + f \frac{\partial \theta}{\partial \eta} \left[ 1 + \frac{\beta}{2\hat{M}} + K_2 \right] \\
& + \frac{K}{2} g \frac{\partial \theta}{\partial \eta} + 2\xi \left[ \frac{\partial f}{\partial \xi} \frac{\partial \theta}{\partial \eta} - \frac{\partial f}{\partial \eta} \frac{\partial \theta}{\partial \xi} \right] + 2\xi \left[ \frac{\partial g}{\partial \xi} \frac{\partial \theta}{\partial \eta} - \frac{\partial g}{\partial \eta} \frac{\partial \theta}{\partial \xi} \right] = 0
\end{aligned}
\tag{II-23}$$

## 2. PERTURBATION GENERATION.

Small cross flow is attained when the surface curvature and dilatation parameters as well as the cross-flow pressure gradient are small in comparison with the stream-wise velocity component. Under this circumstance, a small parameter,  $\epsilon$ , may be introduced such that

$$\left. \begin{aligned}
 f &= f_0 + \epsilon f_1 + \epsilon^2 f_2 + \dots \\
 g &= \epsilon g_1 + \epsilon^2 g_2 + \dots \\
 \theta &= \theta_0 + \epsilon \theta_1 + \epsilon^2 \theta_2 + \dots \\
 K_1 &= \epsilon K_{11} + \epsilon^2 K_{12} + \dots \\
 K_2 &= \epsilon K_{21} + \epsilon^2 K_{22} + \dots \\
 \beta^* &= -K_1 = \epsilon \beta_1^* + \epsilon^2 \beta_2^* + \dots
 \end{aligned} \right\} \quad (\text{II-24})$$

where the subscripts 0, 1, 2 ... represent the zero-, first-, second-order solutions, etc. For simplicity, the following assumptions are also introduced:

- All the  $f$ ,  $g$ , and  $\theta$  functions are similar, i.e., dependent on  $\eta$  only.
- Prandtl number equal to unity
- The viscosity parameter  $N$  can be approximated by unity, this being admissible locally for relatively flat surfaces considered herein.

Equations (II-21) to (II-23) then become:

#### Zero-Order

$$f_0''' + f_0 f_0'' \left(1 + \frac{\beta}{2\hat{m}}\right) + \beta (\theta_0 - f_0'^2) = 0 \quad (\text{II-25})$$

$$\theta_0'' + f_0 \theta_0' \left(1 + \frac{\beta}{2\hat{m}}\right) = 0 \quad (\text{II-26})$$

### First-Order

$$f_1''' + \left[ \left( 1 + \frac{\beta}{2\hat{m}} \right) f_0 \right] f_1'' - (2\beta f_0') f_1' + \left[ \left( 1 + \frac{\beta}{2\hat{m}} \right) f_0'' \right] f_1 + \left[ \beta - 1 + f_0 f_0'' K_{21} \right] = 0 \quad (\text{II-27})$$

$$g_1''' + \left[ \left( 1 + \frac{\beta}{2\hat{m}} \right) f_0 \right] g_1'' + \left[ \left( -\frac{\beta}{\hat{m}} \right) f_0' \right] g_1' + \beta_1^* \hat{m} (\theta_0 - f_0'^2) = 0 \quad (\text{II-28})$$

$$\theta_1'' + \left[ \left( 1 + \frac{\beta}{2\hat{m}} \right) f_0 \right] \theta_1' + \left[ \left( 1 + \frac{\beta}{2\hat{m}} \right) \theta_0' \right] f_1 + f_0 \theta_0' K_{21} = 0 \quad (\text{II-29})$$

And so on. Note that  $\beta^* = -K_1$  is utilized in obtaining Equation (II-28).

For hypersonic flow, these equations can be further simplified because  $\beta/\hat{m}$  becomes negligibly small. Then, we obtain

### Zero-Order

$$f_0''' + f_0 f_0''' + \beta (\theta_0 - f_0'^2) = 0 \quad (\text{II-30})$$

$$\theta_0'' + f_0 \theta_0' = 0 \quad (\text{II-31})$$

### First-Order

$$f_1''' + f_0 f_1'' - (2\beta f_0') f_1' + f_0'' f_1 + (\beta \theta_1 + f_0 f_0'' K_{21}) = 0 \quad (\text{II-32})$$

$$g_1''' + f_0 g_1'' + \bar{\beta}_1^* (\theta_0 - f_0'^2) = 0 \quad (\text{II-33})$$

$$\theta_1'' + f_0 \theta_1' + \theta_0' f_1 + f_0 \theta_0' K_{21} = 0 \quad (\text{II-34})$$

where  $\bar{\beta}_1^* = \beta_1^* \hat{m}$  is a zero-order quantity as seen from the definition of  $\beta^*$ .



It is seen that equations (II-30) and (II-31) are identical to the transformed equations obtained by Cohen and Reshotko (Ref. 57) if  $\theta$  is replaced by  $S$  with

$$S = \theta - 1 \quad (\text{II-35})$$

Furthermore, the first-order cross-flow Equation (II-33) depends on  $f_0$  and  $\theta_0$  but is independent of the other first-order functions,  $f_1$  and  $\theta_1$ . Hence, if attention is focused on the solution of Equation (II-33),  $f_1$  and  $\theta_1$  need not be solved at all. It should be noted also that because the  $f_0$  and  $\theta_0$  values are already available, Equation (II-33) is linear in  $g_1$  for which the numerical solution is quite easy to obtain despite a two-point boundary condition involved.

#### 4. COMPUTATION SCHEME.

The widely used Runge-Kutta-Gill forward integration technique was employed to solve Equation (II-33) and a computer program for UNIVAC 1108 was developed to carry out the numerical calculations. The zero-order values  $f_0$ ,  $\theta_0$ ,  $f'_0$  etc. were obtained from the Cohen-Reshotko results (Ref. 57) which were then used as part of the input data. The problem concerning the two-point boundary condition was resolved by replacing the outer-edge condition by an assumed wall condition with which a tentative cross-flow solution was obtained. Following comparison with the prescribed outer-edge condition, a new wall condition was then assigned. Iteration on this particular boundary condition would eventually lead to the desired solution.

#### 5. RESULTS AND DISCUSSION.

A number of cases in terms of different  $\beta$  and  $S_w$  (wall temperature parameter) have been investigated. The results are presented in Figures II-2 through II-11 which show the cross-flow velocity profiles for different values of  $\beta_1^*$ . In several cases, the result exhibits a reverse profile, but with only a few cases at hand, parameters governing the reverse flow could not be readily established.

The reason that  $\bar{\beta}_1^*$  values were selected to be of the order of  $10^{-2}$  is based on the flow conditions used in Reference 49, i.e.,  $M_e = 6.8$ ,  $T_t = 1500^\circ\text{R}$ . For a 6-degree oil flow streak shown in Figure 45,  $\bar{\beta}^*$  is estimated as follows:

$$\bar{\beta}^* = \beta^* \hat{m} = - \frac{2\xi}{\rho_e u_e^2} \frac{\partial p}{\partial \xi} \left( 1 + \frac{\gamma - 1}{2} M_e^2 \right) = \frac{2e_1 s}{M_e \sqrt{\gamma R T_e}} \left( 1 + \frac{\gamma - 1}{2} M_e^2 \right) \frac{1}{e_2} \frac{\partial u_e}{\partial z}$$

Use  $s = 6$  inches,  $e_1 = e_2$ ,  $T_e = 144^\circ\text{R}$  and  $M_e = 6.8$ , we have

$$\bar{\beta}^* = \left( \frac{1 + 0.2 M_e^2}{49.1 M_e \sqrt{T_e}} \right) \frac{\partial u_e}{\partial z} = 0.023 \left( \frac{\partial u_e}{\partial z} \right) = \bar{\beta}_1^* \epsilon$$

For a flow deviation of 6 degrees,  $\partial u_e / \partial z$  is found to be 0.105. It is assumed that this value would be that for  $\epsilon$  also, from which an approximate value of 0.02 for  $\bar{\beta}_1^*$  results. As a comparison, the Blasius profile which typifies the main stream velocity distribution is about an order-of-magnitude greater than the cross-flow profile (Fig. II-12). Hence, under the small perturbation conditions, the cross-flow effect is indeed of secondary importance.

The cross-flow velocity profiles can be utilized for wall shear and heat transfer estimates. However, the main concern here lies in the determination of inviscid streamline patterns, inversely, based on the cross-flow solution; the other aerothermodynamic aspects mentioned above have not been explored.

Results of inviscid streamline prediction and comparison with the strip theory for the sample delta surface are discussed in Section II and depicted in Figure 45.

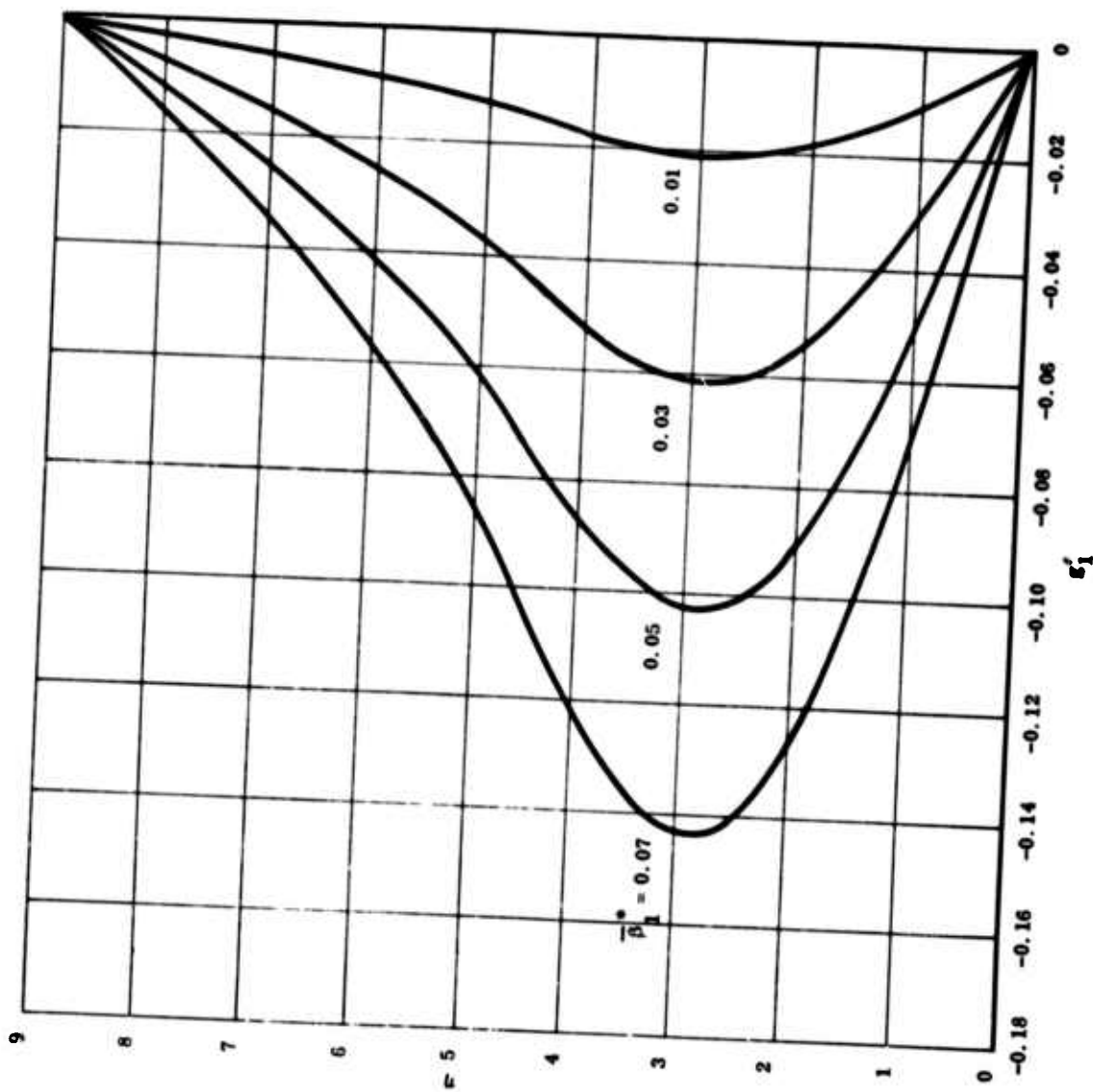


Figure II-2 Cross-Flow Velocity Profile for  $\beta = 0$  and  $S_w = 0$

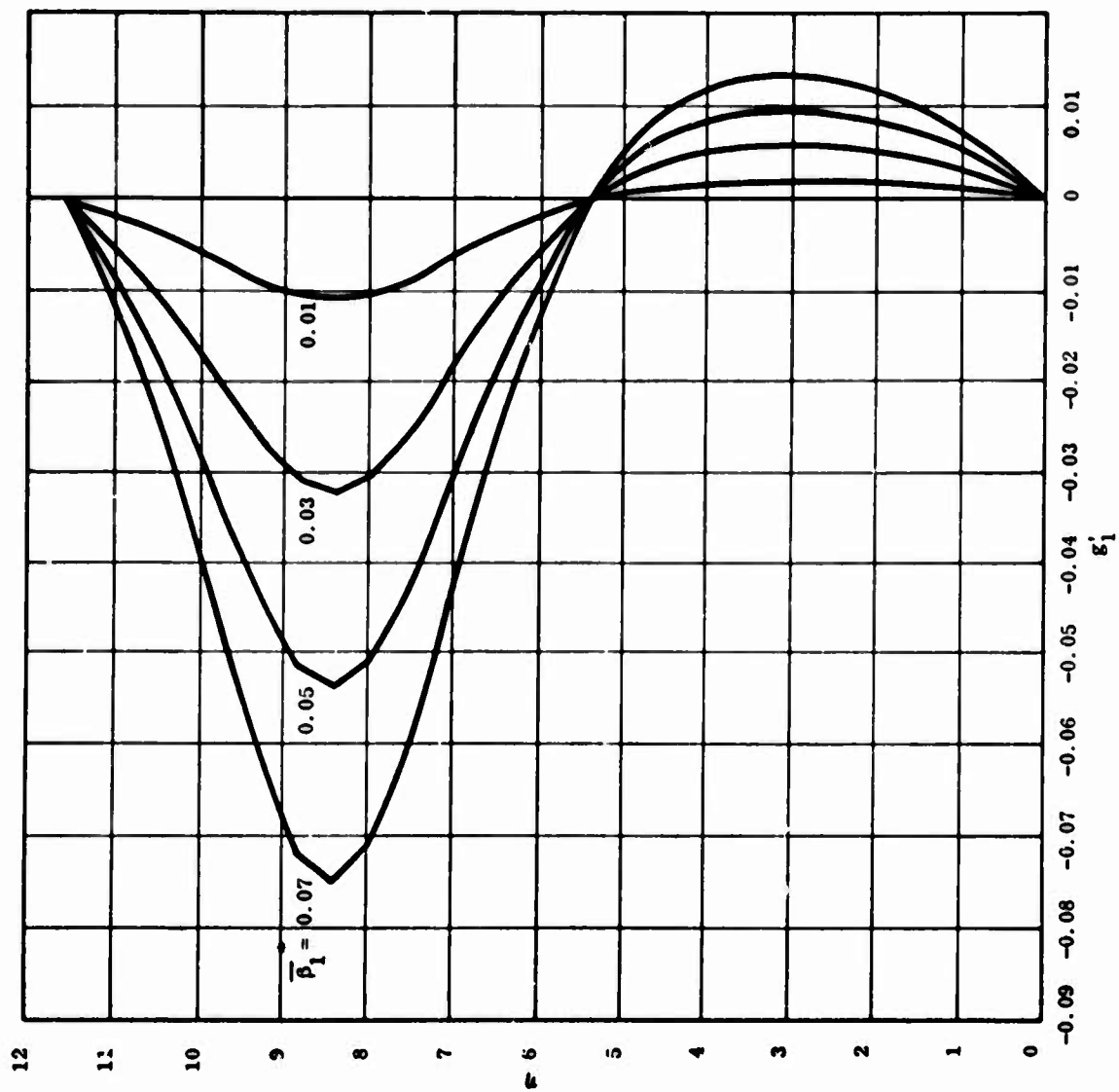


Figure II-3 Cross-Flow Velocity Profile for  $\beta = -0.1$  and  $S_w = -0.8$

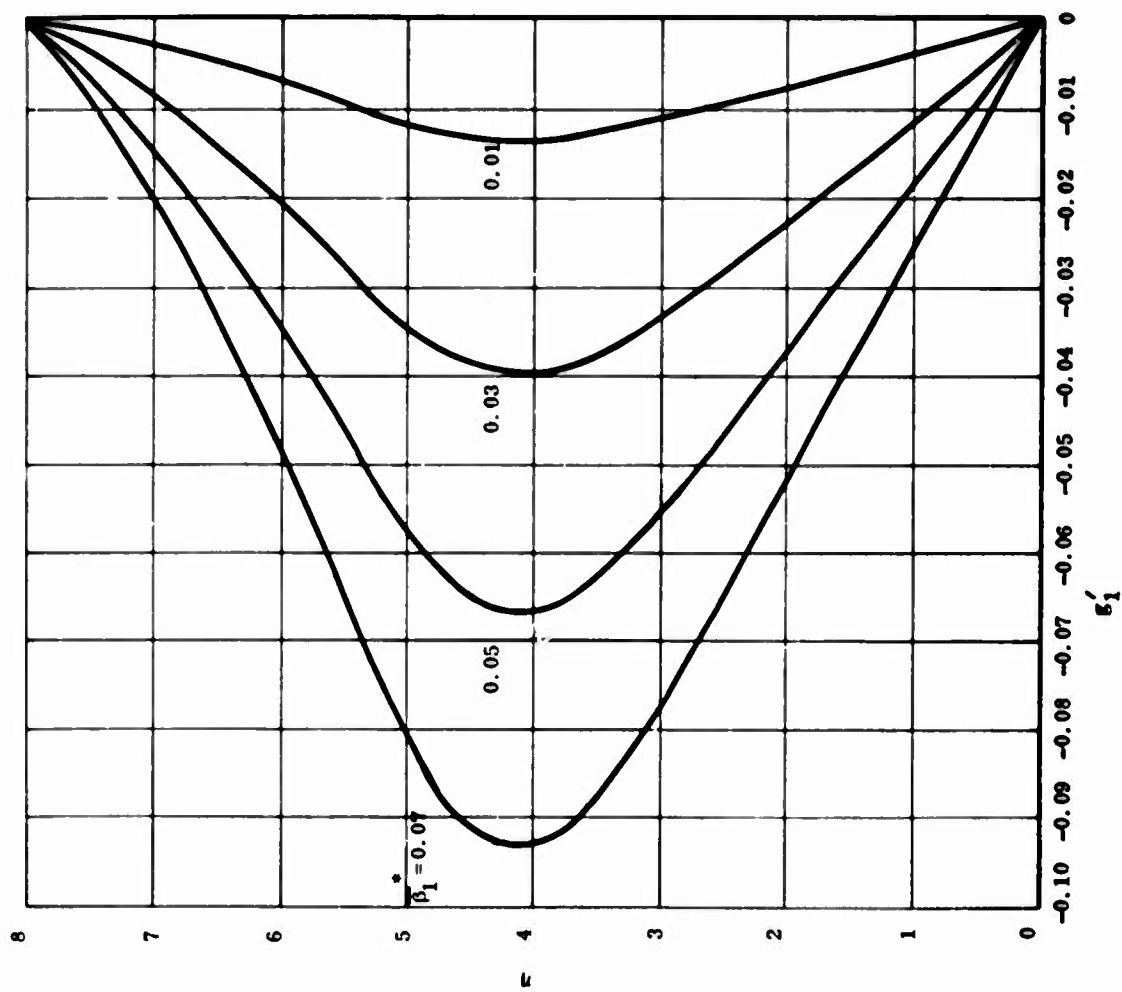


Figure II-4 Cross-Flow Velocity Profile for  $\beta = -0.1$  and  $S_w = 1.0$

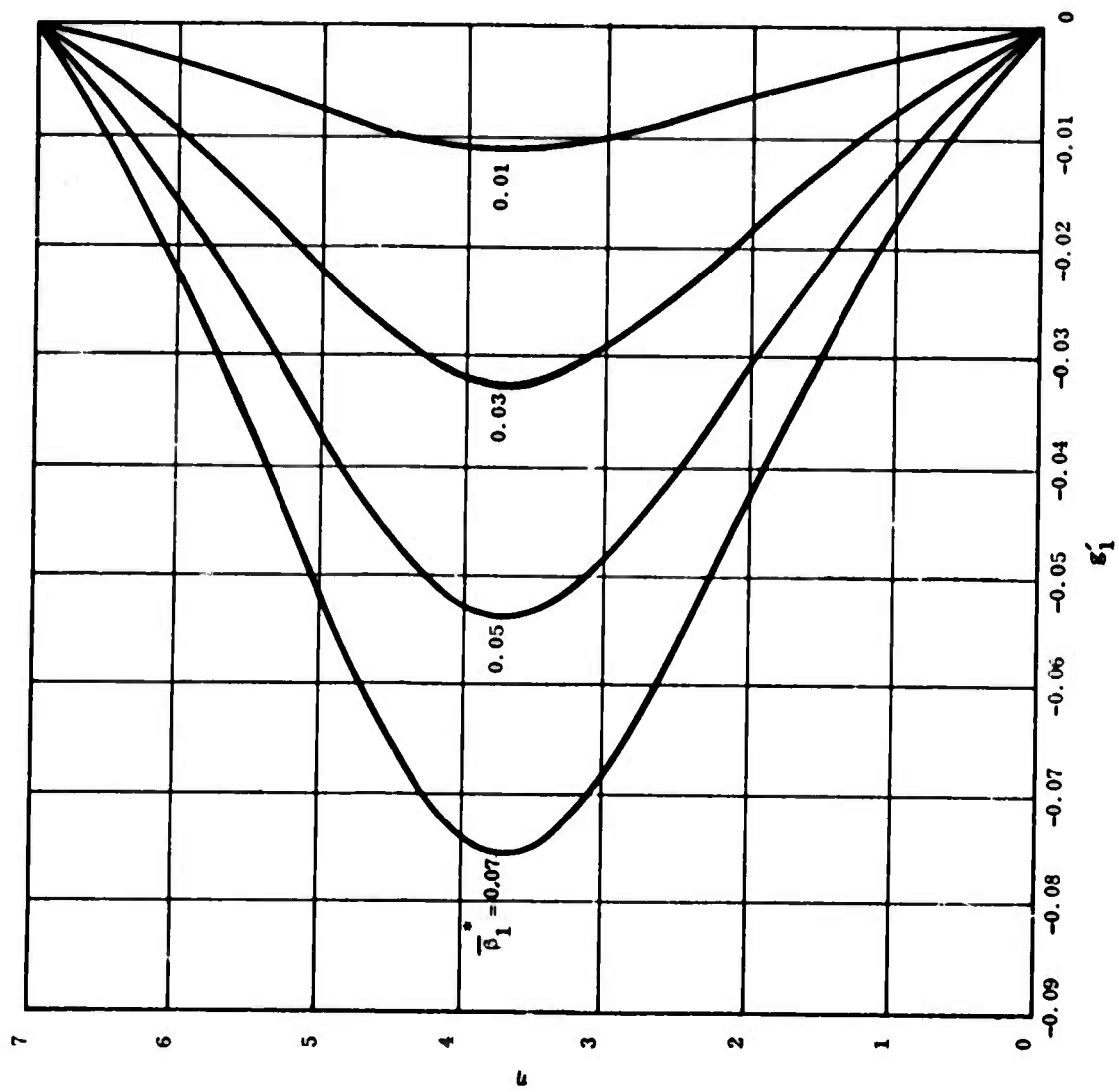


Figure II-5 Cross-Flow Velocity Profile for  $\beta = -0.235$  and  $S_w = -0.4$

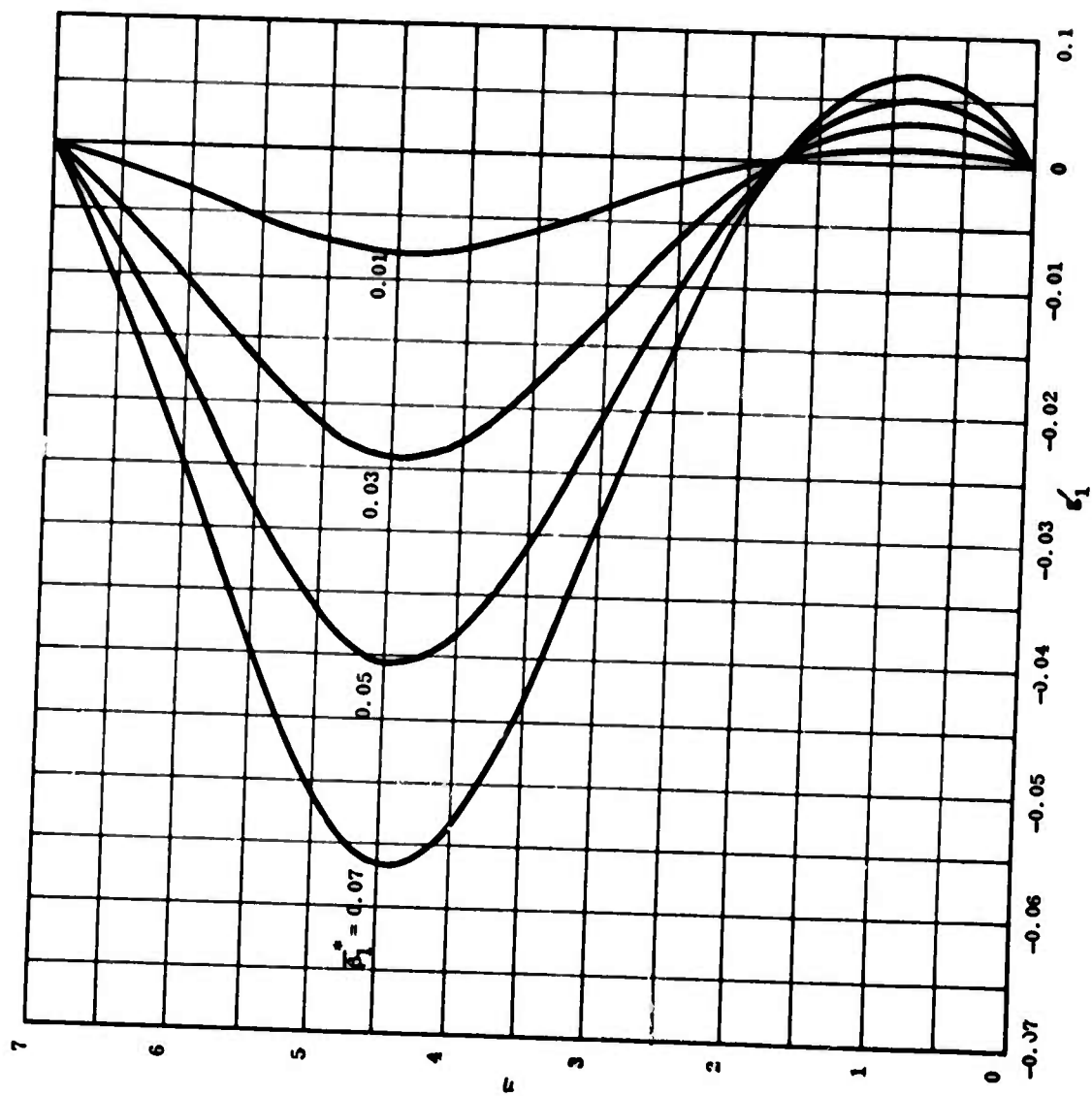


Figure II-6 Cross-Flow Velocity Profile for  $\beta = -0.326$  and  $S_w = -1.0$

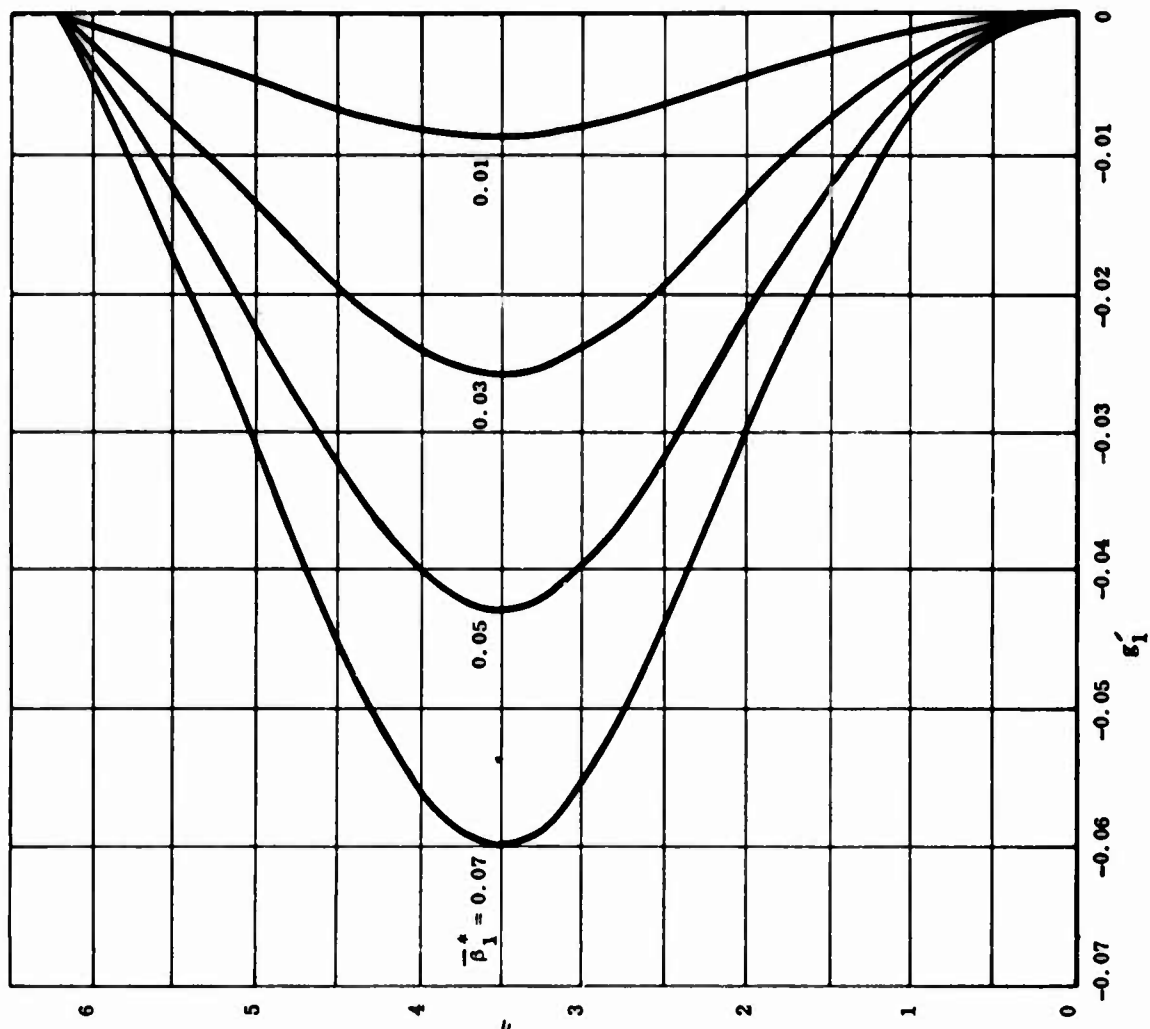


Figure II-7 Cross-Flow Velocity Profile for  $\beta = -0.325$  and  $S_w = -0.325$



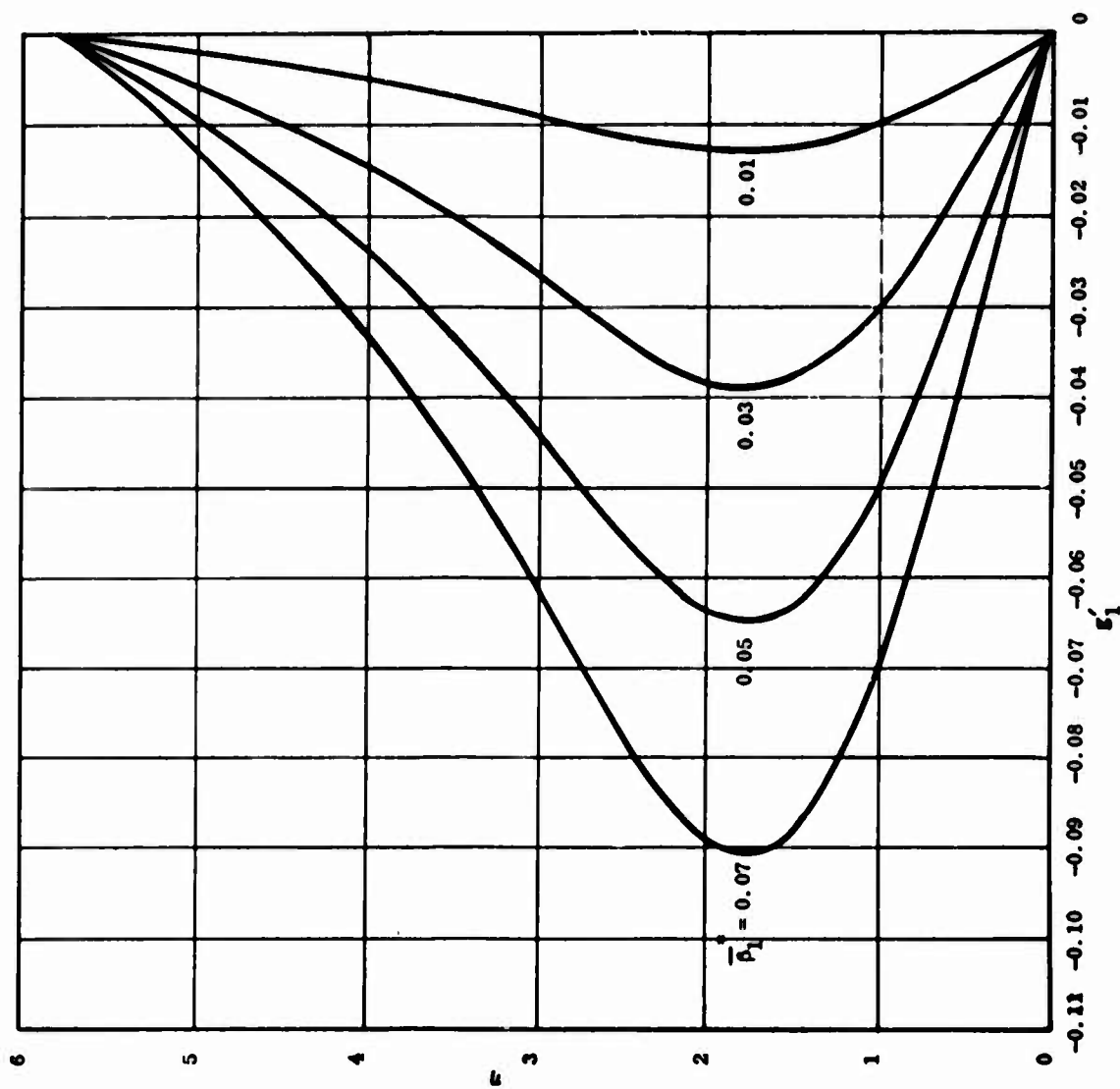


Figure II-8 Cross-Flow Velocity Profile for  $\beta = 0.5$  and  $S_w = 1.0$

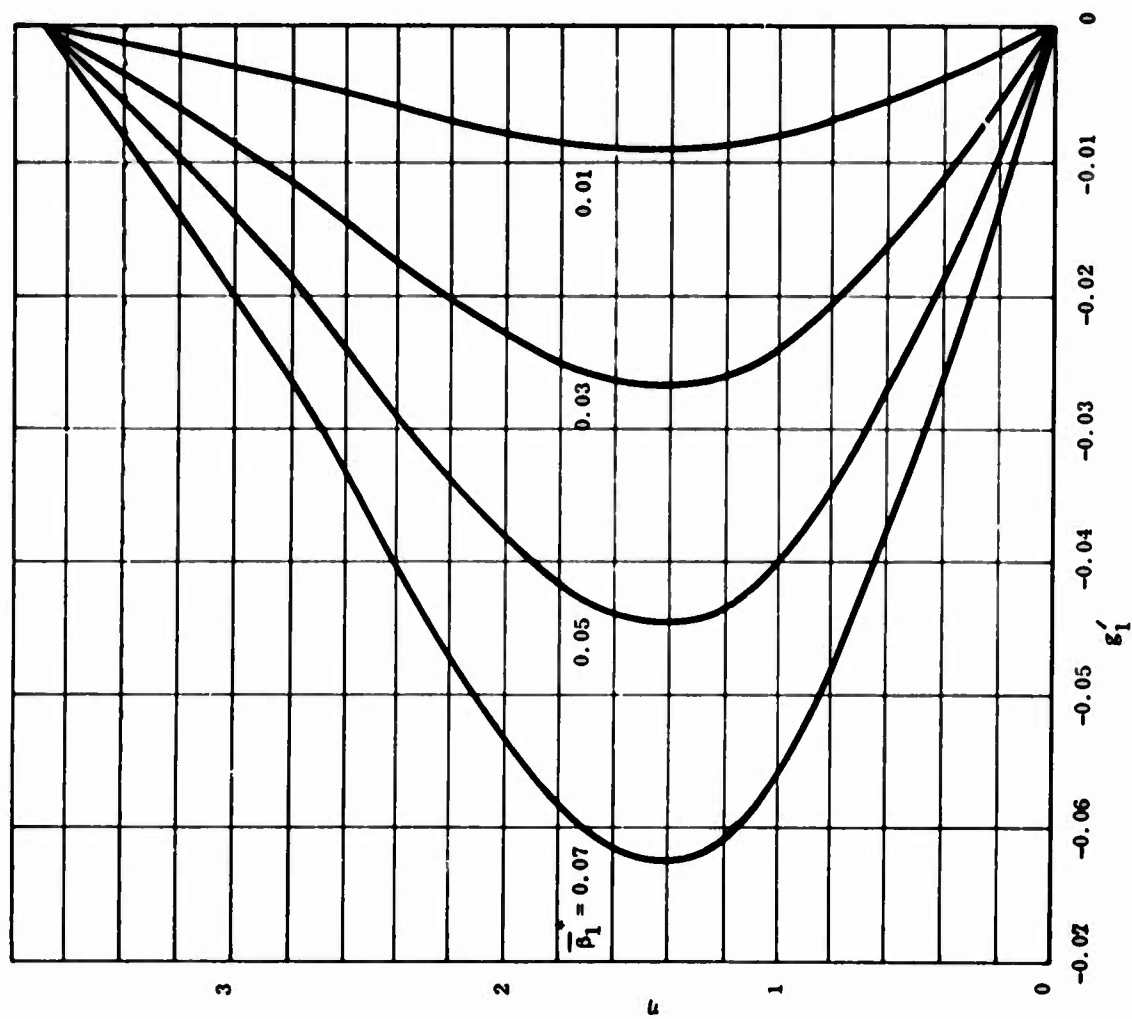


Figure II-9 Cross-Flow Velocity Profile for  $\beta = 1.0$  and  $S_w = 1.0$

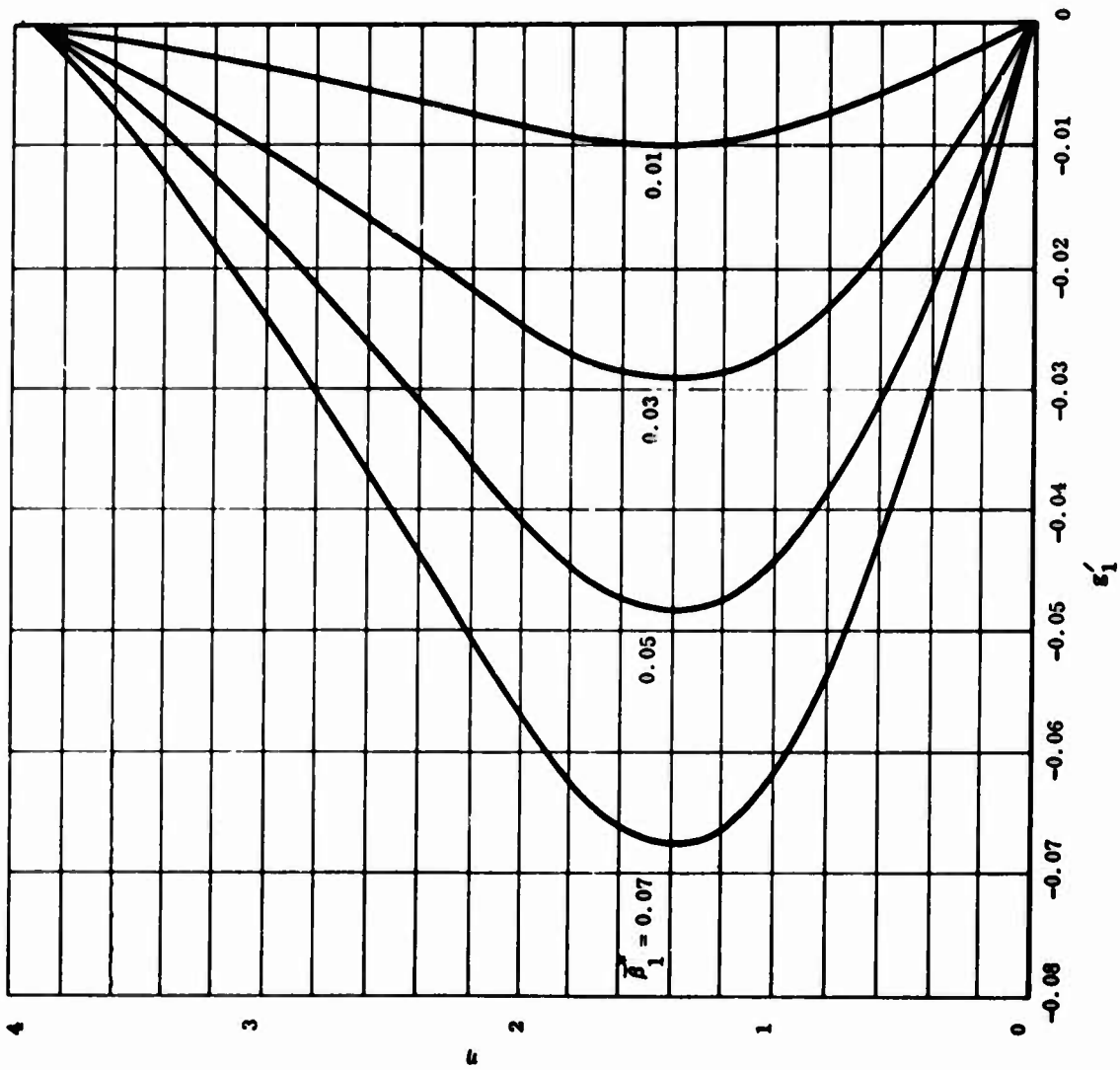


Figure II-10 Cross-Flow Velocity Profile for  $\beta = 1.5$  and  $S_w = 1.0$

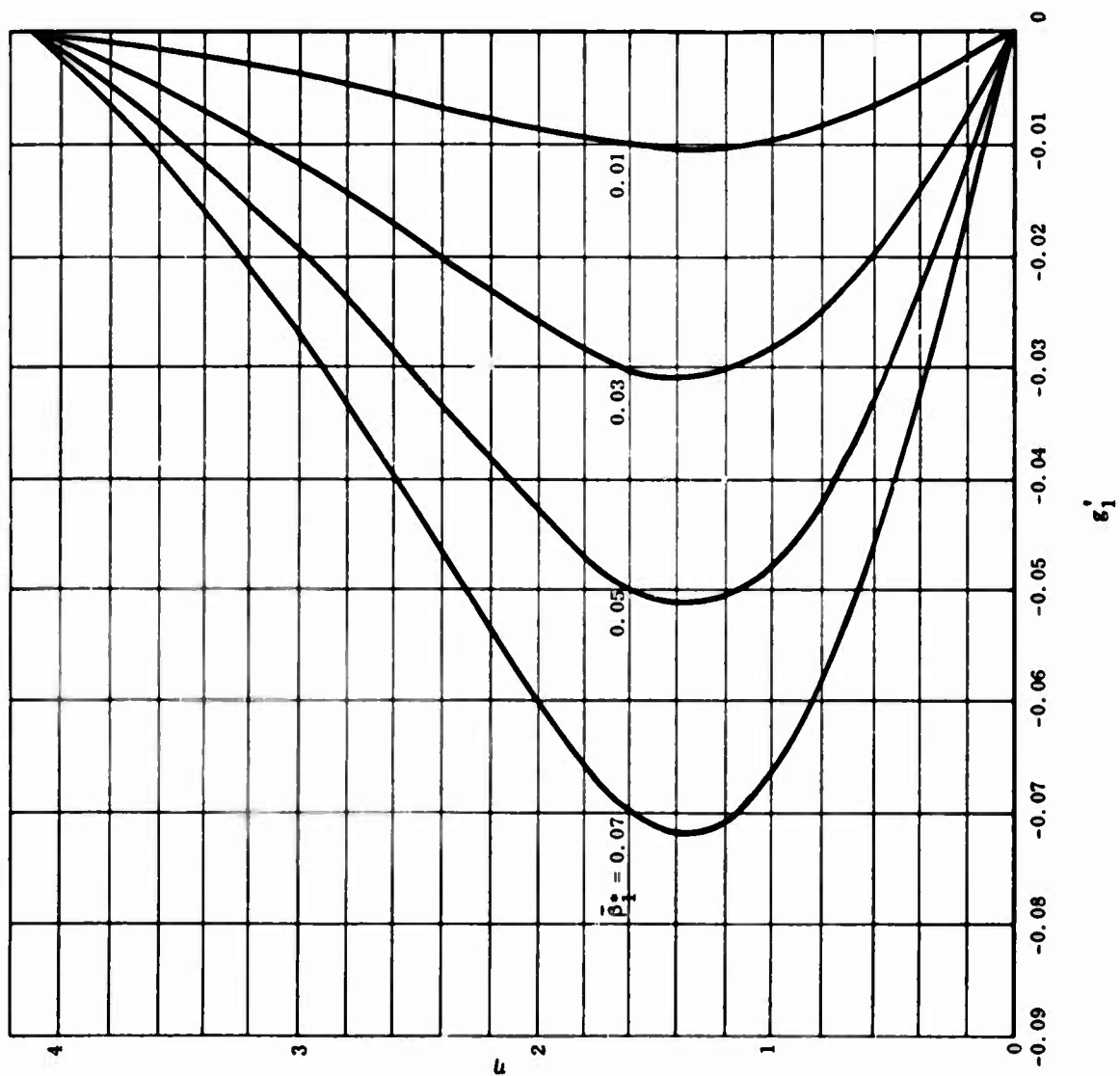


Figure II-11 Cross-Flow Velocity Profile for  $\beta = 2.0$  and  $S_w = 1.0$

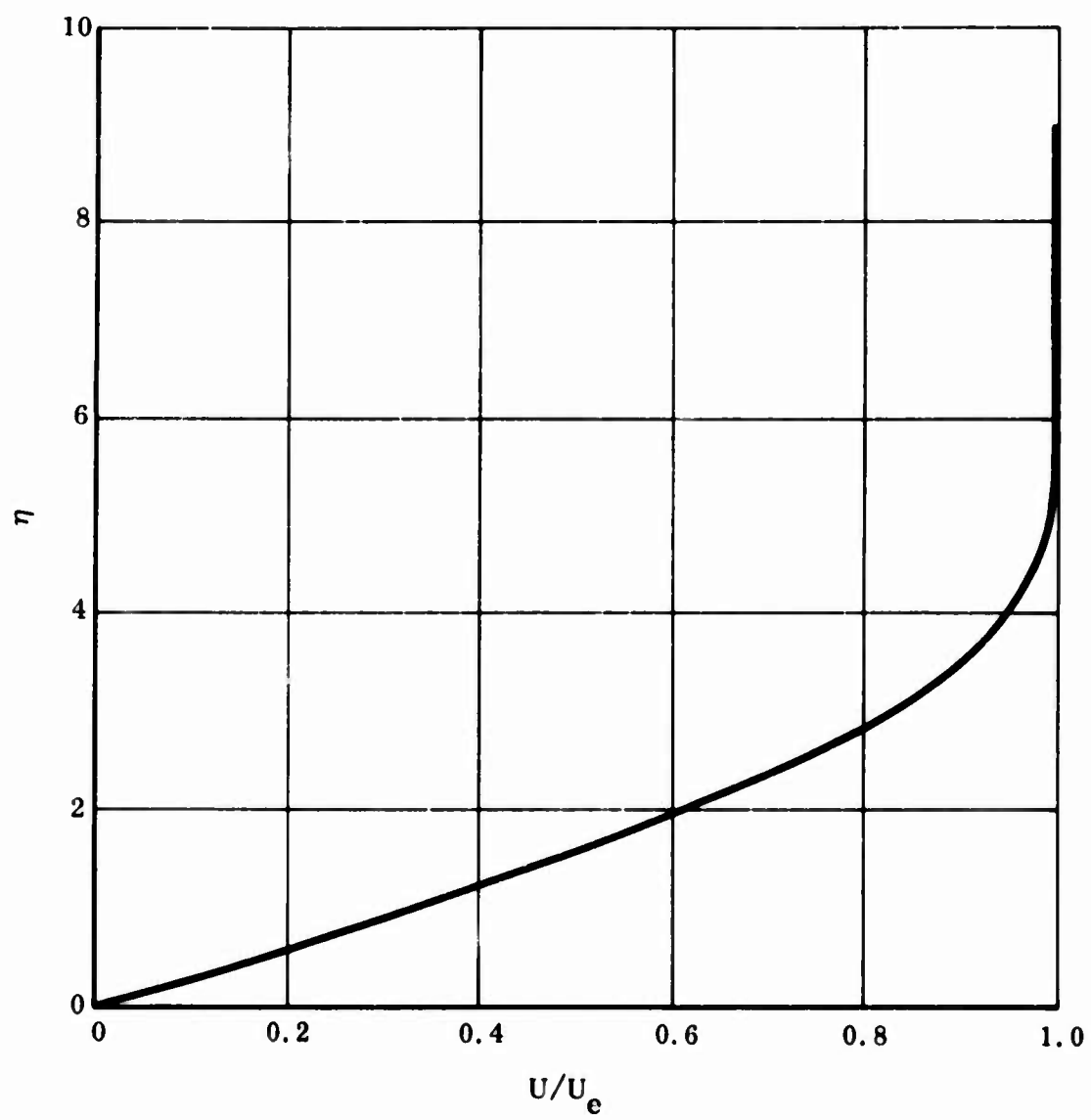


Figure II-12 Blasius Velocity Profile

### APPENDIX III

This section presents illustrations for predicted separation footprints on both the windside and leeward surfaces of the simple lifting body configuration considered in the text. A total of 43 illustrations with various Mach numbers, altitudes, and angles of attack is included in this Appendix; however, those which display negligibly small separation footprints are excluded.

The main physical parameters are:

$$l = \text{chord length} = 45 \text{ ft}$$

$$l' = \text{slope length} = l \sec 10^\circ$$

$$b = \text{Windside base length} = 15.6 \text{ ft}$$

$$b' = \text{leeward base length} = 0.707 b$$

$$d_c = \text{Centroid location measured from base}$$

$$A = \text{Separation footprint area}$$

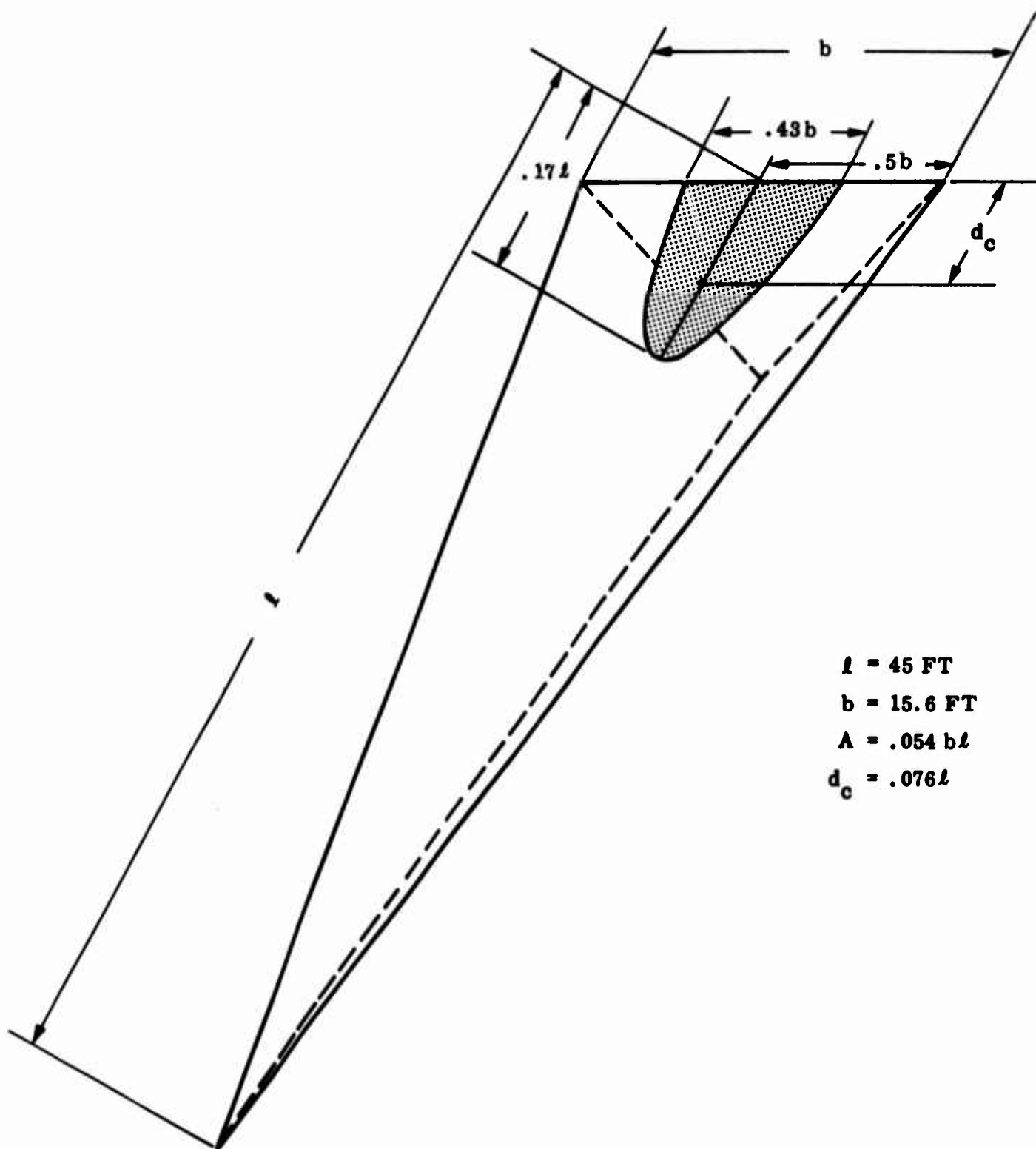


Figure III-1 Separation Footprint on Windside Surface for  $M_\infty = 6$ , 230-Kft Alt, and  $\alpha = 0 \text{ deg}$

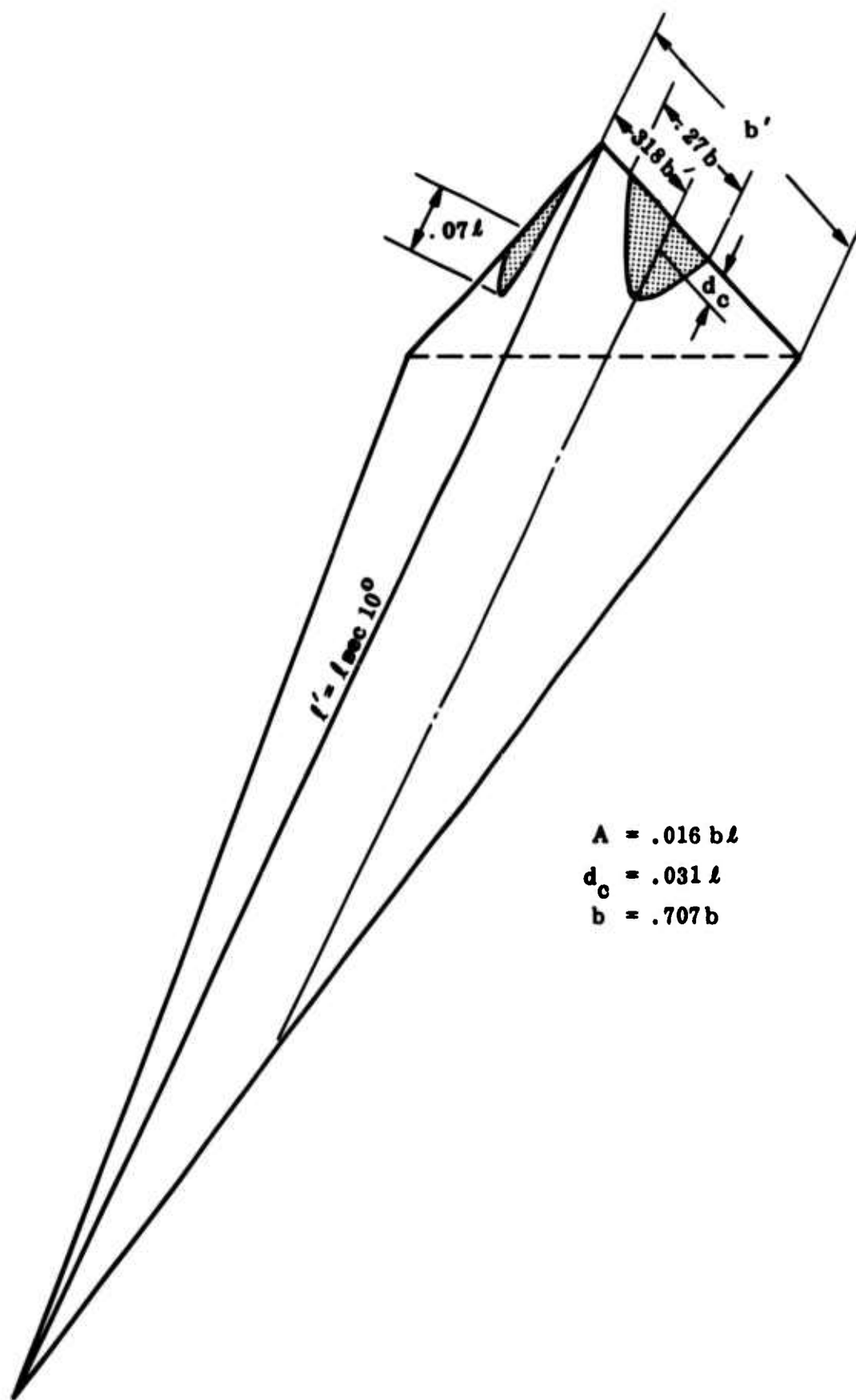


Figure III-2 Separation Footprint on Leeside Surface for  $M_\infty = 6$ , 230-Kft Alt, and  $\alpha = 0^\circ$



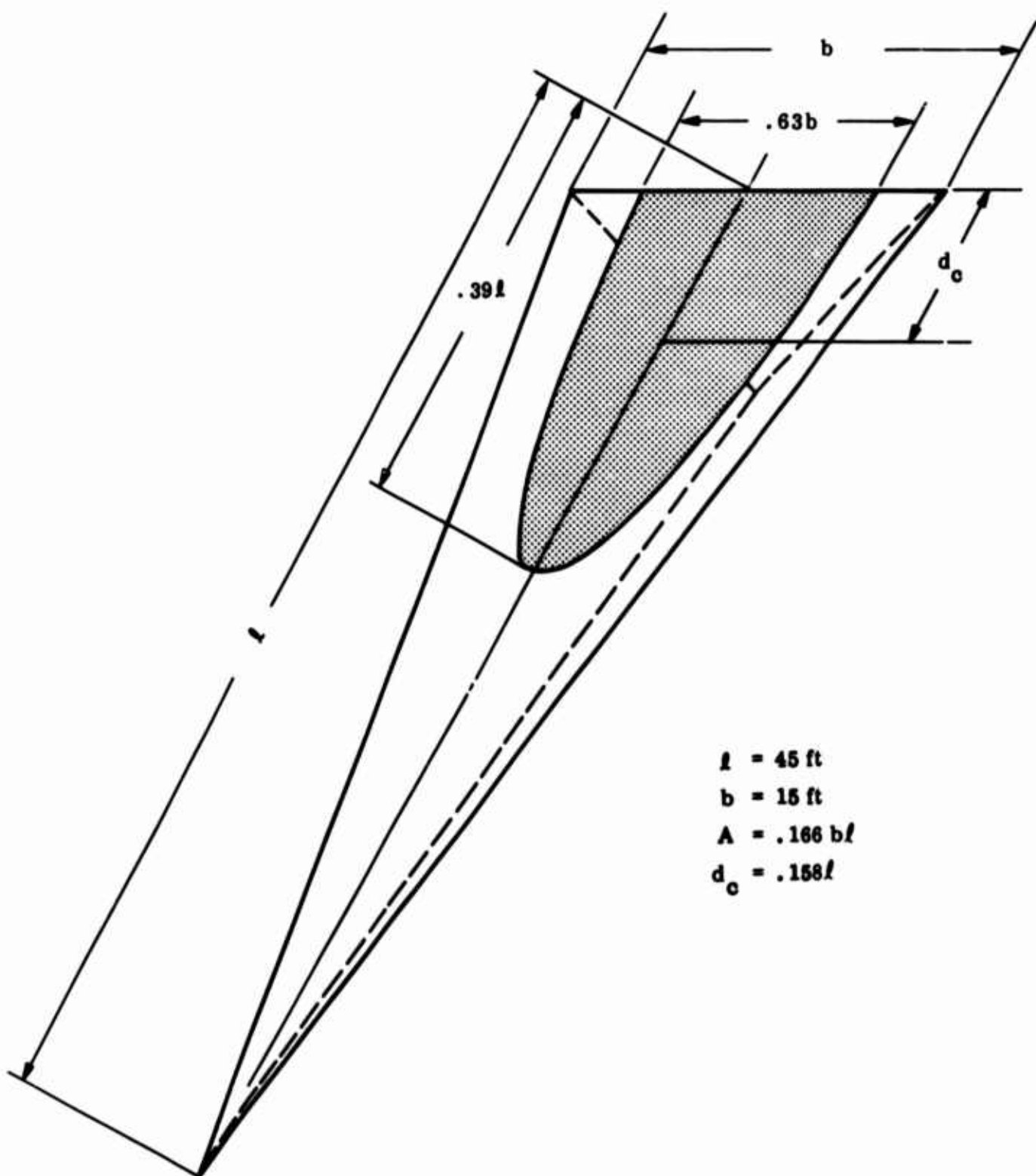


Figure III-3 Separation Footprint on Windside Surface for  $M_\infty = 6$ , 250-Kft Alt, and  $\alpha = 0^\circ$

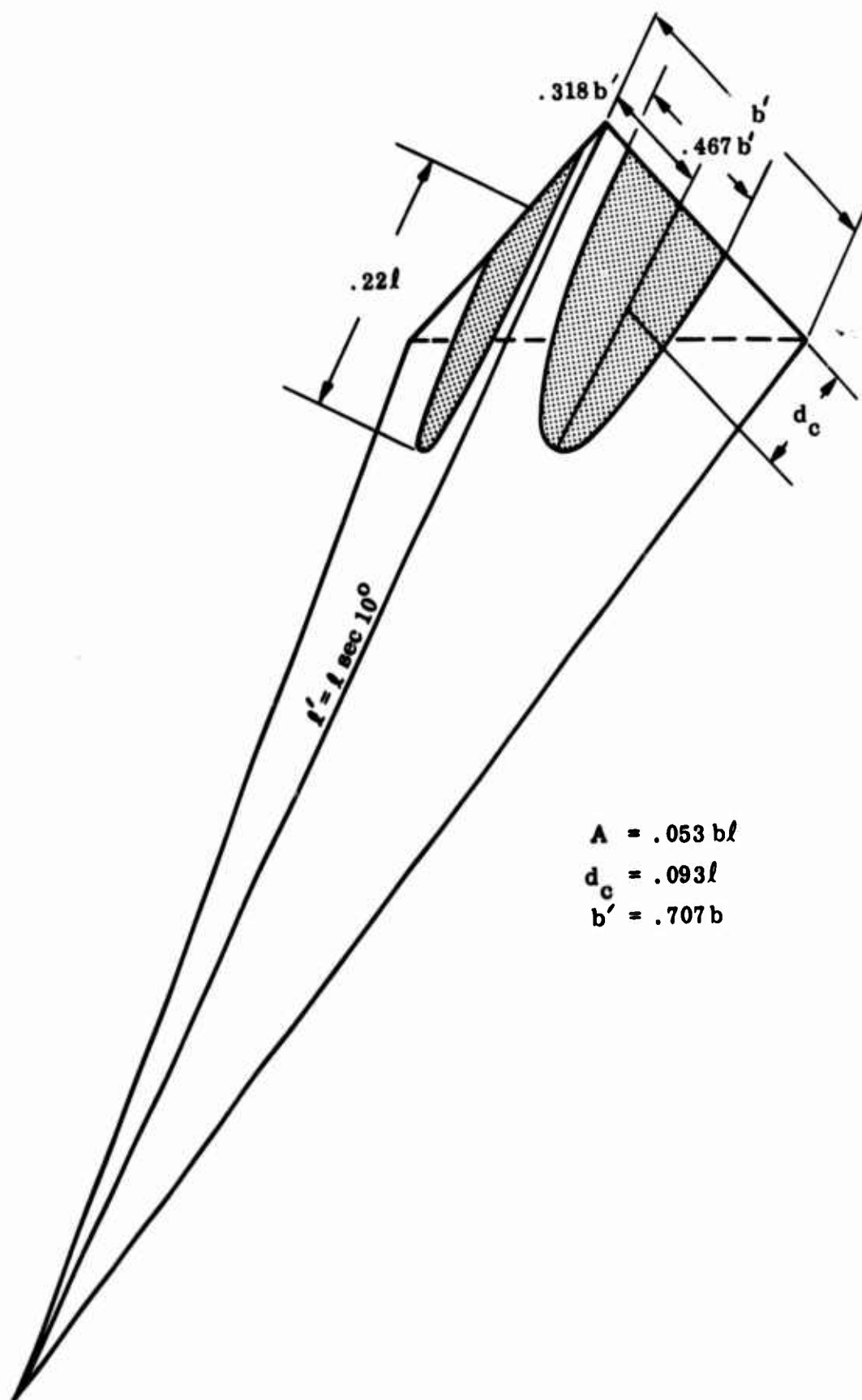


Figure III-4 Separation Footprint on Leeside Surface for  $M_\infty = 6$ , 250-Kft Alt, and  $\alpha = 0^\circ$

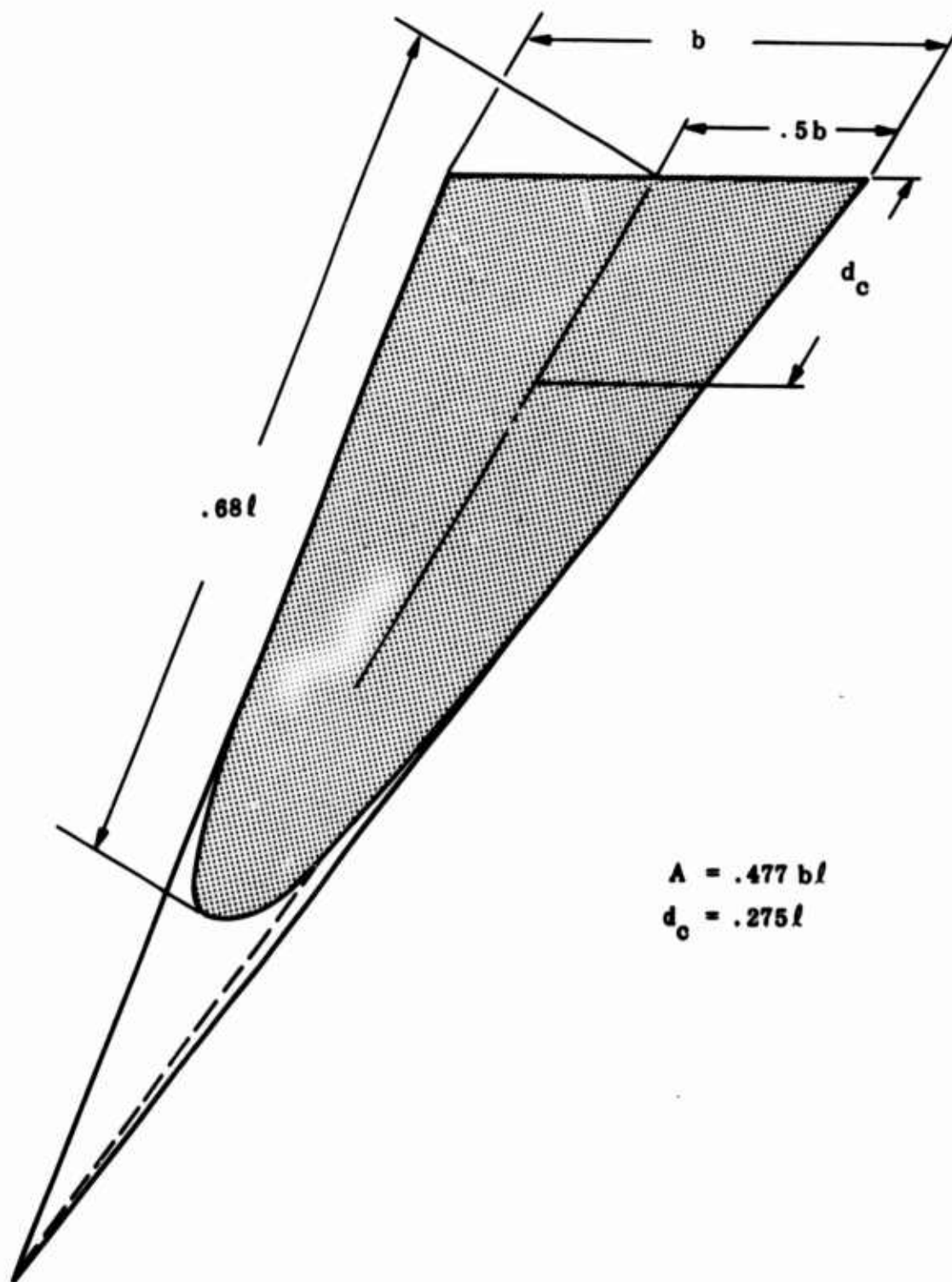


Figure III-5 Separation Footprint on Windside Surface for  $M_\infty = 6$ , 280-Kft Alt, and  $\alpha = 0$  deg

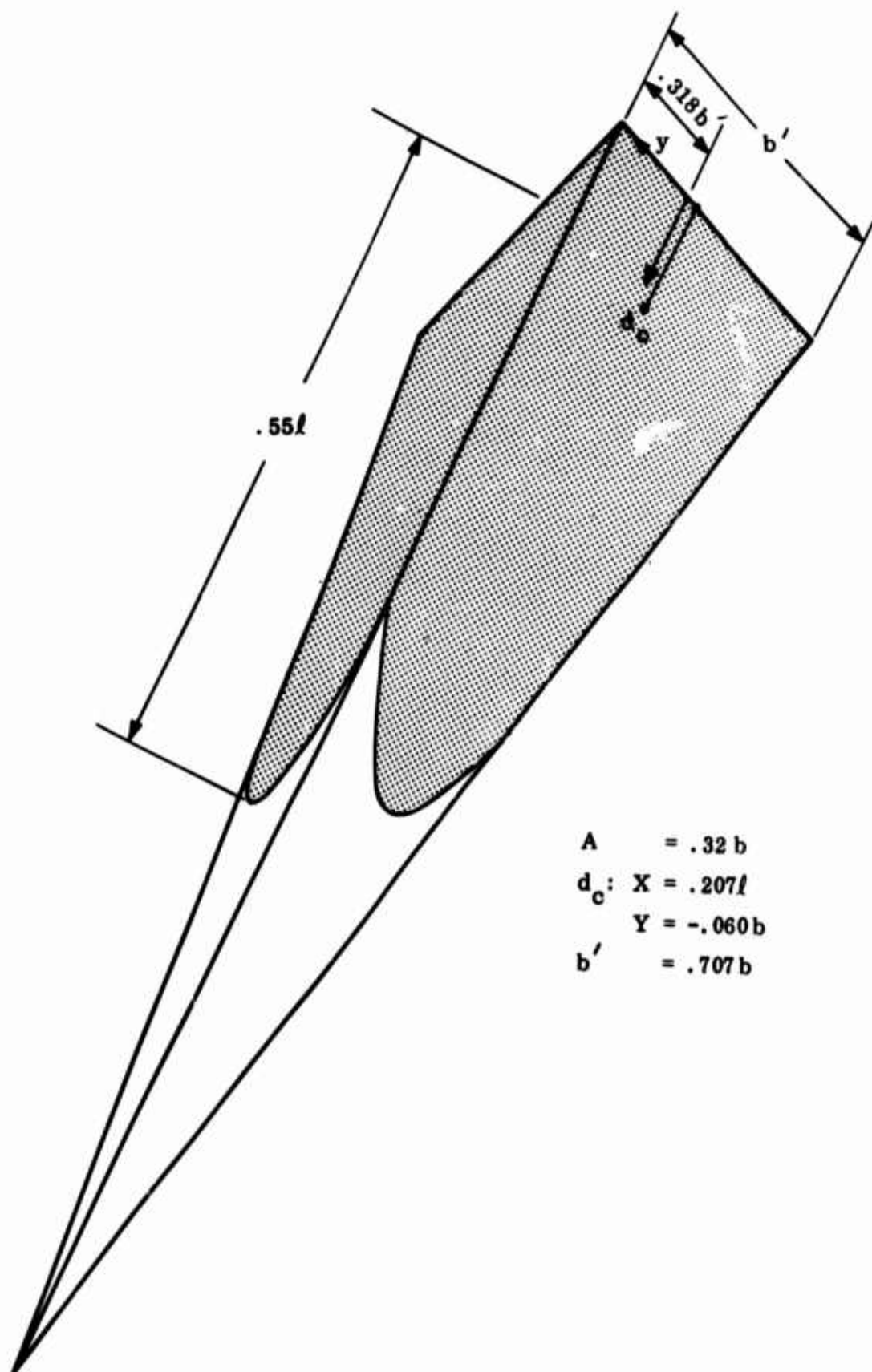


Figure III-6 Separation Footprint on Leeside Surface for  $M_\infty = 6$ , 280-Kft Alt, and  $\alpha = 0$  deg

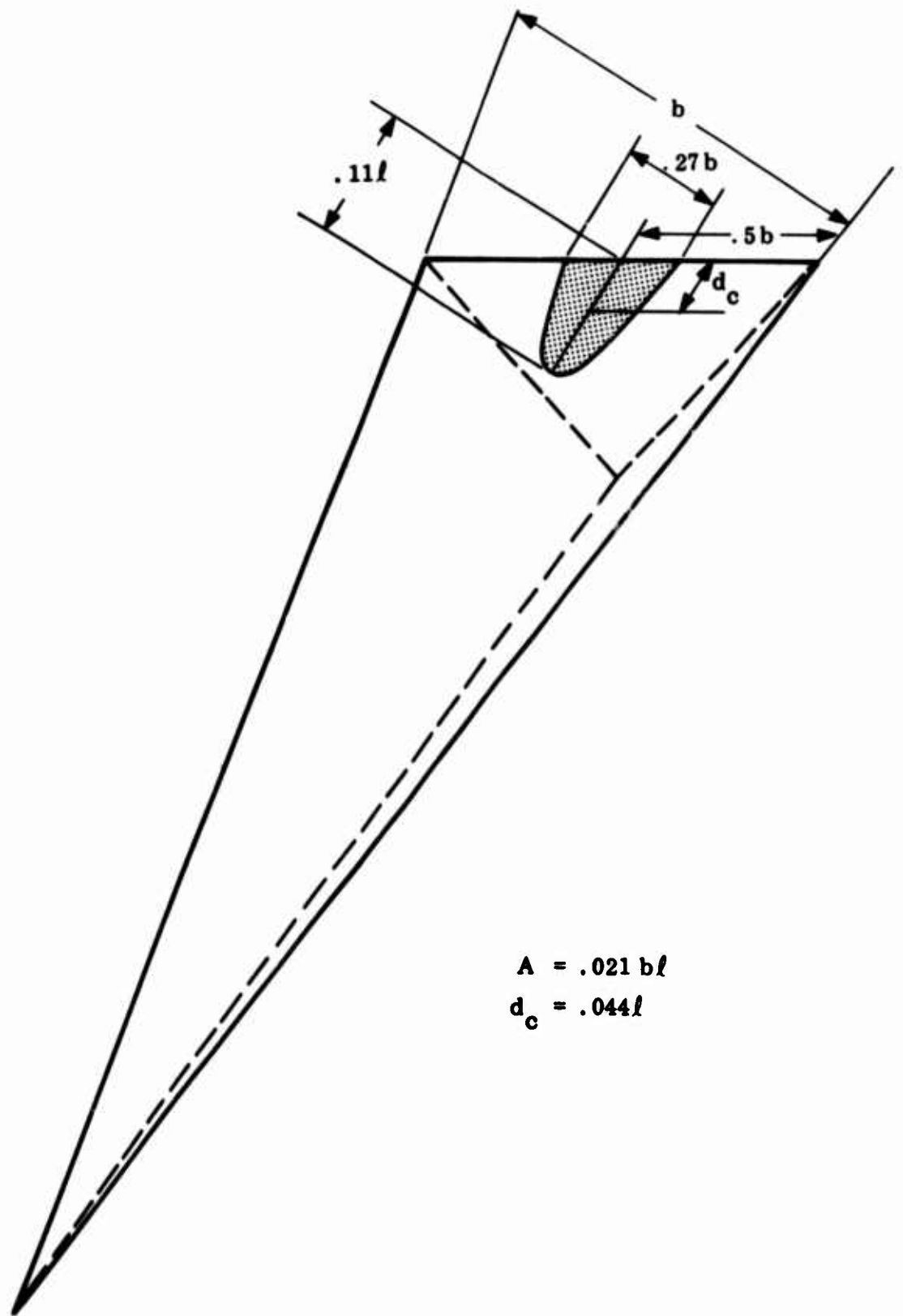


Figure III-7 Separation Footprint on Windside Surface for  $M_\infty = 10$ , 230-Kft Alt, and  $\alpha = 0$  deg

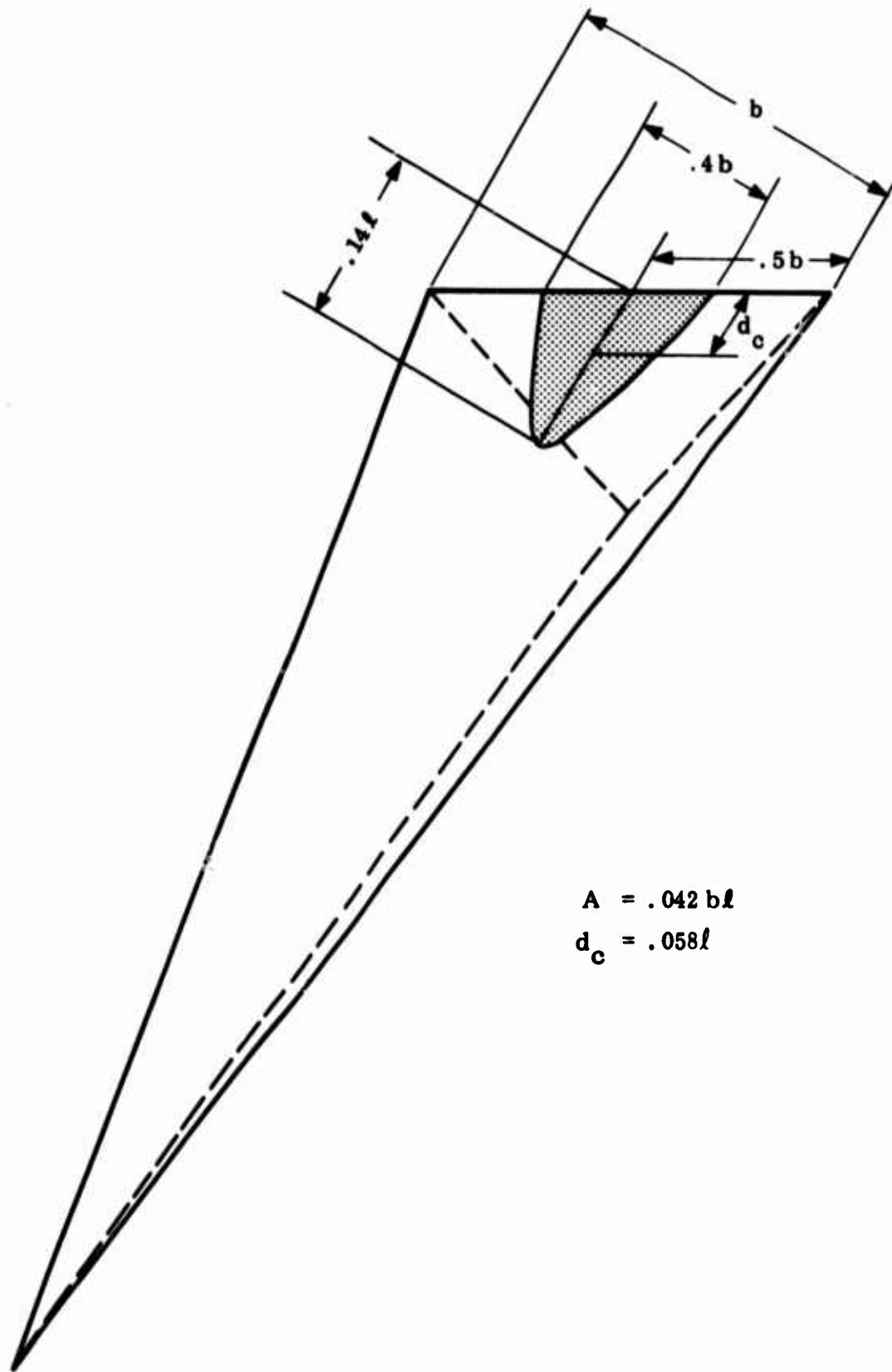


Figure III-8 Separation Footprint on Windside Surface for  $M_\infty = 10$ , 250-Kft Alt, and  $\alpha = 0$  deg

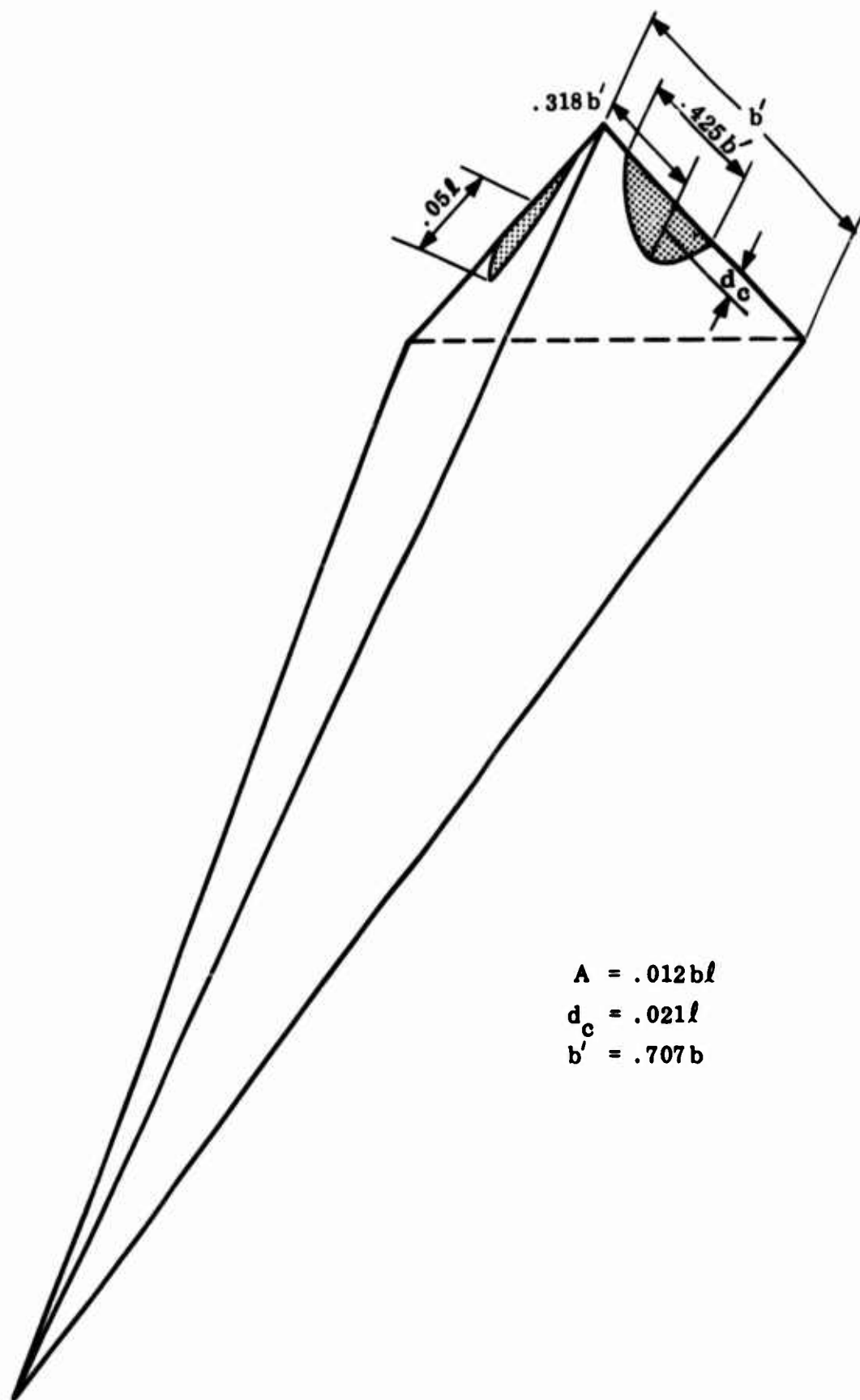


Figure III-9 Separation Footprint on Leeside Surface for  $M_\infty = 10$ , 250-Kft Alt, and  $\alpha = 0$  deg

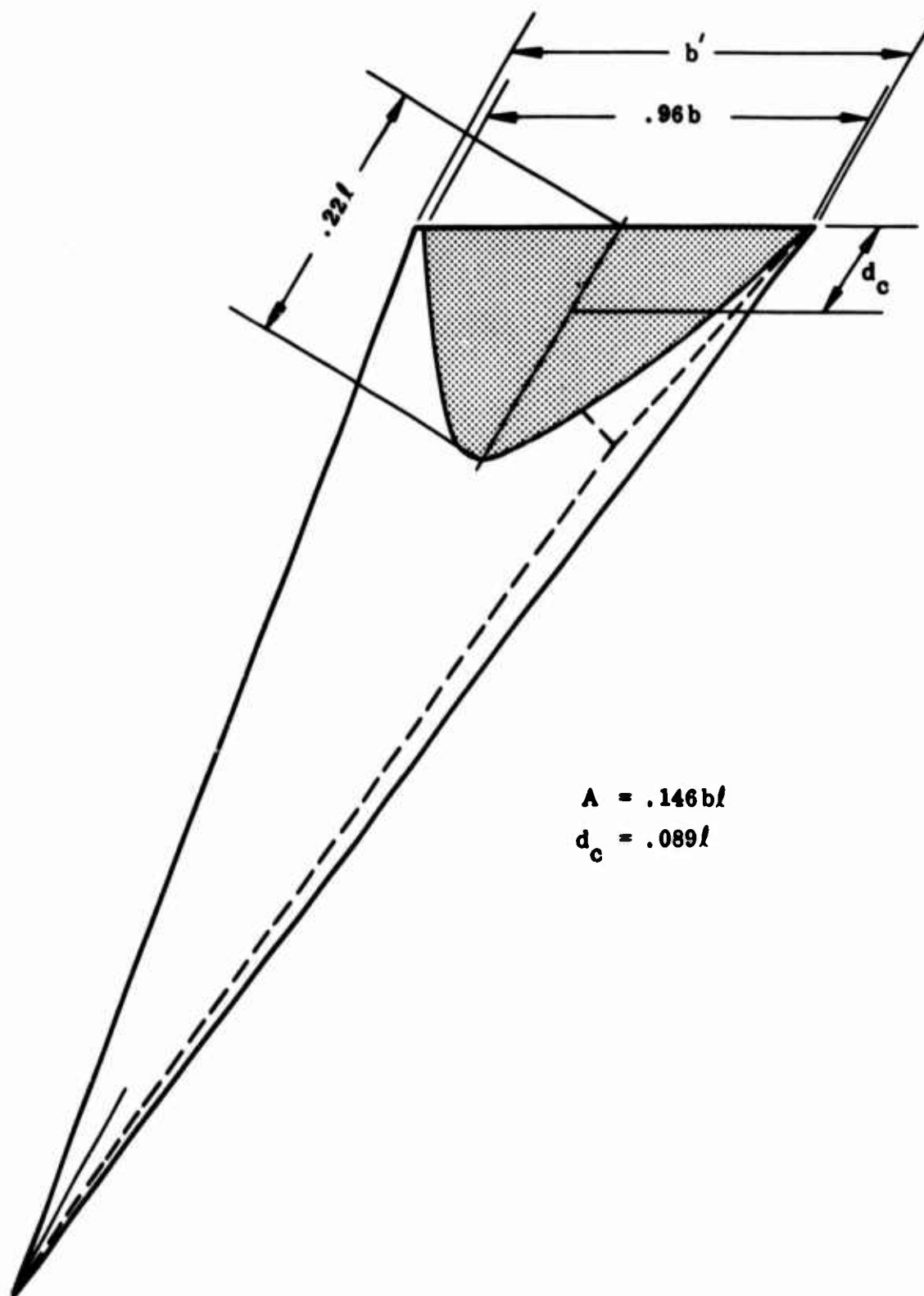


Figure III-10 Separation Footprint on Windside Surface for  $M_\infty = 10$ , 280-Kft Alt, and  $\alpha = 0$  deg



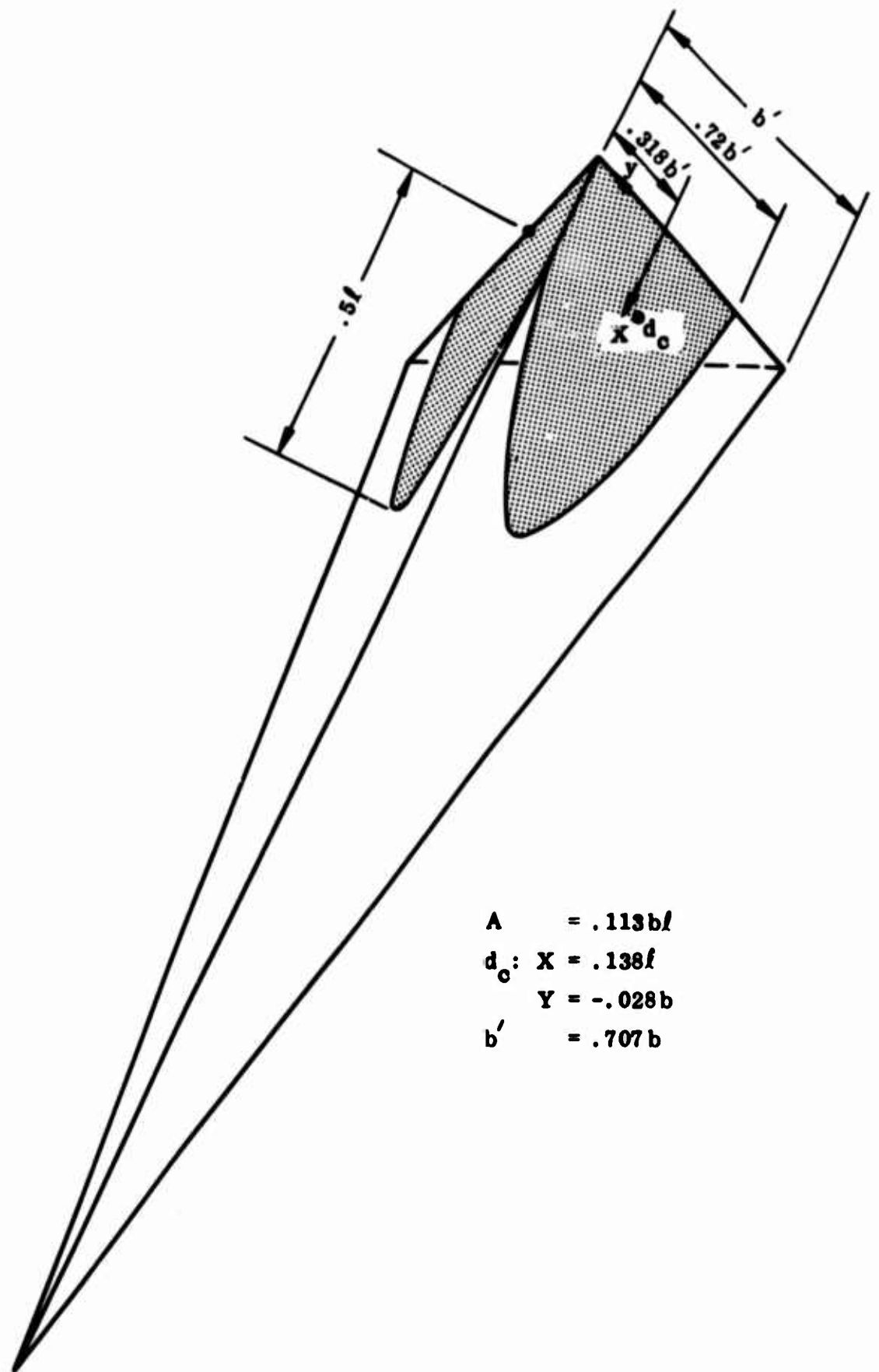


Figure III-11 Separation Footprint on Leeward Surface for  $M_o = 10$ , 280-Kft Alt, and  $\alpha = 0$  deg

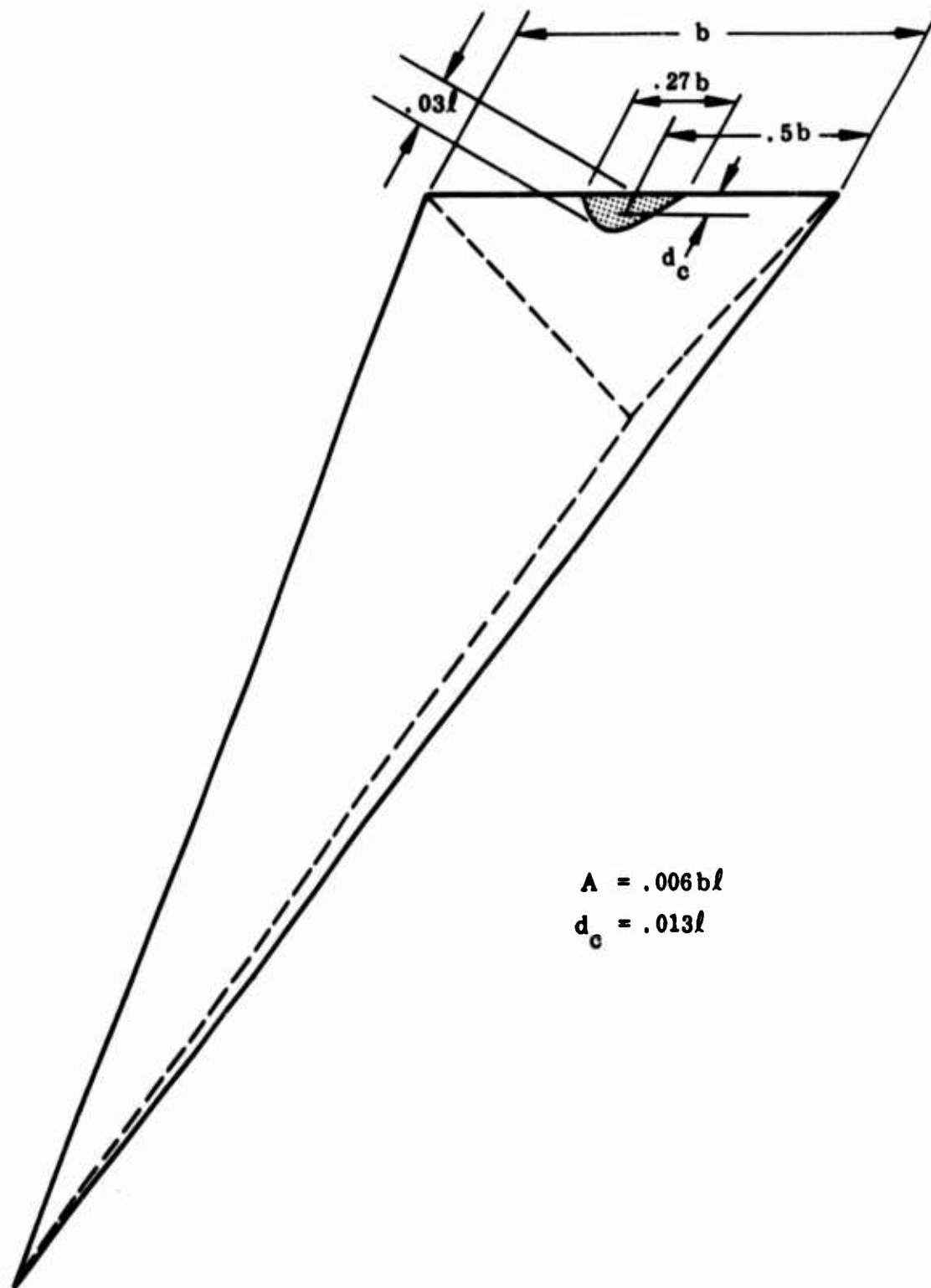


Figure III-12 Separation Footprint on Windside Surface for  $M_\infty = 15$ , 230-Kft Alt, and  $\alpha = 0$  deg

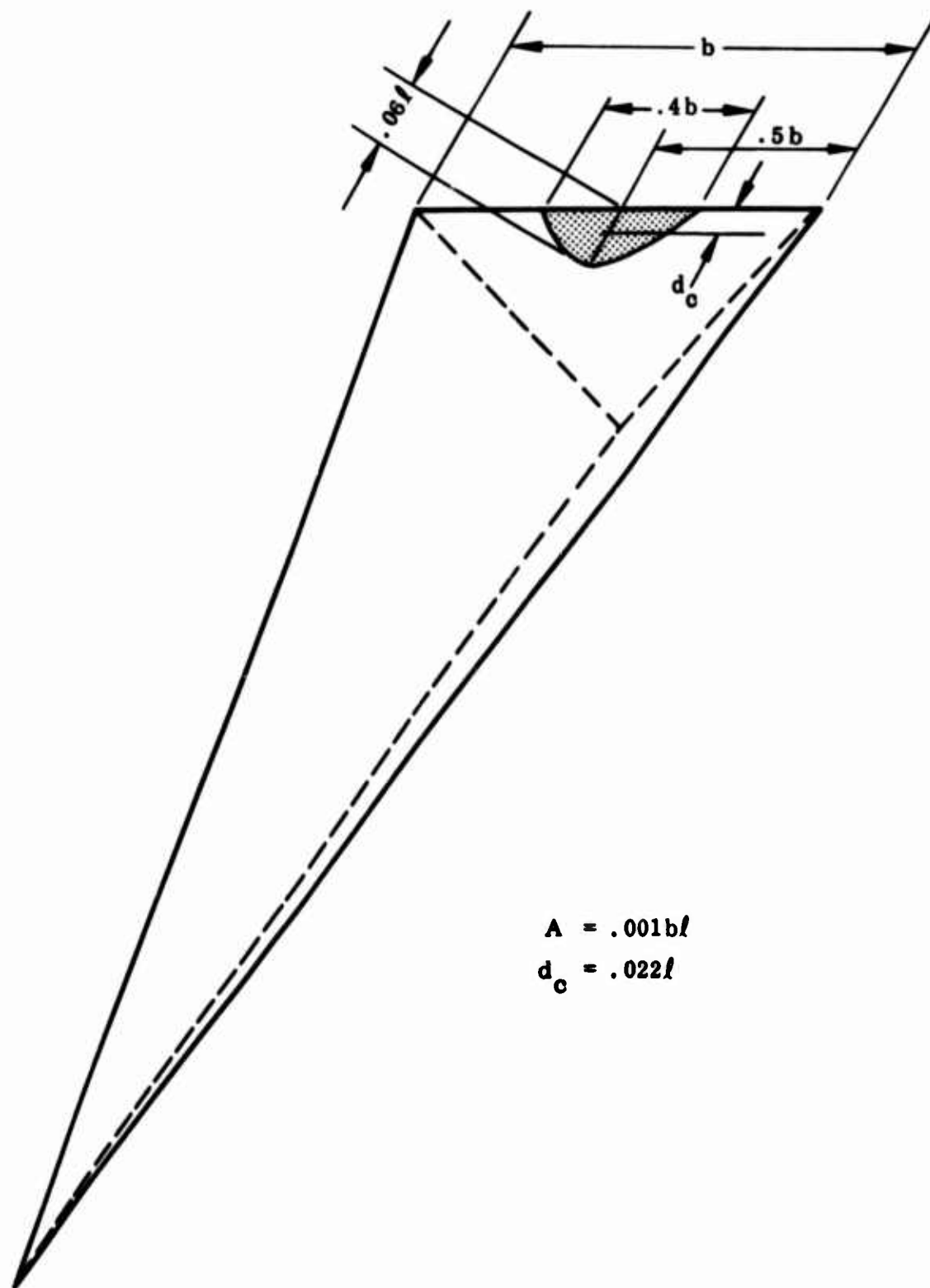


Figure III-13 Separation Footprint on Windside Surface for  $M_\infty = 15$ , 250-Kft Alt, and  $\alpha = 0^\circ$

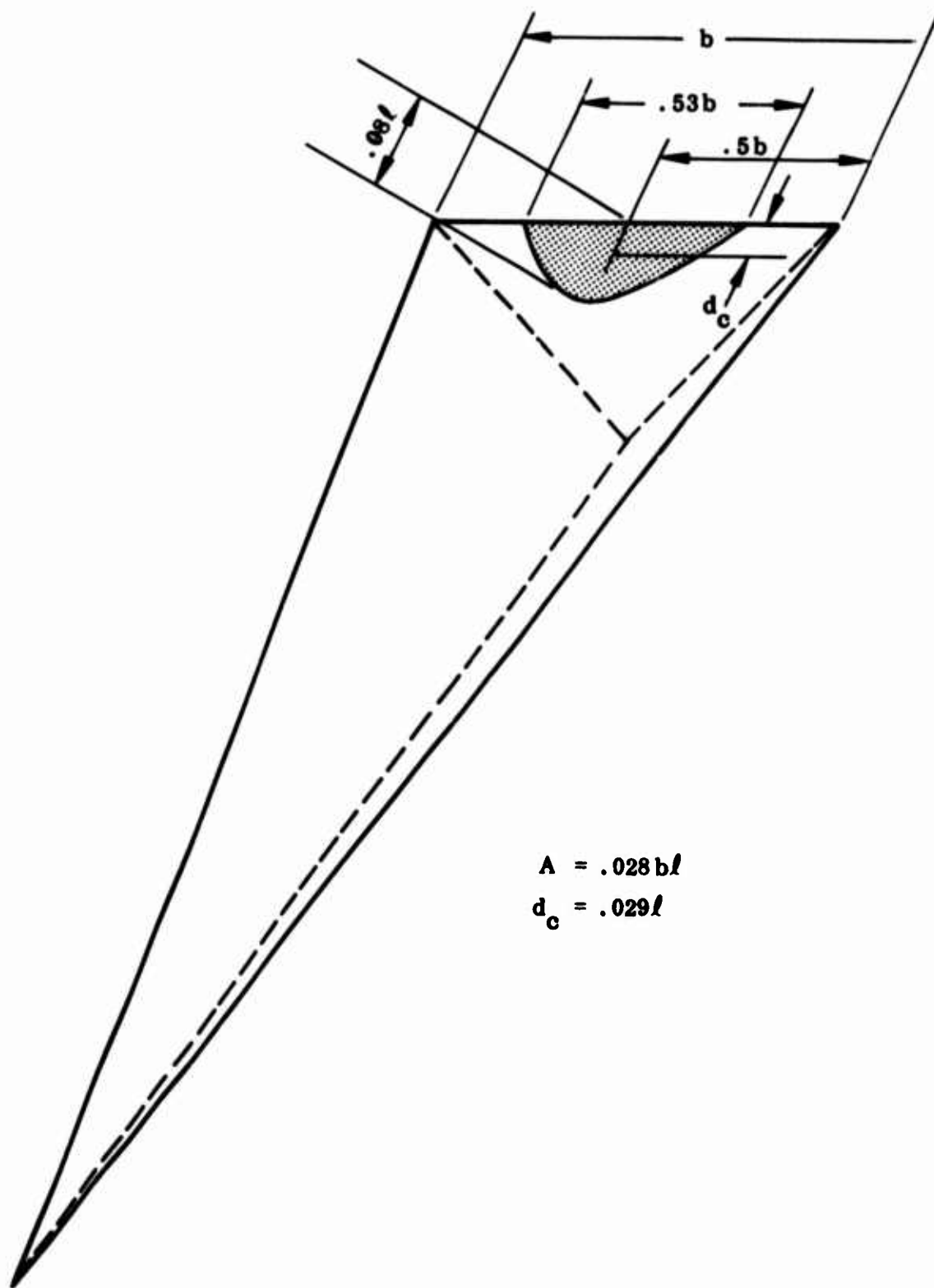


Figure III-14 Separation Footprint on Windside Surface for  $M_\infty = 15$ , 280-Kft Alt, and  $\alpha = 0$  deg

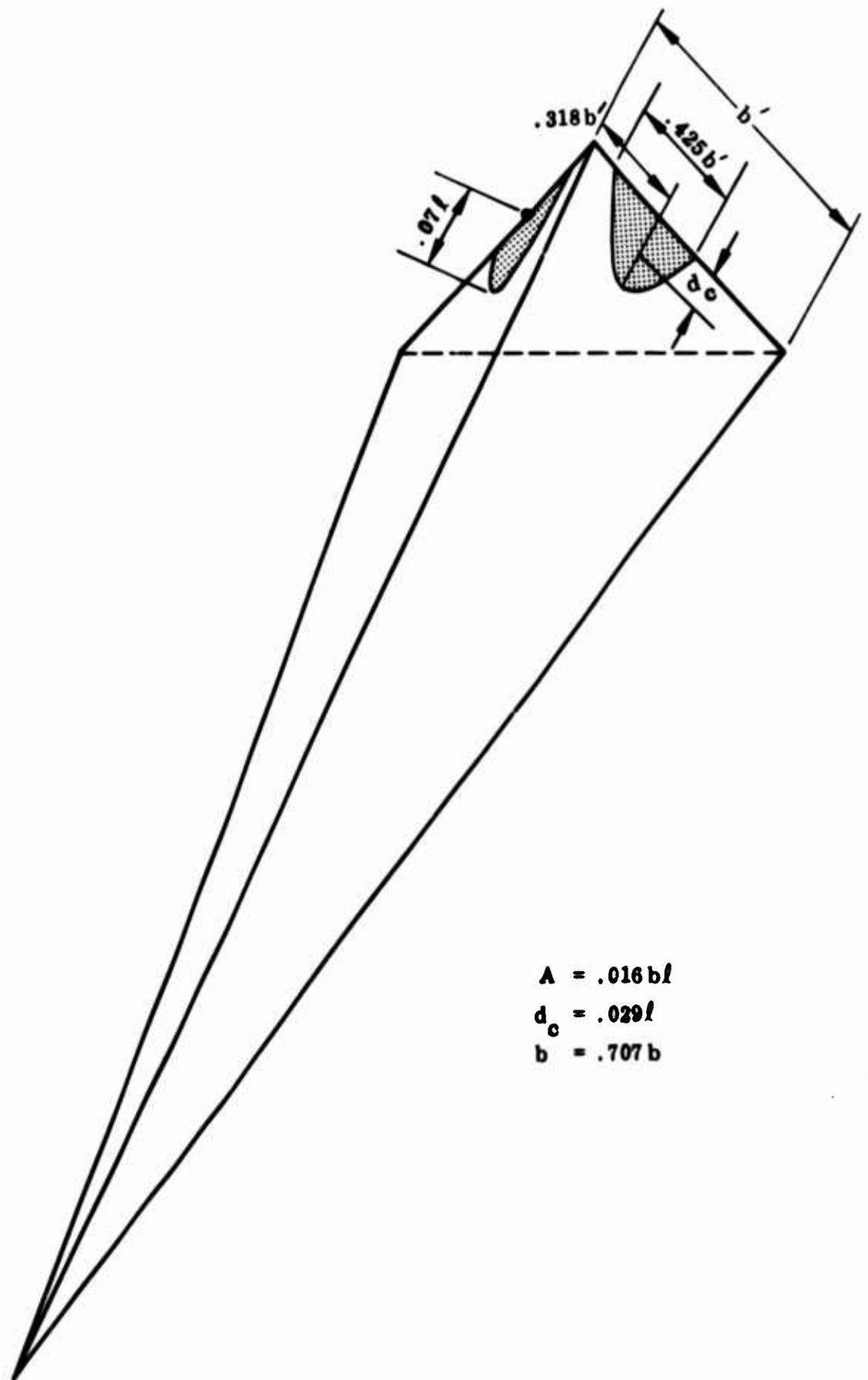


Figure III-15 Separation Footprint on Leeside Surface for  $M_\infty = 15$ , 280-Kft Alt, and  $\alpha = 0$  deg

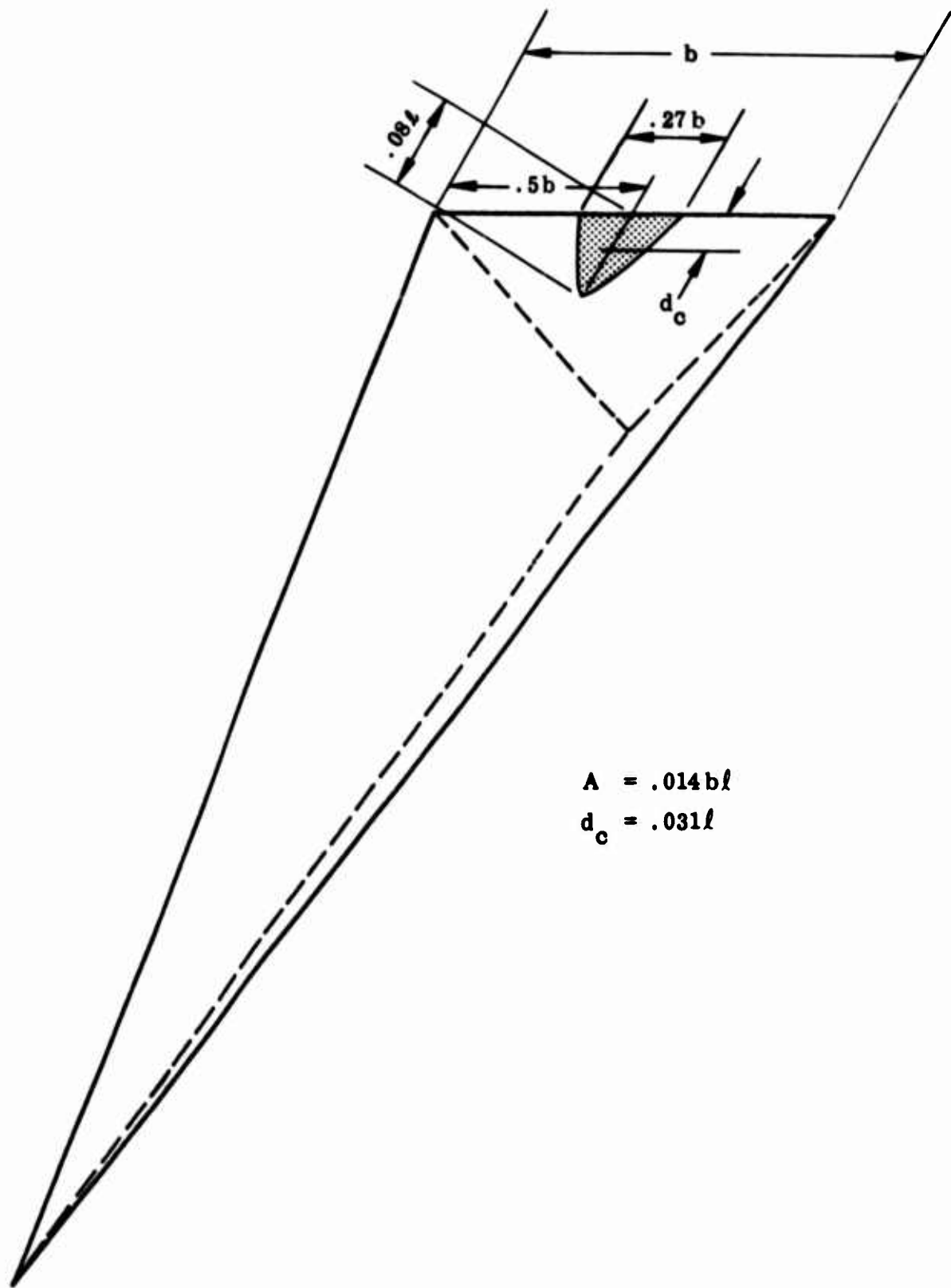
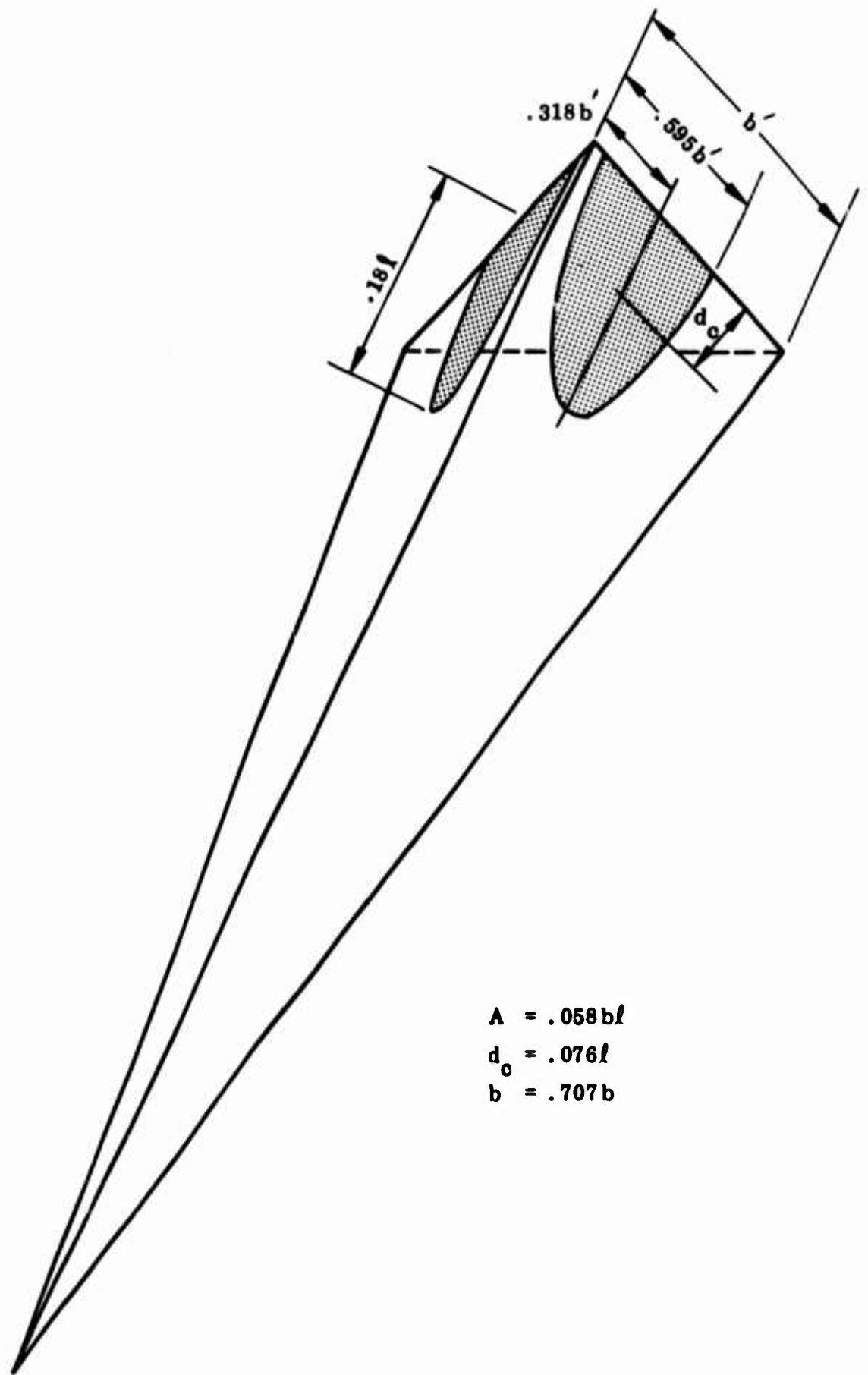


Figure III-16 Separation Footprint on Windside Surface for  $M_\infty = 6$ , 230-Kft Alt, and  $\alpha = +10$  deg



$$A = .058bl$$

$$d_c = .076l$$

$$b = .707b$$

Figure III-17 Separation Footprint on Leeside Surface for  $M_\infty = 6$ , 230-Kft Alt, and  $\alpha = +10$  deg

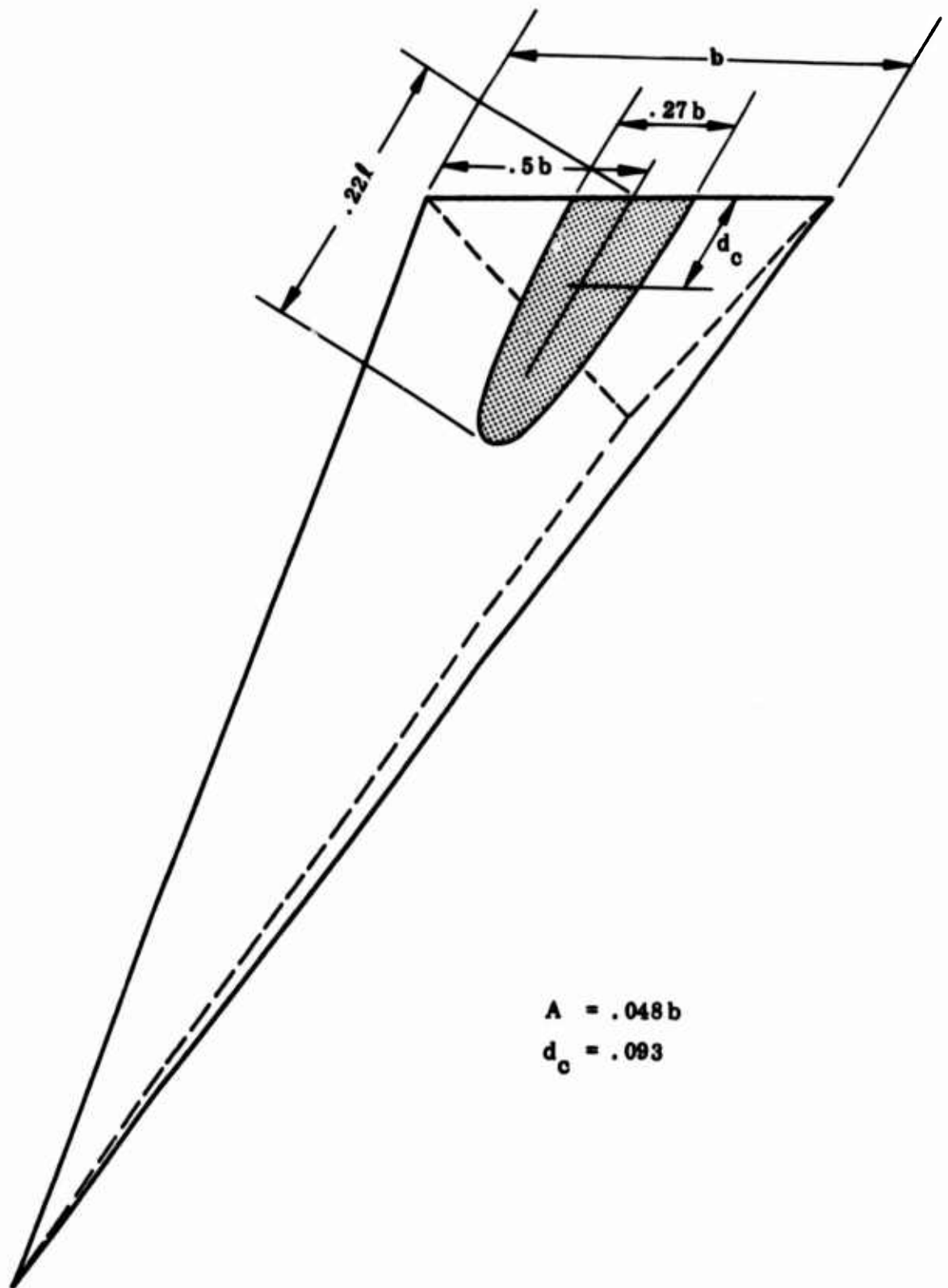
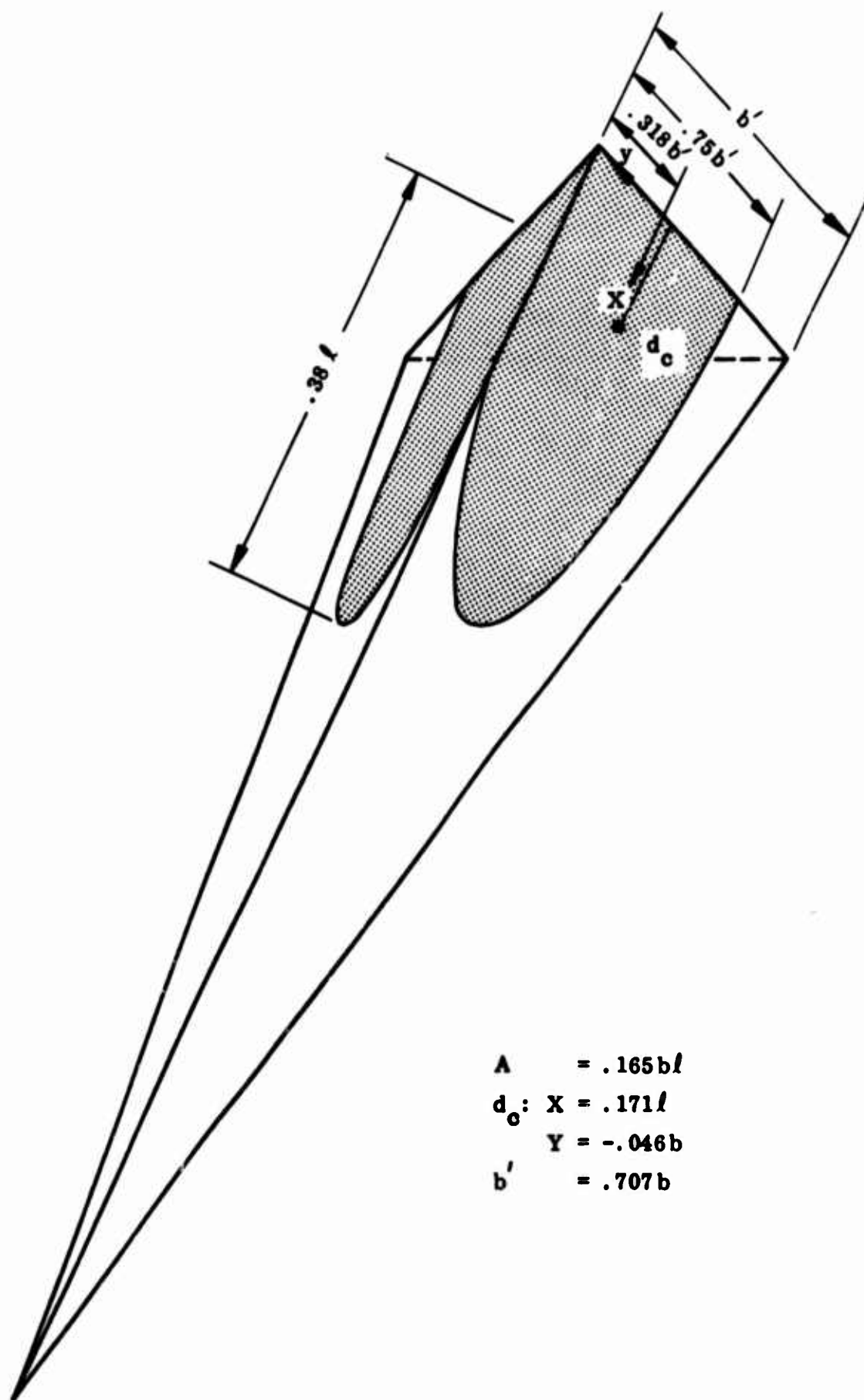


Figure III-18 Separation Footprint on Windside Surface  
 $M_\infty = 6$ , 250-Kft Alt, and  $\alpha = +10$  deg





$$\begin{aligned}
 A &= .165 b l \\
 d_o: X &= .171 l \\
 Y &= -.046 b \\
 b' &= .707 b
 \end{aligned}$$

Figure III-19 Separation Footprint on Leeside Surface for  $M_\infty = 6$ , 250-Kft Alt, and  $\alpha = +10$  deg

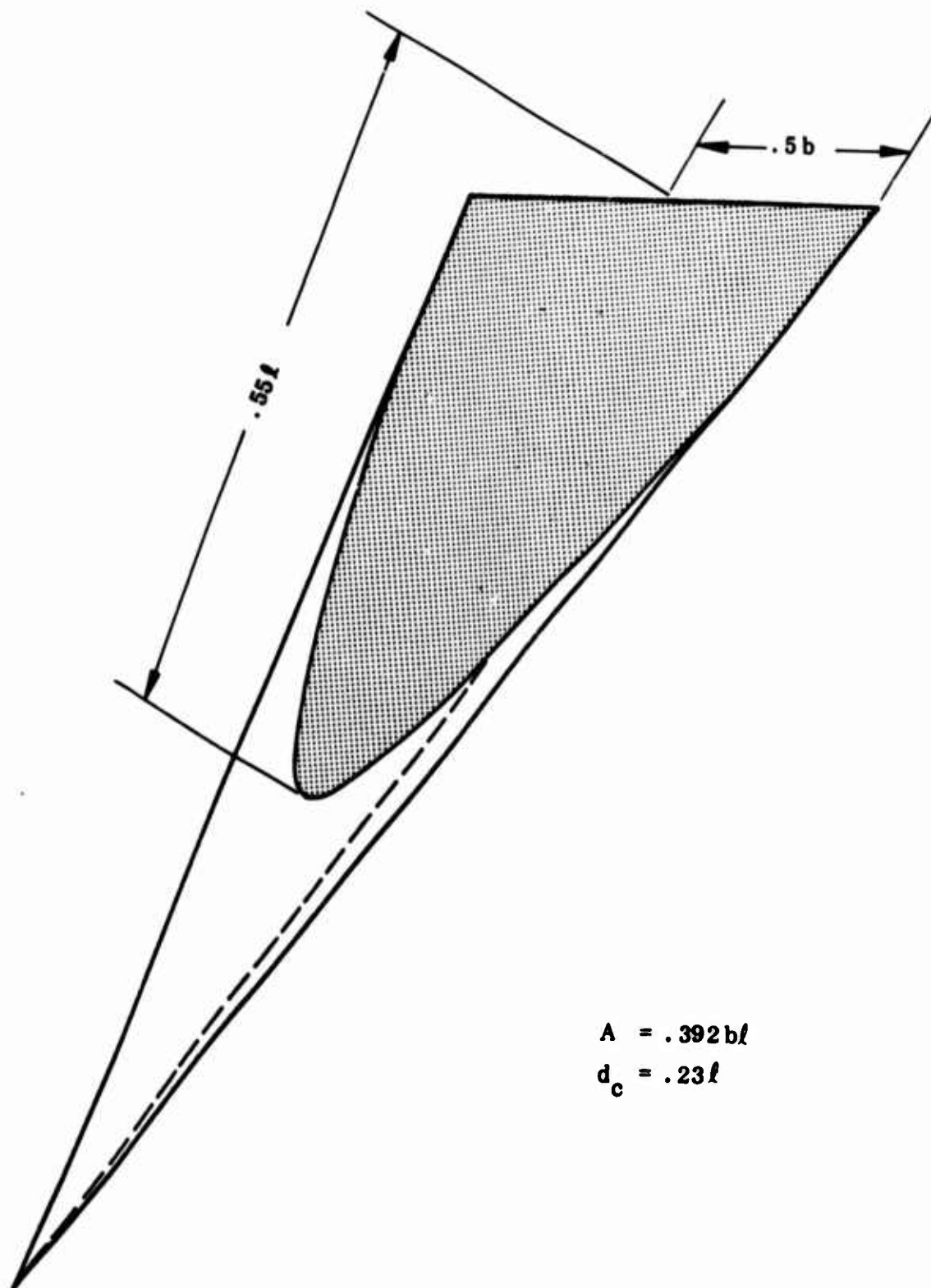


Figure III-20 Separation Footprint on Windside Surface for  $M_\infty = 6$ , 280-Kft Alt, and  $\alpha = +10$  deg

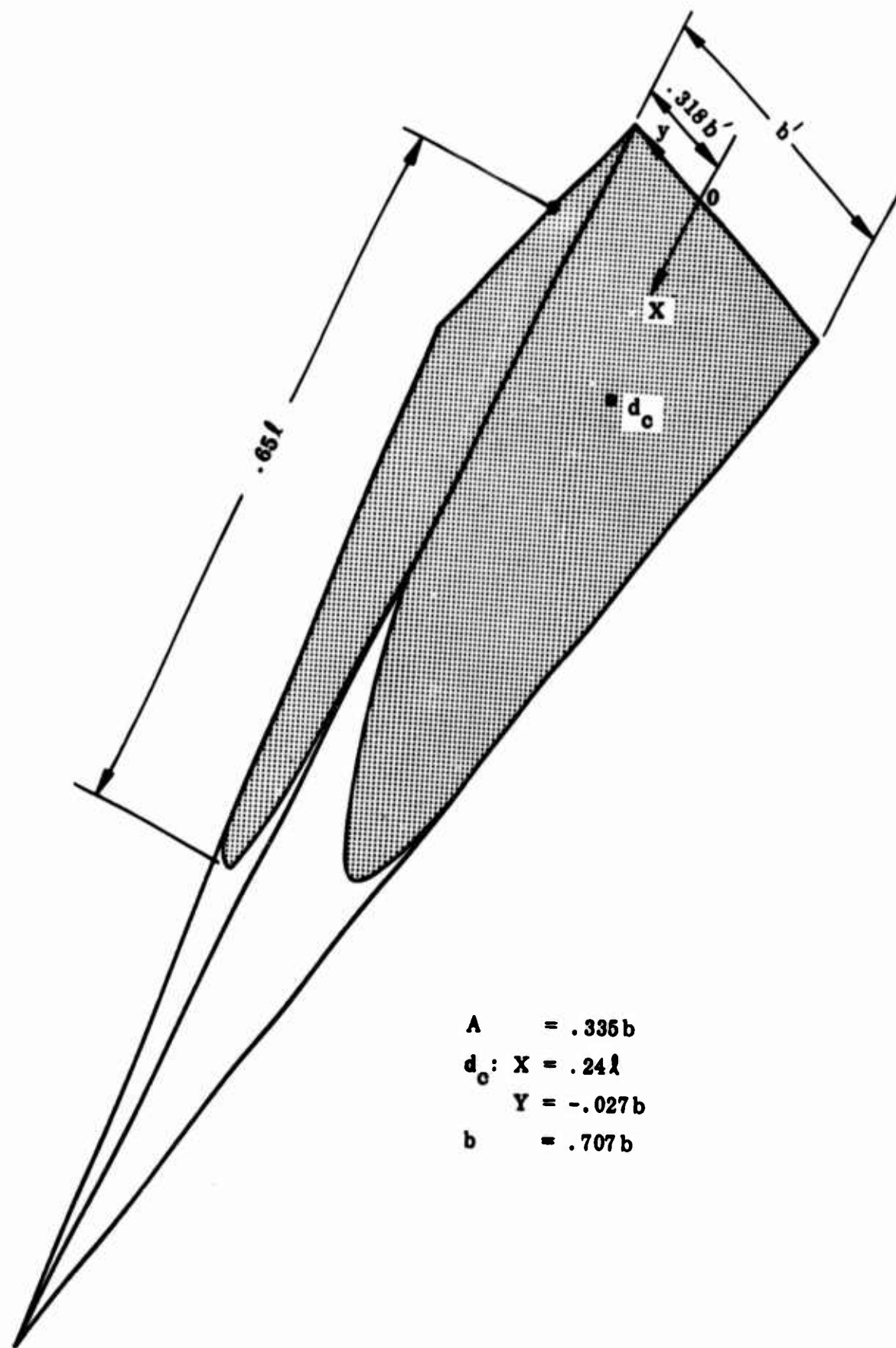


Figure III-21 Separation Footprint on Leeside Surface for  $M_\infty 6$ , 280-Kft Alt, and  $\alpha = +10$  deg

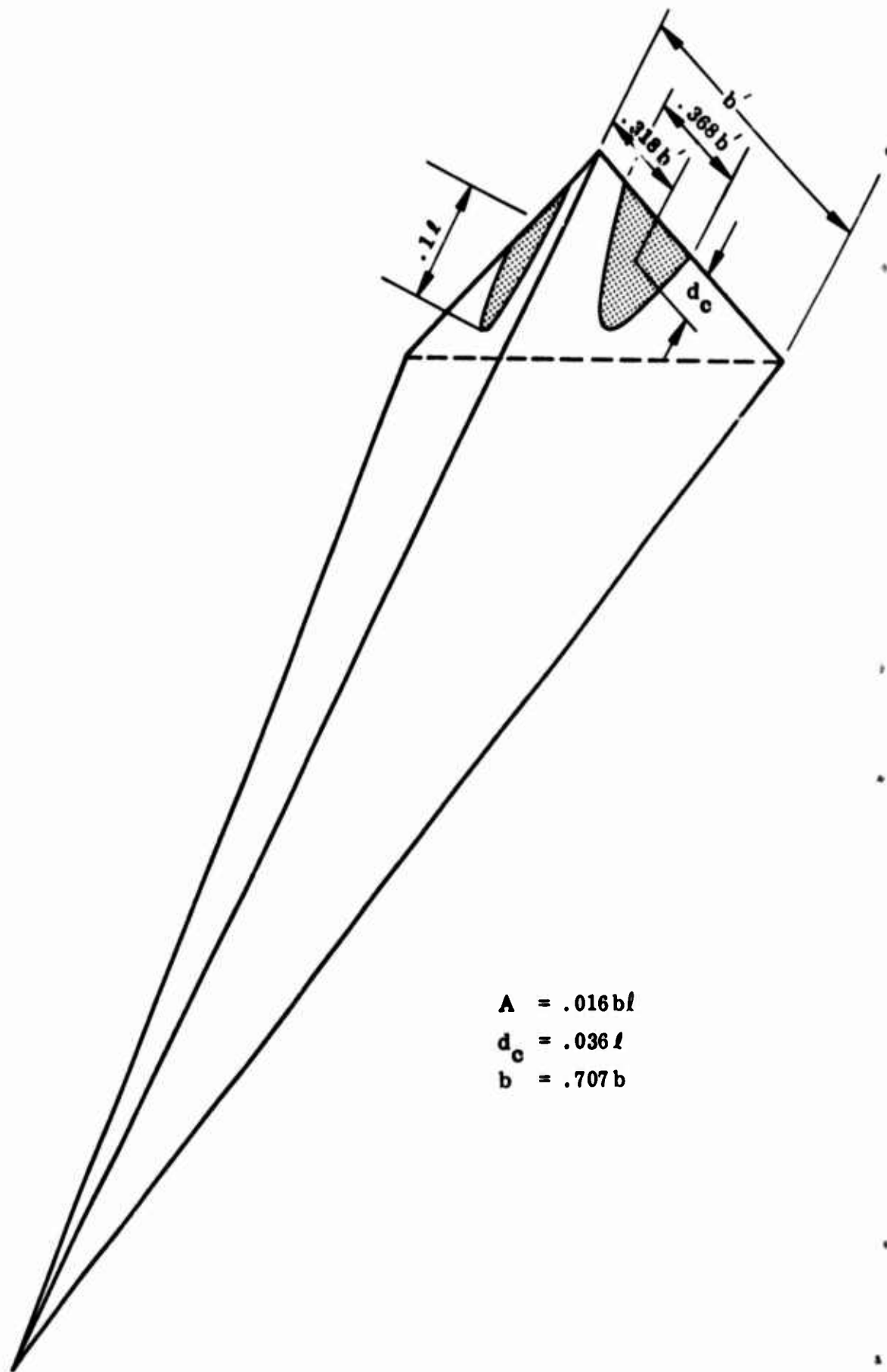


Figure III-22 Separation Footprint on Leeside Surface for  $M_\infty = 10$ , 230-Kft Alt, and  $\alpha = +10$  deg

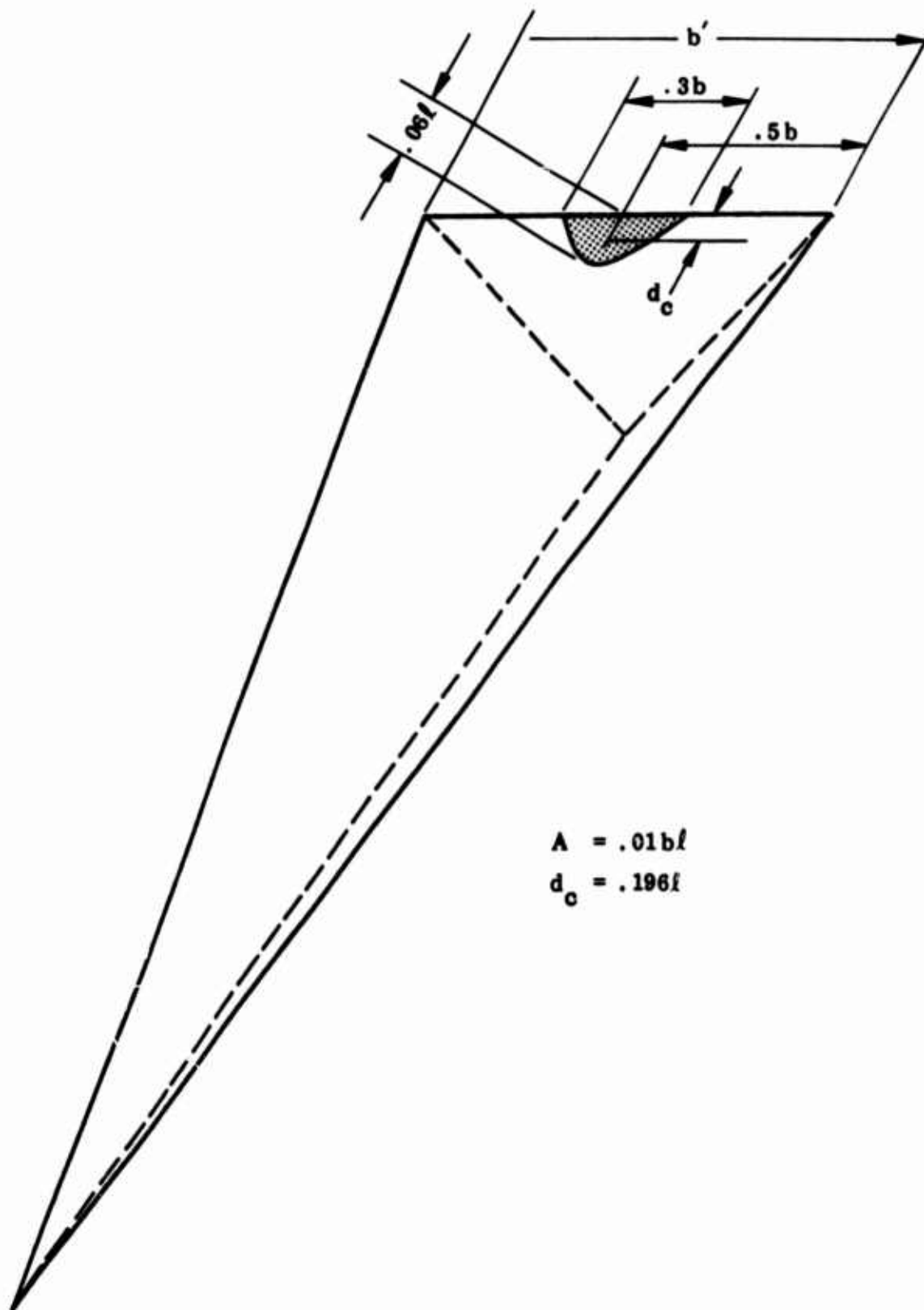


Figure III-23 Separation Footprint on Windside Surface for  $M_o = 10$ , 250-Kft Alt, and  $\alpha = +10$  deg

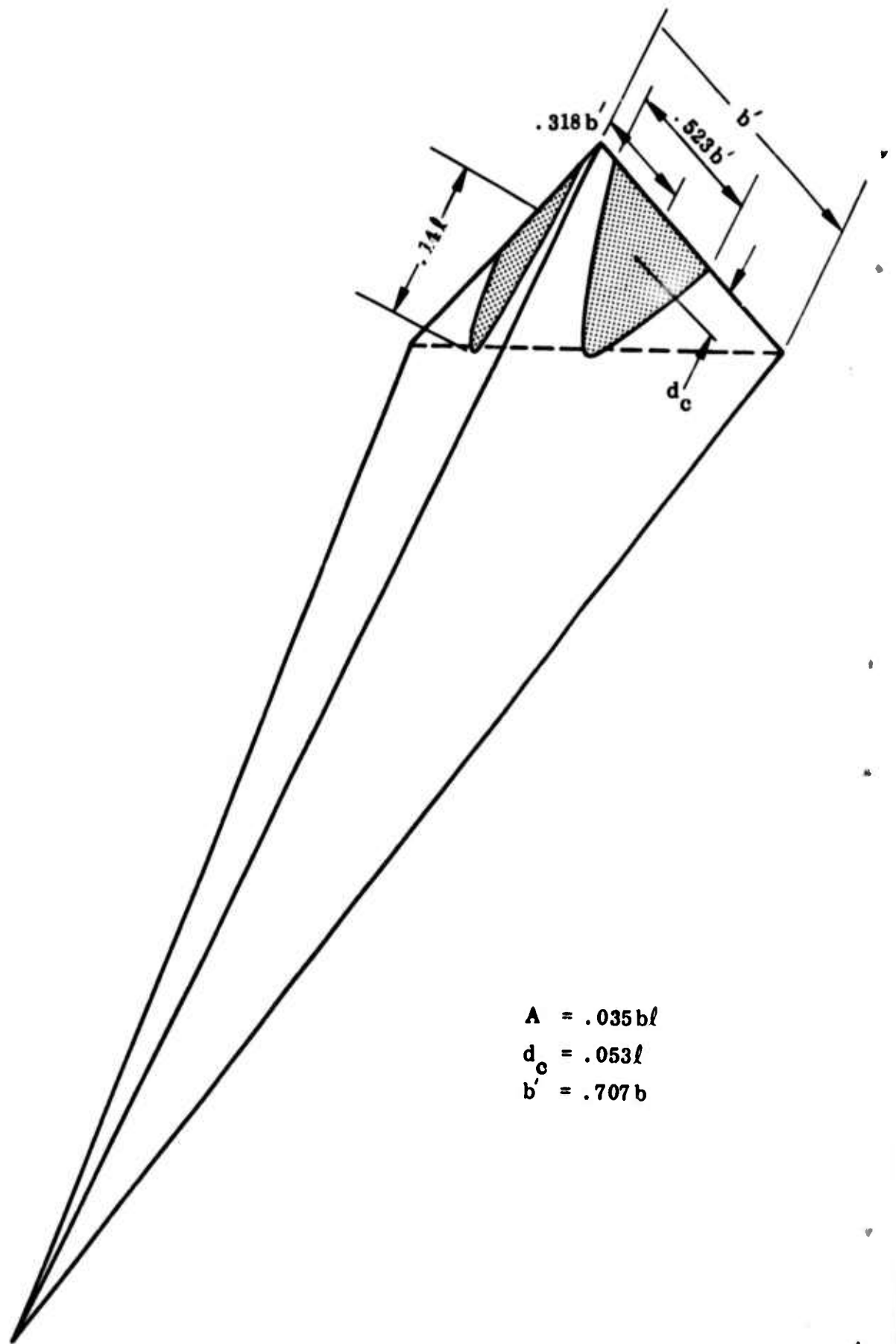


Figure III-24 Separation Footprint on Leeside Surface for  $M_\infty = 10$ , 250-Kft Alt, and  $\alpha = +10$  deg

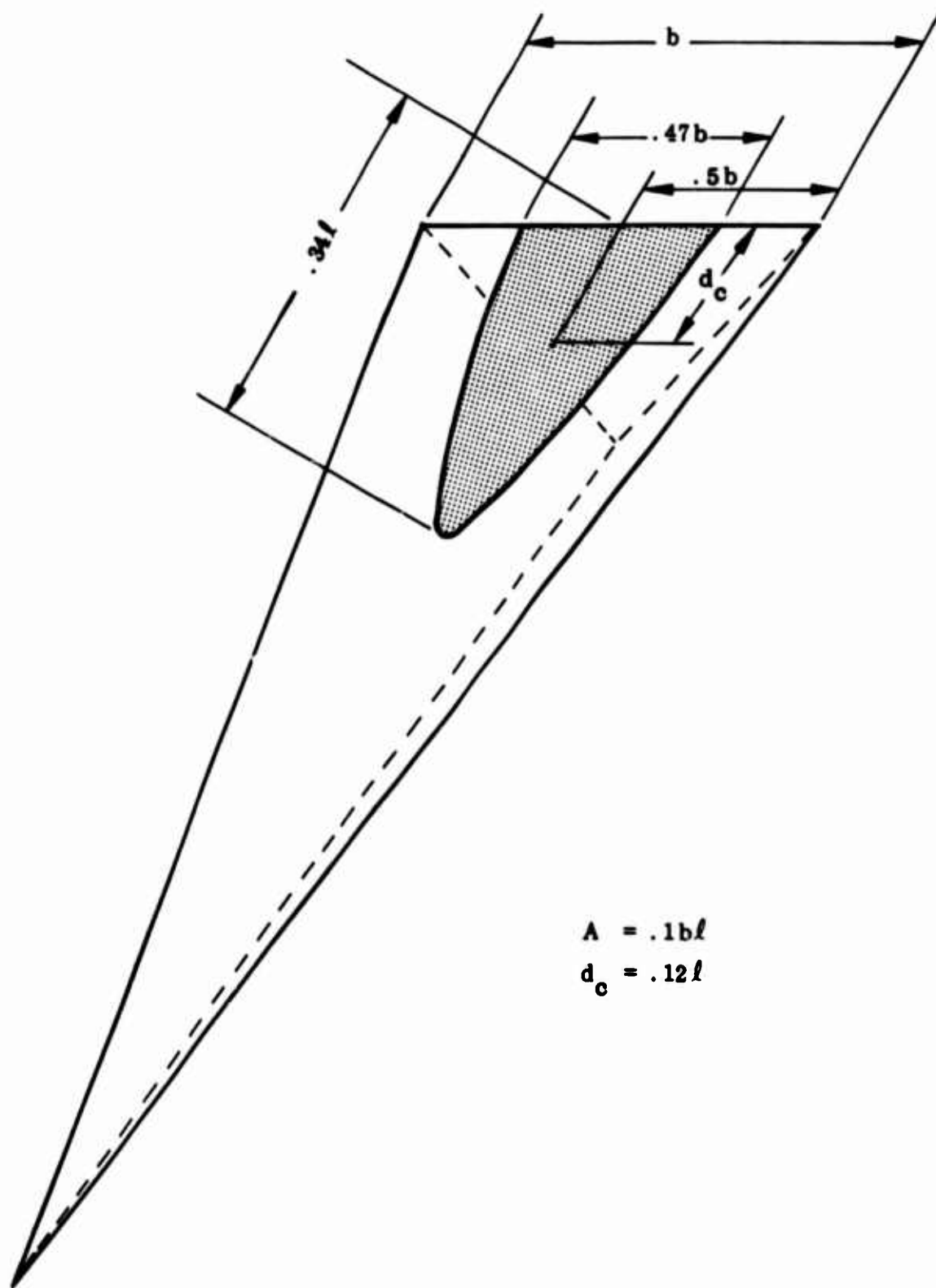
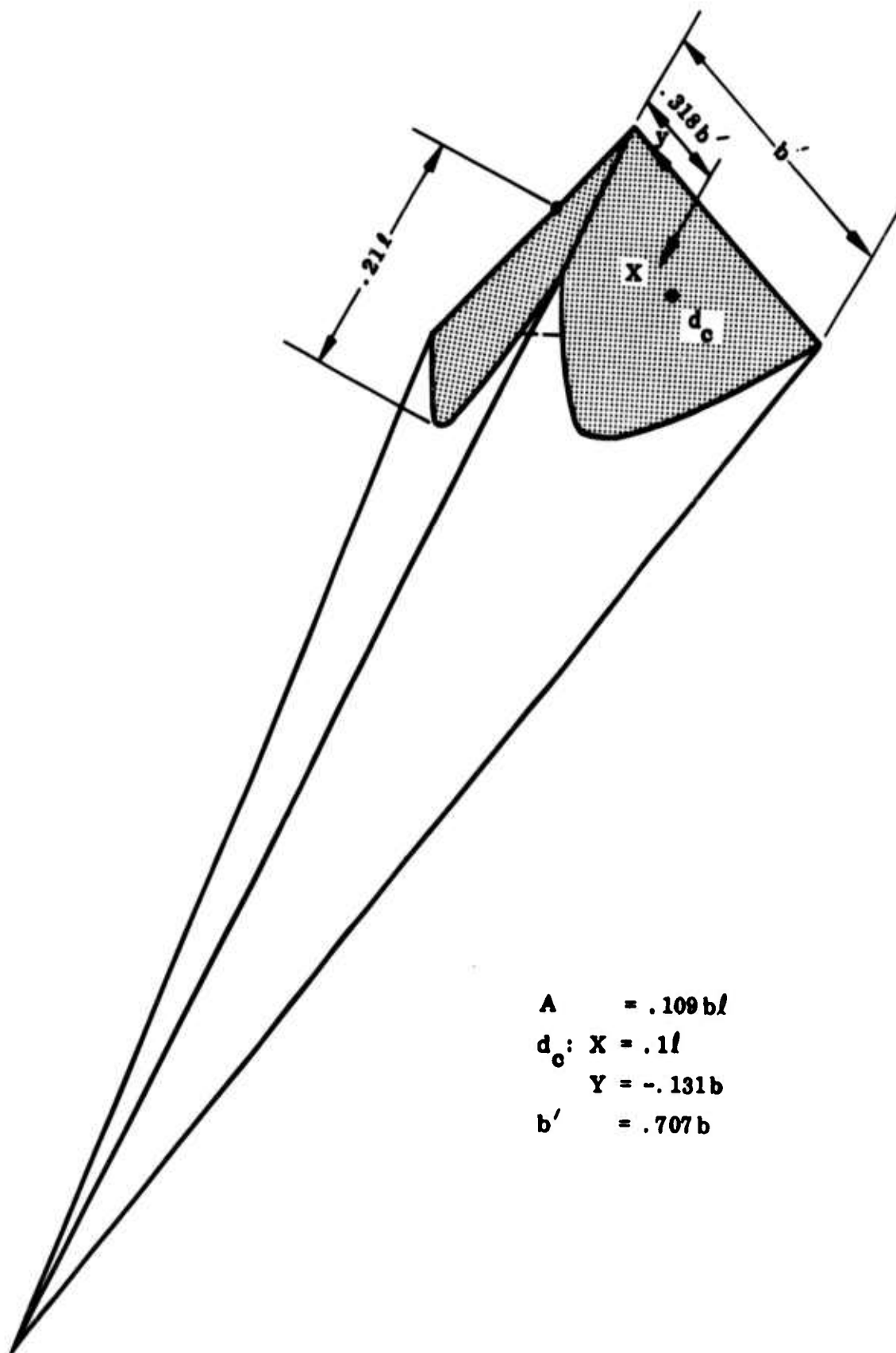


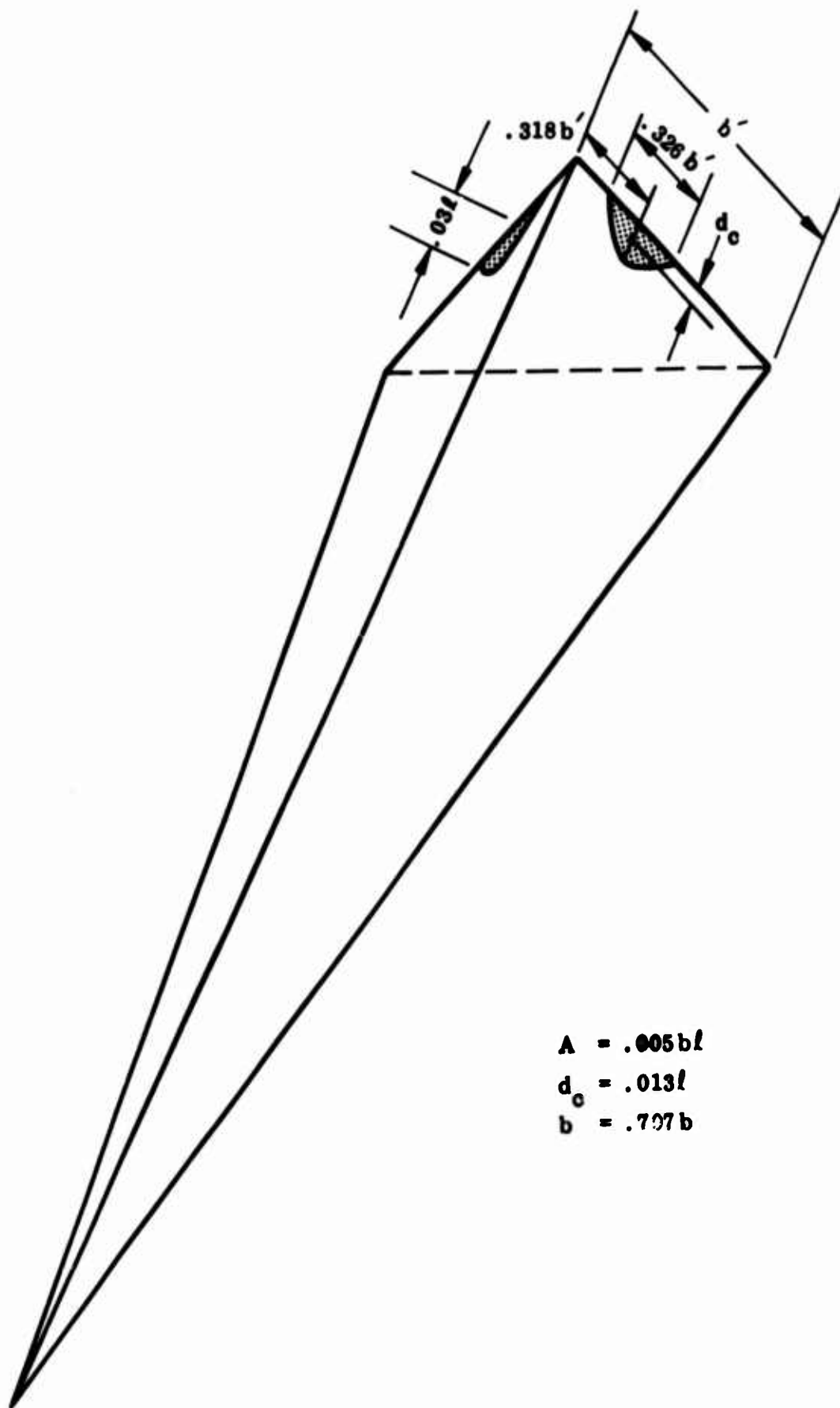
Figure III-25 Separation Footprint on Windside Surface for  $M_\infty = 10$ , 280-Kft Alt, and  $\alpha = +10$  deg



$$\begin{aligned}
 A &= .109 b l \\
 d_o: X &= .1 l \\
 Y &= -.131 b \\
 b' &= .707 b
 \end{aligned}$$

Figure III-26 Separation Footprint on Leeside Surface for  $M_\infty = 10$ , 280-Kft Alt, and  $\alpha = +10$  deg





$$\begin{aligned} A &= .005bl \\ d_c &= .013l \\ b &= .797b \end{aligned}$$

Figure III-27 Separation Footprint on Leeside Surface for  $M_\infty = 15$ , 230-Kft Alt, and  $\alpha = +10$  deg

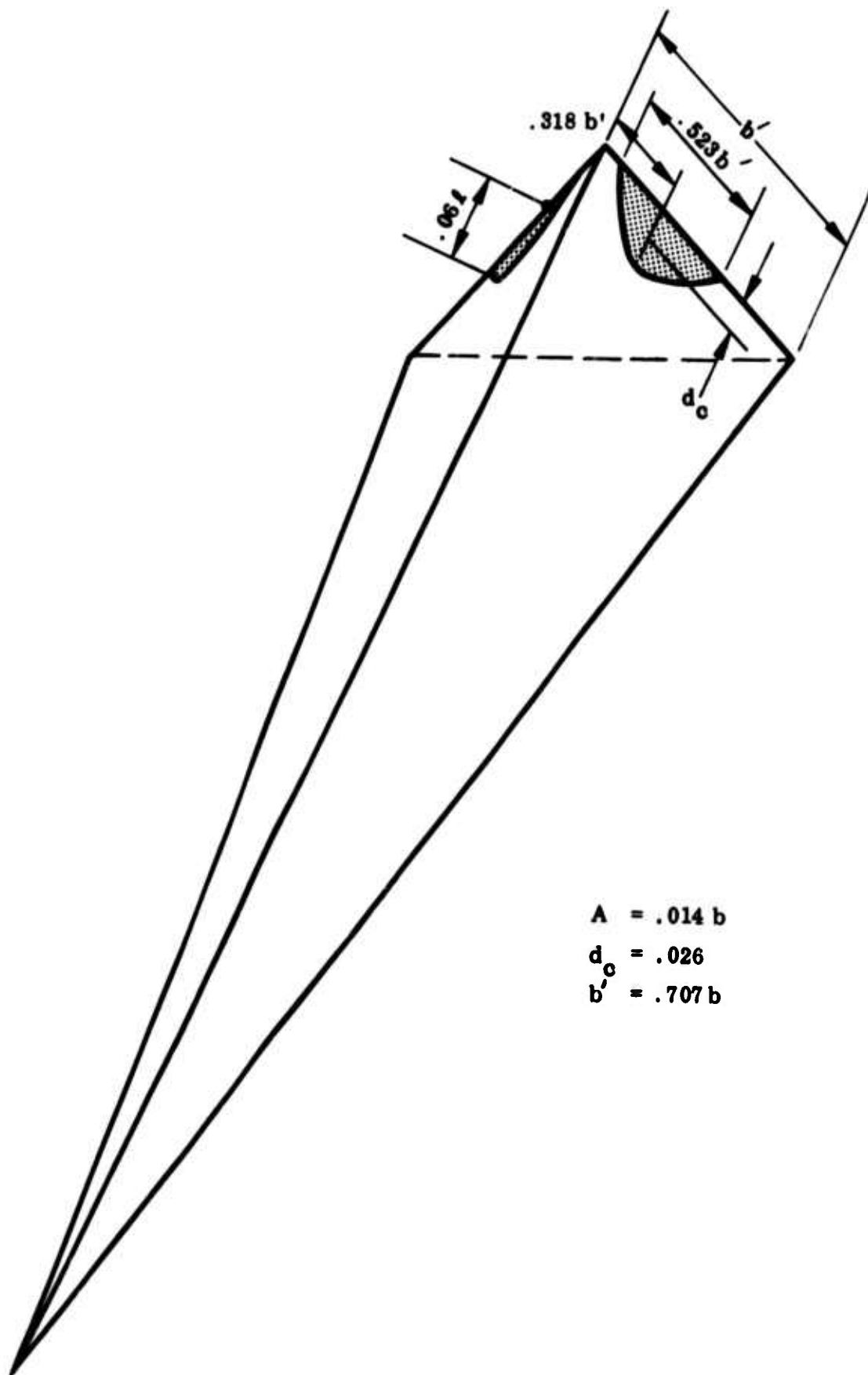


Figure III-28 Separation Footprint on Leeside Surface for  $M_\infty = 15$ , 250-Kft Alt, and  $\alpha = +10$  deg

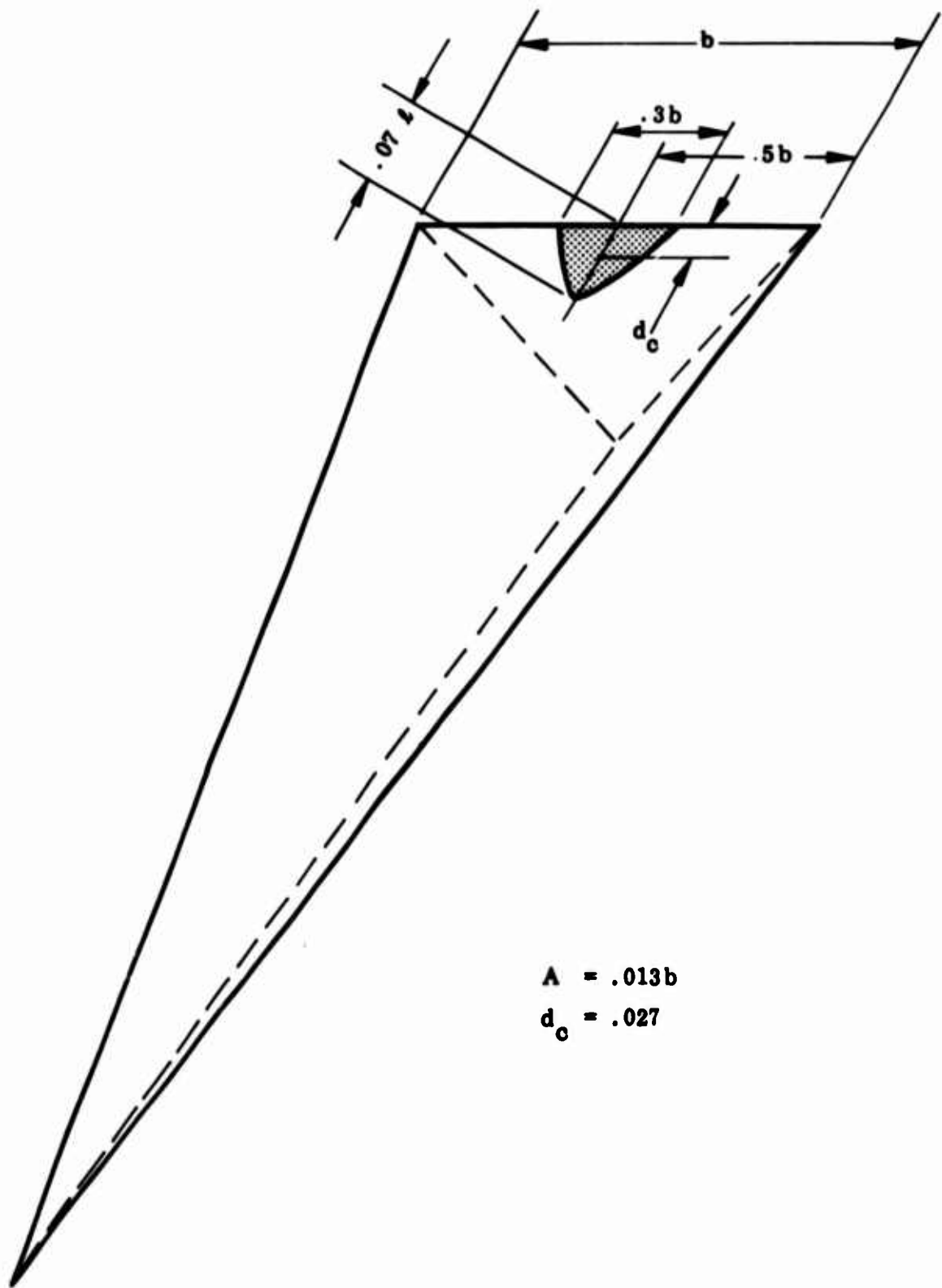


Figure III-29 Separation Footprint on Windside Surface for  $M_\infty = 15$ , 280-Kft Alt, and  $\alpha = +10$  deg

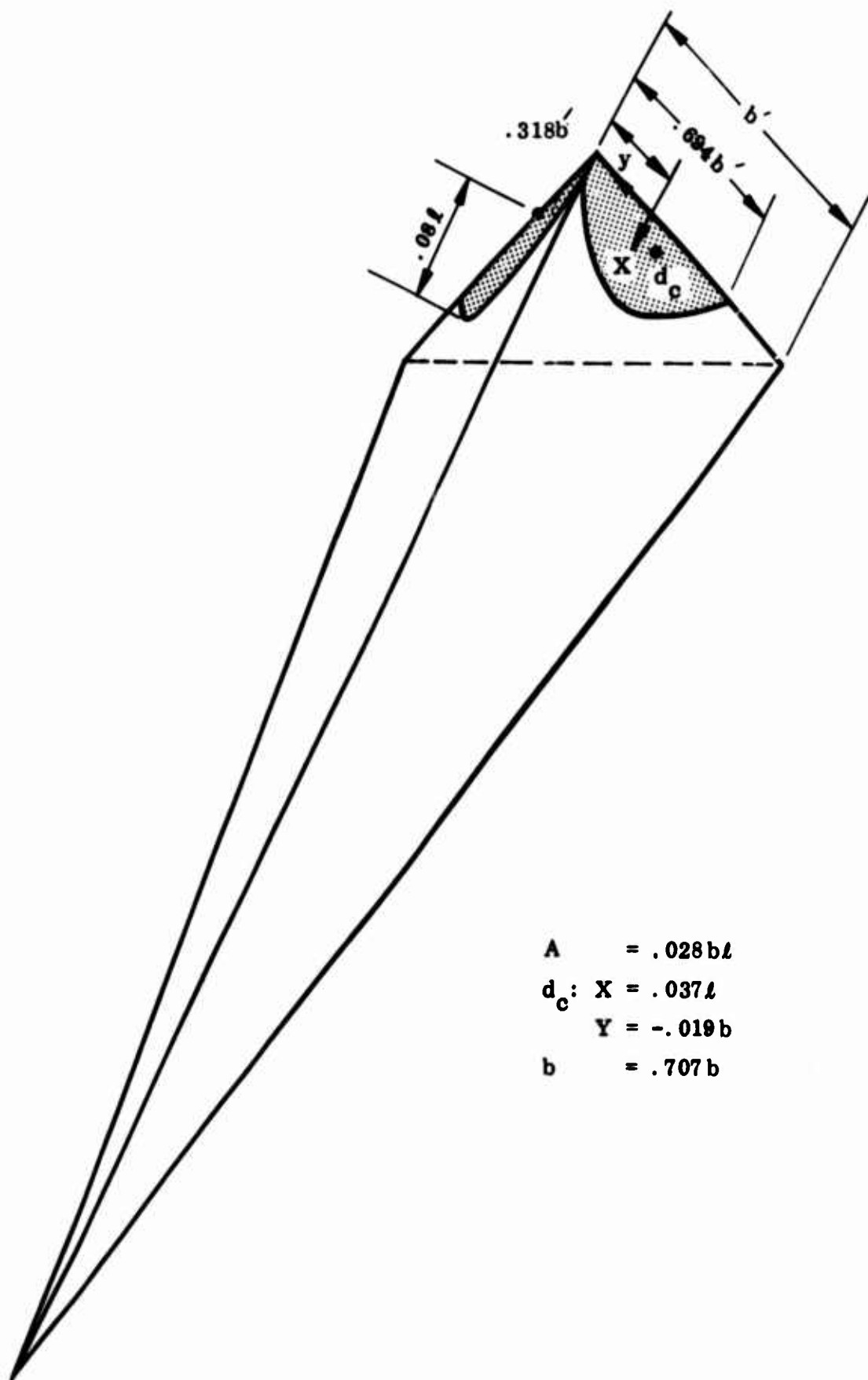
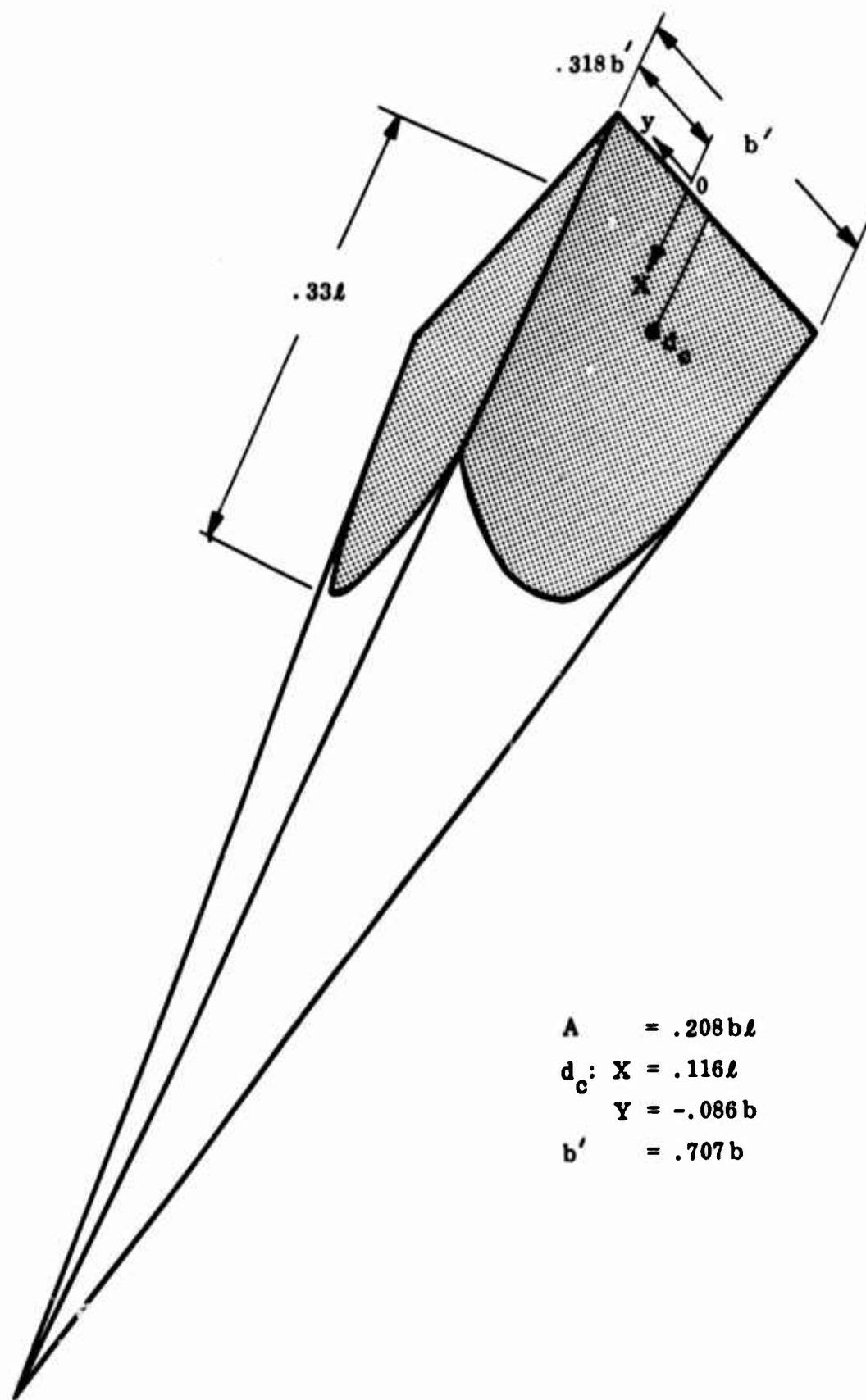


Figure III-30 Separation Footprint on Leeside Surface for  $M_\infty = 15$ , 280-Kft Alt, and  $\alpha = +10$  deg



$$\begin{aligned}
 A &= .208bl \\
 d_c: X &= .116l \\
 Y &= -.086b \\
 b' &= .707b
 \end{aligned}$$

Figure III-31 Separation Footprint on Leeside Surface for  $M_\infty = 6$ , 230-Kft Alt, and  $\alpha = +20$  deg

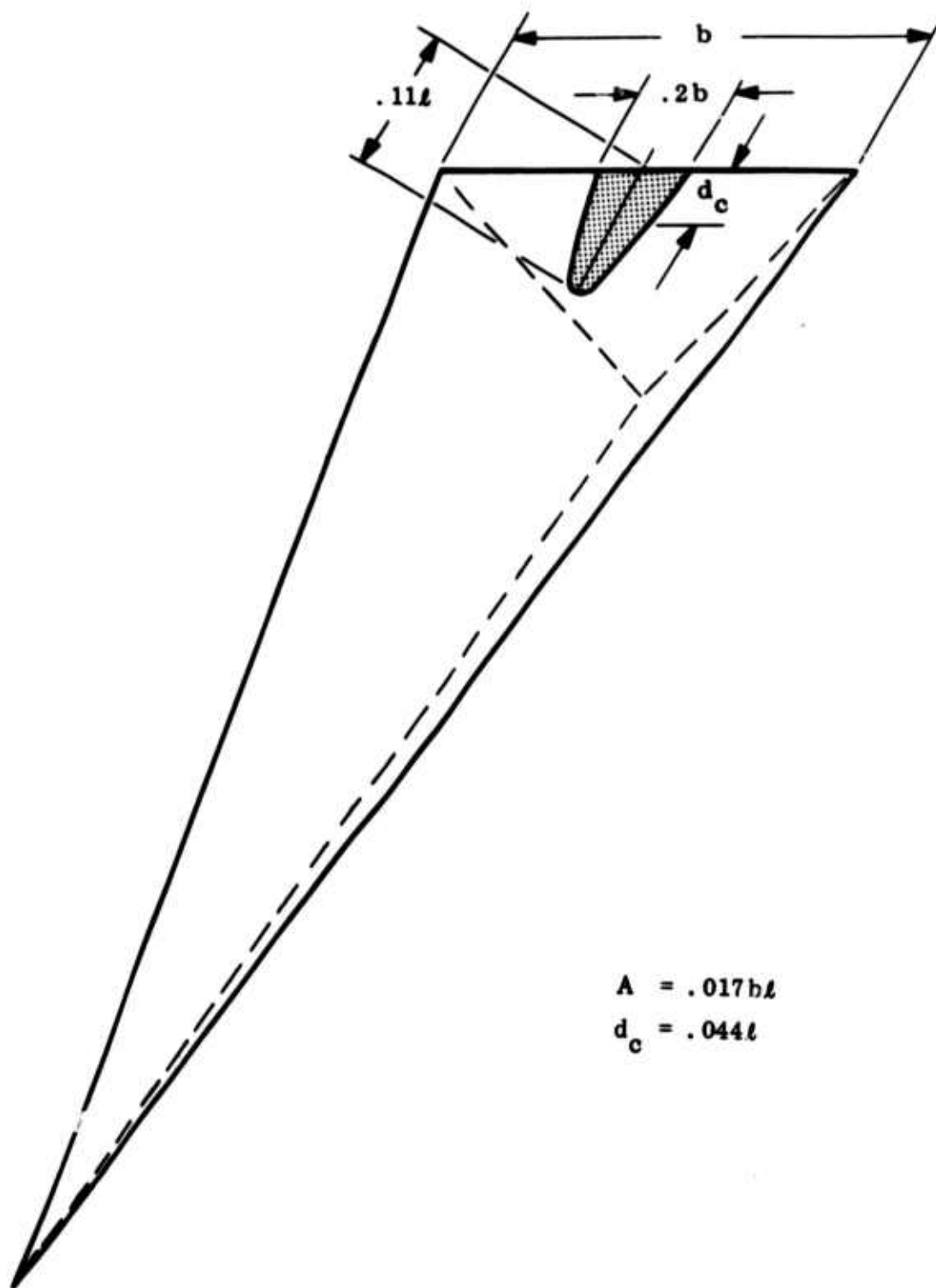


Figure III-32 Separation Footprint on Windside Surface for  $M_\infty = 6$ , 250-Kft Alt, and  $\alpha = +20$  deg

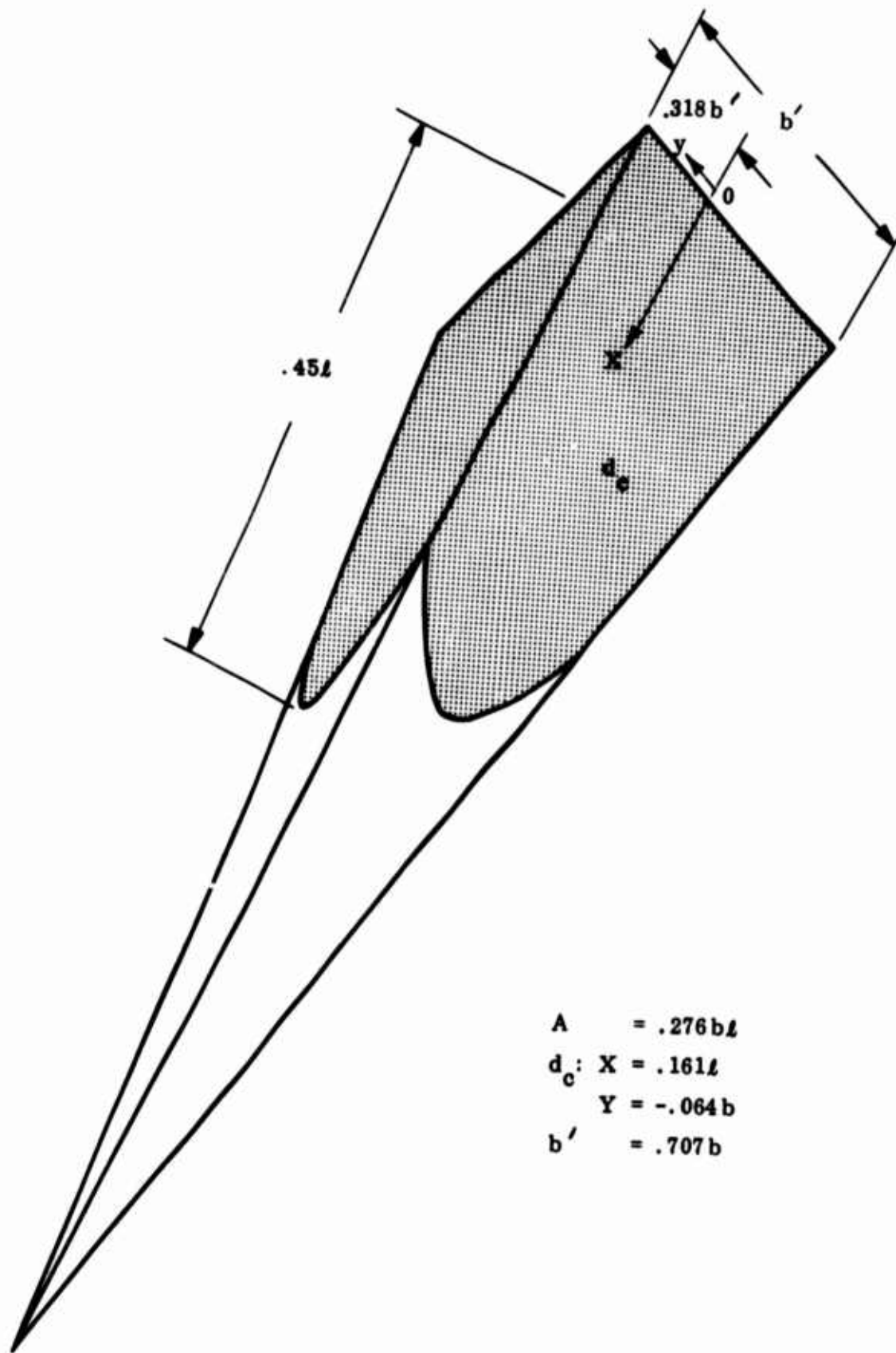


Figure III-33 Separation Footprint on Leeside Surface for  $M_\infty = 6$ , 250-Kft Alt,  $\alpha = +20$  deg

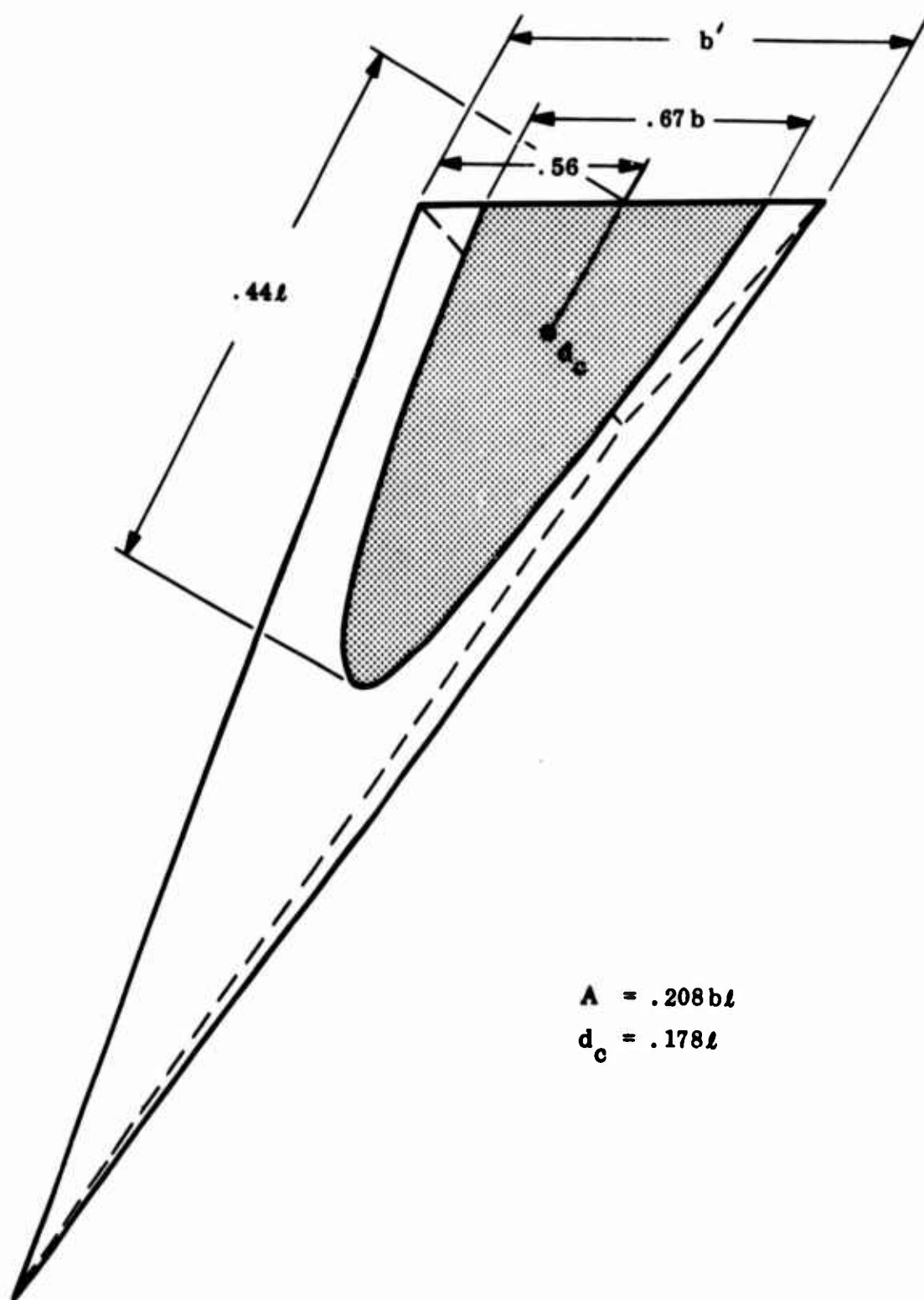


Figure III-34 Separation Footprint on Windside Surface for  $M_\infty = 6$ , 280-Kft Alt, and  $\alpha = +20$  deg



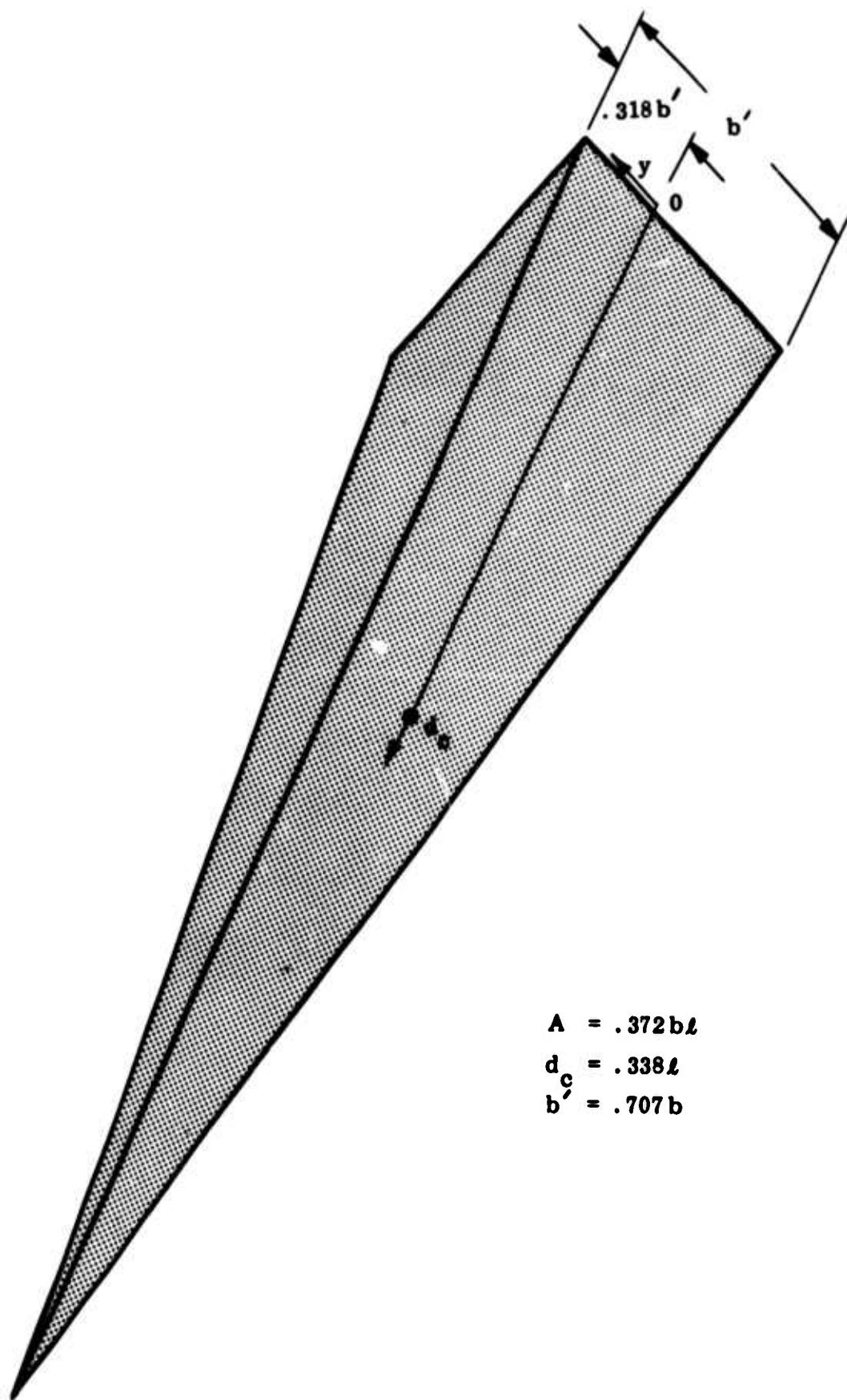


Figure III-35 Separation Footprint on Leeside Surface for  $M_\infty = 6$ , 280-Kft Alt, and  $\alpha = +20$  deg

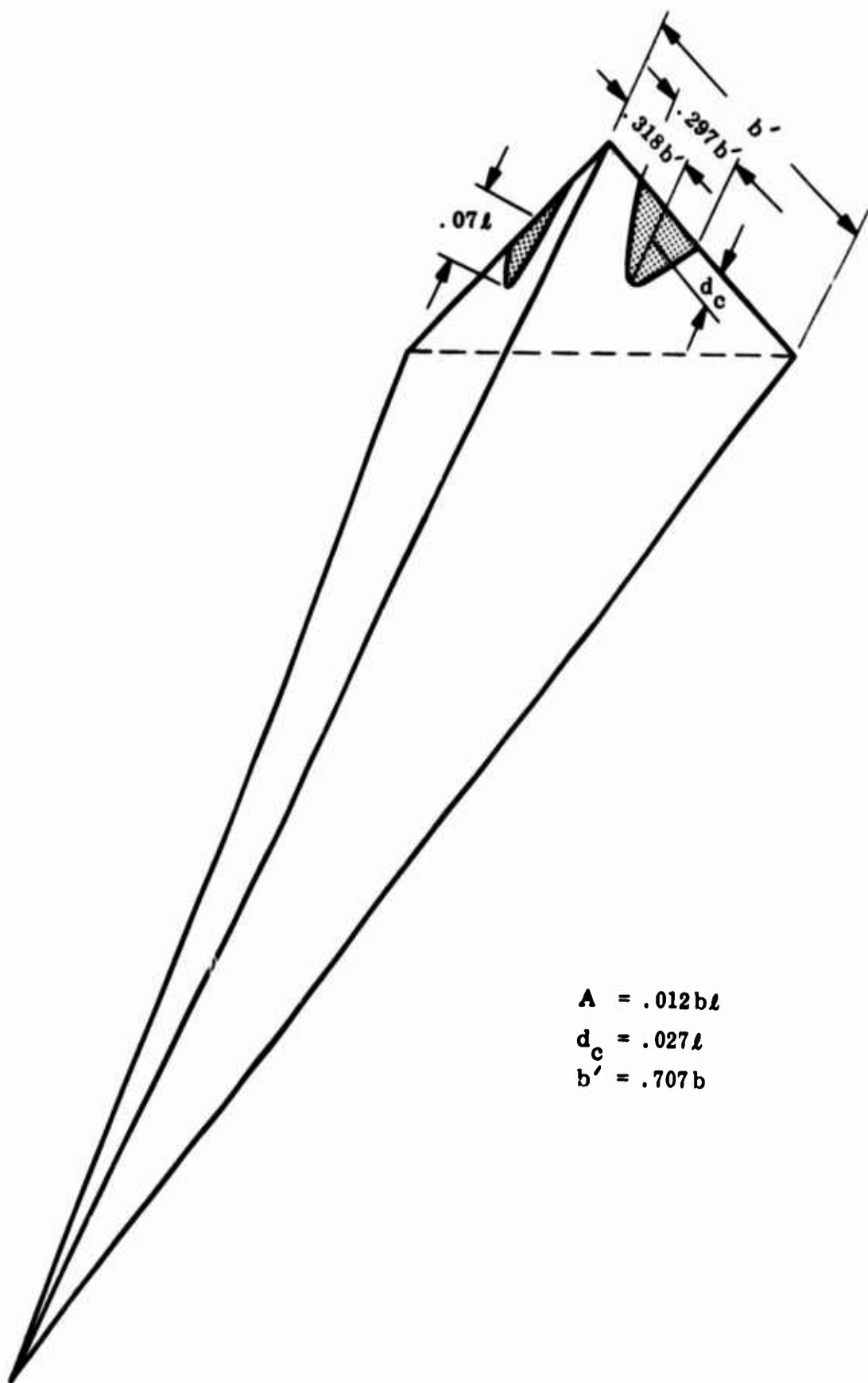


Figure III-36 Separation Footprint on Leeside Surface for  $M_\infty = 10$ , 230-Kft Alt, and  $\alpha = +20$  deg

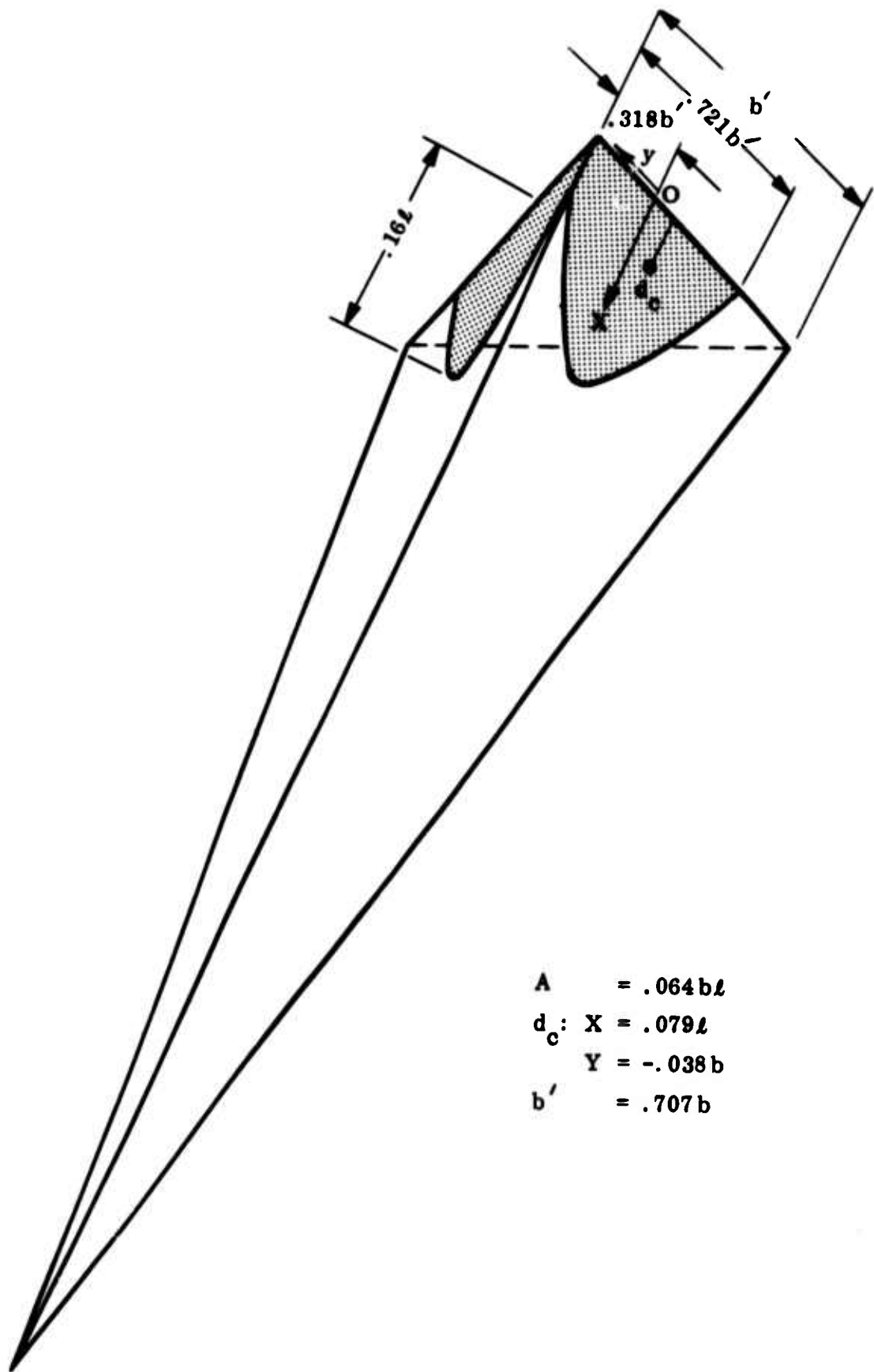


Figure III-37 Separation Footprint on Leeside Surface for  $M_\infty = 10$ , 250-Kft Alt, and  $\alpha = +20$  deg

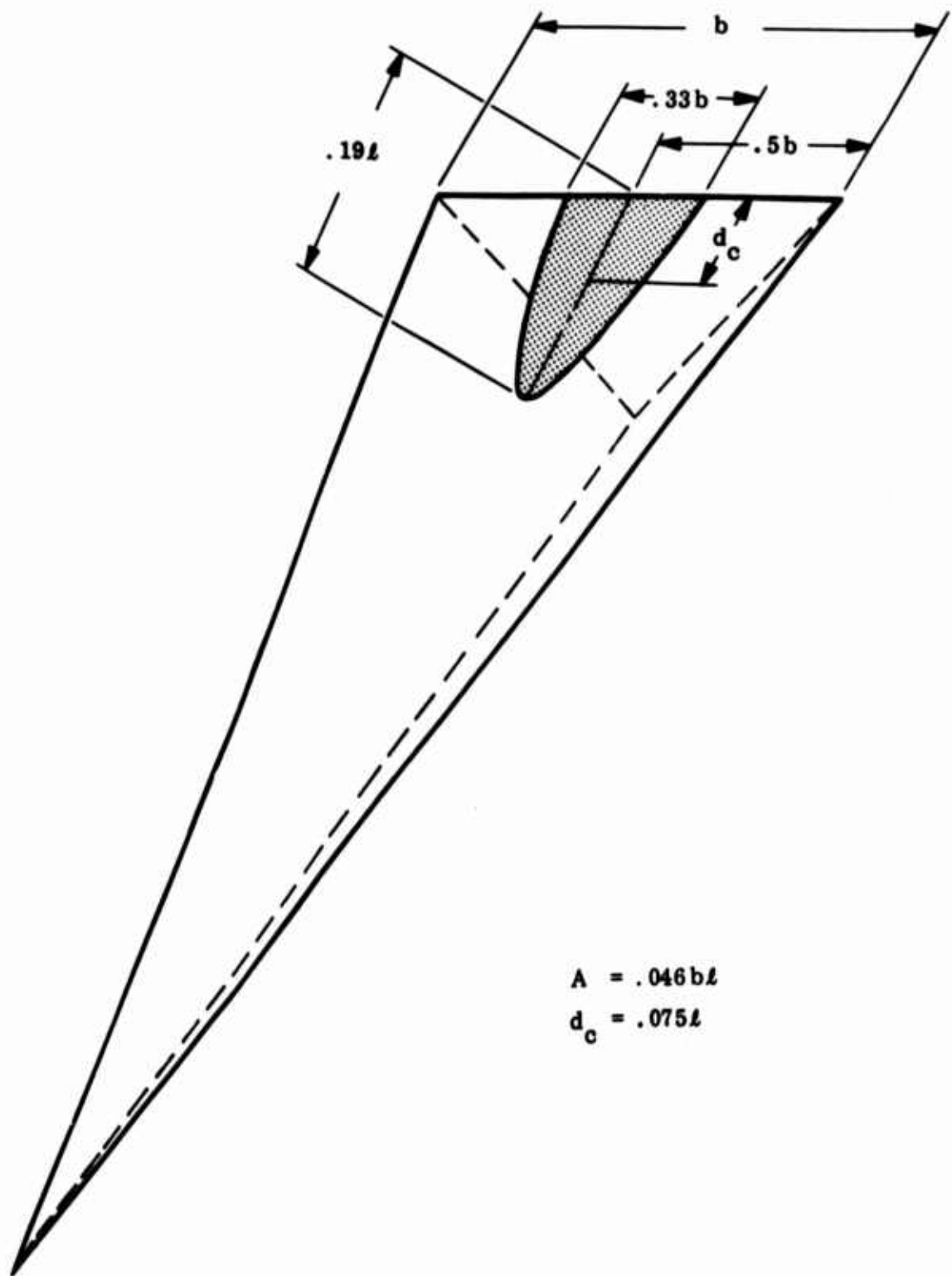


Figure III-38 Separation Footprint on Windside Surface for  $M_\infty = 10$ , 280-Kft Alt, and  $\alpha = +20$  deg

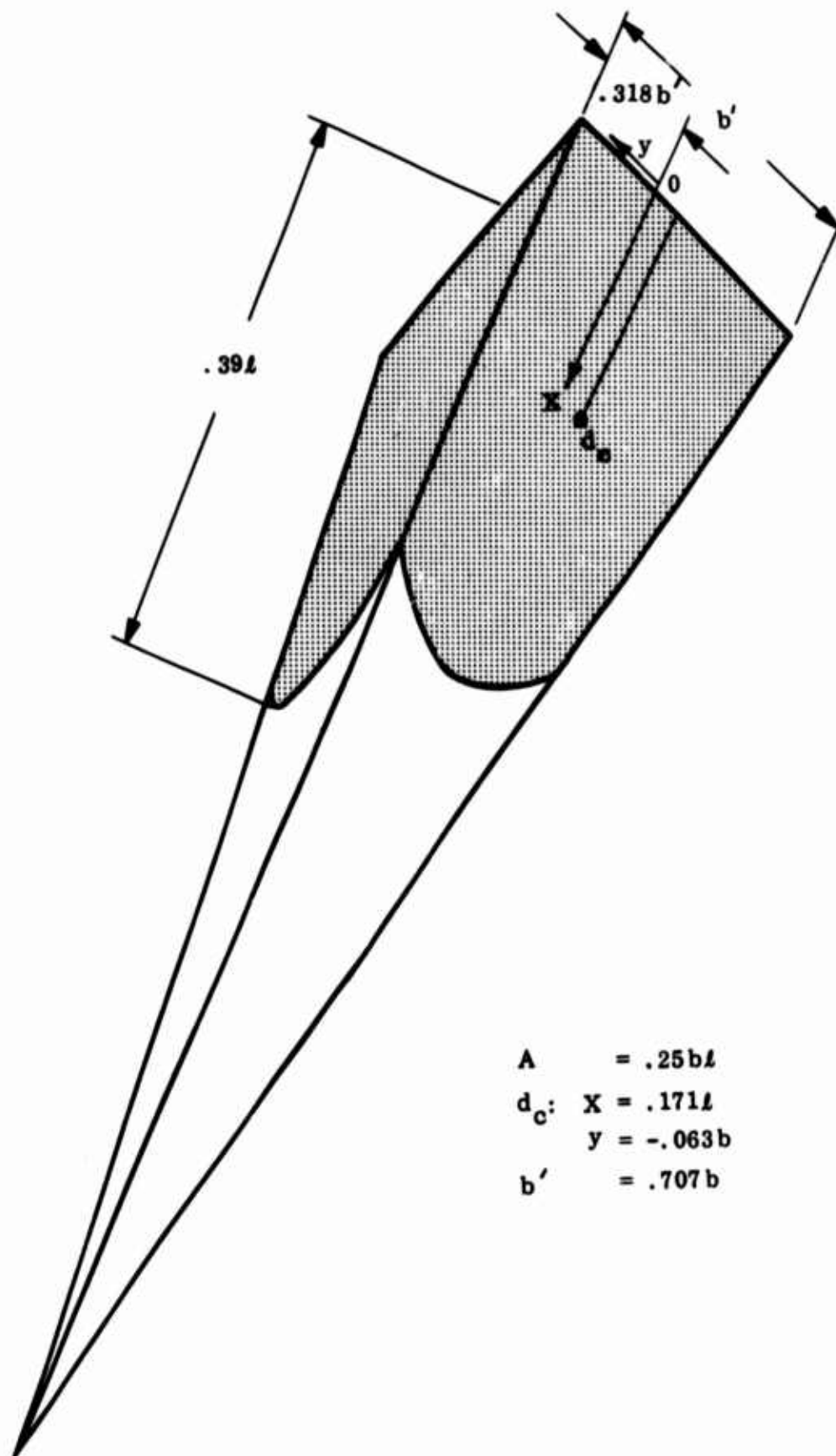


Figure III-39 Separation Footprint on Leeside Surface for  $M_\infty = 10$ , 280-Kft Alt, and  $\alpha = +20$  deg

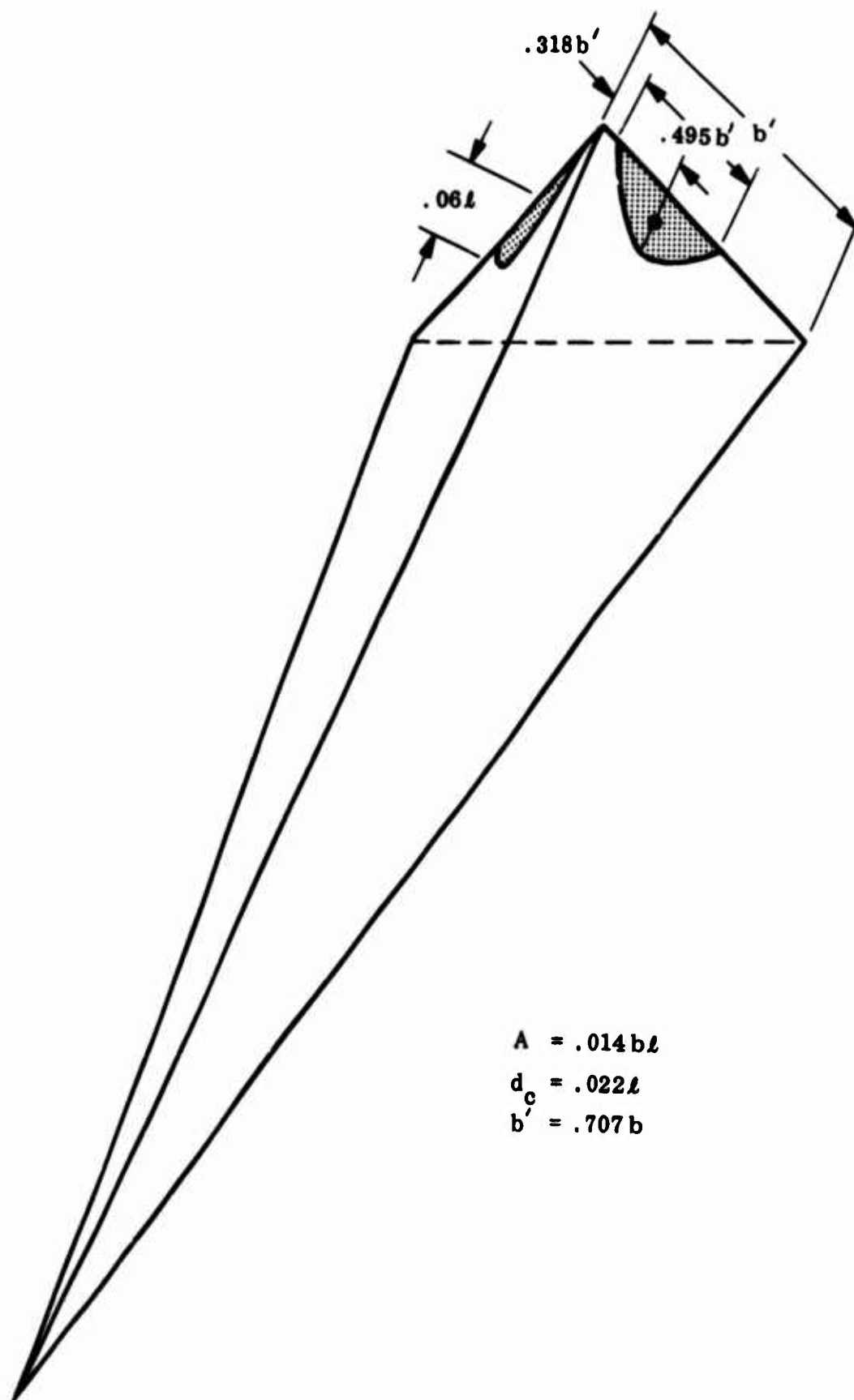
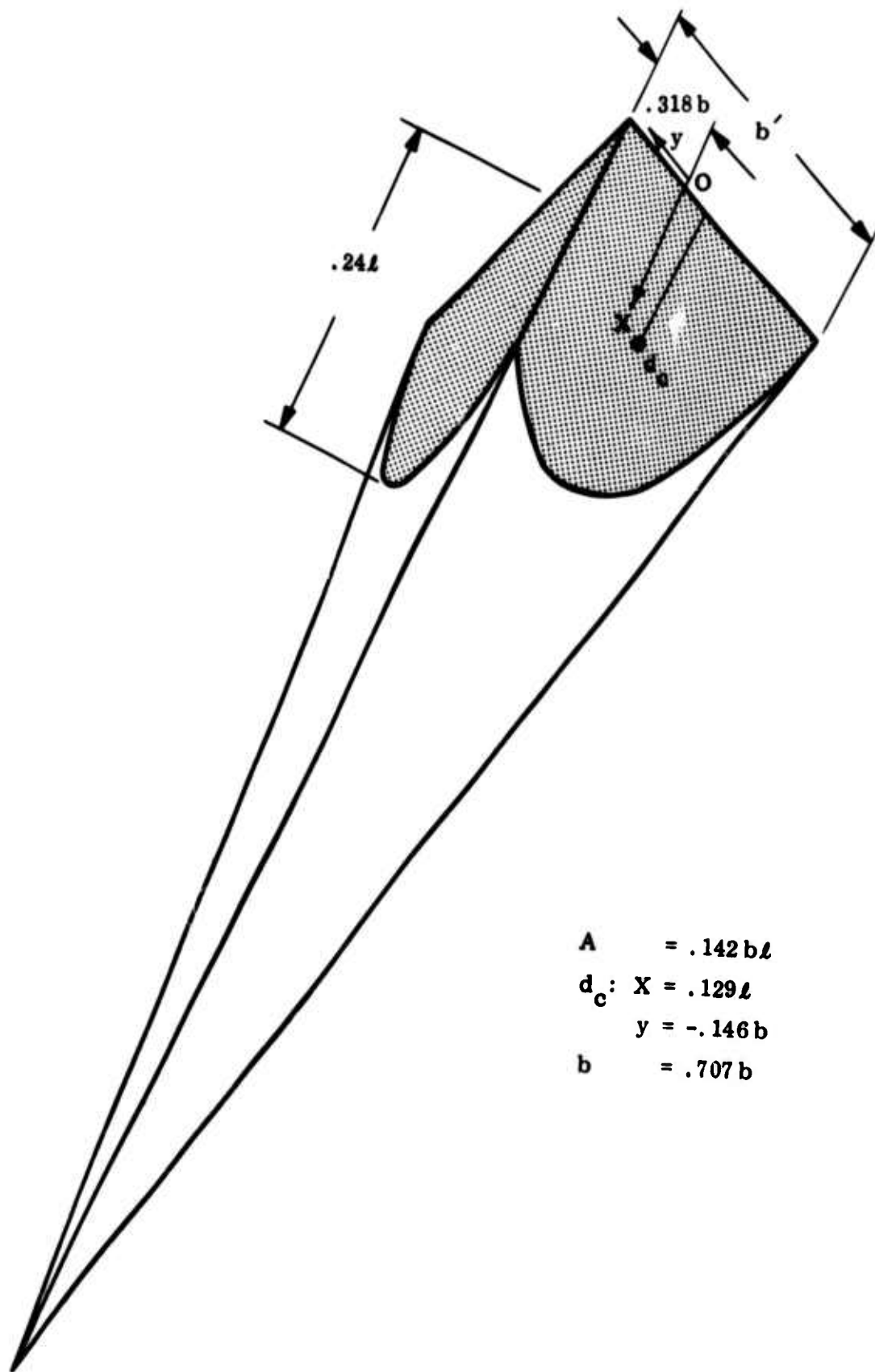
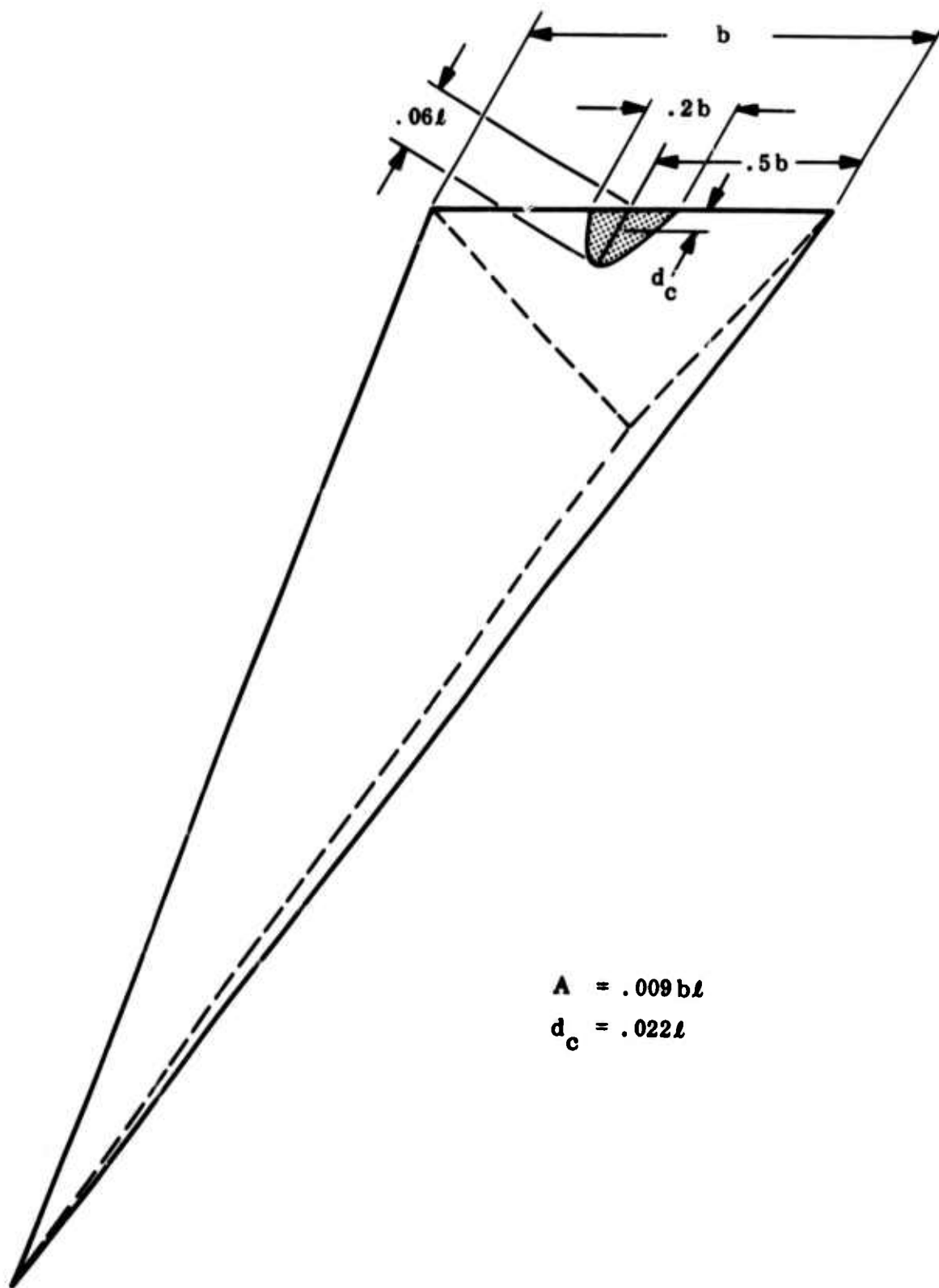


Figure III-40 Separation Footprint on Leeside Surface for  $M_\infty = 15$ , 230-Kft Alt, and  $\alpha = +20$  deg



$$\begin{aligned}
 A &= .142 bl \\
 d_c: X &= .129 l \\
 y &= -.146 b \\
 b &= .707 b
 \end{aligned}$$

Figure III-41 Separation Footprint on Leeside Surface for  $M_\infty = 15$ , 250-Kft Alt, and  $\alpha = +20$  deg



$$A = .009 bl$$

$$d_c = .022l$$

Figure III-42 Separation Footprint on Windside Surface for  $M_\infty = 15$ , 280-Kft Alt, and  $\alpha = +20$  deg



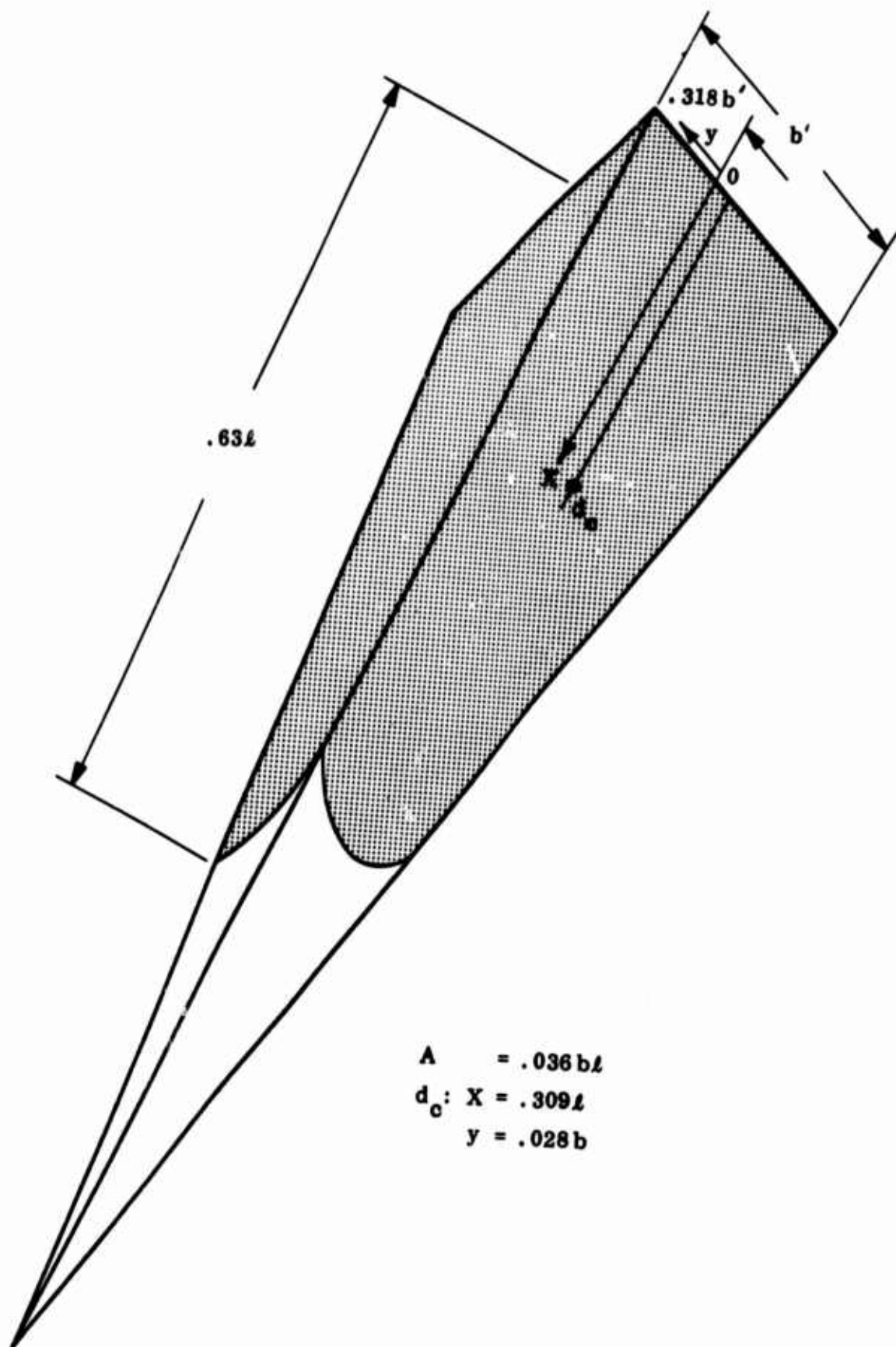


Figure III-43 Separation Footprint on Leeside Surface for  $M_\infty = 15$ , 280-Kft Alt, and  $\alpha = +20$  deg

## REFERENCES

1. Linneman, E. R., "Reentry Maneuver Optimization With Heating Restraints," Lockheed California Company Report LR 21223, 31 Dec 1967
2. Falanga, R. A., Hinson, W. F., and Crawford, D. H., "Exploratory Tests of the Effects of Jet Plumes on the Flow Over Cone-Cylinder-Flare Bodies," NASA TN D-1000, 1962
3. Hinson, W. F., and Falanga R. A., "Effect of Jet Pluming on the Static Stability of Cone-Cylinder-Flare Configurations at Mach Number of 9.64," NASA TND-1352, 1969
4. McGhee, R. J., "Some Effects of Jet Pluming on the Static Stability of Ballistic Bodies at a Mach Number of 6.00," NASA TND-3698, Nov 1966
5. Hinson, W. F., and McGhee, R. J., "Effects of Jet Pluming on the Static Stability of Five Rocket Models at Mach Numbers of 4, 5, and 6 and Static Pressure Ratios up to 26000," NASA TND-4064, 1967
6. Alpinieri, L. J., and Adams, R. H., "Flow Separation Due to Jet Pluming," AIAA Journal, Vol. 4, No. 10, Oct 1966, pp. 1865-1866
7. Adams, R. H., and Holland, A. C., "Wind Tunnel Investigation of the LD Phenomenon," Mithras Report MC 65-115-R4, Dec 1965
8. Lloyd, J. T., et al, "An Analytical and Experimental Investigation of Reusable Launch Vehicle Configurations." Interim Report. USAF FLD Contract F 33615-67-C-1885, Sept 1968
9. Zeleznik, F. J., and Gordon, S., "A General IBM 704 or 7090 Computer Program for Computation of Chemical Equilibrium Compositions, Rocket Performance, and Chapman-Jouguet Detonations," NASA TND-1454, Oct 1962
10. Bray, K. N. C., "Chemical Reactions in Supersonic Nozzle Flows," Proc. Ninth Symposium (Int'l) on Combustion, Cornell University, Ithaca, N. Y., Aug 27 - Sept 1, 1962, pp. 770-784
11. Cohen, L. S., "An Analytical Study of the Mixing and Nonequilibrium Chemical Reaction of Ducted Compressible Streams," AIAA Paper No. 66-617, AIAA Second Propulsion Joint Specialist Conference, Colorado Springs, Colorado, June 13-17, 1966
12. Donaldson, C. duP., and Gray, K. E., "Theoretical and Experimental Investigation of the Compressible Free Mixing of Two Dissimilar Gases," AIAA Paper No. 65-822, AIAA Aerothermochemistry of Turbulent Flows Conference, San Diego, California, Dec 13-15, 1965

13. Libby, P. A. , "Theoretical Analysis of Turbulent Mixing of Reacting Gases With Application to Supersonic Combustion of Hydrogen," ARS Journal, Vol. 32, No. 3, Mar 1962, pp. 388-396.
14. Victor, A. C. , and Buecher, R. W. , "An Analytical Approach to the Turbulent Mixing of Coaxial Jets," NAVWEP Report 9057, Oct 1966
15. Pai, S. I. , Fluid Dynamics of Jets, D. Van Nostrand Co. , N. Y. , 1954
16. Prozan, J. J. , "Development of a Method of Characteristics Solution for Supersonic Flow of an Ideal, Frozen or Equilibrium Reactions Gas Mixture," LMSC/HREC A782535-A, April 1966
17. Rattiff, A. W. , "Comparisons of Experimental Supersonic Flow Fields with Results Obtained by Using a Method of Characteristics Solution," LMSC/HREC A782592, April 1966
18. Vick, A. R. , et al, "Comparisons of Experimental Free-Jet Boundaries with Theoretical Results Obtained with the Method of Characteristics," NASA TN-D-2327, 1964
19. Love, E. S. , Grisby, C. E. , Lee, L. P. , and Woodling, M. J. , "Experimental and Theoretical Studies of Axisymmetric Free Jets," NASA TR R-6, 1959
20. Latvala, E. K. , Spreading of Rocket Exhaust Jets at High Altitudes, AEDC AEDC-TR-59-11, June 1959
21. Latvala, E. K. , and Anderson, T. P. , "Studies of the Spreading of Rocket Exhaust Jets at High Altitudes," Planetary and Space Science, Vol. 4, 1961, pp 77-91
22. Bartz, D. R. , "Turbulent Boundary-Layer Heat Transfer from Rapidly Accelerating Flow of Rocket Combustion Gases and Heated Air," Advances in Heat Transfer, Vol. 2, Academic Press, 1965, pp. 1-108
23. Elliot, D. G. , Bartz, D. R. , and Silver, S. , Calculation of Turbulent Boundary-Layer Growth and Heat Transfer in Axisymmetric Nozzles, JPL TR 32-387, Feb 1963
24. Boynton, F. P. , "Exhaust Plumes from Nozzles with Wall Boundary Layers," J. Spacecraft, Vol. 5, No. 10, Oct 1968, pp. 1143-1147
25. McGhee, R. J. , to be published
26. Chapman, D. R. , "Laminar Mixing of a Compressible Fluid," NACA Report 959, 1958
27. Korst, H. H. , Chow, W. L. , and Zumwalt, G. W. , "Research on Transonic Flow of Real Fluid at Abrupt Increase in Cross Section," Final Report - University of Illinois, Engg Exper. Sta. , ME-TN-392-5, Dec 1959

28. Korst, H. H., and Chow, W. L., "Nonisoenergetic Turbulent ( $P_r = 1$ ) Jet Mixing Between Two Compressible Streams at Constant Pressure," NASA CR-419, April 1966
29. Emmons, D. L., "Analysis of the Chemically Reactive Mixing Region Between a Turbulent Rocket Exhaust and a Confined Air Stream," Boeing Report D2-36251-1, Mar 1965
30. Maydew, R. C., and Reed, J. F., "Turbulent Mixing of Axisymmetric Compressible Jets (in the Half-Jet Region) with Quiescent Air," Sandia Report SAND SC-4764 (RR), Mar 1963
31. Denison, M. R., and Baum, E., "Compressible Free Shear Layer With Finite Initial Thickness," AIAA Journal Vol. 1, No. 2, Feb 1963, pp. 342-349
32. Hill, W. G., Jr., "Initial Development of Compressible Turbulent Free Shear Layers," Ph.D. Thesis, Department of Mechanical Engineering, Rutgers, The State University of, May 1966
33. Kirk, F. N., "An Approximate Theory of Base Pressure in Two Dimensional Flow at Supersonic Speeds," Royal Aeronautical Establishment, TN Aero 2377, Dec 1959
34. Nash, J. F., "The Effect of an Initial Boundary Layer on the Development of a Turbulent Free Shear Layer," National Physical Lab. Aero Rept 1019, June 1962
35. Kessler, T. J., "Two-Stream Mixing with Finite Initial Boundary Layers," AIAA Journal, Vol. 5, No. 2, Feb 1967, pp. 363-364
36. Przirembel, C. E. G., and Page, R. H., "Analysis of Axisymmetric Supersonic Turbulent Base Flow," Proceedings of the 1968 Heat Transfer and Fluid Mechanics Institute, pp. 258-272
37. Popinski, Z., and Ehrlich, C. F., Development Design Methods for Predicting Hypersonic Aerodynamic Control Characteristics, AFFDL-TR-66-85, Sept 1966
38. Bauer, P. T., Zumwalt, G. W., and Fila, L. J., "A Numerical Method and an Extension of the Korst Jet Mixing Theory for Multispecies Turbulent Jet Mixing," AIAA Paper No. 68-112, AIAA 6th Aerospace Sciences Meeting, New York, N. Y., Jan 22-24, 1968
39. Tang, H. H., "Jet Mixing Theory, Extensions, and Applications in Separated Flow Problems," Douglas Missile and Space System Division, DAC 59181, Feb 1967
40. Beheim, M. A., Klann, J. L., and Yeager, R. A., "Jet Effects on Annular Base Pressure and Temperature in a Supersonic Stream," NASA TR R-125, 1962
41. Fong, M. C., "Plume-Induced Boundary Layer Separation," LMSC/687228, TM/55-26-05, Mar 1969

42. Gadd, G. E. , "A Theoretical Investigation of Laminar Separation in Supersonic Flow," J. Aero. Sci. , Vol. 24, p. 759, 1957
43. Buchanan, T. D. , "Study of Flow Separation on Missile by Jet Plume," M. S. Thesis, Univ of Tennessee, Aug 1967
44. Shapiro, A. H. , Compressible Fluid Flow, Vol. I, The Ronald Press Co. , New York. 1954, pp. 553-559
45. Nash, J. F. , "An Analysis of Two-Dimensional Turbulent Base Flow, Including the Effect of the Approving Boundary Layer," Aero. Res. Counc. , R&M No. 3344, 1962
46. Fong, M. C. , and Freeman, C. F. , Laminar Heat Transfer to a Swept Leading Edge in Hypersonic Flow, AFFDL-TR-66-208, April 1967
47. Beckwith, I. E. , "Similarity Solutions for Small Cross Flows in Laminar Compressible Boundary Layers," NASA TR R-107, 1961
48. Fannelop, T. K. , "A Method for Solving the Three-Dimensional Laminar Boundary-Layer Equations with Application to a Lifting Reentry Body," AIAA Journal, Vol. 6, No. 6, June 1968, pp. 1075-1084
49. Whitehead, Jr. , A. H. , and Dunavant, J. C. , "A Study of Pressure and Heat Transfer over an 80° Sweep Slab Delta Wing in Hypersonic Flow," NASA TN D-2708, Mar 1965
50. Bradley, R. G. , Mann, A. R. , Hull, G. H. , and Klein, G. J. , An Analytical and Experimental Study of Slender Sharp-edged Hypersonic Configurations in the Viscous Interaction Regime, AFFDL-TR-68-161, Sept 1968
51. Kawamura, R. , "Reflection of a Wave at an Interface of Supersonic Flows and Wave Patterns in a Supersonic Compound Jet," Journal Physical Society of Japan, Vol. 7, No. 5
52. Weinberg, S. A. , "The Pressure and Shock Shape-Over a Delta Wing at Angle of Attack in a Hypersonic Flow," M. S. Thesis, Dept of Aeronautical and Astronautical Engineering, Ohio State Univ, 1965
53. Stickford, Jr. G. H. , and Nerem, R. M. , Convective and Radiative Heat Transfer to Slab Delta Wing Configuration at High Angle-of-Attack, AFFDL-TR-65-83, Sept 1965
54. Polak, A. , and Li, T. Y. , "Three-Dimensional Boundary-Layer Flow Over a Flat Delta Wing at a Moderate Angle of Attack," AIAA Journal, Vol. 5, No. 2, Feb 1967, pp. 223-240

55. Fong, M. C. , "Similar Solutions for Three-Dimensional Laminar Compressible Boundary Layers," AIAA Journal Vol. 2, No. 12, Dec 1964, pp. 2205-2207
56. Cohen, C. B. , and Reshotko, E. , "Similar Solutions for the Compressible Laminar Boundary Layer With Heat Transfer and Pressure Gradient," NASA TN-3325, Feb 1955

UNCLASSIFIED

Security Classification

## DOCUMENT CONTROL DATA - R &amp; D

(Security classification of title, body of abstract and indexing annotation must be entered when the overall report is classified)

1. ORIGINATING ACTIVITY (Corporate author)		2a. REPORT SECURITY CLASSIFICATION	
Lockheed Missiles & Space Company Sunnyvale, California		UNCLASSIFIED	
		2b. GROUP	
		N/A	
3. REPORT TITLE			
PROPULSION EFFECTS ON AERODYNAMIC CHARACTERISTICS OF LIFTING REENTRY VEHICLES			
4. DESCRIPTIVE NOTES (Type of report and inclusive dates)			
Final Technical Report, December 1968 to October 1969			
5. AUTHOR(S) (First name, middle initial, last name)			
Fong, Michael C. Ehrlich, Carl F., Jr.			
6. REPORT DATE		7a. TOTAL NO. OF PAGES	7b. NO. OF REFS
March 1970		249	56
8a. CONTRACT OR GRANT NO		9a. ORIGINATOR'S REPORT NUMBER(S)	
F33615-69-C-1228		LMSC-A960076	
b. PROJECT NO		9b. OTHER REPORT NO(S) (Any other numbers that may be assigned this report)	
1366		AFFDL-TR-70-12	
c.			
d. Task No. 136609			
10. DISTRIBUTION STATEMENT			
This document is subject to special export controls and each transmittal to foreign governments or foreign nationals may be made only with prior approval of the Air Force Flight Dynamics Laboratory (FDMG).			
11. SUPPLEMENTARY NOTES		12. SPONSORING MILITARY ACTIVITY	
None		Air Force Flight Dynamics Laboratory (FDMG) Wright-Patterson AFB, Ohio 45433	
13. ABSTRACT			
<p>A modified version of the Chapman-Korst model involving mass diffusion, equilibrium thermochemistry, and appropriate semiempirical relations is utilized to predict the overall flow characteristics within the plume-induced separated flow region during synergetic maneuvering of a lifting reentry vehicle. The exhaust plume selected in conjunction with the separated flow analysis is predicted on the basis of the method-of-characteristics solution with an average specific-heat ratio of 1.38. Thermochemical equilibrium is assumed to exist within the plume-induced separated flow region, and equilibrium temperature curves for various altitudes, vehicle Mach numbers, and propellant-air mixture ratios are presented. The strip method is incorporated in the analysis to estimate the three-dimensional separated flow characteristics caused by the vehicle geometry and vehicle attitude during the maneuver. The extent of validity of the strip method is established with the aid of a cross-flow boundary layer solution. On the basis of the present analytical model, the propulsion effects on aerodynamic characteristics of a simple lifting body configuration with delta planform and triangular cross section under a wide spectrum of freestream conditions have been evaluated and illustrated by appropriate design charts. Although the usefulness of the prediction method has been demonstrated, additional relevant data are required to finalize the theory development and to ensure a broad applicability of the analytical model.</p>			

14. KEY WORDS	LINK A		LINK B		LINK C	
	ROLE	WT	ROLE	WT	ROLE	WT
Lifting reentry vehicle						
Separated flow						
Plume-induced separation						
Boundary layer						
Shear layer						
Jet plume (or exhaust plume)						
Three-dimensional (or cross-flow) boundary layer						
Thermochemistry						
Hypersonic flow						
Aerodynamic characteristics						
Chapman-Korst Theory						



**SUPPLEMENTARY**

**INFORMATION**

# ERRATA

In the AFFDL technical report entitled "Propulsion Effects on Aerodynamic Characteristics of Lifting Reentry Vehicles", by Michael C. Fong and Carl F. Ehrlich, Jr. (AFFDL-TR-70-12, March 1970), the following errors should be corrected.

Page xvi, the 7th line from the bottom: The definition of  $\bar{\rho}^*$  should be  $\rho^* \hat{m}$ .

Page 135, line 8:  $\frac{\zeta}{\zeta_a}$  should be changed to  $\frac{\rho}{\rho_a}$

Page 138, equation (I-40): The integrand should be multiplied by  $\rho$ .

Page 139, equation (I-46): The integrand should be multiplied by  $\rho^2$ .

Page 140, equation (I-47): The integrand should be multiplied by  $\Delta \rho$ . However,  $I_3(\eta_a, \eta_b)$  was introduced in an alternate form of energy equation and is not relevant to any of the equations used in this report.

Page 140, equation (I-49): The lower limit of the integral should be  $y_{s_e}$  instead of  $y_{s_j}$ , and the "negative" sign in functions  $F_1(-\zeta_{s_e}, \infty)$  and  $F_2(-\zeta_{s_e}, \infty)$  should be removed.

Page 141, equation (I-50): The "negative" sign in functions  $I_1(-\eta_{s_j}, \infty)$  and  $I_2(-\eta_{s_j}, \infty)$  should be removed.

Page 141, equation (I-51): The equation should be corrected to

$$\dot{Y}_e + \dot{Y}_j = \int_{y_{s_e}}^{\infty} \rho u Y_e dy + \int_{y_{s_j}}^{\infty} \rho u Y_j dy = \int_{y_{s_j}}^{\infty} \rho u dy$$

Page 141, equation (I-52): The equation should be corrected to

$$\begin{aligned} \sum \dot{Y} &= \frac{\sqrt{2s'}}{\kappa \epsilon} Y_B [F_1(\zeta_{s_e}, \infty) - F_2(\zeta_{s_e}, \infty)] - \frac{\rho_j u_j x_j}{\sigma_j} I_1(\eta_{s_j}, \infty) \\ &+ \frac{\rho_j u_j x_j}{\sigma_j} [Y_B I_1(\eta_{s_j}, \infty) + (1 - Y_B) I_2(\eta_{s_j}, \infty)] = 0 \end{aligned}$$

Page 142, equation (I-55): The equation should be corrected to

$$\begin{aligned} \sum \dot{Y} &= \frac{\rho_e u_e x_e}{\sigma_e} Y_B [I_1(\eta_{s_e}, \infty) - I_2(\eta_{s_e}, \infty)] - \frac{\rho_j u_j x_j}{\sigma_j} I_1(\eta_{s_j}, \infty) \\ &+ \frac{\rho_j u_j x_j}{\sigma_j} [Y_B I_1(\eta_{s_j}, \infty) + (1 - Y_B) I_2(\eta_{s_j}, \infty)] = 0 \end{aligned}$$

AD-866735-